Nanomechanical Detection of Drug-Target Interactions using Cantilever Sensors

Manuel Vögtli

London Centre for Nanotechnology and Division of Medicine
University College London

Supervisors:
Dr. Rachel McKendry
Prof. Dr. Gabriel Aeppli

Thesis submitted for the degree of
Doctor of Philosophy at University College London

March 2011

I, Manuel Vögtli, confirm that the work presented in this thesis is my own. Where information has been derived from other sources, I confirm that this has been indicated in the thesis.

Abstract

The alarming growth of antibiotic-resistant superbugs including methicillin-resistant Staphylococcus aureus (MRSA) and vancomycin-resistant Enterococci (VRE) is driving the development of new technologies to investigate antibiotics and their modes of action. Novel cantilever array sensors offer a tool to probe the nanomechanics of biomolecular reactions and have recently attracted much attention as a 'label-free' biosensor as they require no fluorescent or radioactive tags and so biomolecules can be rapidly assayed in a single step reaction. Thereby, cantilever-based sensors are unique in the sense that they can measure an in-plane nanomechanical surface stress which is not purely mass dependent.

This thesis reports the label-free detection of drug-target interactions on microfabricated cantilever arrays focusing on the vancomycin family of antibiotics. Vancomycin has remained at the forefront of the battle against MRSA and works by targeting the outer cell wall of bacteria, nevertheless little is known about how the drug binding interactions lead to a large scale mechanical weakening of the cell and consequently cell death by lysis. In this thesis three key developments are reported: (i) the development of experimental protocols and cantilever instrumentation to enable robust, specific and sensitive drug-target measurements in buffer and blood serum, (ii) a detailed investiga-

tion of the nanomechanical transduction mechanism which identified a critical density of surface ligands for the generation of stress and may have important implications on the mechanical mode of action of glycopeptides on the bacteria cell wall, and (iii) the first use of this technology to analyse drug targets on tethered lipid layers that closely mimic the surface of bacteria. These findings and underlying concepts represent major milestones for this promising technology and may also contribute to our understanding of how antibiotics actually kill bacteria and thereby advance the search for a new generation of drugs in the battle against superbug resistance.

Publications

The work that I was doing during my PhD contributed to several scientific papers and a book chapter:

- J. Wafula Ndieyira, M. Watari, A. Donoso Barrera, D. Zhou, M. Vögtli, M. Batchelor, M. A. Cooper, T. Strunz, M. A. Horton, C. Abell, T. Rayment, G. Aeppli and R. A. McKendry, Nanomechanical Detection of Antibiotic-Mucopeptide Binding in a Model for Superbug Drug Resistance, *Nature Nanotechnology*, 3:691-696, **2008**.
- J. Wafula Ndieyira, A. Donoso Barrera, M. Vögtli, D. Zhou, M. Cooper, C. Abell, T. Strunz, G. Aeppli and R. A. McKendry, Surface-Catalysed Dimerisation enhances Drug Action, *manuscript submitted*, **2011**.
- M. Watari, R. A. McKendry, M. Vögtli, G. Aeppli, Y.-A. Soh, X. Shi, G. Xiong, X. Huang, R. Harder and I. Robinson, Differential Stress Induced by Thiol Adsorption on Facetted Nanocrystals, *manuscript submitted*, **2011**.
- M. Tenje, S. Keller, Z. Davis, M. Vögtli, J. Ndieyira, C. Morasso, R. A. McKendry and A. Boisen, Optochemical Nanosensors, chapter 7: Micro/Nano Cantilevers for Bio/Chemical Sensing, Taylor & Francis, *in press*, **2011**.

Acknowledgements

This thesis would not have been possible without the support and encouragement of many people.

A special thank goes to my supervisors Dr. Rachel McKendry and Prof. Gabriel Aeppli for their guidance and inspiration, for always being extremely supportive and for reviewing this thesis.

I must thank Joseph Wafula Ndieyira for his generous character and optimism, as well as for the preliminary work that was the basis of this thesis. He assisted me with many experiments, especially in the beginning of my PhD, which I acknowledged by the use of the first person plural ('we') at the corresponding sections of the thesis. I would like to thank all the other group members, who were always very helpful and a source of inspiration: Moyu Watari for her help concerning the Scentris instrument and XPS measurements; Benjamin Dueck for his help with instrumental issues and our concert visits; Carlo Morasso for his chemical expertise and his nice Italian espresso; Lars Henrik Skjolding for his help in the clean room and his entrepreneurial ideas; Natascha Kappeler for her helpfulness and critical thinking, as well as for the Swiss chocolate; and Anna Dejardin for insights into her computer simulations.

I would like to thank Richard Thorogate for managing the laboratories and consumables; Steve Etienne for the training and support for the equipment in the clean room; and Rosie

Baverstock-West, Denise Ottley and Nipa Patel for the help with any kind of administrative issues.

I would like to thank Emily Smith and Ignacio Villar from University of Nottingham for their support with the XPS measurements and analysis. I am grateful to Paul Mack from Thermo Fisher who enabled me to perform ARXPS measurements at the University of Surrey in Guildford, and to Kerry Wilson who established this contact for me.

I would like to thank Christoph Gerber and Hans Peter Lang from the University of Basel in Switzerland for his kind helpfulness and support during the modification of the NOSE instrument.

I would like to thank Sanjiv Sharma from Imperial College London for the access to the dynamic light scattering system.

I would like to thank Matt Cooper from the University of Queensland in Australia for his support, especially concerning the work with supported lipid layers.

I would like to thank Al Kolb for giving me the opportunity to present our work at several conferences and for his enthusiasm for our work, which was a great motivation to push the technology to a next step.

I would like to thank Lorenz Mayr and Ulrich Hassiepen from Novartis for their invitation to present our work at Novartis and for their fruitful discussions about the potential of the cantilever technology.

I would like to thank Genki Yoshikawa from the National Institute for Materials Science in Tsukuba, Japan, for our discussions and his insights, and for giving me the opportunity to visit his laboratory in Japan.

Not less important, I would like to thank UCL Graduate School and its head Prof. David Bogle for their financial support, namely the scholarships that funded my PhD, a conference travel grant, and the opportunity to attend a summer school.

I would like to thank all the lovely people I met at the LERU summer school in Utrecht, which was an extraordinary experience and a real motivation for the final part of my PhD.

I thank Redbridge Brass, Regent Brass, UCL Orchestra and their members for their friendship and all the wonderful musical adventures I could experience in the UK.

Finally, I would like to thank all members of my family, my girlfriend, all my friends and the [avã'gard] for their constant support, their numerous visits in London, for always welcoming me back in Switzerland, and the nice days / evenings / fondues / holidays / road-trips / concerts I could experience with you!

Contents

List of Figures

List of Tables

Abbreviations

a	Maximum/saturation surface stress
A	Surface area
α	Percolation exponent
AFM	Atomic Force Microscope
ARXPS	Angle-resolved X-ray photoelectron spectroscopy
BSA	Bovine serum albumin
CE	Chloroeremomycin
CHAPS	3-[(3-cholamidopropyl)dimethylammonio]-1-propanesulfonate
CT	Cholera toxin (B subunit)
d	Sample depth from surface
D*Ala*	Mucopeptide analogues terminating in L-Lysine-D-Alanine-D-Alanine (vancomycin suscebtible)
D*Lac*	Mucopeptide analogues terminating in L-Lysine-D-Alanine-D-Lactate (vancomycin resistant)

DLS	Dynamic light scattering
DNA	Deoxyribonucleic acid
E	Young's modulus
ϵ	Strain
ELISA	Enzyme-linked immunosorbent assay
FWHM	Full width at half maximum height (for XPS peaks)
FRET	Fluorescence resonance energy transfer
G	Gibbs free energy
GlcNAc	N-acetylglucosamine
GM1	Ganglioside GM1
Gly HCl	10 mM Glycine HCl pH 2
H	Enthalpy
HEPES	4-(2-hydroxyethyl)-1-piperazineethanesulfonic acid
HDT	Hexadecane thiol
HTS	High-throughput screening
k	Cantilever curvature
K_d	Equilibrium dissociation constant
k_{off}	Dissociation rate
k_{on}	Association rate
L	Cantilever length
L_{eff}	Effective cantilever length
λ	Photoelectron attenuation length
λ	Wavelength of a light beam
L*Ala*	Mucopeptide analogues terminating in L-Lysine-D-Alanine-L-Alanine (stereoisomer of **D*Ala***)
MRSA	Methicillin-resistant *Staphylococcus aureu*s
MurNAc	N-acetylmuramic acid

n	Refractive index
ν	Poisson ratio
ω	Tilt angle of thiols in SAM
OGP	Octyl β-D-glucopyranoside
p	Surface coverage fraction
p_c	Percolation threshold
PC	L-α-phosphatidylcholine
PDB	Protein Data Bank, http://www.pdb.org
PEG	Thiol terminating in triethylene glycol (reference coating)
PSD	Position sensitive detector
PTFE	Polytetrafluoroethylene (Teflon®)
QCM	Quartz crystal microbalance
R	Radius of curvature of cantilever
RU	Response units for SPR systems
S	Entropy
σ	Surface stress
SAM	Self-assembled monolayer
SLD	Superluminescent diode
SPR	Surface plasmon resonance
SUV	Small unilamellar vesicle
t	Cantilever thickness
T	Temperature
θ	Photoelectron take-off angle in XPS setup
$[Van]$	Vancomycin concentration
VCSEL	Vertical cavity surface emitting laser
VRE	Vancomycin-resistant *Enterococci*
VSE	Vancomycin-sensitive *Enterococci*

XPS	X-ray photoelectron spectroscopy
z_{abs}	Absolute deflection of a cantilever
z_{diff}	Differential deflection of a cantilever

CHAPTER 1

Introduction

1.1 Superbugs and a World without Antibiotics

The discovery of the first antibacterial agents *salvarsan* by Paul Ehrlich in 1909 [Ehrlich13] and *penicillin* by Alexander Fleming in 1928 [Fleming29] marked a new area of medicine. Antibiotics not only permit the treatment of various bacterial infections in humans, they also allow a quick recovery after surgery. Nevertheless, bacterial resistance occurred shortly after the introduction of the first antibiotics, so that new and more powerful antibacterial agents had to be discovered [Fernandes06]. By the 1960s a respectable arsenal of antibiotics was available to treat any known kind of bacterial infection. However, due to the extreme adaptability of bacteria, some strains soon became resistant to the most potent antibiotics and antibiotic-resistant 'superbugs' such as methicillin-resistant *Staphylococcus aureus* (MRSA) spread rapidly since the 1980s and 1990s [Taubes08]. At the same time, the discovery of new antibacterial agents became increasingly difficult and therefore the number of new antibiotics that entered the market dropped drastically. The number of deaths

due to MRSA peaked in 2005/06 with more than 1600 cases in England and Wales but fortunately the number fell to less than 50% in 2009[1] thanks to measures of increased hygiene and the intelligent prescription of antibiotics. However, this does not mean that the fight against superbugs was won. Whereas 10 years ago, concern centred on Gram-positive bacteria (MRSA and VRE), clinical microbiologists now increasingly agree that multidrug-resistant Gram-negative bacteria (such as recently reported Enterobacteriaceae with resistance to carbapenem) pose the greatest risk to public health [Kumarasamy10]. A British newspaper put it aptly: *Are you ready for a world without antibiotics?* (The Guardian, 12th August 2010).

One of the most successful antibiotics to date is vancomycin. For fifty years this glycopeptide has remained at the forefront of the battle against superbugs including MRSA. It is a natural product produced by soil bacteria and works by targeting the outer bacterial cell wall, a conserved feature of virtually all bacteria which confers mechanical strength and protection, and is not found in humans. Vancomycin binds to Lipid II mucopeptide precursors that are tethered to the bacterial cell membrane, thereby interfering with cell wall cross linking and leading to cell death by lysis. While the chemical basis of this interaction has been well characterised, the nanomechanical consequences of drug binding (which ultimately kills the bacteria) are much less understood and remain the subject of much clinical and scientific interest. Moreover, the emergence of vancomycin resistant Enterococci (VRE) is an increasing public health problem, triggered by the deceptively simple alteration of the terminal peptide in Lipid II from D-alanine to D-lactate. This deletes a single hydrogen bond from the drug binding pocket, rendering vancomycin therapeutically ineffective. Therefore, there is an urgent need for new technologies to understand the mechanical mode of action of this important family of antibiotics. The aim of my thesis is to develop such a technology based on nanomechanical cantilever sensors in the hope that it will

[1]Data from the Office for National Statistics, http://www.statistics.gov.uk/cci/nugget.asp?id=1067, accessed on 7th January 2011.

advance the search for a new generation of superdrugs to tackle emerging infectious diseases (fig. 1.1).

1.2 Drug Discovery: both Blessing and Curse

Medications are indispensable in our modern society. They help us cure or ameliorate symptoms of an illness or help us recover after an accident or surgery. As mentioned above, antibiotics are a prime example of drugs and contributed significantly to the increase in life expectancy in the last century. The drug discovery process for a modern drug is very cost intensive and involves several steps [Cooper02], as summarised in figure 1.2. The screening of molecular interactions for the determination of the affinity, activity, toxicity and prediction of *in-vivo* availability of drug candidates is central to the drug discovery process. Since the 1990s, pharmaceutical companies invested huge amounts of money and attention to the development of high-throughput screening (HTS) methods in order to screen the enormous libraries of compounds generated by combinatorial chemistry. Despite these large investments, the HTS method did not deliver the expected results [Dove03] and the number of newly approved drugs was notably low in the last decade. Therefore, big pharma shifted their attention towards a deeper understanding of drug targets in order to get more information from their screening processes. This paradigm is driving the development of new drug discovery methods and technologies to satisfy the everlasting demand for new and improved drugs against recurring medical problems (e.g. antibiotic resistance) and against emerging diseases of the modern society (e.g. diabetes, cancer, depression).

1.3 Nanomechanical Sensors: a Promising Tool for Drug Discovery

Conventional drug screening methods require some type of fluorescent or radioactive labelling of a reporter molecule to measure the binding of a ligand to its receptor, often

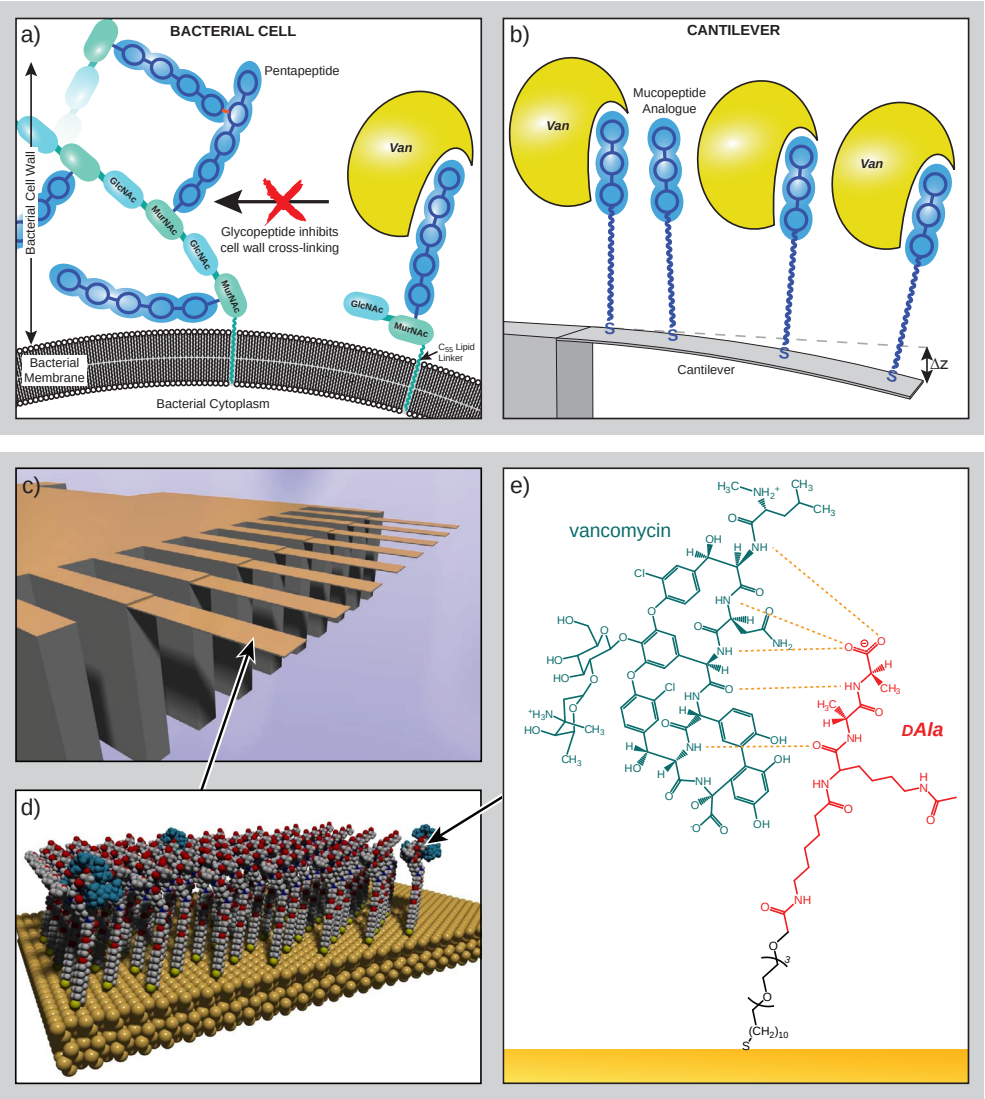

Figure 1.1: Overview of the nanomechanical detection of vancomycin-mucopeptide interactions on cantilever arrays. ***(a)*** *Schematic showing the mode of action of vancomycin on bacteria and* ***(b)*** *the concept to mimic these binding interactions on cantilever sensors. Vancomycin binds specifically to the mucopeptide analogues on the cantilever surface, thereby generating a compressive stress and a downwards bending of the cantilever.* ***(c)*** *Drawing showing a cantilever array. Each cantilever is 500 μm long, 100 μm wide and 0.9 μm thick.* ***(d)*** *Self-assembled monolayers of mucopeptide analogues were tuned to optimise the cantilever sensitivity and to understand the generation of surface stress.* ***(e)*** *The chemical binding interaction between vancomycin and the bacterial mucopeptide analogue.*

in connection with a competitive or enzymatic binding assay [Cooper02]. Labelling of biomolecules is not only time-consuming and expensive, the label can also interfere with the molecular interaction by obstructing the binding site, leading to false negatives. In addition, fluorescent compounds are often hydrophobic which can lead to background binding and false positives. Due to these limitations, there is an increasing interest in novel label-free techniques that allow virtually any complex to be screened with minimal assay development [Cooper03]. Improvements in instrumentation and experimental design allow a wide variety of interactions to be analysed which is leading to an increased applicability for the drug discovery processes (fig. 1.2). The most established label-free technologies at present are surface plasmon resonance (SPR) and quartz crystal microbalance (QCM), however nanomechanical cantilever array sensors recently emerged as a promising biosensing platform. Cantilever sensors are special in the sense that their sensitivity does not rely purely on a mass change due to the analyte binding but rather on a change in in-plane nanomechanical surface stress, making the technology uniquely suited to study the nanomechanics of antibiotic drug-target interactions and a complementary tool in drug discovery. Moreover, due to their compatibility with microfabrication processes, cantilevers can be miniaturised for improved sensitivity and parallelised into large arrays of cantilevers for multiple

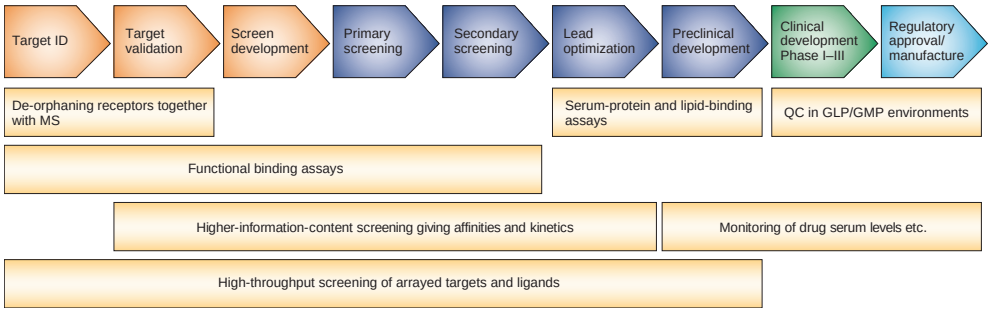

Figure 1.2: Outline of the drug discovery process. *Application areas for label-free biosensors are highlighted below the stages of the drug discovery process. GLP = Good Laboratory Practice; GMP = Good Manufacturing Practice; ID = identification; MS = mass spectrometry; QC = quality control. (Figure adopted from [Cooper02].)*

drug screening and higher throughput. Detailed information about cantilever sensors, their mode of operation and their advantages will be given later in chapter 3.

The method used in this thesis works by coating cantilevers with a self-assembled monolayer that mimics the outer surface of bacteria. When antibiotic molecules are injected over the cantilever surface, they bind to the cell wall peptide analogues, thereby leading to a change in surface stress and the bending of the cantilever (fig. 1.1). It is assumed that this surface stress arises due to steric and electrostatic repulsion between the bound complexes on the cantilever surface. More recently, a percolation model has been proposed [Ndieyira08] which describes the surface stress in terms of chemical and geometric factors. The chemical factor describes local drug-target binding in terms of the Langmuir adsorption isotherm, and the geometric factor describes the large scale mechanical consequences of the formation of a stressed network. It is speculated that nanomechanical percolation may play an important role not only in sensor response but also in the glycopeptide antibiotic mode of action in real bacteria, whereby drug-target binding events may act collectively to disrupt the bacterial cell wall leading to bacterial cell death.

While the first multiple cantilever experiments by Ndieyira *et al.* [Ndieyira08] nicely illustrate the power of this technology to study drug-target interactions, there are many challenges involved in transforming these promising laboratory experiments into a robust drug discovery tool. Key outstanding questions include: What is the specificity and sensitivity of this approach to quantify drug-target interactions and can it operate in blood serum? Can we learn more about the underlying mechanism by which nanometre scale drug-target interactions are transformed into large scale mechanical damage of the bacterial cell wall in terms of a percolation model? Particularly, what is the role of drug dimerisation and the surface ligand density? Can miniaturisation of the fluidics reduce the quantity of drug and time needed per assay? Are cantilevers compatible with lipid-membranes that most closely mimic the outer surface on real bacteria? The aim of this thesis is to investigate these challenges and ultimately

advance this promising technology to the stage where it can search for the next generation of powerful new antibiotics needed to combat resistant infections.

1.4 Thesis Overview

This thesis is focuses on the development of cantilever technology for drug-discovery and to study the nanomechanical transduction mechanism of glycopeptide antibiotics on bacterial cell wall targets. To this end, my thesis is structured as follows:

Chapter 2 gives an overview of antibiotic development with a particular emphasis on vancomycin, antibiotic dimerisation and the bacterial cell wall structure.

Chapter 3 is a summary of cantilever sensors including their mode of operation, geometries, readouts and a literature review of different applications.

Chapter 4 is a review of the formation and properties of self-assembled monolayers (SAMs), focusing on alkanethiols which are commonly used to tailor cantilever sensors.

Chapter 5 is the Materials and Methods chapter and details the different cantilever instruments, sample preparation protocols and data analysis used in this work. It also contains a review of the different surface characterisation techniques employed in this thesis.

Chapter 6 is the first results chapter and reports several important advances in cantilever technology for drug discovery, namely a study of the uniformity of surface stress along the cantilever beam, optimised washing and regeneration protocols to enable quantitative thermodynamic binding analysis and the first measurements in blood serum.

Chapter 7 reports the investigation of antibiotics in terms of a percolation model. This involved repeating previous work by Ndieyira and Watari and the first analysis of the dimerising antibiotic chloroeremomycin.

Chapter 8 is a detailed systematic investigation of the role of the underlying sensing film on the magnitude of surface stress using complementary surface analysis methods to disentangle the role of ligand density, orientation and drug binding.

Chapter 9 reports the development of an improved cantilever sensor instrumentation for the analysis of drug-target interactions, thereby minimising the sample volume and duration of measurements, and enabling kinetic analysis.

Chapter 10 reports the first use of lipid membrane coated cantilevers to study drug-target interactions. Initial work uses the choleratoxin-ganglioside model system and then the first attempts to investigate a synthetic lipid II target are described, representing the closest mimic of the outer surface of real bacteria studied to date on cantilever arrays.

Chapter 11 is the final chapter and summarises the key findings in this thesis and outlines my ideas for future work.

Additionally, equation derivations and XPS depth profiles are included in the appendix together with gas phase thiol adsorption measurements that I performed to complement the measurement of strain on nanocrystals (Robinson *et al.*, manuscript in preparation, 2011).

CHAPTER 2

Antibiotics

2.1 Introduction

Antibiotics are therapeutic agents with activity against microorganisms such as bacteria or fungi. Nowadays they help us to fight bacterial infections and thus play a vital role in clinical practice. However, the recent emergence of antibiotic-resistant bacteria and the lack of new and potent antibiotics puts us at risk to return to a phase comparable to the pre-antibiotic era [Fernandes06].

This chapter gives a historical perspective of the discovery and development of antibiotics, the emergence of bacterial resistance and the challenges facing the pharmaceutical industry. It introduces the vancomycin family of glycopeptide antibiotics and their biological target – the bacterial cell wall. Finally, I present their nanomechanical mode of action and the mechanism of resistance, which highlights the need for a better understanding of the antibiotic - cell wall interaction.

2.2 History of Antibiotics

The birth of the antibiotic era was in 1928 when Alexander Fleming discovered an interesting phenomenon on a Staphylococcus culture plate he has put aside on the laboratory bench for a while. Due to exposure to air these plates were contaminated by a mould. The mould was forming colonies itself and the Staphylococci around the mould colonies were undergoing lysis [Fleming29]. Similar phenomena had been observed earlier but Fleming was the first who interpreted this by the activity of a bacteriolytic substance produced and secreted by the mould. The mould was identified as *Penicillium rubrum* and thus Fleming was calling this substance *penicillin*. Although he was aware that such a substance would be highly useful if it would kill pathogenic bacteria in humans, the development of penicillin as a practical therapeutic agent took more than 10 years, largely due to the pioneering work of Florey, Chain and coworkers, and was not launched until 1942 [Lee Ligon04].

The success of penicillin showed people that many natural antibiotics may be awaiting discovery and thus in the 1940s and 50s many antibacterial drugs were found and developed [Hopwood07, Fernandes06, Taubes08] (see timeline in fig. 2.1). By the 1960s, however, the rate of discovery of natural antibiotics fell dramatically and the development of new antibiotics focused mainly on semi-synthetic derivatives of natural products. But 20 years later this approach also seemed to be exhausted and pharma concluded that nature had given up nearly all her treasures [Fernandes06]. In the early 1990s they reverted to their origins, that is synthetic chemistry, and tried their luck with combinatorial chemistry and high-throughput screening of small drug libraries. Unfortunately this strategy yielded only a very poor return for antibacterial agents so that today research is often returning to more traditional approaches and revisiting older and natural products [Singh06].

In parallel with the decrease in development of new antibiotic classes since the 1960s, the occurrence of antibiotic-resistant bacteria increased rapidly (see timeline in fig. 2.1). This alarming trend is continuing until today and the emergence of multi-drug-resistant bacteria such as methicillin-resistant *Staphylococcus aureus* (MRSA) and

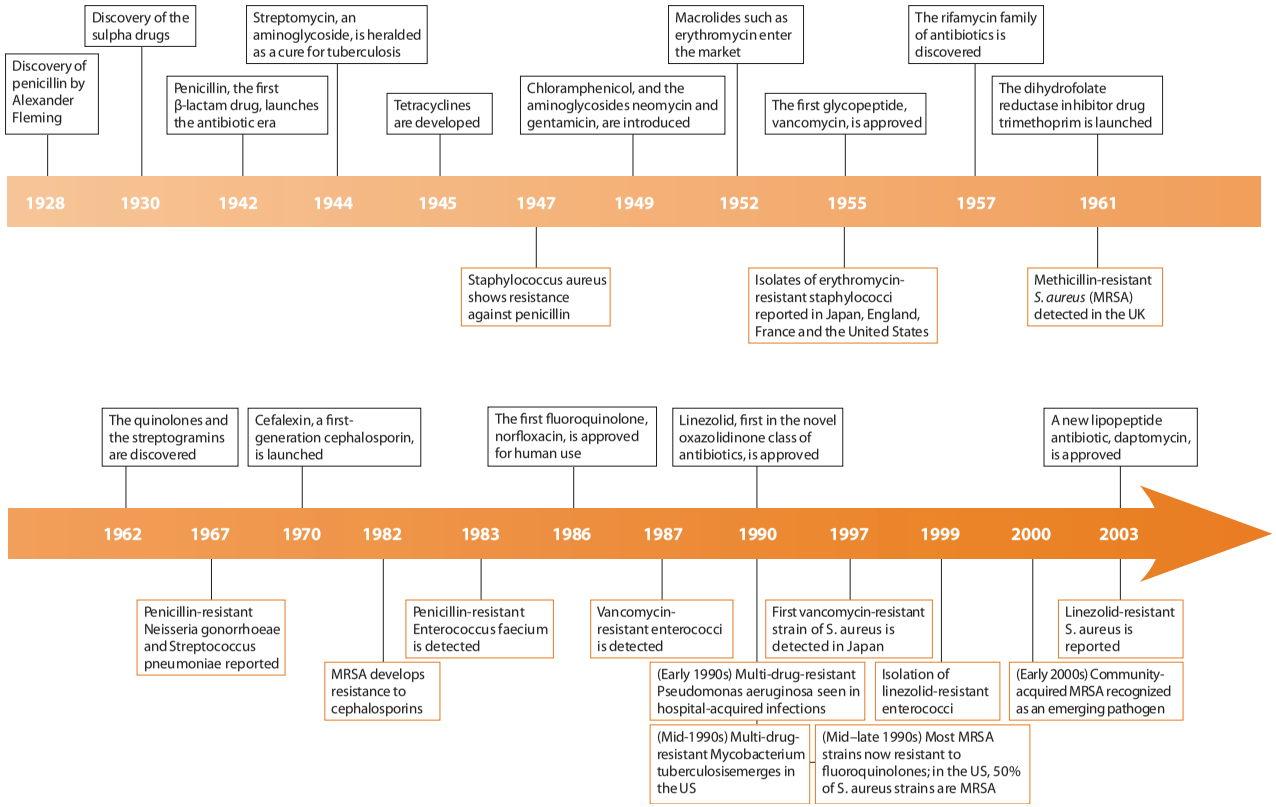

Figure 2.1: Antibiotics timeline. *Black boxes (above arrow) indicate milestones in antibiotic drug development and the orange boxes (below arrow) indicate landmarks in the evolution of bacterial resistance. (Illustration from [Hopwood07].)*

vancomycin-resistant *Enterococci* (VRE) represents a real clinical problem [Taubes08]. For example in England and Wales the number of deaths due to MRSA has jumped from 51 in 1993 to 1,652 in 2006 but then fell to 781 in 2009[1]. The reasons for this trend are diverse and complex [Hopwood07, Fernandes06, Christoffersen06]. Of course bacteria are prone to mutations by nature [Cox76] but the overuse of antibiotics in the past has also intensified this behaviour by applying a selective pressure to the bacteria [Fernandes06]. The lack of new antibiotics entering the market cannot only be explained by technological challenges. It is rather that the risk for pharmaceutical industry to invest into the development of new antibiotics is too high [Christoffersen06] because of its high costs and poor return compared to drugs for chronic diseases, as antibiotics are usually taken only for a week. Furthermore, if a powerful new antibiotic would be launched, clinicians would not subscribe it generously but rather keep it as a last remedy to avoid the rapid development of resistance by bacteria. And last but not least, antibiotics are a risky investment because there is a lack of regulatory guidance for clinical trials and they have to fulfil very high safety hurdles where virtually no side effects are accepted [Opar07].

2.3 Composition of Bacteria and Formation of Bacterial Cell Wall

In order to understand the action of antibiotics and the challenges in antibiotic development, I will give a short overview about bacteria. I will also introduce the processes behind the formation of the bacterial cell wall, a remarkable material that will be subject of interest for this thesis.

The general structure of bacteria consists of a cell membrane that surrounds the cytoplasm and acts as a barrier for ions and organic molecules [Madigan01]. Inside the cell we find the typical cell components such as RNA, plasmids, proteins, ribosomes

[1] Data from the Office for National Statistics, http://www.statistics.gov.uk/cci/nugget.asp?id=1067, accessed on 7th January 2011.

and nutrients. Due to the high turgor pressure inside bacterial cells, bacteria are enclosed by a cell wall that provides mechanical strength. We distinguish between Gram-positive and Gram-negative bacteria. Whereas Gram-positive bacteria consist of a single plasma membrane and cell wall, Gram-negative bacteria have an inner and outer cell membrane that comprise the periplasmic space including a thin cell wall. Here, we concentrate on Gram-positive bacteria because they are in the focus of interest of this thesis (fig. 2.2a).

The bacterial cell wall consists of peptidoglycan, a rigid polymer that provides structural strength and shape to the bacteria. Without this rigid shell, bacteria would burst due to their high turgor pressure, a weakness that is exploited by some antibiotics as explained later. The peptidoglycan itself is made up of chains of alternating sugar units of *N*-acetylglucosamine (GlcNAc) and *N*-acetylmuramic acid (MurNAc) cross-linked by short peptides (fig. 2.2b). The constitution of the peptide can vary but for gram-positive bacteria usually takes the form of L-Ala-D-Glu-L-Lys-D-Ala-D-Ala. The cross-linking of these pentapeptides is achieved by binding of the D-Ala-D-Ala to the lysine group of another chain whereby the terminal alanine is lost. Sometimes the alanine binds directly to the lysine, however often a peptide bridge is present as a linker (e.g. a chain of 5 glycine amino acids attached to the lysine in the case of *Staphylococcus aureus*).

The biosynthesis of the peptidoglycan involves several intra- and extracellular steps (fig. 2.3). The GlcNAc-MurNAc-pentapeptide is synthesised inside the bacterial cell, linked to the bacterial cell membrane and then flipped to the external side of the bacterium [vanHeijenoort01]. The sugar backbone is then polymerised to long chains (transglycosylation) and finally cross-linked via the peptides to form a rigid mesh-work (transpeptidation).

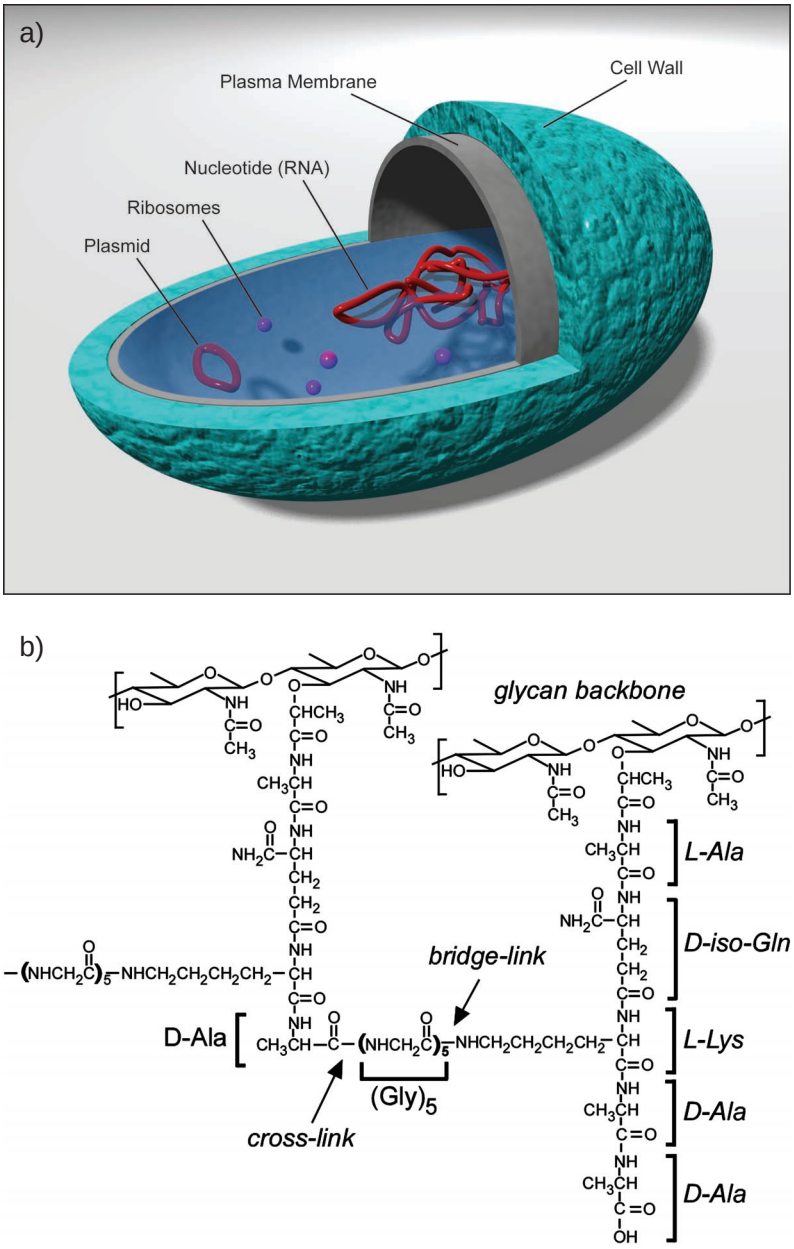

Figure 2.2: Composition of bacteria and the bacterial cell wall. *(a) Representation of a Gram-positive bacterium showing the cell content, cell membrane and cell wall. (b) Chemical structure of a peptidoglycan fragment of S. aureus. Two GlcNAc-MurNAc-pentapeptides are shown in their cross-linked state. The* $(Gly)_5$ *peptide bridge can be different in other bacteria or can be missing completely. (Subfigure (b) adapted from [Kim08].)*

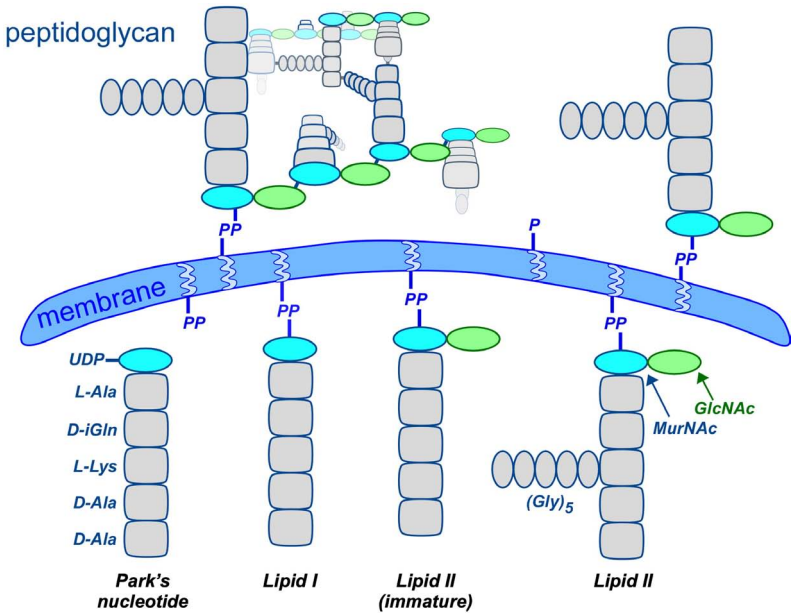

Figure 2.3: Schematic representation of peptidoglycan biosynthesis. *The UDP-MurNAc-pentapeptide (Park's nucleotide) is synthesised inside the cytoplasm and then linked to the inner side of the bacterial cell membrane via undecaprenyl phosphate (lipid I). After the addition of GlcNAc and an optional peptide bridge (lipid II) the complex is flipped to the external side of the membrane, followed by polymerisation and cross-linking. UDP = uridine diphosphate. (Figure adapted from [Kim08].)*

2.4 Glycopeptide Antibiotics

Glycopeptide antibiotics are natural compounds active against Gram-positive bacteria and are produced by several genera of actinomycetes [Malabarba97]. Vancomycin is the archetype of this class of antibiotics and is still nowadays one of the most powerful antibiotics on the market [Williams99]. It is mainly used for staphylococcal bacterial infections such as MRSA [Fishman03]. Derivatives of vancomycin that were used or mentioned in this work are chloroeremomycin and oritavancin (formerly known as LY333328), the latter of which is a semi-synthetic derivative [Allen97].

A multitude of different glycopeptide antibiotics have been identified and all consist of a heptapeptide core of seven amino acid residues (fig. 2.4) [Barna84,

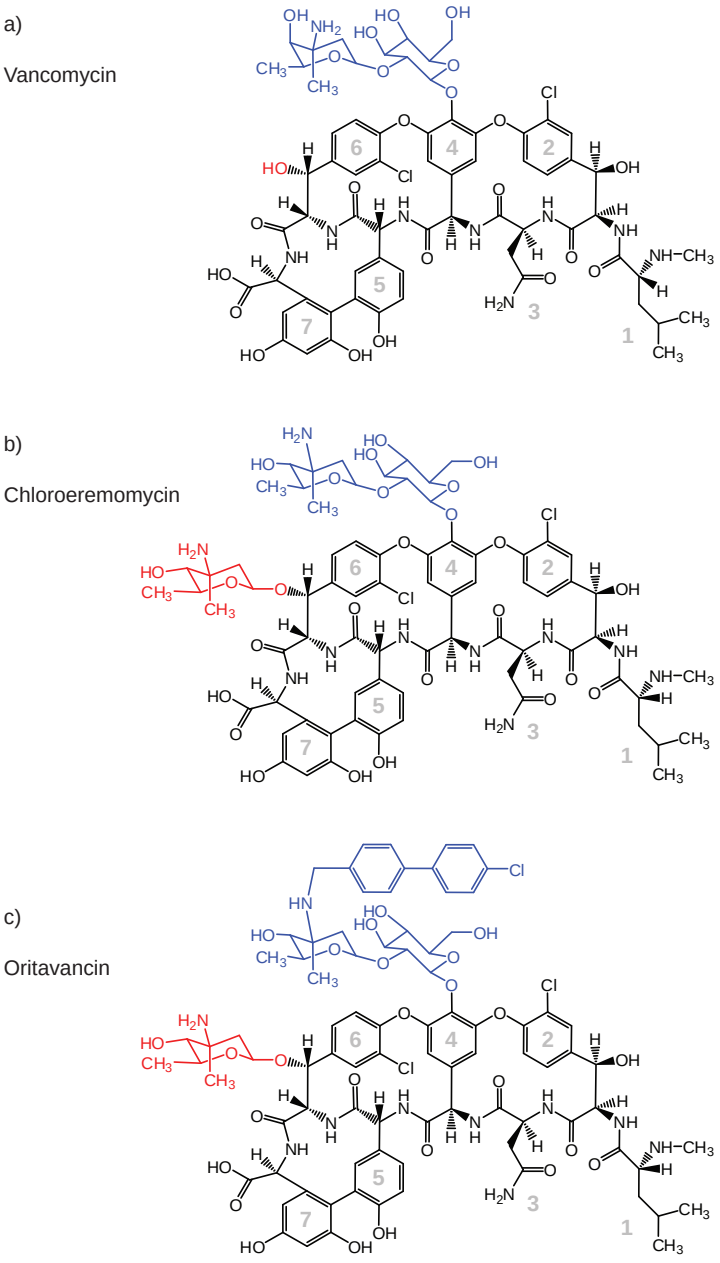

Figure 2.4: Overview of glycopeptide antibiotics used in this thesis. ***(a)*** *Vancomycin.* ***(b)*** *Chloroeremomycin.* ***(c)*** *Oritavancin. The only differences between those antibiotics occur in the side groups highlighted in colour. Residue numbers of the seven amino acids backbone are displayed in grey.*

Malabarba97]. The side chains of residues 2 and 4, 4 and 6, and 5 and 7 are covalently cross-linked and there are sugar substituents at various positions depending on the type of antibiotic. Glycopeptide antibiotics are classified into groups I – III based on the type of residue at positions 1 and 3 [Loll00]. Vancomycin, chloroeremomycin and oritavancin all belong to group I. The difference between those three compounds is found in the substituents at residues 4 and 6 [Malabarba97]. Whereas vancomycin has a glucosyl-vancosamine sugar at residue 4 and no sugar at residue 6, chloroeremomycin has a glucosyl-4-*epi*-vancosamine at residue 4 and an additional 4-*epi*-vancosamine sugar at residue 6 (fig. 2.4a/b). Oritavancin is derived from chloroeremomycin but has a *p*-chlorophenylbenzyl added to the 4-*epi*-vancosamine at residue 6 (fig. 2.4c) [Allen97].

2.5 Mode of Action and Bacterial Resistance

The antibacterial activity of vancomycin and other glycopeptide antibiotics results from the inhibition of the bacterial cell wall formation [Allen03, Williams96, Williams99]. Vancomycin binds to the cell wall peptides (mucopeptides) terminating in D-Ala-D-Ala and thus blocks transglycosylation and transpeptidation [Perkins69, Allen03, Kahne05]. This in turn prevents the formation of the bacterial cell wall and hence bacteria lose their mechanical strength and undergo lysis.

The structure of vancomycin and its binding interactions with the mucopeptide precursor have been extensively studied by X-ray crystallography [Schäfer96, Loll97, Loll98, Nitanai09] and NMR [Williams84, Williams83]. The strong binding affinity is based on three different types of interactions within the binding pocket (fig. 2.5a-c):

- Binding of the mucopeptide's C-terminal carboxylate anion with three amide NH groups of the antibiotic.
- Two C=O ---- H–N hydrogen bonds between the antibiotic backbone and the backbone of the mucopeptide precursor.

- Hydrophobic interactions formed by the alanine methyl groups in their proximity to the hydrocarbon portions of the antibiotic.

The 3-dimensional models in figure 2.5a/b illustrate the shape of vancomycin and show the pocket for the binding of the mucopeptide precursors. The five hydrogen bonds which are stabilising the interaction are nicely displayed in figure 2.5b.[2]

Since its introduction into clinical use, vancomycin has always been one of the most potent antibiotics. Historically, because no bacteria had developed resistance against it, vancomycin has been at the forefront of the fight against MRSA. In 1988, however, vancomycin-resistant *Enterococci* were reported for the first time [Uttley88] and since then such infections are becoming increasingly common. Resistant enterococci have mutated in a way that mucopeptide precursors no longer terminate in D-Ala-D-Ala, but rather terminate in D-Ala-D-Lac [Bugg91]. Enterococci have obtained a set of five genes (*vanS,R,H,A,X*) from other bacteria which enables them to switch from the expression of D-Ala-terminating peptides to D-Lac-terminating peptides in the presence of vancomycin [Walsh96, Arthur92, Arthur96]. Table 2.1 summarises the activity and function of the proteins encoded by these genes. This transition from D-Ala to D-Lac is a deceptively simple change because it only involves the exchange of an amide with an ester. However, this substitution deletes one hydrogen bond of the antibiotic-mucopeptide binding interaction and instead places a repulsive oxygen-oxygen interaction at this location (fig. 2.5d). This substitution lowers the binding affinity of the antibiotic to the mucopeptide precursor by a factor of ~ 1000 which makes vancomycin ineffective for clinical use [Allen03].

The way in which bacteria have formed resistance against vancomycin and drastically reduced the binding affinity of vancomycin suggests that other glycopeptide antibiotics may not be able to exhibit useful activity against such bacteria. However, some vancomycin derivatives show an astonishingly high activity against VRE

[2]Those vancomycin-pentapeptide models were derived from an X-ray crystallography structure [Nitanai09] (protein data bank ID: 1FVM, http://www.rcsb.org/pdb). Chimera software from University of California in San Francisco (http://www.cgl.ucsf.edu/chimera) was used to display the models.

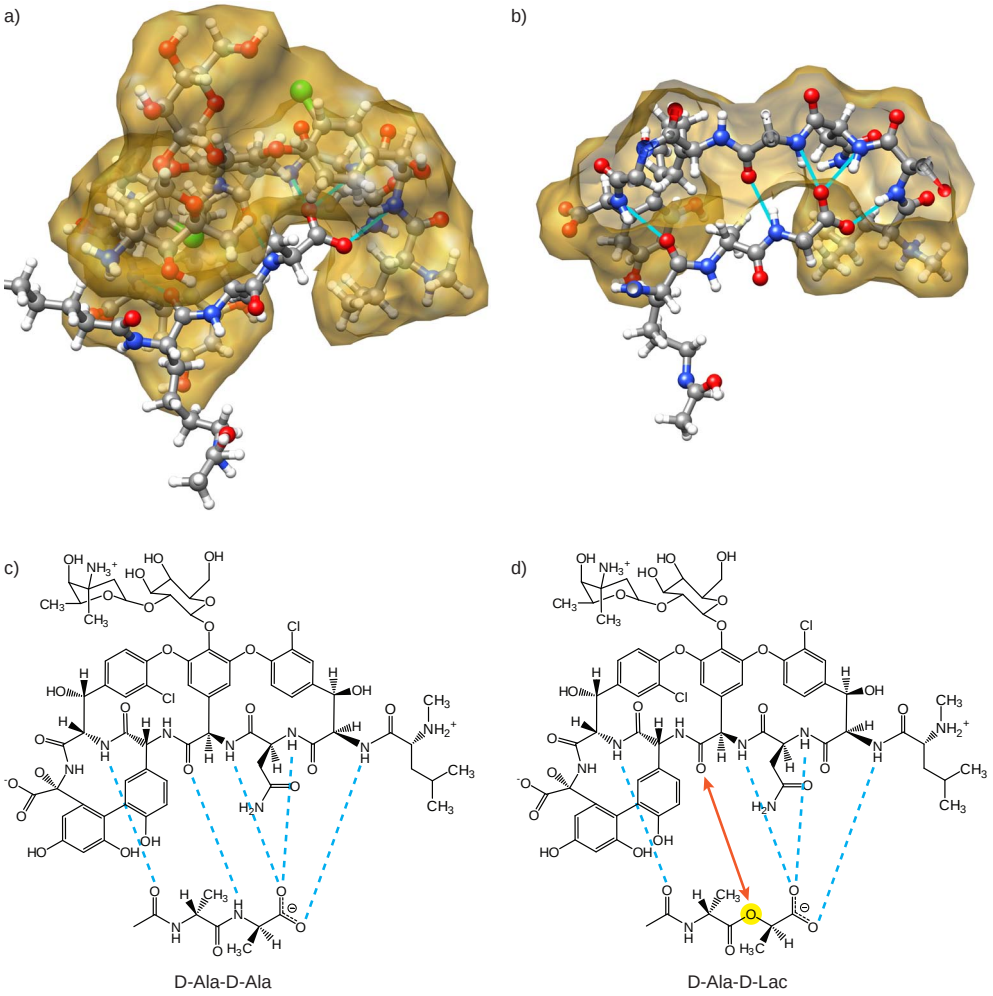

Figure 2.5: Binding interaction between vancomycin and the mucopeptide precursor terminating in* D*-Ala-*D*-Ala, and the mechanism of bacterial resistance.** ***(a) *3-dimensional model of vancomycin bound to the mucopeptide. A surface (brown) is added to vancomycin to highlight its shape and the binding pocket.* ***(b)*** *A cross section through (a) shows nicely the interaction of the vancomycin backbone with the mucopeptide. The five hydrogen bonds are shown in cyan.* ***(c)*** *Schematic representation of the vancomycin-mucopeptide binding interaction with the five hydrogen bonds (cyan).* ***(d)*** *The exchange of the mucopeptide's terminal* D*-Ala with a* D*-Lac replaces an amide by an ester (yellow circle). This simple change adopted by vancomycin-resistant bacteria deletes one hydrogen bond (orange arrow) and renders the antibiotic ineffective for clinical use.*

Table 2.1: *Activities and functions of the products of the five* van *genes that are necessary and sufficient for vancomycin resistance (adopted from [Walsh96]).*

Protein	**Activity**	**Function**
VanS	Transmembrane histidine kinase	Sensor protein that initiates signal transduction pathway
VanR	Two-domain response regulator	Accepts $PO_3{}^{2-}$ group from phospho-VanS, activates *vanH,A,X* transcription
VanH	D-Specific α-keto acid reductase	Generates D-lactate required for VanA action
VanA	Depsipeptide ligase for D-Ala-D-lactate	Generates an ester D-Ala-D-lactate in competition with normal amide D-Ala-D-Ala
VanX	Zn^{2+}-dependent D-Ala-D-Ala dipeptidase	Selective removal of D-Ala-D-Ala allows accumulation of D-Ala-D-lactate for addition to growing UDP-muramyl-tripeptide

[Malabarba97]. Because those derivatives share the same backbone and binding pocket, other effects such as cooperativity must play a crucial role. And indeed it is known that some glycopeptide antibiotics tend to spontaneously form back-to-back dimers in solution [Waltho89] (fig. 2.6). For example chloroeremomycin has a higher tendency to form dimers than vancomycin and it has also a higher potency against VRE [Mackay94]. Oritavancin takes the concept of cooperativity one step further [Allen03]. In this semi-synthetic derivative of chloroeremomycin, a hydrophobic *p*-chlorophenylbenzyl chain was added to the sugar residues, which enables the antibiotic to be anchored to the lipid membrane of the bacteria [Allen97]. This anchoring, together with a very high dimerization affinity, makes oritavancin a very potent agent against vancomycin resistant bacteria.

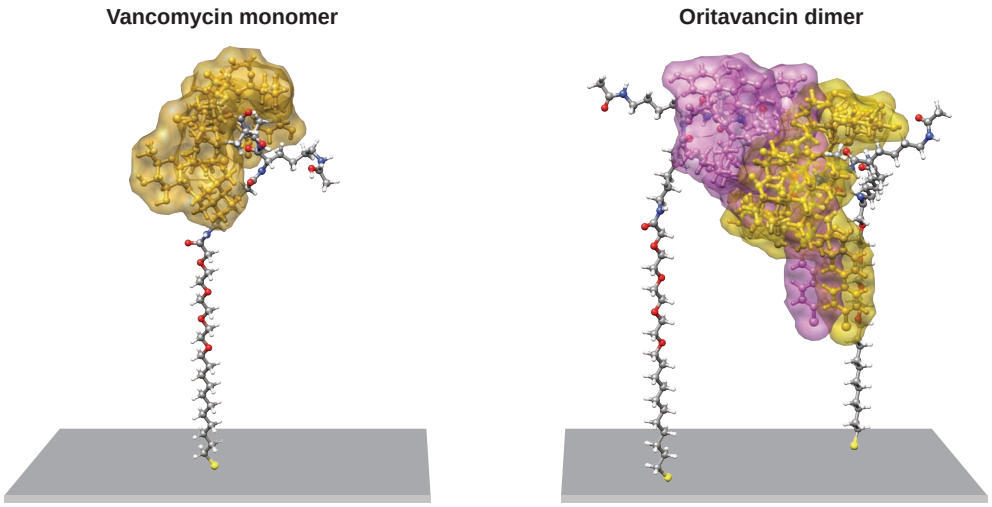

Figure 2.6: Illustration of antibiotic dimerisation. *A vancomycin monomer and an oritavancin dimer are displayed. They are bound to cell wall peptide analogues tethered to a surface.*

CHAPTER 3

Cantilever Sensors

3.1 Introduction

Cantilevers are a novel kind of sensor based on nanomechanical interactions. They integrate two fundamental fabrication concepts from nanotechnology, on the one hand the *top-down* approach used in microfabrication and on the other hand the *bottom-up* approach for self-assembly of molecular layers.

This chapter introduces the concepts of cantilever arrays as a biosensing platform. The different modes of operation are described, as well as the principle of surface stress, which is the cause for the cantilever deflections. I present variations in cantilever geometry and different approaches for the readout of cantilever deflection. Moreover, the chapter gives a literature review about the diverse applications of cantilever sensors in biomedical analysis, diagnostics and environmental monitoring. Finally, I will focus on the measurement of surface stress and review the current theories of the origin of stress on cantilever arrays.

3.2 General Concept of a (Bio)Sensor

Any kind of sensor can be divided into three parts (fig. 3.1). The *sensing part* specifically recognizes a designated signal which is transferred to the *recorder* via a *transducer*. The transducer is the most variable part of a sensor and can work in an optical, electrical, magnetic, thermal, chemical or mechanical manner. Prominent examples in the field of biosensors are surface plasmon resonance (SPR) which uses an optical transducer [Cooper02], glucose sensors using electrochemical technology [Oliver09], and quartz crystal microbalance (QCM) using an electromechanical transducer [Janshoff00]. In contrast, cantilever sensors work in a purely mechanical manner and transduce a biochemical binding event into a nanomechanical signal.

Cantilever array sensors offer some advantages over other bioassay techniques. However, at the moment it should not be regarded as a magic tool that is better than everything else on the market. Instead, it is a complementary technology which has potential as a drug-screening tool in the future. A main advantage of cantilever sensors is that they work label-free, meaning that they can detect drug-target interactions in a rapid single-step process without the need for fluorescent or radioactive labelling in contrast to many well established techniques such as fluorescence resonance energy transfer (FRET), enzyme-linked immunosorbent assays (ELISA) or microarrays. Cantilever sensors are very sensitive and are able to detect analyte solution concen-

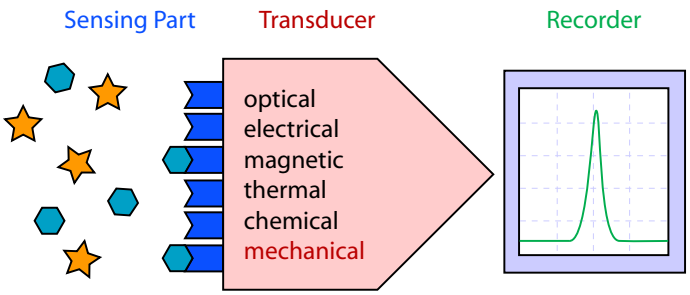

Figure 3.1: Set-up of a general sensor. *It is composed of a specific sensing part, a variable transducer and a recorder. In the case of the cantilever array sensor, the transducer works mechanically.*

trations in the picomolar range for strong binding interactions. Compared to other label-free techniques such as SPR and QCM, the sensitivity of cantilever sensors is not limited by mass but cantilever bending is caused by changes of in-plane forces on their surface. This can be an advantage for the detection of small molecules which is the basis of pharmaceutical industry. In addition, surface forces are a nanomechanical phenomenon and may reflect the mode of action of many drug-target interactions, where a binding event triggers a conformational change in the receptor molecule. Moreover, this mechanical information may prove vital to understand the mode of action of drugs such as vancomycin since the mechanical damage in the outer bacterial cell wall introduced by the antibiotic is what actually kills bacteria. Cantilever sensors consist of arrays of multiple cantilevers, which allows the use of *in-situ* reference cantilevers in order to assure the specificity of a signal. Furthermore, due to its miniature dimensions, compatibility with low-cost microfabrication techniques and capability of integration with microfluidics, cantilever sensors have potential for applications in high-throughput screening of drug-target interactions or as miniaturised point-of-care devices in medical diagnostics [Johnson08].

3.3 Modes of Operation

The core of a cantilever sensor is a microfabricated silicon chip comprising typically eight very thin silicon bars, so-called cantilevers (fig. 3.2a/b). Those cantilevers are usually about 500 μm long, 100 μm wide and only 0.3 - 1.0 μm thick. Due to those microscopic dimensions, cantilevers become very flexible and can be elastically deformed without breaking. This property constitutes the cantilever as the actual sensor unit, whereby tiny bendings of the cantilever due to molecular interactions occurring on the cantilever surface are measured. In order to be able to detect these tiny bendings a laser beam is targeted to the free end of the cantilever which is reflected and then recorded by an optical detector (position sensitive detector, PSD). Due to optical scaling laws, a nanometre-scale bending of the cantilever will lead to a micrometre-

scale deflection of the laser beam. One laser beam is needed for each cantilever of the array but one PSD is sufficient if the lasers are controlled in a time-multiplexed manner [Lang98, Lang05] (fig. 3.2c/d).

If a cantilever is coated with a specific sensing layer ('functionalized'), it can act as a sensor for various kinds of external factors such as pH, temperature, DNA or proteins [Lang05, Fritz08]. In addition, if several differently functionalized cantilevers are placed side by side, the device is sensitive to a multitude of distinct analytes. In our case, we functionalized the cantilevers with thiolated mucopeptide analogues which can be tethered to a gold layer on the cantilever surface by thiol-gold surface chemistry (fig. 3.3). If antibiotics bind to those peptides, intermolecular forces lead to a surface stress and a downward bending of the cantilever [Ndieyira08]. The ability to functionalize every cantilever specifically gives us the opportunity to measure multiple signals in parallel. The use of *in-situ* reference cantilevers allows differential measurements for an improved robustness of the system.

There exist two main modes in which cantilever sensors can be operated: *static mode* and *dynamic mode* [Lang02]. The cantilever experiments described in this thesis were performed in static mode only but for reasons of completeness the following sections will describe the physical principles of both modes.

3.3.1 The Static Mode

The transduction mechanism of a cantilever sensor operated in the static mode relies on changes in surface stress upon adsorption of target molecules on the cantilever surface. The molecular interactions that are leading to this surface stress include steric competition, charge effects, swelling, mechanical expansion, structural changes or a combination of them (this will be discussed more in section 3.9).

Thereby, the static mode relies on an asymmetry effect and it is important that the cantilevers are functionalized on only one side, otherwise the surface stresses of both sides would cancel each other out. If the molecular interactions upon analyte binding are repulsive, the microcantilever bends away from the functionalized side (downwards

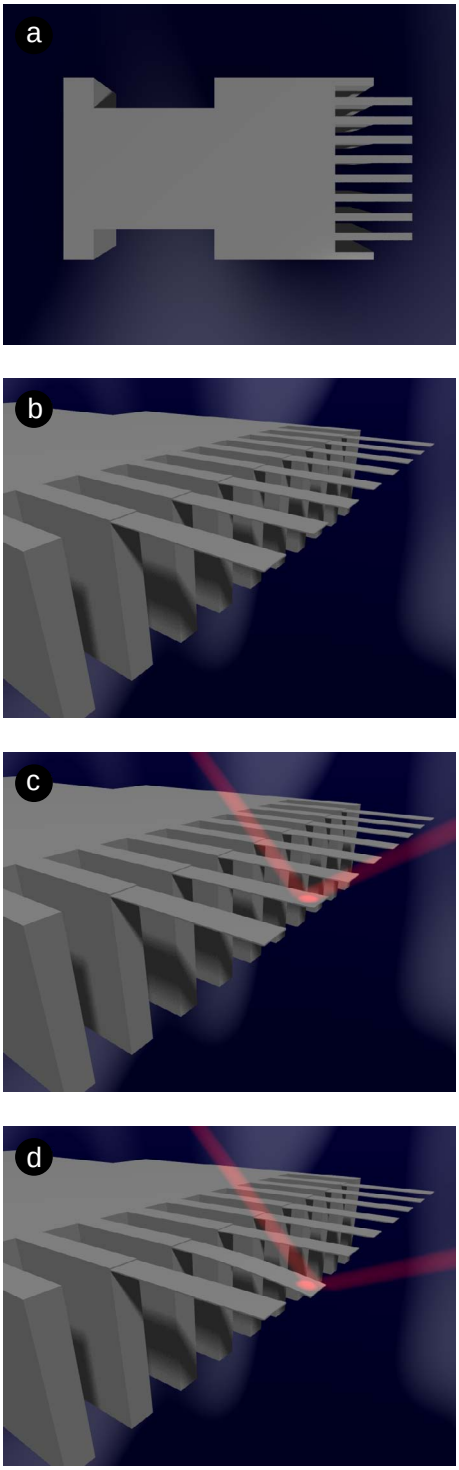

Figure 3.2: Illustration of the dimensions and the readout of cantilever sensors. ***(a)*** *The microfabricated silicon chips typically consist of eight cantilevers that are 500 μm long, 100 μm wide and 0.9 μm thick.* ***(b)*** *From a side-view it is visible how thin those cantilevers are, which makes them very flexible.* ***(c)-(d)*** *The cantilevers are the actual sensor unit. During binding experiments, tiny deflection of the cantilevers due to reactions occurring on the surface are measured. In order to be able to detect these deflections, a laser beam is targeted at the free end of the cantilevers. If the cantilevers bend, the laser beam will be redirected which can be measured with an optical detector.*

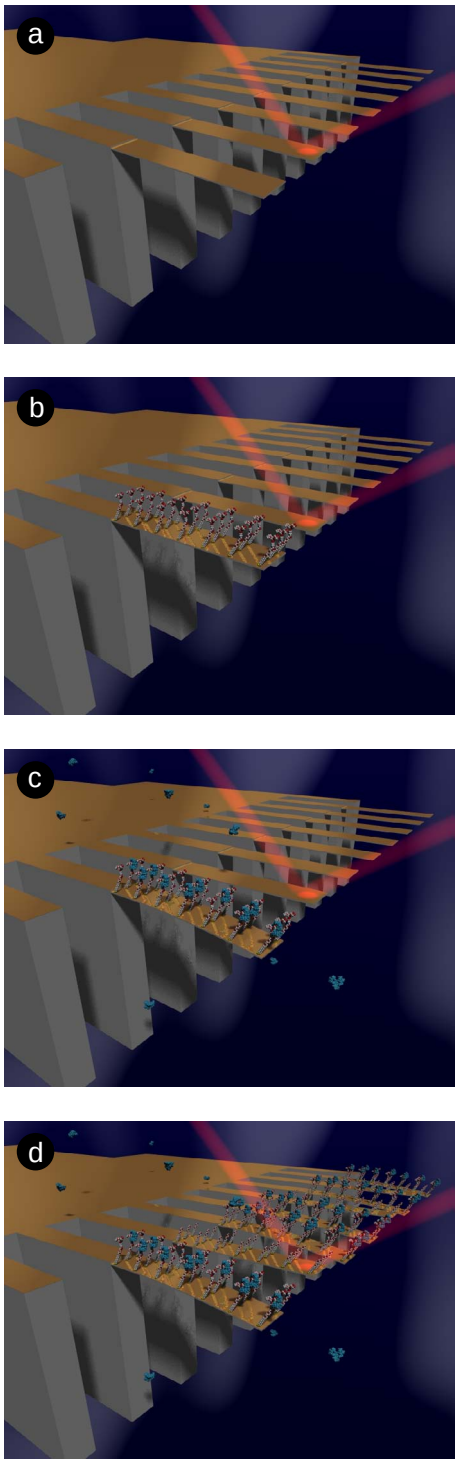

Figure 3.3: Mode of operation of cantilever sensors. *In order to be able to detect a specific biochemical signal, cantilevers need to be functionalized with a sensing layer.* ***(a)*** *In a first step a 20 nm thin layer of gold is evaporated onto the upper side of the chip.* ***(b)*** *In a second step thiolated molecules with a specific recognition site can be added to the gold layer to form a self-assembled monolayer by thiol-gold surface chemistry. In this thesis we used mucopeptide analogues (consisting of three terminal amino acids mimicking the bacterial cell wall peptides) with a chemical linker terminating in a thiol.* ***(c)*** *When antibiotics are injected into the measurement chamber, they bind to the mucopeptide analogues on the cantilever. This leads to a surface stress on the functionalized side of the cantilever due to intermolecular forces, resulting in a downwards bending of the cantilever.* ***(d)*** *Eight cantilevers in parallel can be functionalized individually with different targets. This allows multiple measurements to be performed simultaneously with an* in-situ *reference (PEG coated cantilevers).*

if the functionalization layer is on the upper side of the cantilever), producing a so-called *compressive* surface stress. In the opposite case, attractive intermolecular forces lead to an upwards bending of the cantilever and a so-called *tensile* surface stress. (Theoretical details about the concept of surface stress will be given in section 3.4.)

A special case of static mode is the *heat mode*. If a silicon cantilever are coated with a layer of another metal such as gold, it is subject to a bimetallic thermal effect. Because of the larger thermal expansion coefficient of gold compared to silicon, the gold layer is expanding more than the silicon substrate when the temperature is increased, leading to a downwards bending of the cantilever. The opposite happens when the temperature is decreased. We use this thermal effect for the calibration of the cantilever system after the alignment of the read-out lasers.

3.3.2 The Dynamic Mode

In the dynamic mode the cantilevers are treated as mechanical oscillators. Mass changes can be determined by actuating a cantilever at its eigenfrequency. If an analyte molecule binds to the functionalization layer on the cantilever, the mass of the cantilever-ligand complex increases, resulting in a shift of the cantilever's eigenfrequency to a lower value. The mass change on a rectangular cantilever [Thundat94] can be approximated as

$$\Delta m = \frac{k}{4\pi^2} \cdot \left(\frac{1}{f_1^2} - \frac{1}{f_0^2} \right) \tag{3.1}$$

where k is the cantilever's spring constant, f_0 is the initial eigenfrequency and f_1 is the eigenfrequency after the adsorption of the analyte. The dynamic mode works well in vacuum or air but poses a challenge in liquid environment because of strong damping of the cantilever oscillation due to the high viscosity of the surrounding medium, which results in a low quality factor. Furthermore, the adsorption of molecules on the cantilever surface can result in a change in stiffness of the cantilever, which can lead to an opposite effect, i.e. a shift of the eigenfrequency to higher values.

3.4 The Concept of Surface Stress

3.4.1 Surface Free Energy and Surface Stress

The properties of solid surfaces compared to liquid surfaces are fundamentally different. If a solid surface is stretched, the amount of surface atoms remains constant because they are aligned with the underlying bulk (elastic deformation). By contrast, if a liquid surface is stretched atoms from the interior can flow freely to the surface (plastic deformation). Due to these different concepts for the formation of surface area, we need two different thermodynamic units to describe these processes: the *surface free energy* and the *surface stress*[1] [Haiss01].

Surface Free Energy

A surface atom has a higher potential energy than a bulk atom because it has fewer neighbouring atoms and therefore experiences fewer energetically favourable attractive interactions. If new surface area is created, for example by cutting a crystal into two pieces, the total energy of the system must increase. This increase in surface energy can simply be quantified by $F \cdot A$, where F is the (Helmholtz) surface free energy per unit area and A is the created surface area [Shuttleworth50].

Surface Stress

Surface stress is the work per unit area that is needed to elastically stretch a pre-existing surface [Haiss01]. To understand the relation between surface free energy and surface stress, we consider the reversible paths illustrated in figure 3.4 according to [Shuttleworth50, Haiss01]. In the first path (a $\rightarrow$ b $\rightarrow$ c), a solid is first cut into two unstrained pieces which are then elastically strained. In the second path (a $\rightarrow$ d $\rightarrow$ c), the solid is first elastically strained and then cut into two pieces. If the two paths are

[1] In the case of liquids, where surface free energy and surface stress are the same, the term *surface tension* is used often.

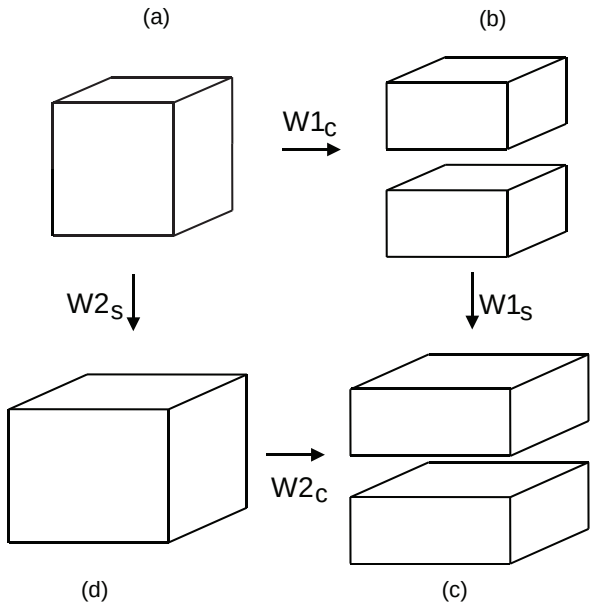

Figure 3.4: Schematic illustrations to demonstrate the concepts of surface energy and surface stress. *Two reversible paths are shown to create strained surfaces with a total area A from an unstrained volume element (adopted from [Haiss01]).*

assumed to be reversible, the corresponding energies $W1_C + W1_S$ and $W2_S + W2_C$ must be equal and we can write

$$W2_C - W1_C = W1_S - W2_S \tag{3.2}$$

The left-hand side of this equation represents the difference in surface free energy when the strained and the unstrained solid are cut, that is $F(\epsilon)A(\epsilon) - F_0A_0$. The right-hand side represents the work performed against the surface stress, as four surfaces are strained in path 1 but only two surfaces in path 2 (the bulk strain is the same for both paths). We can therefore write

$$F(\epsilon)A(\epsilon) - F_0A_0 = \int A_0\sigma_{ij}d\epsilon_{ij} \tag{3.3}$$

where σ_{ij} is the surface stress tensor and ϵ_{ij} is the strain tensor with $\epsilon = dA/A$. (The subscripts i and j indicate the direction – x, y, or z – of the applied and observed stress, respectively.) This can be written in the differential form

$$d(FA) = A_0\sigma_{ij}d\epsilon_{ij} \tag{3.4}$$

Because $d(FA) = FdA + AdF$ and $dA = A_0\delta_{ij}d\epsilon_{ij}$ (where δ_{ij} is the Kronecker delta, equal to zero for $i \neq j$ and equal to unity for $i = j$) this finally gives

$$\sigma_{ij} = F\delta_{ij} + \frac{dF}{d\epsilon_{ij}} \tag{3.5}$$

which is the so-called Shuttleworth equation [Shuttleworth50].

3.4.2 Cantilever Bending

The cantilever bending method is used to perform measurements of adsorbate-induced surface stress (static mode). The changes in cantilever curvature can be described by a difference in surface stress between its upper and lower surface [Haiss01]. The concept of surface stress-induced cantilever deflection can be understood as follows: Before adsorption takes place (fig. 3.5a), it is assumed that the magnitudes of surface stress on both sides are equal and do not induce a bending of the cantilever. When chemisorption occurs exclusively on one side of the cantilever, the difference in surface stress $\Delta\sigma = \sigma^t - \sigma^0$ induces a bending moment and cantilever deformation.

Some simplifications are made for the analysis of the cantilever deformation. It is assumed that the bending of the cantilever is very small compared to its dimensions. The length of the cantilever has to be large compared to its width, which itself is large compared to its thickness. Furthermore, the adsorbate layer is assumed to be very thin compared to the thickness of the cantilever and therefore its material properties are negligible. It is also assumed that only components of stress which act in the x direction (i.e. along the cantilever axis, see fig. 3.5b) determine the bending in the x-z plane, and that the cantilever holder does not exert any forces on the cantilever.

The bending shape of a cantilever in the x-z plane can be described as a section of a circle with radius R since the surface stress and bending of the cantilever is constant along the x axis. The strain $\epsilon_{xx}(z)$ induced in the cantilever can be written as

$$\epsilon_{xx}(z) = \frac{z - t_0}{R} \tag{3.6}$$

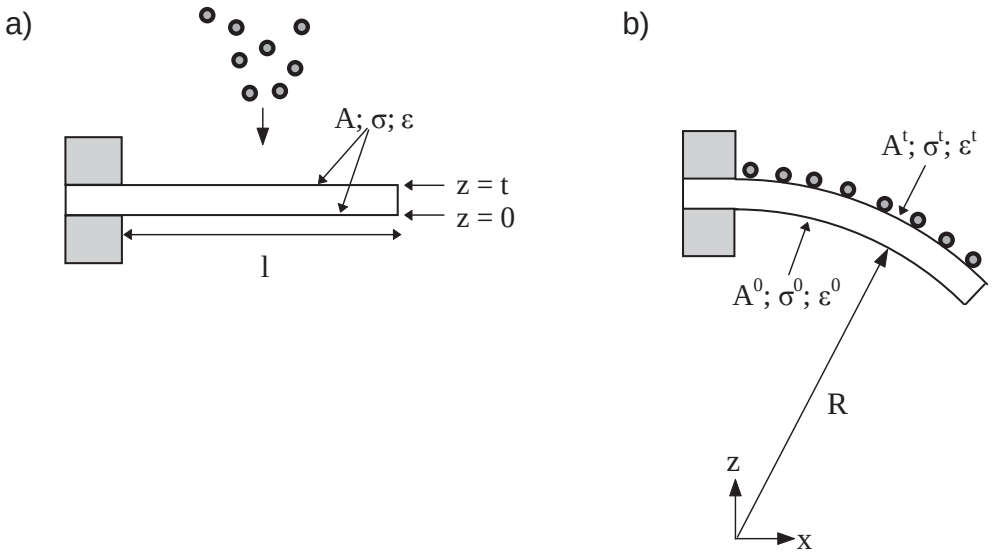

Figure 3.5: *Schematic of setup to measure adsorbate induced surface stress with the bending cantilever method. (Figure adopted from [Haiss01].)*

where t_0 is the distance of the unstrained plane within the cantilever from the cantilever's lower surface A_0. The bulk stress in x direction $\Sigma_{xx}(z)$ is then given by

$$\Sigma_{xx}(z) = \frac{E}{1-\nu}\epsilon_{xx}(z) \tag{3.7}$$

where E is the Young's modulus and ν is the Poisson ratio of the cantilever material. Using these two equations, Stoney's equation [Stoney09] can be derived (see [Haiss01] for details):

$$\sigma^t_{xx} - \sigma^0_{xx} = \frac{Et^2}{6R(1-\nu)} \tag{3.8}$$

This can be expressed in terms of the cantilever curvature $k = 1/R$ and the change in surface stress between the upper and lower side of the cantilever $\Delta\sigma = \sigma^t_{xx} - \sigma^0_{xx}$ to give

$$\Delta\sigma = \frac{Et^2}{6(1-\nu)}k \tag{3.9}$$

which relates the change in surface stress to the material properties and cantilever curvature.

3.5 Cantilever Materials and Geometries

Initial experiments with cantilever sensors used conventional AFM (atomic force microscope) cantilevers. With the emergence of cantilever sensors at a tool for (bio)chemical sensing, special arrays of cantilevers with purpose-made cantilever geometries were designed[2]. Up to the present, cantilevers with many different shapes, dimensions, sensitivities and materials have been reported.

The cantilever geometry is usually based on a rectangular or triangular shape that is connected to a supporting chip body, however many variations to these basic geometries are known (fig. 3.6). The width and length of cantilevers are normally in the range of tens to hundreds of micrometres and the thickness is around 1 μm or less. Therefore, the thickness is small compared to length and width, resulting in a high surface-to-volume ratio which is characteristic for nanomechanical cantilevers. Cantilevers are micro-fabricated with polycrystalline silicon, silicon oxide, silicon nitride or – more recently – polymers such as SU-8 [Keller10]. Spring constants are generally in the range of 0.001 – 10 N/m and depend on the application.

3.6 Multiple Cantilever Arrays

During the early developments of cantilever sensors, a lot of work was reported using single cantilever experiments [Gimzewski94, Berger97]. These measurements are problematic because non-specific effects can dominate the cantilever bending. Thanks to the development of multiple cantilever arrays, differential measurements can be performed using *in-situ* reference cantilevers [McKendry02]. Simultaneous and parallel measurements are vital to overcome convoluting effects due to changes in temperature, drift of the signal, changes in refractive index or interactions occurring

[2]There are fundamental differences in the functionality of cantilevers for AFM and chemical sensing, which should be considered when designing the cantilevers. In AFM applications, cantilevers are subject to a point force at the free end of the cantilever beam. Contrarily, in chemical sensing applications, a uniform surface stress is distributed over the whole cantilever surface.

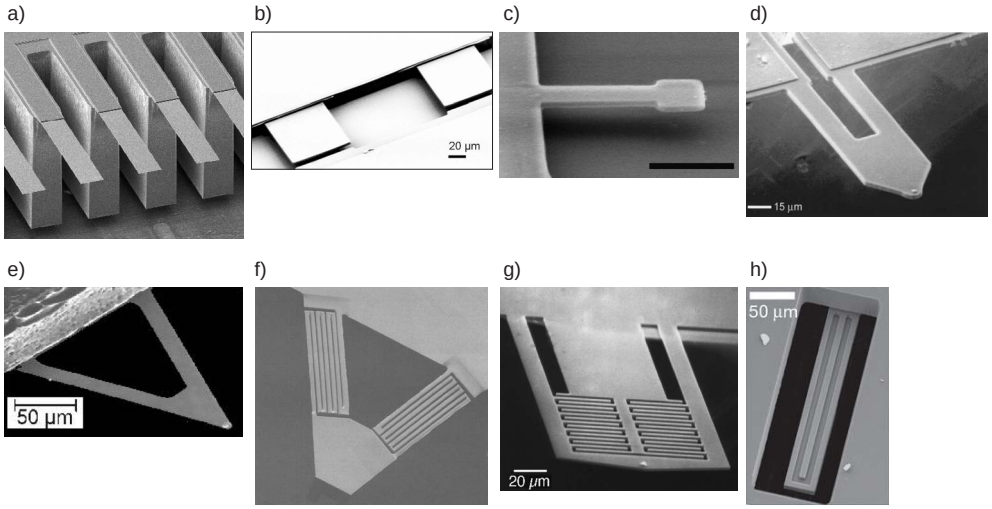

Figure 3.6: Overview of different cantilever geometries. *(**a**) Rectangular cantilevers that were used in this thesis. (**b**) Rectangular SU-8 cantilevers inside a microfluidics channel [Nordström08]. (**c**) Rectangular cantilever with a paddle for mass sensing [Ilic04]. (**d**) Cantilever with two legs [Lavrik04]. (**e**) Triangular cantilever [Raiteri02]. (**f**) Special triangular cantilever for improved calorimetric performance [Lavrik04]. (**g**) Cantilever design with interdigitated sensing and reference cantilever [Yaralioglu98]. (**h**) Cantilever beam with built-in microfluidics channel [Burg07].*

at the underside of the cantilever. Moreover, the choice of the reference coating is crucial and has to be considered carefully for every experiment in order to mimic the mechanical and chemical properties of the active sensing layer as well as possible and still resist the binding of the analyte.

3.7 Cantilever Deflection Readouts

Several read-out methods have been described for the detection of cantilever bending and the operation of cantilever sensors [Raiteri01, Lavrik04] and will be reviewed in this section.

3.7.1 Optical Readouts

The optical lever technique is the original readout method that was used for the AFM [Meyer88] and has been applied successfully to cantilever sensors [Gimzewski94]. A laser beam is targeted at the free end of a cantilever and is reflected onto a position sensitive detector (PSD). If the cantilever bends, the position of the laser beam on the PSD changes which can be measured electronically. The optical lever method was used in the cantilever experiments described in this thesis and will be described in more detail in chapter 5.

More sophisticated optical methods used interferometric techniques [Helm05, Kelling09, Wehrmeister07]. In simple words, a light beam is split into a measuring and reference beam. The measuring beam is reflected on the cantilever surface and then combined again with the reference beam, which results in a typical interference pattern due to phase shifts. This interferogram also allows the calculation of the bending profile of a cantilever and not only the deflection at the free end. Furthermore, this technique is extremely sensitive and can be used on very small cantilevers.

Other optical methods for the readout of cantilever deflections include the tracking of diffraction patterns that are generated when a cantilever is entirely illuminated by a laser beam [Dueck10], or the use of an embedded optical waveguide inside a cantilever [Nordström07].

3.7.2 Piezoresistive Readout

Piezoresistive materials change their conductance when they are strained mechanically. If such a material is embedded in a cantilever, its electrical properties can be used to detect changes in cantilever deflection [Tortonese93, Mukhopadhyay05, Wee05, Rowe08, Yoshikawa09]. The sensitivity of piezoresistive readout depends highly on the materials and geometry. So far, sensitivities around 10 – 50 nm have been reported but are expected to be improved in the near future. The advantage of piezoresistive cantilevers is that the detector can be directly embedded into the cantilever which

would be ideal for portable devices and allows the analysis of opaque liquids such as blood. The main disadvantage so far is the low sensitivity.

3.7.3 Capacitive Readout

Capacitors can store energy between two plates that are separated by a dielectric medium, whereby the capacitance changes when the distance between these electrodes changes. If the cantilever is used as electrode and placed in parallel to a counter electrode, the cantilever deflection can be measured by tracking the change in capacitance [Brugger92, Britton00, Amirola05]. This method has very good resolution of about 10 pm but is usually limited to applications in gaseous environments.

3.7.4 MOSFET Readout

Another readout scheme uses a metal-oxide semiconductor field-effect transistor (MOSFET) embedded into cantilevers [Shekhawat06, Tark09]. Here, the channel mobility changes when the surface is strained, which can be detected by a change in drain current. This method has a resolution in the nanometre range which should be good enough for most biological applications.

3.8 Applications of Cantilever Sensors

Cantilevers are a very versatile sensor platform due to their compatibility with various media (vacuum, gas, liquid) and their static or dynamic modes of operation through which fundamentally different responses can be measured. Dynamic mode cantilevers can sense small changes in resonant frequencies due to adsorbed mass or changes of the viscosity or density of the surrounding medium. Static mode takes advantage of a particular asymmetry effect: If only one side of the cantilever is coated with an application-specific sensing layer, the cantilever bends upon adsorption of molecules or chemical modifications of the sensing layer. The bending of the cantilevers can have many reasons such as electrostatic repulsion, steric repulsion, hydration forces or

interactions with the substrate causing a redistribution of surface charge [Godin10b, Hagan02].

More than 100 publications, most of them in the last 10 years, have described various applications of cantilever sensors. In this section some of the most typical applications will be described.

3.8.1 Chemical Sensors

One of the simplest applications of cantilever sensors is the sensing of the pH of a solution. Cantilevers coated with self-assembled monolayers (SAMs) terminating in an amino- or carboxyl-group can be used as a pH sensor. The functional end groups protonate or deprotonate depending on the pH of the solution, and can generate a surface charge which then leads to the cantilever bending [Watari10].

Other applications include the detection of ions and chemicals in a liquid solution. For example the detection of Ca^{2+} ions was reported using cantilever sensors [Cherian02]. In another example, cantilevers functionalized with horseradish peroxidase were able to sense hydrogen peroxide [Yan06].

For the detection of various solvent vapours, cantilevers have been coated with different polymer layers [Baller00]. Depending on the analyte molecules the polymers exhibit characteristic swelling behaviours and different solvents could therefore be discriminated using principal component analysis.

3.8.2 Biomedical Analysis and Drug discovery

Medical research still relies mostly on assays that require the labelling of targets (i.e. fluorescence) or multi-step preparation procedures (i.e. ELISA). Emerging label-free technologies allow for the investigation of biological reactions, such as drug-target interactions, in a simple single-step assay.

Different approaches have been reported for the label-free detection of biomolecules on cantilevers. One report demonstrated the specific binding of Taq DNA polymerase to cantilevers coated with DNA aptamers [Savran04]. Another application used single-

chain Fv antibody fragments as receptor molecules on cantilevers which have the specificity to bind different peptides [Backmann05]. Cantilevers coated with double-stranded DNA oligonucleotides exhibited the ability to probe the transcription factors SP1 and NF-κB [Huber06]. All these applications demonstrated sensitivities in the nanomolar range or below. For the work described in this thesis and for previous work in our group, we used sensor surfaces coated with special thiols that model the bacterial cell wall to investigate the binding of the glycopeptide antibiotic vancomycin [Ndieyira08]. In nature, these antibiotics bind to bacterial cell wall precursors, therefore inhibiting the formation of the bacterial cell wall and lead to lysis of bacteria. Cantilever sensors are a unique tool to study these drug-target interactions as they are measuring in-plane surface forces due to antibiotic binding, which are thought to be involved in the destabilisation of the cell wall of live bacteria.

Some attempts have been made towards the investigation of membrane proteins on cantilever sensors. Membrane proteins are central to many biological processes and are the targets of many drugs. However, measuring interactions with membrane proteins remains difficult. Initial experiments demonstrated the feasibility to form supported bilayers on cantilevers [Pera07]. The subsequent insertion of the pore-forming peptide melittin revealed a change in surface stress. Another research group coated cantilevers with the model trans-membrane protein bacteriorhodopsin in liposomes and reported a change in surface stress upon induction of conformational changes in this protein [Braun06]. Subsequent cantilever experiments showed the binding of T5 bacteriophages to liposomes with FhuA receptors from *Escheria coli* [Braun09].

An innovative cantilever design with an incorporated microfluidic channel allowed for the measurement of mass and growth rates of single cells [Godin10a]. This technology will prove beneficial to the study of cellular responses to different growth factors or drugs.

3.8.3 Medical Diagnostics

Omnipresent concerns about increasing healthcare costs and the urge towards personalized medicine stimulate the need for improved medical diagnostic devices. Cantilever technology offers a novel tool to detect a multitude of biomarkers in a simple and quick way, and positions itself as a promising technology for future medical and point-of-care applications.

The detection of DNA hybridisation on a cantilever was amongst the first biological applications of cantilever sensors and is probably the best characterized and understood biological application of cantilevers [Fritz00, Hansen01, McKendry02, Mukhopadhyay05, Stachowiak06]. Cantilever surfaces were coated with single-stranded DNA oligomers and upon hybridisation of the complementary strand, a surface stress was measured. Thereby, this method is sensitive enough to discriminate between single base mismatches in the DNA strands. This technique was then used to detect mRNA biomarker transcripts in a complex background which positions the cantilever technology as a promising candidate for a label-free gene expression diagnostics device without the need for target amplification [Zhang06].

In the context of applications in gaseous environments, cantilevers coated with different polymers that exhibit distinct swelling properties when exposed to different vapours were able to discriminate between breath samples of healthy persons and persons with diabetes or uremia. This opens possibilities for diagnosing some diseases by a non-invasive and simple breath test [Schmid08, Lang09]. Furthermore, the specific detection of glucose or ethanol in liquid using cantilever technology could also be used as simple diagnostic or monitoring tests [Pei04, Kim09].

The recent trend towards personalized medicine demands the detection of specific cardiac or cancer biomarkers to make an early diagnosis of the possibility for heart attacks or cancer. The prostate specific antigen (PSA) has been detected using cantilever sensors, even in the background of human serum proteins [Wu01a]. Additionally, cantilever sensors detected the prostate cancer biomarker AMACR directly in patient urine [Maraldo07]. Other examples include the detection of the cardiac

biomarker proteins creatin kinase and myoglobin [Arntz03], as well as C-reactive proteins [Wee05].

In a fundamentally different application cantilevers were coated with a nutritive layer that served as a platform to study the growth of bacteria [Gfeller05]. As the bacteria divide and proliferate, the resonance frequency of the cantilever decreases. With this method the growth of *E. coli* could be detected within one hour which is a huge improvement compared to current bacterial culture plates. If antibiotics are added to the nutritive layer this allows quick testing of the bacteria's susceptibility to certain antibiotics which would help to prescribe the correct antibiotic to patients.

3.8.4 Environmental Sensors

Due to their versatility, small size and robustness, cantilever sensors can be used to monitor several environmental factors. Cantilever-based sensors have been shown to detect toxic and harmful gases that can escape in laboratory or industrial production environments, such as hydrofluoric acid [Mertens04] or hydrogen cyanide [Porter07]. Different cantilever applications recognised small amounts of heavy metals which can be a major hazard to nature. These include the detection of Pb^{2+} using hydrogel swelling on cantilevers [Liu04] or detection of Cd(II) on an antibody-modified cantilever [Velanki07].

Cantilevers have also been applied to sense explosives like TNT [Pinnaduwage04] or the nerve agent simulant dimethyl-methylphosphonate DMMP [Voiculescu05]. In the context of biological weapons and pathogenic microorganisms, it has been shown that *Bacillus subtilis* (a simulant of *Bacillus anthracis* which causes anthrax) can be captured on cantilevers using selective peptide substrates [Dhayal06]. Another report demonstrated the feasibility to detect epidemic viruses using cantilevers coated with anti-viral antiserum. The technology could measure an exposure to the severe acute respiratory syndrome associated coronavirus (SARS CoV) which caused a serious worldwide epidemic in the year 2002 [Velanki06]. Recently, the detection of *Giardia lamblia* cysts in non-filtered water sources using cantilever sensors was reported

[Xu10]. This parasite causes giardiasis, a diarrheal infection with high prevalence in developing countries. This application exemplifies the potential of cantilever sensors to monitor drinking water supplies within a portable device.

3.9 Current Theories for the Generation of Surface Stress

Although several biosensing applications have been reported on cantilever sensors in recent years, the understanding of the molecular forces behind the generation of surface stress is lacking behind this development. Only very recently some papers have been published on these issues.

The most detailed work on this topic has been done for the formation of alkanethiol monolayers on gold substrates. Although this is not directly associated with a biosensing application but rather with the formation of the sensing layers, it might provide us with valuable knowledge. Srinivasan *et al.* [Srinivasan08] reported that a bare gold surface has an intrinsic tensile stress (2.88 N/m) due to the electronic structure of the surface atoms. The sulphur atoms of adsorbed thiols remove electronic charge from the gold surface and therefore lead to a local stress relief. As we are usually measuring changes in surface stress on cantilevers, a relief in tensile stress would be regarded as a compressive stress. Godin *et al.* [Godin10b] took up this model and compared it to other possible interactions that can play a role in the formation of alkanethiol SAMs. They predicted that Lennard-Jones interactions between the thiol molecules (attractive van der Waals forces or repulsive forces due to Pauli exclusion) have a low impact on the surface stress compared to experimental results. Furthermore, electrostatic repulsion between Au-S dipoles are expected to have a much lower impact than the surface stress measured experimentally. They therefore proposed that the major factor for the generation of surface stress is the redistribution of the electronic structure of substrate surface atoms. Recently it has also been revealed that a special Au-adatom-thiolate (R-S-Au-S-R) structure is involved in the formation of thiol SAMs

[Maksymovych10, Li10]. This structural rearrangement of the gold surface might also play a role in the generation of surface stress.

The situation becomes more complex when we are looking into chemical or biological sensing applications on cantilevers. Moreover, every application has to be discussed separately, as different effects play a role for different sensing systems. Sushko [Sushko09] reported a model for surface stress generated by pH-sensitive carboxy-terminated alkanethiol SAMs and suggests that for this system pure electrostatic repulsion due to charged carboxy-groups could generate the surface stress which was measured experimentally. She also adopted this model for DNA hybridisation on cantilever sensors and showed that the volume charge density produced by DNA strands can account for the surface stress measured experimentally. These results were in agreement with a paper from Stachoviak *et al.* [Stachowiak06] who showed that the surface stress scales with the grafting density of DNA strands. Nevertheless, this field remains the subject of much interest and debate. For example Wu *et al.* [Wu01b] even measured a tensile surface stress upon DNA hybridisation and attributed this to configurational entropy, i.e. steric effects (dsDNA is stiffer than ssDNA and adopts a different conformation). Hagan *et al.* [Hagan02] on the other hand proposed that hydration forces play a dominant role in the surface stress generation during DNA hybridisation, and electrostatic repulsion and conformational entropy reveal only minor effects. The effect of hydration forces was later shown experimentally by Mertens *et al.* [Mertens08]. Nevertheless, under constant humidity (which is the case in buffer) hydration forces can be regarded as a special kind of steric force if the proteins/DNA are considered in their entirety including a water shell. Interestingly, Hagan *et al.* also suggested that disorder of the surface-tethered DNA strands increases the cantilever deflection. They argue that the chain-chain interactions follow an exponential dependence on the distance between the chains. In a less ordered layer some strands will have very small separations and therefore dominate the overall stress generation. And last but not least, the quality and grain size of the gold substrate is assumed to have

a large influence on the formation of SAMs and therefore the generation of surface stress for different applications [Godin04].

After this overview it is needless to say that there is still a lot of confusion and uncertainty in the explanation of the surface stress for biological applications. We can assume that in reality it is often a combination of the interactions mentioned above that together yield the surface stress. The problems arise because many researchers initially only used single cantilever measurements which are notoriously problematic because non-specific interactions can dominate, for example temperature, changes in refractive index and reactions occurring on the underside of the cantilever. Moreover, even multiple measurements can suffer from problems due to poor choice of *in-situ* reference cantilevers and a lack of understanding of what makes a good reference coating. Indeed, this is a major driving force for much of the work in this thesis. Cantilever coatings are often poorly characterised and often there is a distinct lack of statistics to determine if the observed effect is significant. Therefore, cantilevers remain an active area of research where more systematic experiments and theoretical work is needed to more fully understand the fundamental origins of surface stress on these complex multilayer and multiscale systems comprising metallic and organic interfaces (Si/Au/SAM/ligand).

CHAPTER 4

Self-Assembled Monolayers

4.1 Introduction

Nanometer-scale systems have the distinguishing characteristic that a high percentage of their constituent atoms are located at the surface. This is unlike macroscopic materials where most of the atoms are within the bulk material and surfaces usually play a negligible role. Hence the structure of nanosystems is affected by surface effects. In the case of self-assembled monolayers, functional molecules are directed onto metallic surfaces to form a molecular film of organic assemblies. Those molecules have a headgroup with a specific affinity for the substrate and provide a convenient system to tailor the interfacial properties of metals [Love05].

To date most applications of cantilever technology take advantage of SAM coatings to detect biospecific analytes. The cantilever coatings are a key factor for the success of cantilever sensor applications and hence it is important to understand their formation. Therefore, in this chapter I will review of basic principles of self-assembly, different

types of SAMs and their mechanism of formation. I will then focus on two types of SAMs that are of particular relevance to this thesis – peptide and lipid SAMs.

4.2 Concept of Self-Assembly

Self-assembly is omnipresent in biology and inspired researchers for decades. In 1991 George Whitesides defined molecular self-assembly as *the spontaneous association of molecules under equilibrium conditions into stable, structurally well-defined aggregates joined by noncovalent bonds* [Whitesides91]. Eleven years later he broadened the concept beyond molecules and wrote that s*elf-assembly is the autonomous organisation of components into patterns or structures without human intervention* [Whitesides02].

In other words, molecular self-assembly looks at naturally occurring or man-made structures that are too large and therefore inaccessible for chemical synthesis but also too small for conventional microfabrication. Importantly, self-assembly uses well-designed building blocks, and the formation of the final structure involves non-covalent (or weak covalent) interactions. Thereby, the assembled structure is at a thermodynamic minimum and the components can equilibrate between aggregated and non-aggregated states, or adjust their positions relative to one another once in an aggregate. Due to these equilibrium reactions the components have to be mobile and hence self-assembly processes are usually performed in liquid. Sometimes these processes are not completely free in three dimensions but are linked to templates such as surfaces (for example self-assembled monolayers).

Self-assembly processes are generally guided by many weak bonds to give an overall stable complex. One single interaction would often be too weak to hold two components together and thus cooperativity between multiple interactions is a main driving force for the assembly of aggregates. Cooperativity in this sense means that the modification of the conformation of individual components upon binding increases their affinity for other components. Hence, an aggregate is only stable

if all components contribute to the overall stability. The types of interactions that are applicable to molecular self-assembly are summarised below [Israelachvili92, Whitesides91]:

- Coulomb/electrostatic interactions between charged groups such as ions or deprotonated acidic groups, which can be attractive or repulsive.
- Electrostatic interactions involving dipoles.
- Hydrogen bonds (H-bonds), which are ubiquitous in biological systems and mostly cooperative.
- Hydrophobic interactions. This is actually a combination of different forces that occurs mainly in aqueous environments when water is restricted from hydrogen bonding near a non-polar interface.
- Aromatic π-stacking between aromatic rings.
- Van der Waals interactions, for example between alkane chains.

Because the enthalpies of these interactions are relatively weak, the interplay of enthalpy ΔH and entropy ΔS in the formation of self-assembled structures is more important than for assemblies with covalent bonds. The sum of a multitude of unfavourable entropic terms such as reduction of translational or conformational entropy can contribute significantly to the change in free energy $\Delta G = \Delta H - T\Delta S$. Therefore it has been suggested that building blocks for self-assembly should be as rigid as possible to achieve good intermolecular contact [Whitesides91]. Nevertheless, entropic contributions are not restricted to the aggregating components themselves but also to the solvent, especially water. In bulk, water molecules participate in average in 3.0 – 3.5 H-bonds with each other [Israelachvili92]. If water molecules come into contact with a non-polar molecule, they reorient themselves in a way that they form a well-structured network of H-bonds around this molecule (so-called structured water molecules), thereby loosing translational and rotational entropy [Israelachvili92]. This

hydrophobic effect can be a major driving force for self assembly processes because it brings hydrophobic components/surfaces together in an aqueous environment (similarly, the hydrophobic effect is also responsible for the insolubility of non-polar substances in water).

Self-assembly is omnipresent in biology, so self-assembly processes can be considered the basis of life. Prominent examples are the hybridisation of complementary DNA strands through H-bonds and π-stacking, as well as the folding of proteins which can involve a multitude of the interactions mentioned above. Interestingly, DNA has a very high specificity for its complementary strand and only a single base-pair mismatch can prevent the hybridisation of DNA strands. This feature has been used to design artificial functional DNA or patterns of DNA on a surface [Rothemund06]. Another prime example from nature is the tobacco mosaic virus which has been shown to spontaneously reassemble *in-vitro* into a functional virus from its components [Klug83]. Moreover, the principles of self-assembly are also used in supramolecular chemistry for the synthesis of large molecules or functional materials [Lehn95].

4.3 Overview of Self-Assembled Monolayers

Self-assembled monolayers (SAMs) are a special case of self-assembly where a surface acts as a template for the formation of a well-defined functional layer. They are ordered molecular assemblies that are formed spontaneously by the adsorption of a surfactant with a specific affinity of its headgroup to a substrate [Schreiber00, Love05]. A number of headgroups/substrates have been reported to form SAMs such as thiols on noble metals or silanes on SiO_2 but the most extensively studied SAMs are formed by alkanethiols on gold (fig. 4.1). Thereby, the molecular components of the SAM can be used to tailor organic structures on metal surfaces.

SAMs are particularly attractive for the following reasons: (i) they are easy to prepare; (ii) they can tune surface properties and add functions to them via modifications of the molecular structure; (iii) they can link molecular structures to macroscopic

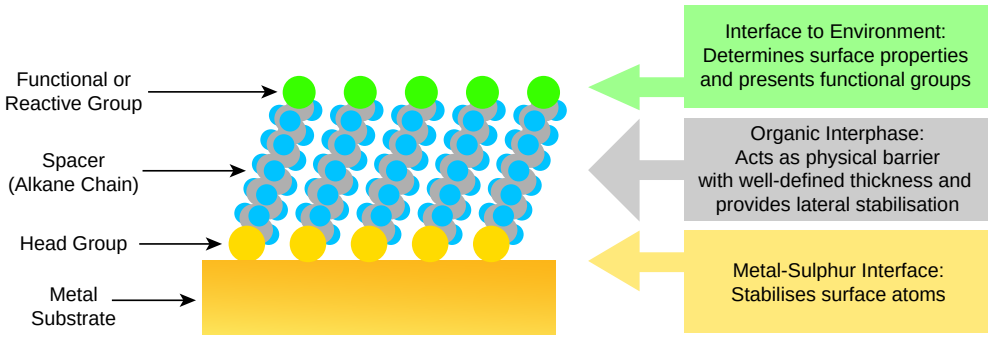

Figure 4.1: Schematic of an ideal SAM of alkanethiols on gold. *The anatomy and characteristics are highlighted [Love05].*

interfacial phenomena, such as wetting, adhesion or friction; (iv) they can be used as building blocks for more complex structures by designing multi-layered structures; (v) they can be structured laterally into patterns, for example using micro-contact printing; (vi) thanks to these features they allow new applications in many areas.

4.4 Mechanism of SAM Formation and Characterization

As mentioned above, the most frequently used and best known type of SAMs is the adsorption of alkanethiols on gold surfaces [Nuzzo83, Dubois92, Ulman96, Laibinis91]. A common way to prepare metal substrates is by adding a thin film of metal onto silicon wafers, glass, mica or plastic substrates using physical vapour deposition (PVD) methods such as thermal or electron beam evaporation [Wanunu04]. The protocol for the preparation of SAMs is then fairly easy. The freshly prepared or clean gold substrate is immersed into a dilute (typically $1 - 10$ mM) ethanolic solution of thiols [Bain89] or exposed to a gas containing the thiol molecules [Schreiber00]. Dense coverages of thiols are obtained within minutes but the reorganization process to maximize the density of molecules and minimize defects in the SAM is slow and requires several hours. A number of factors can influence the formation of SAMs and need to be considered when designing functional layers: solvent, temperature, concentration of adsorbate, immersion time, purity of the adsorbate, cleanliness of the substrate,

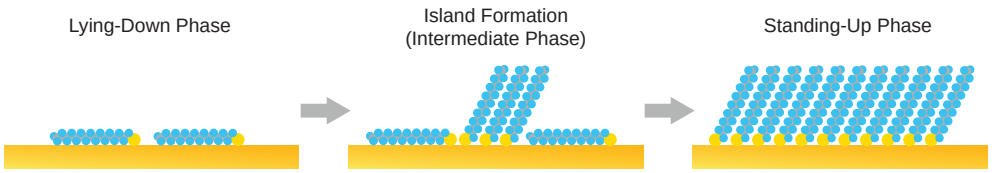

Figure 4.2: Schematic showing the sequential phases of SAM formation.

concentration of oxygen in solution and chemical structure of the adsorbate [Love05]. As illustrated in figure 4.2, it is known that thiols first form a dilute layer where the adsorbed molecules are lying flat on the substrate (striped phase or lying-down phase). When the number of adsorbed thiols increases, islands with densely packed molecules are formed which grow until a complete monolayer is formed covering the whole substrate (standing-up phase).

SAMs have been extensively studied by spectroscopic techniques (X-ray photoelectron spectroscopy, reflection-adsorption infrared spectroscopy, ellipsometry, etc.), scanning probe microscopy (scanning tunnelling microscopy and atomic force microscopy), and physical methods (mostly studies of wetting) [Dubois92, Schreiber00, Yang03, Schwartz01]. The most important interaction in the formation of SAMs occurs at the metal-SAM interface and the strength of the homolytic Au-S bond is believed to be in the order of ca. -50 kcal/mol [Nuzzo87]. The exact bonding mechanism of the Au-S interaction is still subject of scientific debate and the involvement of a structural gold-adatom has been proposed [Maksymovych10], nonetheless the bonding habit of high-coverage thiol phases on Au(111) is generally accepted to be based on a $(\sqrt{3} \times \sqrt{3})$R30° overlayer[1] [Dubois92, Dubois93, Schreiber00, Poirier97]. The formation of SAMs involves a subtle interplay of the energetics of the Au-S bond and lateral (van der Waals) interactions among the thiols. Bulkier thiols generally lead to a less dense monolayer due to steric crowding.

[1]The term $\sqrt{3} \times \sqrt{3}$ means that the lattice distance of the thiol molecules is a factor of $\sqrt{3}$ larger than the lattice constant of the gold crystal and R30° indicates that the thiol axis is tilted by 30° to the surface normal.

4.5 Applications of Self-Assembled Monolayers

A wide range of applications of SAMs have been reported so far including patterned SAMs as etch resists, barriers to electron transport in electrochemistry and molecular electronics, model surfaces for biology and functional surfaces on nanoparticles and biosensors (for an extensive review see [Love05]). Here I focus on two biomimetic applications that were of particular relevance to my thesis: SAMs presenting peptides and tethered lipid layers.

4.5.1 Peptide SAMs

Self-assembled monolayers can present a wide range of organic functionalities (including large or complex ligands) and are therefore frequently used in biosensing applications to capture analytes. There are basically two ways of preparing S-Au SAMs with functional properties: (i) synthesis of functionalized thiols for the formation of single-component SAMs, and (ii) modification of the surface of a preformed SAM by means of thiols with a reactive endgroup. The first method only requires a simple one-step reaction to coat the gold substrate with functional molecules and allows careful tuning of this layer (e.g. thiol density, preparation of mixed monolayers). However, the synthesis of functional thiols is often laborious and usually difficult to achieve. The second method often simplifies the preparation of complex SAMs, as it enables the incorporation of ligands that are not compatible with thiols and allows the use of multiple types of ligands. The disadvantage however is that the extent of surface coverage is unknown (depending on the reaction efficiency and ligand size) and that the reactions can produce a mixture of functional groups in the surface. For the experiments described in this thesis we used thiolated peptides for the formation of sensing layers (method one) because this allowed us to tailor the density of the sensing layer and form very dense layers. Nevertheless, many other biosensing applications can be found in literature that use multi-step reactions to form sensing layers, for example for the attachment of peptides or DNA [Brockman00, Cooper00a, Su02].

4.5.2 Lipid Layers on SAMs

The biological membranes that define the boundaries of living cells are natural examples for self-assembly in organic materials with complex and dynamic functions. They consist of fluid lipid layers that are held together by non-covalent interactions and contain other molecular assemblies such as proteins, glycoproteins or oligosaccharides. Moreover, these membranes not only provide structure to cells, they also control many processes in living cells. Ligand-receptor interactions on the membrane trigger cellular processes and therefore enable the cell to sense its environment, communicate with other cells and regulate intracellular functions. This complexity and dynamic nature makes it difficult to study certain fundamental aspects of biological systems and hence model systems are required as a tool to study processes at the cell membrane.

Self-assembled monolayers can provide a template to mimic such biological membranes. There are in general two different ways to prepare artificial lipid membranes on surfaces, either hybrid bilayers [Lingler97] or supported bilayers [Jenkins02]. Hybrid bilayers consist of a single lipid layer on top of a hydrophobic alkanethiol SAM, which is a fairly primitive model for a cell membrane. Nevertheless, it allows the insertion of receptor molecules with an alkyl chain (e.g. ganglioside GM1) and the subsequent study of ligand binding interactions [Cooper04]. Supported bilayers are formed by adsorbing an intact lipid bilayer onto a hydrophilic SAM, often including some kind of linker molecules that insert into the membrane and thereby tether it to to surface. This method even allows the immobilisation of trans-membrane proteins in their native environment.

CHAPTER 5

Materials and Methods

5.1 Materials

All chemicals and consumables were purchased from Sigma-Aldrich (Dorset, UK) unless otherwise specified. Ultrapure DI water was produced with an ELGA Purelab Ultra water purification system (ELGA, Buck, UK). The first batch of mucopeptide analogues **D*Ala*** and **D*Lac*** (used in chapters 6 and 7) was synthesized by the Department of Chemistry, University of Cambridge, UK. The new batch of **D*Ala*** (chapters 8 and 9) was synthesized by Targanta Theurapeutics (Cambridge, MA, U.S.A.). Hexadecanethiol (HDT) and triethylene glycol undecanethiol (***PEG***) were ordered from Asemblon (Redmond, WA, U.S.A.).

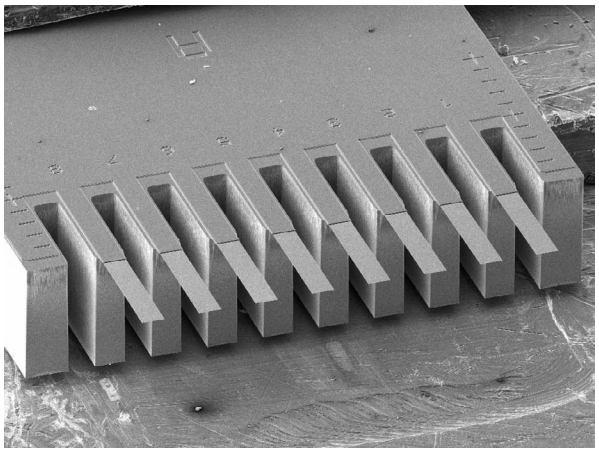

Figure 5.1: Image of a cantilever array chip. *All of the eight cantilevers are 500 μm long, 100 μm wide and 0.9 μm thick. The image was recorded using a scanning electron microscope (courtesy of Benjamin Dueck).*

5.2 Cantilever Sensor Instrumentation

5.2.1 Cantilever Array Chips

The microcantilever arrays were fabricated by the IBM Research Laboratory in Rüschlikon (Switzerland) and purchased either from Veeco Instruments (Santa Barbara, CA, U.S.A.) or Concentris (Basel, Switzerland). Each Si(100) cantilever array consisted of an array of 8 cantilevers attached to a chip body which was needed to fix the cantilevers in the measurement chamber. The cantilevers used in our experiments had the dimensions of $500\ \mu\mathrm{m}$ length, $100\ \mu\mathrm{m}$ width, $0.9\ \mu\mathrm{m}$ thickness and a pitch of $250\ \mu\mathrm{m}$ (fig. 5.1).

5.2.2 Optical Beam Deflection Method

In this thesis the absolute bending of the cantilevers was monitored using an optical beam deflection method. A laser beam was targeted at the free end of a cantilever and its deflection due to bending of the cantilever was recorded using a position sensitive detector (PSD). A separate laser beam was used for every cantilever in the array. The

eight laser beams were operated in a time-multiplexed manner with a single PSD for the read-out of all cantilevers.

For cantilever deflections much smaller than the cantilever length, the change in cantilever curvature Δk is linearly proportional to the change in cantilever deflection Δz at the free end of the cantilever, and also linearly proportional to the change of the angle of reflection of the laser beam $\Delta\theta$. The change in curvature can thus be approximated by

$$\Delta k \cong 2\frac{\Delta z}{L^2} = \frac{1}{2}\frac{\Delta\theta}{L} \tag{5.1}$$

where L is the length of the cantilever. In our experiments L was not the absolute length of the cantilever (500 μm) but rather the effective length of the cantilever, i.e. the distance from the hinge to the centre of the laser spot near the cantilever's free end ($\sim$ 450 μm).

Due to the distance D between the position of reflection on the cantilever and the PSD, sub-μm cantilever deflections Δz are amplified to sub-mm changes in the position of the laser beam spot on the PSD ΔZ, which can be described as

$$\Delta Z = D \cdot \Delta\theta = \frac{4D}{L}\Delta z. \tag{5.2}$$

Stoney's equation (3.9) and equation 5.1 can be combined in order to convert the absolute cantilever deflections Δz to changes in surface stress between the upper and lower side of the cantilever $\Delta\sigma$,

$$\Delta\sigma = \frac{1}{3}\left(\frac{t}{L}\right)^2 \frac{E}{1-\nu}\Delta z \tag{5.3}$$

where t is the cantilever thickness (0.9 μm), L the effective length of the cantilever and $E/(1-\nu) = 180$ GPa is the ratio between the Young's modulus E and Poisson ratio ν of Si(100) [Brantley73].

5.2.3 Cantilever Systems

Two different cantilever readout systems were used for this work (*Scentris* in chapters 6, 7 and 8; *NOSE* in chapters 9 and 10). These systems have some differences in terms

of liquid cells, flow systems and laser read-out which will be explained in this section or in the relevant chapters.

Scentris Instrument

The Scentris instrument (Veeco Instruments, Santa Barbara, CA, U.S.A.) was used to measure the bending of each of the 8 cantilevers of an array upon reactions with an analyte solution [Watari07a]. A functionalized cantilever array chip was inserted into a liquid chamber with a volume of approximately 80 μl. For the read-out of the cantilever bending an optical beam deflection method was used. Laser beams (superluminescent diodes, SLD) were targeted at the end of the cantilever, where they were deflected and recorded by a position sensitive detector (PSD). The injection of the analyte solution was achieved using gravity flow with a flow rate of around 150 μl/min. Six different solutions could be used and selected with a rotary switch valve (figure 5.2).

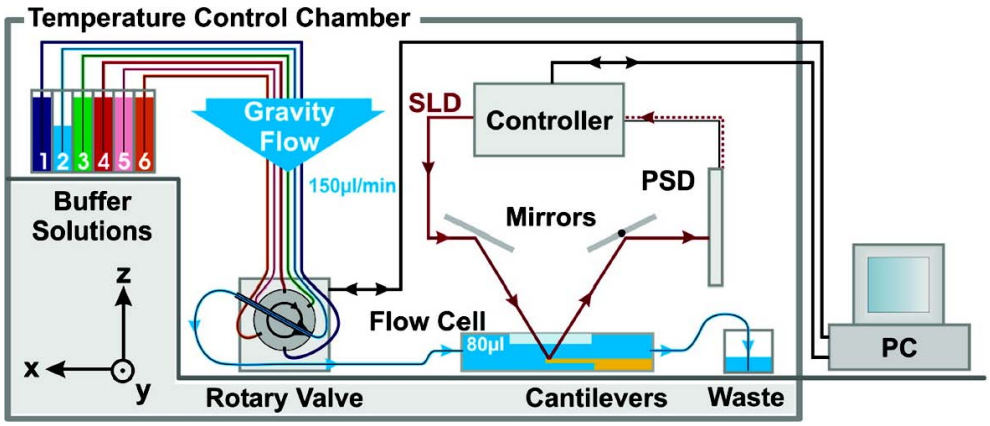

Figure 5.2: Scentris instrument set-up. *The path of the laser beam for the read-out of the cantilever deflection is indicated with red arrows. The cantilever array is shown in yellow. (Figure from [Watari07b].)*

NOSE Instrument

The NOSE set-up was built by a research group at the Physics Institute of the University of Basel (Switzerland). We acquired it as a gas sensing device from the previous user. As part of this thesis, the system was then modified and optimized for liquid measurements. Details are given in chapter 9.

The set-up of the NOSE system is similar to the Scentris system. It also uses the optical beam deflection method for the cantilever readout, however the laser beams were produced by an array of vertical cavity surface emitting lasers (VCSEL) with a wavelength of 760 nm. Furthermore, the system has an optimized liquid cell with a volume of only 8 μl and allows quick alignment of the readout lasers. The flow rate was controlled with a syringe pump.

5.3 Cantilever Experiments

5.3.1 Preparation of Cantilevers

In order to measure a specific binding reaction the cantilevers had to be coated with a functional layers prior to every experiment. This involved three major steps.

Cantilever Cleaning

Cantilever arrays were immersed into freshly prepared piranha solution ($H_2SØ_4$ and $H_2Ø_2$ in a ratio of 1:1 – CAUTION: piranha solution is hazardous and can cause explosions and severe skin burns if not handled with great care) for $20\ \mathrm{min}$. The arrays were then rinsed six times with DI water and three times with ultrapure ethanol, and subsequently dried on a hotplate at 70°C. To verify the cleanliness of the cantilevers, the array was inspected for organic debris under an optical microscope. If the cantilevers were clean, the chip was accepted and transferred to the next step. Otherwise, the cleaning procedure described above was repeated.

Metal Deposition

The cantilever arrays were brought into the in-house cleanroom directly after the cleaning procedure where they were fixed onto a home-built cantilever array holder designed to fit into an e-beam evaporator. The holder with the clamped arrays was then mounted into the metal deposition system (Edwards EB Evaporator Auto500 - FL500, Crawley, UK) and vacuum was pumped overnight. Once a base pressure of $\sim 2 \times 10^{-7}$ mbar was reached inside the evaporation chamber, 2 nm of Ti (adhesion layer) was evaporated followed by 20 nm of Au, with evaporation rates of 0.03 nm/s for Ti and 0.07 nm/s for Au respectively. After the evaporation process the samples were allowed to cool down for at least 1 hour before removing them from the evaporation chamber. The roughness of the gold surface was expected to be around 3–4 nm, according to previous AFM measurements [Watari07a].

Cantilever Functionalization

Gold-coated cantilever arrays were functionalized with self-assembled monolayers of thiolated molecules within a few hours after evaporation. The functionalization was performed with the help of a special stage where the cantilevers can be inserted into small glass capillaries containing typically 2 mM ethanolic solution of the thiols. The outer diameter of the glass capillaries (King Precision Glass, Claremont, CA, U.S.A.) is exactly the same as the pitch of the cantilevers, allowing us to insert all 8 cantilevers of a chip in parallel (fig. 5.3). The cantilevers were incubated within the capillaries for 20 min, followed by 3 washing steps with ethanol to wash off of excess thiols. The arrays were then stored in small petri-dishes filled with DI water until their use for binding experiments, however no longer than two weeks.

For the antibiotic experiments we used the following two mucopeptide analogues to form the sensing layers:

- **D*Ala***: the analogue to the mucopeptide present in the cell walls of VSE strains, $HS(CH_2)_{11}(OCH_2CH_2)_3O(CH_2)(CO)NH(CH_2)_5$(CO)-L-Lys-($\epsilon$-Ac)-D-Ala-D-Ala.

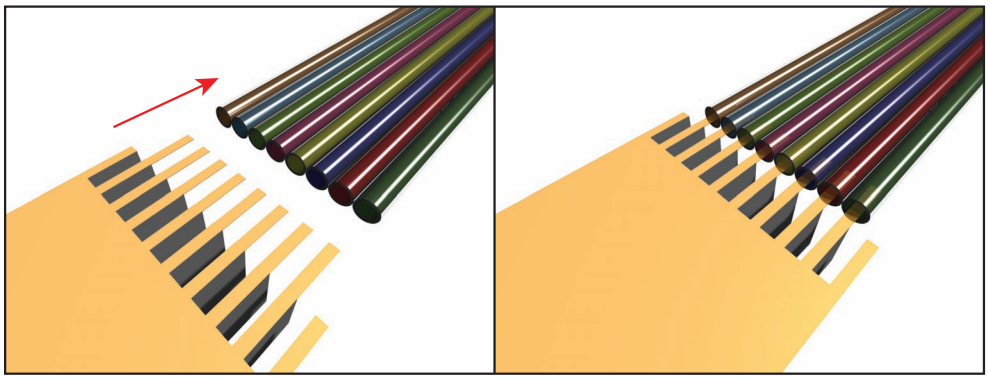

Figure 5.3: Schematic representation of the capillary method to functionalise cantilever arrays. *Left: before insertion. Right: after insertion.*

- **D*Lac***: the analogue to the mutated mucopeptide present in the cell walls of VRE strains,
  $HS(CH_2)_{11}(OCH_2CH_2)_3O(CH_2)(CO)NH(CH_2)_5(CO)$-L-Lys-($\epsilon$-Ac)-D-Ala-D-Lac.

In-situ reference cantilevers were functionalized with a thiol terminating in triethylene glycol, $HS(CH_2)_{11}(OCH_2CH_2)_3OH$, which is denoted by ***PEG***. Surfaces coated with polyethylene glycol are known to minimise biomolecule adsorption [Knowles08, Shu07, Savran03].

5.3.2 Preparation of Solutions

Phosphate Buffer Solution

0.1 M mono-basic sodium phosphate and 0.1 M di-basic sodium phosphate solutions in water were prepared and mixed in the right ratio to give pH 7.4. The solution was filtered through a 0.22 μm PTFE membrane before use and ultra-sonicated for 30 min to remove any gas bubbles. In all experiments except in chapter 10 phosphate buffer was used. Hence, the term *buffer solution* will denote the herewith defined phosphate buffer unless otherwise specified.

HEPES Buffer Solution

10 mM HEPES and 150 mM NaCl were dissolved in water. The pH was adjusted to 7.4 by the addition of 1 M NaOH. Before usage the buffer solution was filtered through a 0.22 μm PTFE membrane. This buffer solution was only used in chapter 10 and is sometimes simply referred to as *buffer* in that chapter.

Vancomycin and Chloroeremomycin Solutions

Freshly filtered phosphate buffer solution was used to dissolve vancomycin hydrochloride (Sigma-Aldrich) and chloroeremomycin diacetate (Targanta Therapeutics, Cambridge, MA, U.S.A.) in various concentrations.

Hydrochloric Acid Solution

Hydrochloric acid was dissolved in ultrapure water to give a concentration of 10 mM. The solution was filtered through a 0.22 μm PTFE membrane before use.

5.3.3 Performing Binding Experiments

Preparation and Alignment

Cantilever chips were inserted into the liquid chamber that was pre-filled with buffer. Care had to be taken that no air bubble was introduced into the liquid cell when mounting the chip. The cantilevers were then equilibrated for several hours (ideally overnight) because the cantilevers were often drifting for a while after insertion. Buffer, antibiotic and HCl solutions were usually stored in the same room as the cantilever instrument several hours before the measurement was recorded to allow all the solutions to have the same temperature. The eight lasers were aligned at the free ends of the cantilevers (1) by watching the reflections of the laser spots on the cantilevers through a magnifying lens and a camera, and (2) by tracking the sum signal and deflection of the lasers on the PSD. The position of the liquid chamber with the

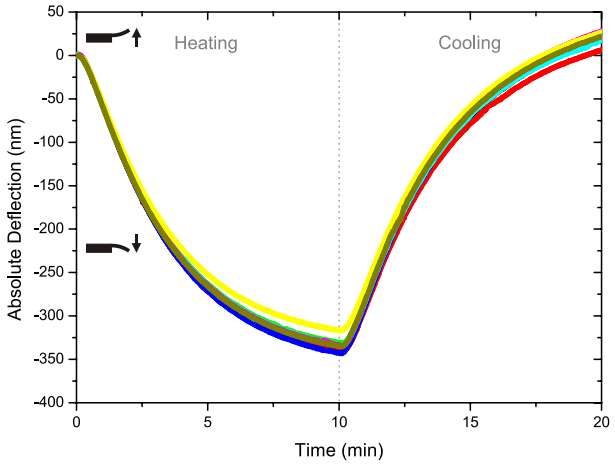

Figure 5.4: Typical 1°C heating test. *The bending signal of all eight cantilevers of one array is recorded in order to confirm the correct alignment of the lasers.*

cantilever array chip was adjusted in order to assure that the lasers hit the PSD in the centre of the sensitive region.

To check that the laser alignment was successful, a heating test was performed by making use of the bimetallic effect of the silicon/gold interface. The entire liquid cell holding the cantilever array was heated by 1°C within 10 min and allowed to cool down again for another 10 min (fig. 5.4). Because the gold layer has a larger thermal expansion coefficient than the underlying silicon cantilever, the whole cantilever bends downwards when the temperature is raised. Heating tests were generally regarded as successful when the relative deviation of the absolute bending signals of all eight cantilevers was less than 10%.

Tuning of every cantilever in each array was performed using an application within the Scentris software (this feature was not available on the NOSE system). For this purpose their spring constants were determined by recording the resonance frequency where the cantilevers were driven only by thermal fluctuations. Assuming that the cantilever is a harmonic oscillator, the following equation can be derived:

$$k = \frac{k_B T}{\langle z^2 \rangle} \tag{5.4}$$

where k is the spring constant, k_B is the Boltzmann's constant, T is the temperature and $\langle z^2 \rangle$ is the time-averaged square of the cantilever deflection signal [Hutter93]. The latter is determined by integration of the power spectral density curve at resonance. Spring constants were then calculated in order to compare the mechanical properties of different cantilevers.

Measurement Protocol

After alignment and preparation of solutions, the binding experiments were performed, where the change in bending of the cantilevers due to exchange of solution in the liquid cell was observed. One experiment typically consisted of the following consecutive steps:

1. Buffer solution
2. Analyte solution (e.g. antibiotic)
3. Buffer solution (optional)
4. Washing solution (usually HCl or NaOH)
5. Buffer solution

Injection times varied for some experiments but typically each injection was performed for 30 min. Sometimes the injection of buffer solution after the antibiotic solution was omitted. The injection of the 10 mM HCl solution helped to wash off the antibiotic molecules from the peptides and regenerated the cantilever surface for further experiments.

The absolute deflection of the cantilevers was recorded continuously during an experiment. Each cantilever array contained at least one *in situ* reference cantilever and the corresponding differential deflection signal could be displayed in real-time by subtracting the deflection of the reference cantilever from the sensitive cantilevers. A reference cantilever is essential to account for unspecific interactions such as temper-

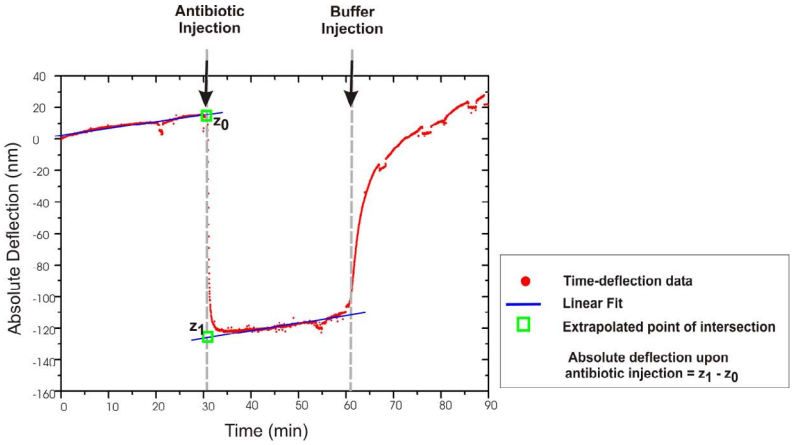

Figure 5.5: Principle of semi-automated analysis of equilibrium cantilever deflection signals. *(Figure adopted from [Barrera08].)*

ature changes, changes in refractive index or interactions on the non-functionalized underside of the cantilever [Fritz00, Lang05].

5.3.4 Data Analysis

A semi-automated software was used to analyse the cantilever deflection data in order to minimize user bias. A linear fit was applied to equilibrated/saturated areas of the raw time-dependent cantilever deflection data before and after a liquid exchange. This fit was then extrapolated to the time point where the liquid exchange occurred and the deflection difference between those two points was calculated (fig. 5.5). This value is called the absolute deflection signal Δz_{abs} which can be converted to changes in surface stress between the upper and lower side of the cantilever $\Delta\sigma_{abs}$ using Stoney's equation [Stoney09] (see sections 3.4.2 and 5.2.2):

$$\Delta\sigma_{abs} = \frac{1}{3}\left(\frac{t}{L}\right)^2 \frac{E}{1-\nu}\Delta z_{abs} \tag{5.5}$$

where t is the cantilever thickness (0.9 μm), L the effective length of the cantilever (the distance from the hinge to the laser spot; usually around 450 μm, that is a bit less than the actual length of the cantilever which is 500 μm) and $E/(1-\nu) = 180$ GPa is the ratio between the Young's modulus E and Poisson ratio ν of Si(100) [Brantley73].

Here the downward bending of a cantilever due to a compressive surface stress is indicated as a negative absolute bending signal, whereas an upward bending of a cantilever due to a tensile surface stress is indicated as a positive absolute bending signal.

The data obtained from each cantilever array was analysed separately. The arithmetic mean of the stress $\overline{S}$ and the standard error E for cantilevers with the same functionalization within one array were calculated using equations 5.6 and 5.7 respectively.

$$\overline{S} = \frac{1}{N}\sum_{i=1}^{N} S_i \tag{5.6}$$

$$E = \frac{\sigma}{\sqrt{N}} = \sqrt{\frac{1}{N(N-1)}\sum_{i=1}^{N}(S_i - \overline{S})^2} \tag{5.7}$$

where S_i is the absolute stress of a cantilever, N is the number of cantilevers with the same coating and σ is the standard deviation.

The average differential stress was then calculated by subtracting the average absolute stress of the reference cantilevers from the average absolute stress of the sensitive cantilevers (e.g. **D*Ala*** or **D*Lac***):

$$\overline{S}_{dif,\,sensitive} = \overline{S}_{abs,\,sensitive} - \overline{S}_{abs,\,reference} \tag{5.8}$$

The estimated error P of the average differential stress was calculated using

$$P = \sqrt{E^2_{sensitive} + E^2_{reference}} \tag{5.9}$$

5.3.5 Cantilever Curvature Measurements

A cantilever array chip was inserted into the Scentris fluid cell and the lasers were aligned onto the free end of the cantilevers as described previously. A heat test and a stress measurement upon injection of 250 μM vancomycin solution was performed. To investigate the curvature of the cantilevers due to surface stress during binding experiments, the liquid cell was moved so that the laser spot was positioned on different locations on the cantilever (from the free end towards the hinge) and the

same measurement was repeated for each position. The value for the effective length of the cantilever L_{eff} (distance from the hinge to the laser spot) had to be adjusted in the Scentris software for each measurement.

5.4 Surface Analysis Methods

5.4.1 Atomic Force Microscopy

Atomic force microscopy (AFM) was used to image SAMs on a gold surface. Ultraflat gold samples were prepared in a similar way as described in [Hegner98]. Therefore a 20 nm thick gold layer was evaporated onto freshly cleaved mica sheets using an e-beam evaporator (Edwards EB Evaporator Auto500 - FL500, Crawley, UK). The gold deposited mica sheets were then glued onto glass slides (gold layer facing down) using epoxy glue (epo-tek 377, Polyscience, Cham, Switzerland) and the glue was hardened at 150°C for 2 hours. Prior to the AFM measurements, the mica sheet was stripped off using tweezers, yielding a clean and flat gold surface. A drop of the thiol solution (50 μl) was added onto the gold surface, which was then incubated for 20 min and washed three times with ethanol. AFM measurements on these samples were performed using a JPK Nanowizard (JPK Instruments, Berlin, Germany) and silicon nitride cantilever (MLCT-AUNM, Veeco, Cambridge, UK).

5.4.2 X-ray Photoelectron Spectroscopy

X-ray photoelectron spectroscopy (XPS) is a quantitative tool to analyse the elemental composition of a surface. The sample surface is irradiated with a monoenergetic X-ray beam causing electrons to be ejected from the surface (fig. 5.6). These photoelectrons have a characteristic kinetic energy depending on the electronic state of the element [Hollander70]:

$$E_{kin} = E_{photon} - E_B - \phi \tag{5.10}$$

where E_{kin} is the kinetic energy of the ejected electron measured by the instrument, E_{photon} is the X-ray energy, E_B is the electron binding energy and ϕ is a correction

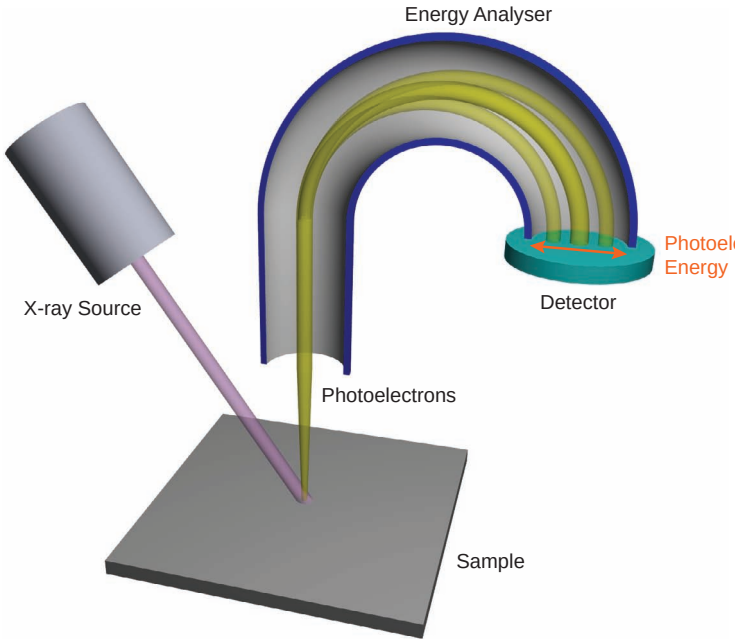

Figure 5.6: Functional principle of XPS. *An X-ray beam irradiates the sample and ejects photoelectrons. These electrons are collected by an energy analyser which can determine the energy of the ejected electrons.*

factor of the spectrometer (work function). An electron energy analyser can count each electron in the specified energy range and thus a typical XPS spectrum is obtained (fig 5.7). An empirical chemical formula of the surface layer can then be extracted from the quantification of the elemental peaks of this spectrum. The electron binding energy is also a function of the chemical environment of an atom and therefore chemical shifts allow the assessment of the chemical bonding within an element.

In our XPS experiments we investigated the relation between the solution concentration and surface coverage of **D*Ala*** molecules. Because of the miniaturised dimensions of cantilevers, XPS measurements were performed on silicon pieces with the dimension of 1×1 cm^2 which were functionalized with SAMs in a way very similar to the preparation of cantilever arrays (see section 5.3.1). The silicon pieces were cleaned in piranha solution and covered with a thin layer of Ti and Au. For the formation of the SAM, samples were put into small glass dishes, covered with

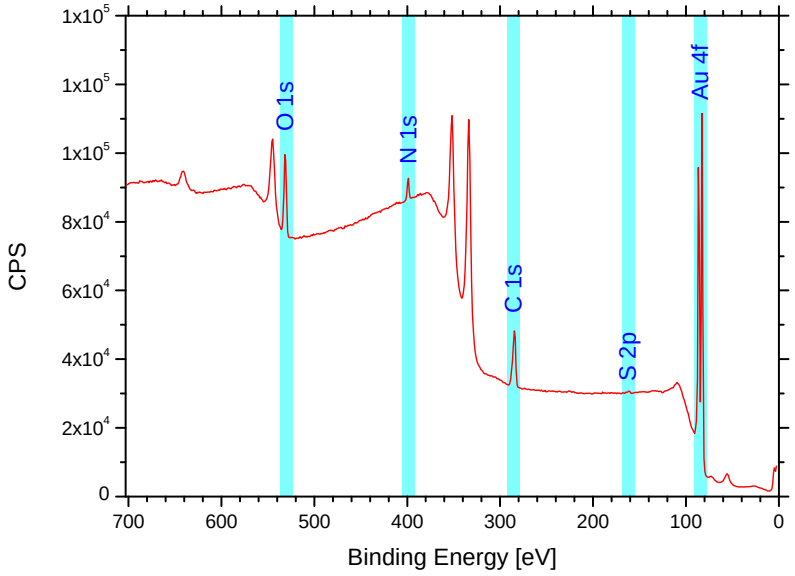

Figure 5.7: Typical XPS overview spectrum. *Peaks that were relevant for our experiments are highlighted. Large differences in peak intensities can be recognised, depending on the occurrence of the element (S 2p smallest, Au 4f largest peak). CPS = counts per second.*

ethanolic solution of **D*Ala*** and incubated for 20 min while the lid of the glass dish was closed to prevent evaporation of solution. The samples were then washed with ethanol three times, air-dried and transported to University of Nottingham for the XPS analysis.

The data was captured using Kratos VISION II software (version 2.2.6) on a Kratos Axis Ultra spectrometer (Kratos Analytical, Manchester, UK) equipped with an Al K_α source and 1486.6 eV line energy. The X-ray spot size was 1 mm^2 and the analysis area was defined by the slot aperture of 300 $\times$ 700 μm^2 with a hybrid (magnetic/electrostatic) optics and a multichannel plate and delay line detector (DLD) with a take-off angle[1] of 0° and a collection angle[2] of 30°. The pressure in the chamber was 3 $\times$ 10^{-9} Torr. Preliminary wide scans were taken with a step size of 1 eV (overview spectrum, see also fig. 5.7) and then reduced down to a step size of 0.1

[1]The take-off angle is the angle from the surface normal at which the photoelectrons are collected.

[2]The collection angle is the angular range around the take-off angle in which photoelectrons are collected.

eV for the main analysis of the high resolution scans (Au 4f, S 2p and N 1s). Scans were performed with a pass energy of 20 eV.

The peak fitting of the raw spectra was carried out using commercial software (CasaXPS) by using the same line shape and full width half maximum on each sample, with a linear background subtraction. Errors in the fitted area under the photoemission peaks were calculated as the standard error between the raw and fitted data. The data was charge-corrected by shifting the C (1s) peak to 285 eV and applying the same shift to every spectrum of the corresponding sample.

5.4.3 Angle-Resolved X-ray Photoelectron Spectroscopy

Angle resolved XPS (ARXPS) provides all the features of conventional XPS but it addition it allows the generation of depth profiles of sample surfaces with a thickness < 10 nm. ARXPS uses the fact that photo electrons are scattered elastically and inelastically when they travel through the surface layer. Only electrons which are not scattered or only scattered elastically contribute to the intensity of the photoelectron peak. The fraction of these electron can be expressed by

$$\frac{I}{I_0} = e^{-\Delta x/\lambda} \tag{5.11}$$

where I is the measured photoelectron intensity, I_0 is the photoelectron intensity at the point of origin, Δx is the distance which the photoelectron travels within the material and λ is the attenuation length which is depending on the photoelectron energy and the material properties. A photoelectron that is ejected from its atom at a depth d has to travel a distance d until it reaches the surface if it takes the most direct route, i.e. perpendicular to the surface (take-off angle $\theta = 0$). For angles $\theta > 0$ the path length increases by a factor of $1/\cos\theta$, hence the chance for inelastic scattering increases (fig. 5.8a). The photoelectron intensity at the surface can thus be described as

$$I = I_0 e^{-d/\lambda\cos\theta} \tag{5.12}$$

In other words, XPS measurements performed at a small take-off angle are more sensitive for depth information and measurements performed at large take-off angles

are more sensitive for surface information. ARXPS uses this phenomenon and by comparing intensities from different angles it can reconstruct a depth profile of the sample surface.

In conventional ARXPS systems the take-off angle was varied by tilting the sample. However, this involved some difficulties such as sample alignment or different exposure to the X-ray beam at different angles. Some modern ARXPS systems therefore use cleverly designed analysers with a two-dimensional photoelectron detector. These detectors can measure the photoelectron energy on one axis and the take-off angle on the other axis (fig. 5.8b). This overcomes the problems associated with the tilting of the sample and allows the simultaneous analysis of a multitude of take-off angles.

We employed ARXPS to investigate the conformations of different **D*Ala*** monolayers. Silicon wafer pieces with the dimensions of 1 x 1 cm^2 were gold-coated in the same way as described for cantilever arrays. A 100 μl drop of **D*Ala*** solution was added on the pieces and incubated for 20 min. The samples were then washed 3x with ultrapure ethanol and air-dried. Angle-resolved XPS spectra were recorded using a Theta Probe system from Thermo Scientific (Waltham, MA, U.S.A.) located at University of Surrey, Guildford, UK. Measurements were performed with an X-ray spot size of 400 μm. Spectra were acquired for the Au 4f, S 2p, N 1s, C 1s and O 1s peaks with a pass energy of 120 eV and a step size of 0.1 eV.

We measured the XPS spectra on 10 different spots on every sample and the detector could discriminate between 16 different take-off angles (equally spaced between 24.875° and 81.125° from the surface normal). For a simple elemental analysis of the surfaces, all spectra from different spots and angles were summed up (collapsed) in order to increase the signal-to-noise ratio. This was especially useful for the S 2p signal which had very low intensity on all samples.

The raw data was processed using Avantage software from Thermo Scientific (version 4.41.0.2661) and the area under the peaks (i.e. the intensity of the peak) was used as a measure for the occurrence of the corresponding element (see also

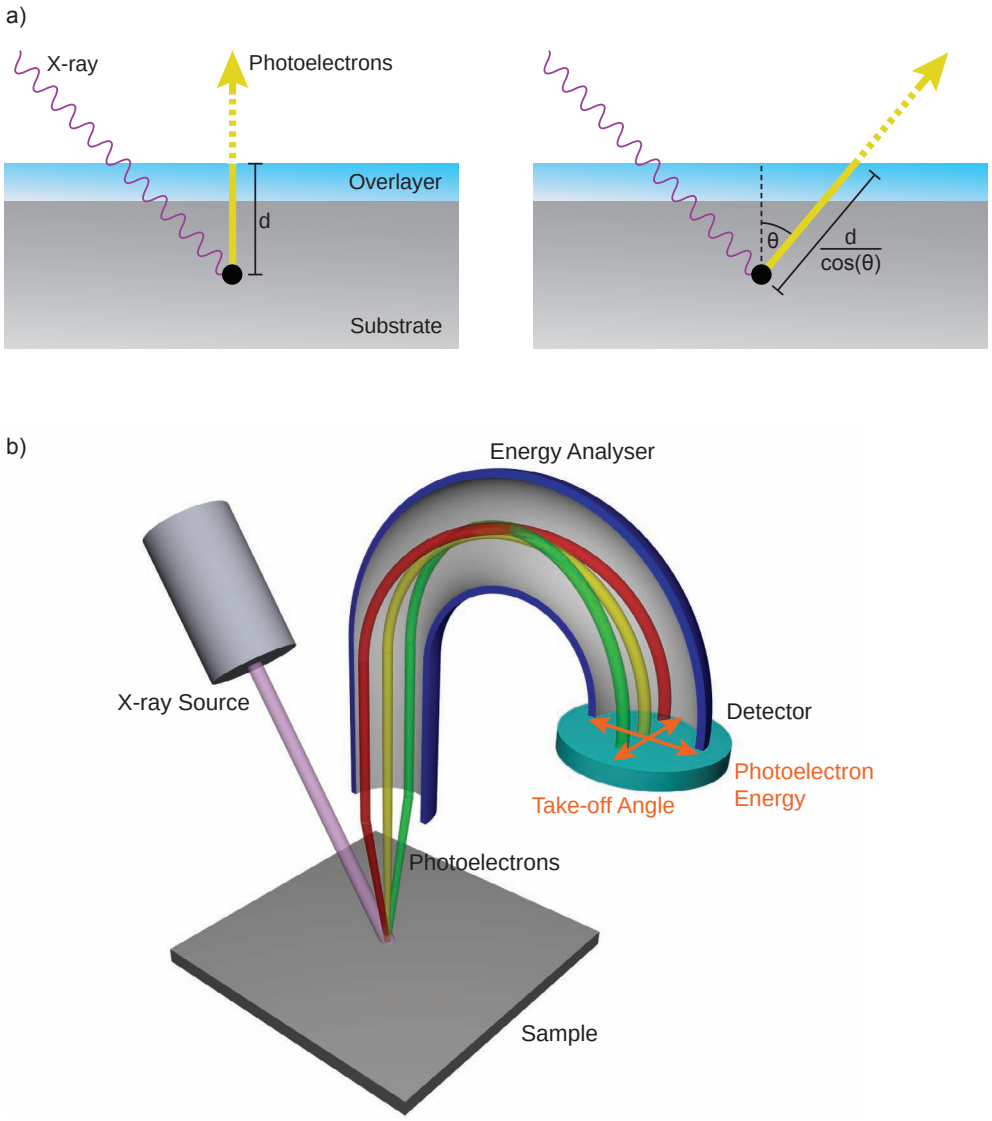

Figure 5.8: Functional principle of ARXPS. ***(a)*** *Illustration to show the photoelectron attenuation as a function of take-off angle* θ*.* ***(b)*** *Schematic of an ARXPS system with a 2-dimensional detector for the simultaneous detection of different photoelectron energies and take-off angles.*

appendix B). The Avantage software can also normalise the peak area using a number of element-specific sensitivity factors and uses this normalised area to calculate values for the relative atomic percentage for each element. The values for atomic percentage should be considered when comparing different samples in order to reduce experimental errors. Moreover, the Avantage software uses depth information from data collected at different take-off angles and calculates depth profiles of the surface layers with the help of iterative models. Therefore ARXPS allows the assessment of the conformation and orientation of molecules within a self-assembled monolayer (see appendix B).

5.4.4 Ellipsometry

Ellipsometry is a non-destructive optical technique that allows the thickness determination of thin films. It is mostly used in semiconductor physics but has also applications in biology. An ellipsometer measures the change in polarization of a light beam upon reflection on the sample surface [Tompkins05]. Precisely, it measures the complex reflectance ratio ρ, which is the ratio of two perpendicular components of the incident light beam (usually denoted as p and s components). This complex reflectance ratio can also be expressed in terms of the amplitude ratio upon reflection $\tan(\Psi)$ and the phase shift Δ through the relation

$$\rho = \frac{r_p}{r_s} = \tan(\Psi)e^{i\Delta} \tag{5.13}$$

For the determination of the layer thickness, the sample surface has to be composed of discrete, homogeneous and optically isotropic layers with known optical properties (refractive index or dielectric function). The measured parameters Ψ and Δ can then be used in a computer model to calculate the thickness of the layers.

Samples for ellipsometry measurements were prepared by cutting a Si wafer into pieces of 1.5 $\times$ 1.5 cm^2. Those pieces were piranha cleaned (according to section 5.3.1) and a reference ellipsometer spectrum was recorded on each sample using a Horiba MM-16 Spectroscopic Ellipsometer (Horiba Jobin Yvon, Middlesex, UK). The

samples were then coated with 2 nm Ti and 20 nm Au according to section 5.3.1 and a reference spectrum was recorded again on each sample. A drop of thiol solution (170 μL) was then added onto the samples which covered them completely with liquid, and they were incubated for 20 min. The samples were put into a small petri dish during incubation to diminish evaporation of thiol solution. Samples were then washed with ethanol three times to get rid of excess thiols.

The thickness of the self-assembled monolayers formed by those thiols was then examined using ellipsometry. The system was calibrated using the Cauchy model

$$n(\lambda) = A + \frac{B \cdot 10^4}{\lambda^2} + \frac{C \cdot 10^9}{\lambda^4} \tag{5.14}$$

where n is the refractive index and λ is the wavelength of the light beam [Tompkins05]. The equation was fitted to three spectra recorded on SAMs with known thickness (1-Propanethiol, 1-Undecanthiol and 1- Hexadecanethiol), which revealed values for the constants $A = 1.3156140$, $B = 0.9312068$ and $C = -0.1257395$.

With equation 5.14 and the known factors A, B and C it was then possible to estimate the thickness of SAMs formed by **D*Ala*** thiols of different concentrations. The previously recorded spectra of Au/Ti on Si were used as substrate for the fitting procedure. 10 samples were prepared with **D*Ala*** concentrations ranging from 10^{-4} mM to 4 mM **D*Ala*** and 3 spectra were recorded on each sample at slightly different positions. The weighted average of those three measured thicknesses

$$\overline{x}_\omega = \frac{\sum_{i=1}^{N} \omega_i x_i}{\sum_{i=1}^{N} \omega_i} \tag{5.15}$$

and weighted standard deviation

$$\sigma_{\omega}^{2} = \sqrt{\frac{\sum_{i=1}^{N} \omega_i (x_i - \overline{x}_{\omega})^2}{\frac{N-1}{N} \sum_{i=1}^{N} \omega_i}} \tag{5.16}$$

was then calculated for each sample, taking the χ^2 of each fit into account. x_i is the measured thickness, $\omega_i = \frac{1}{\chi_i^2}$ is the weight and N is the number of weights/values.

5.4.5 Contact Angle Goniometry

Contact angle goniometry is a simple method to determine the wetting properties of a surface. When a drop of a liquid (usually water) is deposited on a surface, its shape is determined by the interactions between the interfaces. If the surface is strongly hydrophilic, the interactions between the water drop and the surface are favourable and the drop spreads completely (contact angle of 0°). In contrast, if the surface is hydrophobic the water drop keeps its spherical shape in order to minimise the contact area with the surface (contact angle of 90° or more).

Contact angle measurements were performed on the samples used for XPS and ellipsometry analysis using a Krüss drop shape analysis system DSA 10 Mk2 (Krüss, Hamburg, Germany). A small droplet (3 μL) of DI water was added onto the sample surface and the volume was increased and decreased in 3 cycles to measure the advancing angle of the substrate/liquid interface [Lam01]. The advancing angle was calculated as the average of all measured contact angles in the range of the advancing angle, i.e. when the contact angle did not increase any more with added volume (fig. 5.9).

5.5 Surface Plasmon Resonance

Surface plasmon resonance (SPR) is a label-free method for the detection of biomolecular interactions. It is able to measure small changes in dielectric constant that can be

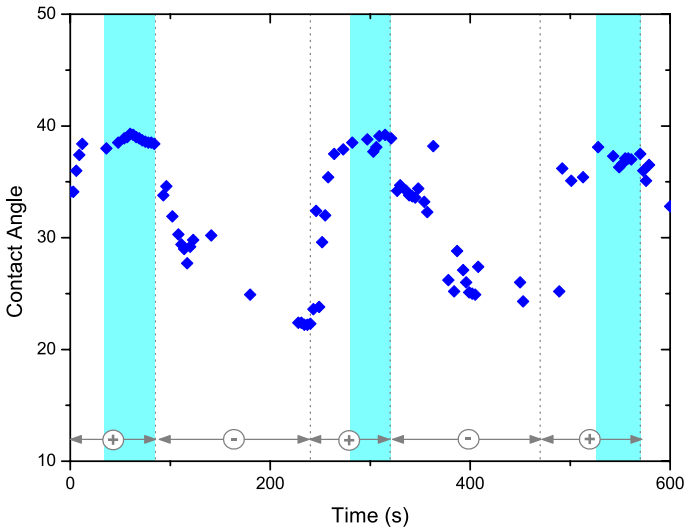

Figure 5.9: Plot of a typical advancing contact angle measurement. *Grey arrows with plus and minus signs indicate phases with growing and shrinking drop volume, respectively. Advancing angles were calculated as the average of all data point within the regions of stable contact angles (shown in cyan).*

related to adsorbed mass near the sensor surface and therefore allows determination of binding affinities and binding kinetics.

The principle of SPR relies on optical excitation of surface plasmons [deMol10]. The main sensor part of SPR consists of a glass prism and a thin metal film deposited on a glass slide where the biological sensing layer can be immobilized. A light beam travels through the prism and hits the gold layer. Thereby, the photons from the light beam can excite free oscillating metal electrons. At a particular angle of incident of the light beam, the energy of the photons of the light equals exactly the momentum of the plasmons. Under these resonance conditions, the intensity of the reflected light drops drastically. Moreover, a plasmon resonant wave and evanescent field is generated at the interface of the metal and the dielectric medium, whereby the electromagnetic field of the incident light is coupled to the oscillations of free electrons. The evanescent field depends on the dielectric constant of the medium close to the metal surface and has a limited penetration depth of about 300 nm. If molecules

bind to the surface, the dielectric constant changes and therefore resonant conditions are met at a different angle of incidence. By varying the angle of the incident light beam and by simultaneously detecting the intensity of the reflected light, the SPR system therefore enables the indirect detection of mass changes on the sensor surface.

Our SPR experiments were performed on a Biacore T100 system (Uppsala, Sweden; now part of GE Healthcare) located at UCL Cancer Institute. We used bare gold-coated sensor chips for the experiments (Sensor Chip Au, purchased from Biacore), so that binding experiments could be conducted in the same way as cantilever and XPS measurements. For the sensor surface preparation 100 μl of **D*Ala*** solution was deposited on the SPR chip and incubated for 20 min. The chip was then rinsed 3 times in ethanol, dried in air and mounted on the SPR chip holder. The antibiotic binding experiments were performed in the same way as the cantilever experiments, using the same analyte and buffer solutions.

5.6 Lipid Layers on Cantilevers

This section describes the methods and protocols that were used to prepare supported lipid layers on cantilevers (see chapter 10).

5.6.1 Preparation of Lipid Vesicles

A 10 mM solution of L-α-phosphatidylcholine (PC, from egg yolk) in chloroform was prepared in a 100 ml round bottomed flask (typically 1 – 6 ml). In case that liposomes containing ganglioside GM1 were prepared, the desired amount of GM1 (Enzo Life Sciences, Exeter, UK) was added to this mixture. The mixture was then slowly dried over 2 h using a rotary evaporator at a temperature of 34°C, a pressure of 475 mbar and a spin speed of 30 rpm. The flask was dried for a further 5 h in the rotary evaporator at low pressure in order to completely remove the solvent. A specified amount HEPES buffer (10 mM HEPES, 150 mM NaCl, pH 7.4 adjusted with NaOH) was added to the dried lipids to give a 20 mM PC suspension. This mixture was shaken by hand

for 30 min with occasional 5 second bursts of sonication to improve the dissolution. After the sonication steps the solution was placed immediately on ice to minimise heating. A white cloudy suspension resulted. This mixture was then passed through a mini-extruder 17 times (odd number of times) using polycarbonate filter membranes with 50 nm pore size to give small unilamellar vesicles (SUV). The extruder and membranes were purchased from Avanti Polar Lipids (Alabaster, Alabama, U.S.A.). The SUV suspension was stored in a 4°C fridge until usage.

5.6.2 Dynamic Light Scattering

Dynamic light scattering (DLS) is an optical method to determine the size distribution of small particles in a suspension. It is based on fluctuations in the intensity of a light beam that is back scattered by the particle suspension, which are characteristic for the particle size.

In our experiments we used a Malvern Zetasizer Nano ZS (Malvern Instruments Ltd, Malvern, Worcestershire, UK) at Imperial College London to determine the size of liposomes. SUV were prepared as described above and diluted to 0.002% w/v PC for the DLS measurement. On each sample solution 3 $\times$ 12 runs were performed.

5.6.3 Preparation of Lipid Layers

We used and compared four different methods to prepare hybrid lipid layers on cantilevers, as described below. All of the methods used cantilevers coated with a hexadecanethiol (HDT) SAM as a substrate.

Capillary Method

HDT-coated cantilevers were immersed in 40 mM octyl β-D-glucopyranoside (OGP) for 5 min to clean the chip, and rinsed 3 $\times$ 1 min with water. The chip was then functionalized using the capillary method, as described previously in section 5.3.1. Capillaries were filled either with 2 mM pure PC SUV (reference) or 2 mM PC + GM1

SUV (active cantilevers). The chip was incubated for 90 min or longer and then put directly into buffer.

Injection Method

A cantilever chip coated with HDT (and optionally ***PEG*** as reference) was inserted into the liquid cell, rinsed with detergent and buffer. Then a SUV suspension (typically 2 mM PC) was injected *in-situ* for a duration of up to 2 h.

Incubation Method

The chip was immersed in 40 mM OGP for 5 min and washed 3×1 min with water. It was then transferred in a small dish containing the SUV solution (typically 1 – 5 mM lipid concentration) and incubated overnight. On the next day, the chip was put into buffer and used for the measurement.

Detergent Method

The detergent method was adopted from [Terrettaz93]. A 1 ml solution in methanol containing 90 mM OGS, 1 mM PC and 0.4 mM GM1 was prepared in a round bottomed flask. The mixture was dried on a rotary evaporator for 2 h at a pressure of 400 mbar and a spin speed of 30 rpm, and then another hour at reduced pressure of 30 mbar. The dry film was then dispersed in 1 ml HEPES buffer, thoroughly shaken and sonicated for 5 min to give a homogeneous suspension. 200 μl of this mixture was then added to a small dish together with a cantilever chip. Every 5 min one third of this solution was removed with a pipette and replaced by the same amount of buffer. This was repeated until the OGP concentration reached 0.001 mM. The chip was then transferred into pure buffer and used for the measurement.

CHAPTER 6

Nanomechanical Detection of Vancomycin

6.1 Introduction

Microcantilever array sensors have been proven to be a highly sensitive and label-free tool to detect biochemical interactions, as already presented in the introduction of this thesis. Thereby, cantilever-based sensing is unique in the way that cantilevers measure in-plane surfaces forces due to changes in surface stress, which is not limited to the mass of the analyte. Therefore, they are particularly suited to small molecule detection which is largely the basis of the pharmaceutical industry. Cantilever can also be fabricated by low cost silicon technology and are therefore amenable to parallelisation for HTS of small scale information-rich screening assays.

Previous work by Ndieyira, Barrera and Watari [Barrera08, Ndieyira08] showed that cantilevers were able to detect drug-target interactions using the model vancomycin-mucopeptide system (fig. 6.1). The use of nanomechanical cantilever sensors to study this particular binding interaction is interesting because glycopeptide antibiotics are thought to be involved in the disruption of the bacterial cell wall, which in the end is

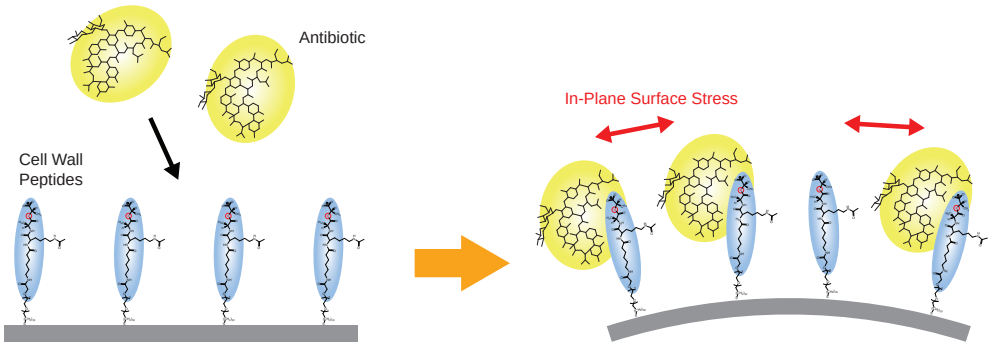

Figure 6.1: Schematic illustration of the generation of the cantilever response. *Binding of antibiotic molecules to bacterial cell wall peptide analogues lead to an in-plane surface stress.*

a mechanical phenomenon. This is different to for example beta-lactam antibiotics which bind to and inactivate the bacteria's transpeptidase enzyme.

The initial aim of my PhD when joining the group was to reproduce this data and then to further investigate and develop the technology for robust, specific and sensitive analysis. The development of robust measurement protocols is central to all future applications of this technology. Therefore in this chapter I will describe initial drug-target measurements to determine the lowest concentration of antibiotic that could be detected in buffer. Experiments then went onto investigate the uniformity of stress along the cantilever and protocols to most efficiently wash and regenerate active chips, thereby allowing sensitive measurements and reducing costs. Finally the system was used to investigate drug-target binding in blood serum, which is indeed the very medium where antibiotics must work – our bodies – and which positions cantilever sensors as a useful tool for pharmacokinetics studies and medical diagnostics.

6.2 Detection of Vancomycin

The aim of initial experiments was to reproduce data to detect vancomycin using multiple cantilever arrays coated with alkanethiols that mimic the outer surface of bacterial cell walls (fig. 6.2). Details of all experimental methods are given in chapter 5.

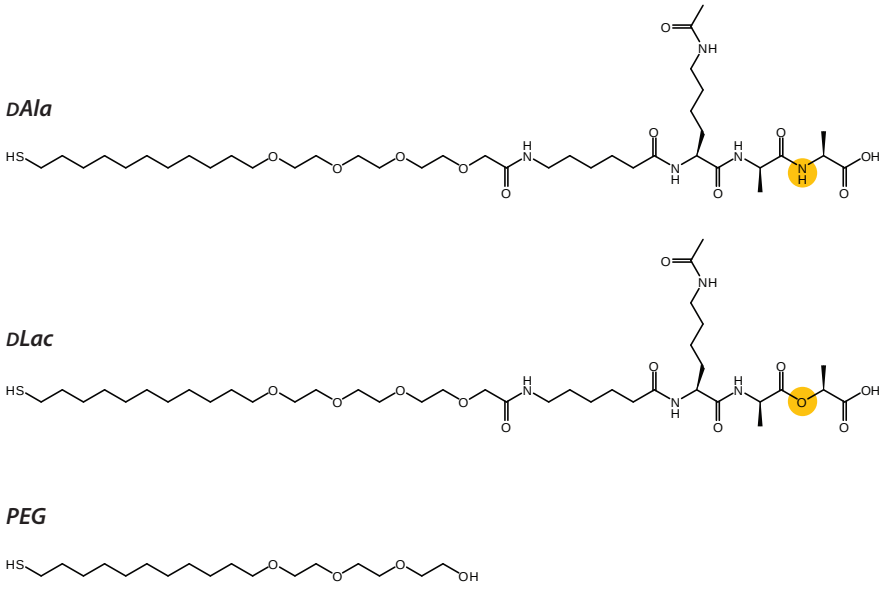

Figure 6.2: Chemical structures of mucopeptide analogues used to coat cantilevers for the drug-target interaction stress measurements. **DAla** *represents VSE phenotypes and* **DLac** *represents VRE phenotypes.* **PEG** *was used as a reference coating. The only difference between* **DAla** *and* **DLac** *is the exchange of an amide group by an ester within the binding site (marked with a circle).*

To mimic the surface of vancomycin-sensitive *Enterococci* (VSE), cantilevers were coated with a thiolated peptide terminating in L-Lysine-D-Alanine-D-Alanine (**D*Ala***). The corresponding analogues for vancomycin-resistant *Enterococci* were thiolated peptides terminating in L-Lysine-D-Alanine-D-Lactate (**D*Lac***). Reference cantilevers were functionalized with thiols terminating in triethylene glycol (***PEG***) which is known to minimise adsorption of biomolecules on surfaces. Those *in-situ* reference cantilevers were needed for differential deflection measurements and are crucial to eliminate unspecific effects such as changes in temperature, drift of the signal, changes in refractive index or reactions at the underside of the cantilever. In a typical deflection experiments the 8 cantilevers of one array were functionalized in the following way: 3 $\times$ **D*Ala***, 3 $\times$ **D*Lac*** and 2 $\times$ ***PEG***.

This particular design of peptide analogues was chosen for the following reasons: The hydrophobic undecane chain promotes the attachment to the gold surface and a dense packing of the thiols on the surface due to Van-der-Waals interactions between the molecules. The triethylene glycol linker renders the surface hydrophilic but is not susceptible to specific binding interactions with molecules in the analyte solution. It also acts as a spacer that reduces steric constraints and therefore allows the analyte to interact with the surface peptides. The terminal tripeptides represent the actual receptor part enabling the specific detection of antibiotics.

The aim of these investigations was to demonstrate that cantilever arrays have the sensitivity to quantify vancomycin-D***Ala*** binding interactions and detect the deletion of a single hydrogen bond associated with antibiotic resistance in the mutated peptide analogue, D***Lac***. Figure 6.3a shows typical absolute bending signals for a cantilever array chip upon injection of a 7 μM vancomycin solution, a concentration that lies within the clinically relevant level of vancomycin [Rotschafer82]. During injection of buffer solution at the beginning there is only a small drift of the signal but all cantilevers behave roughly the same, independent from their functionalization. Upon injection of the vancomycin solution however, the cantilevers respond specifically to the analyte. Whereas the D***Ala***-coated cantilevers rapidly bend downwards, reaching equilibrium after about 10 min, the D***Lac***- and ***PEG***-coated cantilevers do not show an apparent response. Upon the subsequent buffer injection, the D***Ala*** signal goes back towards the baseline but does not reach it, indicating that not all the vancomycin molecules unbind from the cantilever surface. This experiment demonstrates that cantilevers are sensitive to an in-plane surface stress resulting from the specific binding of vancomycin molecules to D***Ala***-terminating peptides and that cantilever sensors are able to discriminate between mucopeptide analogues found in vancomycin-sensitive and vancomycin-resistant bacteria, respectively.

For the quantification of the bending signals and the elimination of unspecific effects, the differential signal has to be calculated by subtracting the signal of the *in-situ* reference cantilever (***PEG***) from the active cantilevers (D***Ala*** and D***Lac***), that

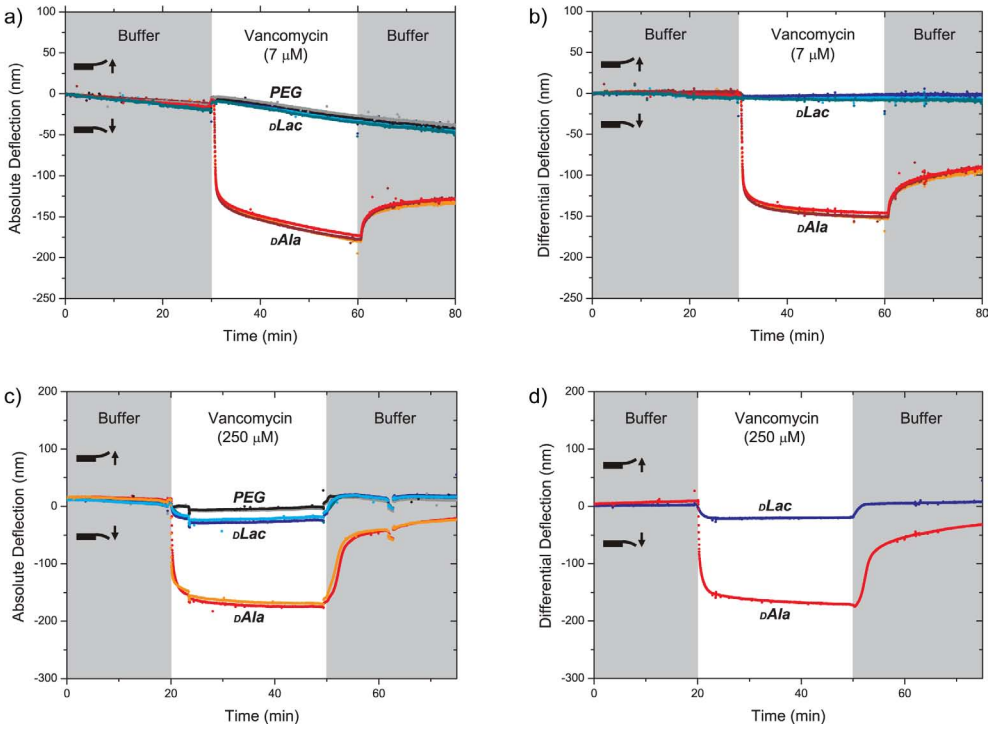

Figure 6.3: Investigation of the specificity and sensitivity of antibiotic-mucopeptide interactions on cantilever arrays. ***(a)*** *Absolute bending signal of cantilevers coated with* **DAla** *(red, orange and wine red),* **DLac** *(blue, cyan and dark cyan) and* **PEG** *(black and grey) upon injection of phosphate buffer, 7 mM vancomycin, and again phosphate buffer.* ***(b)*** *Corresponding differential bending signal of* **DAla** *(***DAla** *minus* **PEG***) and* **DLac** *(***DLac** *minus* **PEG***).* ***(c)*** *Absolute bending signal of cantilevers coated with* **DAla** *(red and orange),* **DLac** *(blue, cyan and dark cyan) and* **PEG** *(black and grey) upon injection of phosphate buffer, 250 mM vancomycin, and again phosphate buffer.* ***(d)*** *Corresponding differential bending signals of one* **DAla** *(red) and* **DLac** *(blue) cantilever. (c and d adopted from [Ndieyira08].)*

is $z_{diff}(\mathbf{DAla}) = z_{abs}(\mathbf{DAla}) - z_{abs}(\mathbf{PEG})$ where z_{diff} and z_{abs} are the differential and absolute cantilever deflection, respectively. Figure 6.3b shows that the calculation of the differential deflection removes drift and unspecific effects from the signal (such as the small jump upon injection of the vancomycin solution). The analysis of the data reveals differential deflections of -147, -143 and -138 nm for **DAla**-coated cantilevers and -4, -3 and -1 nm for **DLac**-coated cantilevers.

Deflection experiments were performed with varying vancomycin concentrations. Cantilever bending signals became larger for increasing vancomycin concentration, not only for **D*Ala*** but also for **D*Lac***, indicating that vancomycin is also binding to **D*Lac*** but with a much lower affinity compared to **D*Ala***. Figure 6.3c/d shows the previously reported absolute and differential deflection of a cantilever array upon injection of a 250 μM vancomycin solution [Ndieyira08]. This measurement gave differential deflections of -167 and -159 nm for **D*Ala*** and -25, -18 and -18 nm for **D*Lac***, which is higher than the deflections recorded upon injection of 7 μM vancomycin solution, especially for **D*Lac***.

The sensitivity of the set-up was investigated by decreasing the vancomycin concentration in solution. The differential **D*Ala*** bending signal scaled with vancomycin concentration (10, 100 and 1000 nM), giving equilibrium differential signals of -8, -29 and -114 nm, respectively (fig. 6.4a). The lowest concentration to be detected was 10 nM vancomycin, giving rise to a **D*Ala*** differential bending signal of -9 $\pm$ 2 nm on three cantilevers (fig. 6.4b). Thereby, the detection limit is given by the noise level of the cantilever signal (around 1 nm for the Scentris system) and the drift of the signal. We also observed that the kinetics of the binding reaction vary with the antibi-

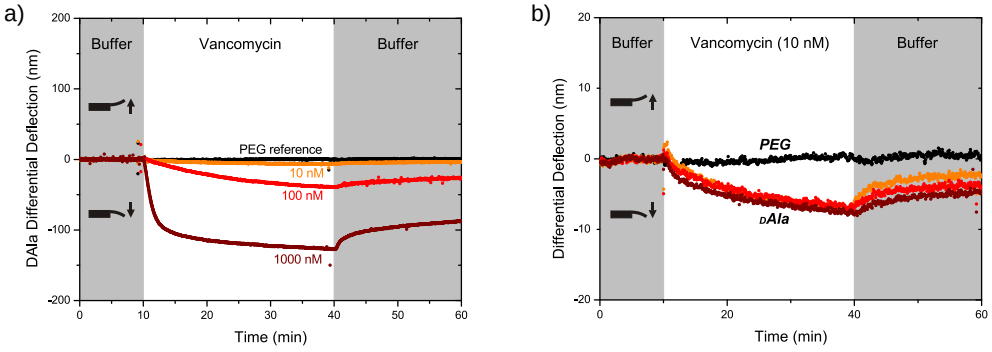

Figure 6.4: Low concentration vancomycin binding experiments. *(a) Differential* **DAla** *signals for 10, 100 and 1,000 nM vancomycin. The differential* **PEG** *reference signal is shown in black.* ***(b)*** *Differential signals of three* **DAla** *cantilevers for 10 nM vancomycin. The differential* **PEG** *reference signal is shown in black.*

otic concentration, i.e. it takes a longer time to reach equilibrium for low antibiotic concentrations. We attribute this phenomenon to two effects: (i) a binding rate effect, as the surface binding rate is concentration dependent and is slower at low analyte concentrations, and (ii) a mass transport effect, as at low analyte concentrations it takes a longer time to transport enough vancomycin molecules into the measurement chamber so that the available receptors can be occupied. The volume of the liquid cell of the Scentris instrument is fairly large (80 μl) and thus it takes about half a minute to replace the solution in the cell.

6.3 Curvature of Cantilevers

In order to examine if cantilevers bend uniformly during vancomycin binding experiments, the curvature of cantilevers was investigated by aligning the read-out laser spot onto four different locations along the cantilever. Figure 6.5b shows the deflection results upon injection of a 250 μM vancomycin solution for a cantilever array where 6 cantilevers were coated with **D*Ala*** and 2 cantilevers with ***PEG***. The ***PEG*** cantilevers revealed only a very small deflection of some nanometres whereas the **D*Ala*** cantilevers showed deflection between -103.1 nm and -166.5 nm at the free end of the cantilever. The data points were fitted with Stoney's equation. However, the bending did not seem to be completely uniform, with slightly reduced bending towards the free end of the cantilever. This is also supported by the surface stress values that were calculated from deflection signals, which show a higher stress towards the hinge (fig. 6.5c).

Furthermore, the 6 **D*Ala***-coated cantilevers were functionalised using two different **D*Ala*** stock solutions (solution 1: cantilevers shown in orange and red colour; solution 2: blue and green colours). Both solutions should have the same **D*Ala*** concentration but were stored in different vials. Yet, those two types of cantilevers split into two groups with the latter ones giving a larger deflection. We recognise that even very small differences in the stock solution (concentration differences, impurities) can lead

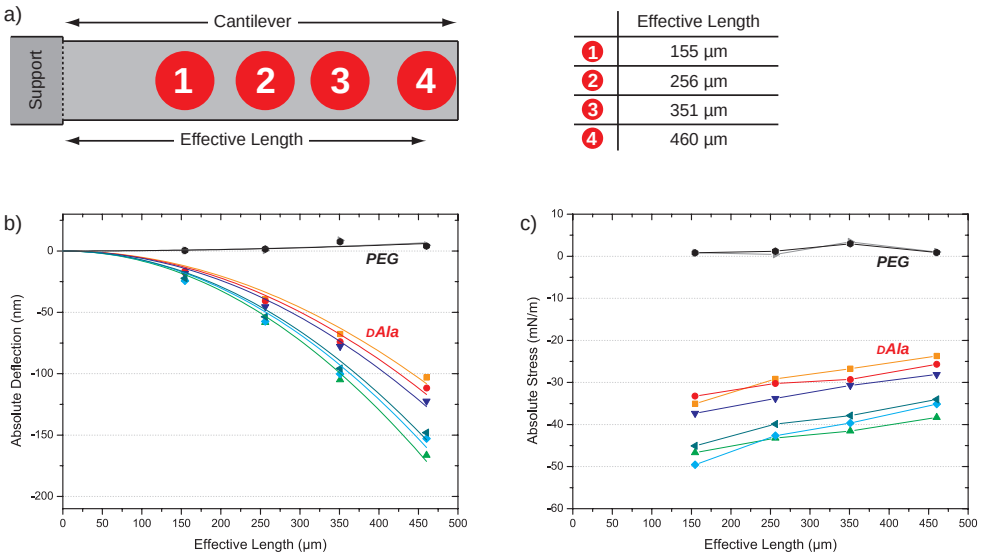

Figure 6.5: Investigation of cantilever curvature upon injection of a 250 μM vancomycin solution. ***(a)*** *Schematic of a cantilever showing the four different effective lengths investigated, which are defined as the distance from the hinge to the centre of the laser spot on the cantilever. Red circles represent the laser spots.* ***(b)*** *Absolute cantilever deflection for different L_{eff} (symbols) and fit of Stoney's equation (solid lines).* **PEG** *cantilevers are shown in black and grey and* **DAla** *cantilevers in colour.* ***(c)*** *Surface stress calculated from the absolute deflection values for different L_{eff}.*

to a significantly different surface stress, a phenomenon that will be covered in more detail in chapter 8.

6.4 Washing off the Antibiotic

After a completed antibiotic binding experiment, the cantilever surface could be regenerated and therefore multiple binding experiments could be performed on a single chip. This was achieved by purging the liquid chamber containing the cantilever array with a 10 mM HCl solution (fig. 6.6), leading to the unbinding of the antibiotic molecules but leaving the mucopeptide analogues intact.

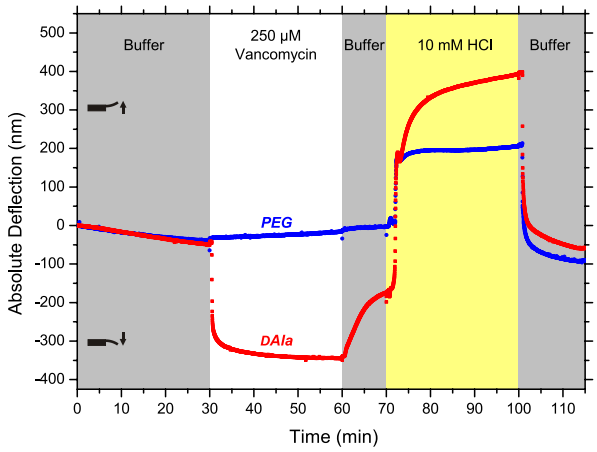

Figure 6.6: Typical experimental sequence of an antibiotic binding experiment including the regeneration of the cantilever surface. *After the injection of the antibiotic solution and an optional buffer wash, the chamber and cantilevers were purged with a 10 mM HCl solution (yellow area) leading to the unbinding of the antibiotic molecules.*

The duration of the HCl washing step needed to completely regenerate the cantilever surface was examined by performing the same vancomycin binding experiment multiple times and thereby varying the duration of the preceding HCl washing step. The data was collected from 6 D*Ala*-coated cantilevers from one array. It was found that a washing step of 30 min or longer is needed to regenerate the cantilever coating and thus giving the same stress signal as the initial experiment, i.e. $\sim$ 16 mN/m for a 1 μM vancomycin solution (fig. 6.7).

6.5 Regeneration of Cantilever Array Chips

A simple method to clean used cantilever array chips was tested which allows us to re-functionalise cantilevers and perform multiple successive experiments with the same chip. Therefore, previously used chips were immersed into a solution of *aqua regia* (HCl and HNO_3 in a ratio of 3:1) for 5 minutes, a solution which is known to dissolve gold [Sheng07]. They were then rinsed with water three times, dried on a hot plate at 75°C and checked under a light microscope. Subsequently, the chips were

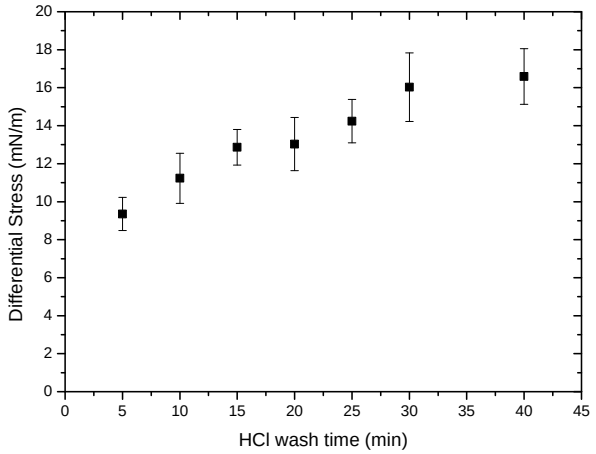

Figure 6.7: Influence of HCl wash times on regeneration of cantilever surface. *The surface stress upon injection of 1 μM vancomycin was measured after varied HCl wash times. A wash time of 30 min or more was needed to regenerate the surface. Note that a wash time of 35 min wash not measured and is therefore missing from this data set.*

cleaned in piranha solution, gold-coated and functionalized using the same protocol as with new chips (see section 5.3.1).

Figure 6.8 shows different steps in the regeneration process of a used cantilever array. This particular chip was stored in DI water for several weeks after it has been used for binding experiments. Its cantilevers were heavily bent and even fungi were grown thereon. The cleaning with *aqua regia* removed the gold layer (and maybe the underlying titanium layer) but did not eliminate the fungi nor made the cantilevers straight again. The piranha solution managed to remove the organic remains and made the cantilevers appear as 'new' so that they could be used for another set of experiments.

6.6 Investigation of Antibiotic Binding Affinity

A major goal of the studies described here was to quantify the strength of the drug-target binding interactions using cantilever array sensors. For that purpose a set of deflection experiments were performed using a dilution series of vancomycin.

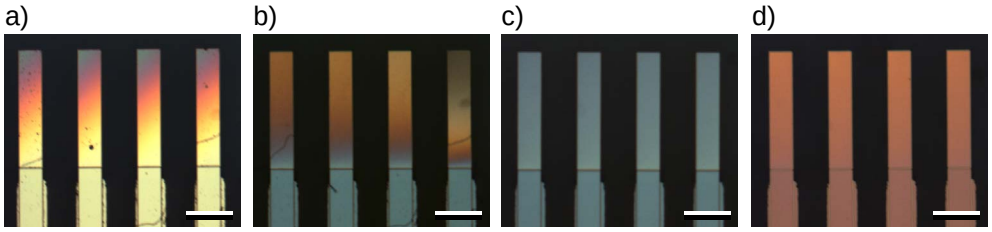

Figure 6.8: Phase contrast image sequence illustrating the regeneration of a cantilever array chip (only four cantilevers are shown). ***(a)*** *A chip that has been stored in water for several weeks after previous measurements. Fungi were grown on the chip as seen by the black rods, and cantilevers are bent as seen by the colour gradient.* ***(b)*** *The same chip after cleaning with* aqua regia. *The fungi are still present and the cantilevers are still bent but the change in colour indicates that the gold layer is removed.* ***(c)*** *The chip after cleaning with* piranha solution. *All organic debris is removed and the cantilevers appear clean and straight.* ***(d)*** *The cantilever array after evaporation of a thin layer of titanium and gold. Scale bars measure 100 μm.*

The maximum surface stress values for each measurement (i.e. the stress when the attachment and detachment of antibiotic molecules to the cantilever surface is in equilibrium) was then plotted against the corresponding vancomycin solution concentration. These data points can be fitted to the Langmuir adsorption isotherm, a model which describes the concentration dependent adsorption of molecules on a solid surface [Langmuir18]. The model is based on the assumption that target-probe binding events are independent and unaffected by surface coverage. If we further assume that the cantilever bending is proportional to the surface coverage, the model can be used to describe the concentration dependent surface stress on cantilevers [McKendry02] (see appendix A for derivation):

$$\Delta\sigma_{eq} = \frac{a \cdot [Van]}{K_d + [Van]} \tag{6.1}$$

where $\Delta\sigma_{eq}$ is the change in cantilever surface stress upon analyte binding (the subscript eq indicates that we are measuring equilibrium signals), a is the maximum surface stress when all accessible mucopeptide analogues are occupied by a vancomycin molecule, $[Van]$ is the vancomycin solution concentration and K_d is

equilibrium dissociation constant on the cantilever surface. By applying this equation to a set of binding experiments, we can calculate K_d which is a measure for the binding affinity of the antibiotic to the bacterial cell wall peptides on the cantilever surface.

The cantilever response to different vancomycin solution concentrations was measured on 7 cantilevers from 7 different arrays. The bending signals of the **D*Ala***-coated cantilevers were converted into surface stress signals using Stoney's equation (see section 5.3.4). Figure 6.9a shows the absolute surface stress of 1 **D*Ala***-coated and 2 ***PEG***-coated cantilevers from the array with the identification code R18. Whereas the **D*Ala*** cantilever exhibits a rapid increase in surface stress for increasing vancomycin concentrations, reaching a saturation value of $\sim$ 60 mN/m for vancomycin concentrations larger than 50 μM, the ***PEG*** cantilevers showed no significant surface stress in any measurements. Although there was a slight variance in ***PEG*** signals for different vancomycin concentrations, the surface stress for the two ***PEG*** cantilevers was almost identical for a given binding experiment. The corresponding differential surface stress signal, which was calculated as the response of the **D*Ala*** cantilever minus the mean of both ***PEG*** cantilevers, is displayed in figure 6.9b.

Figure 6.9c shows the differential stress signals for all 7 cantilevers. It is evident that there is a large variation in stress signals for different arrays although the values always follow the same shape and reach saturation at a vancomycin concentration of $\sim$ 50 μM. This is consistent with previous findings that there is a high reproducibility of within-array measurements but an increased variance when using different cantilever array chips [Watari07b] (see also discussion section of this chapter).

Figure 6.9d shows the average differential stress of all 7 cantilevers and the corresponding standard error bars. The data was fitted to the Langmuir adsorption isotherm (equation 6.1) which gave a K_d of 0.9 $\pm$ 0.2 μM and an a value of -42.0 $\pm$ 1.5 mN/m. This K_d value is in agreement with previously reported values from cantilever sensor, surface plasmon resonance and solution-phase UV spectroscopy data (table 6.1). However, the a value is significantly higher compared to the average of previous results

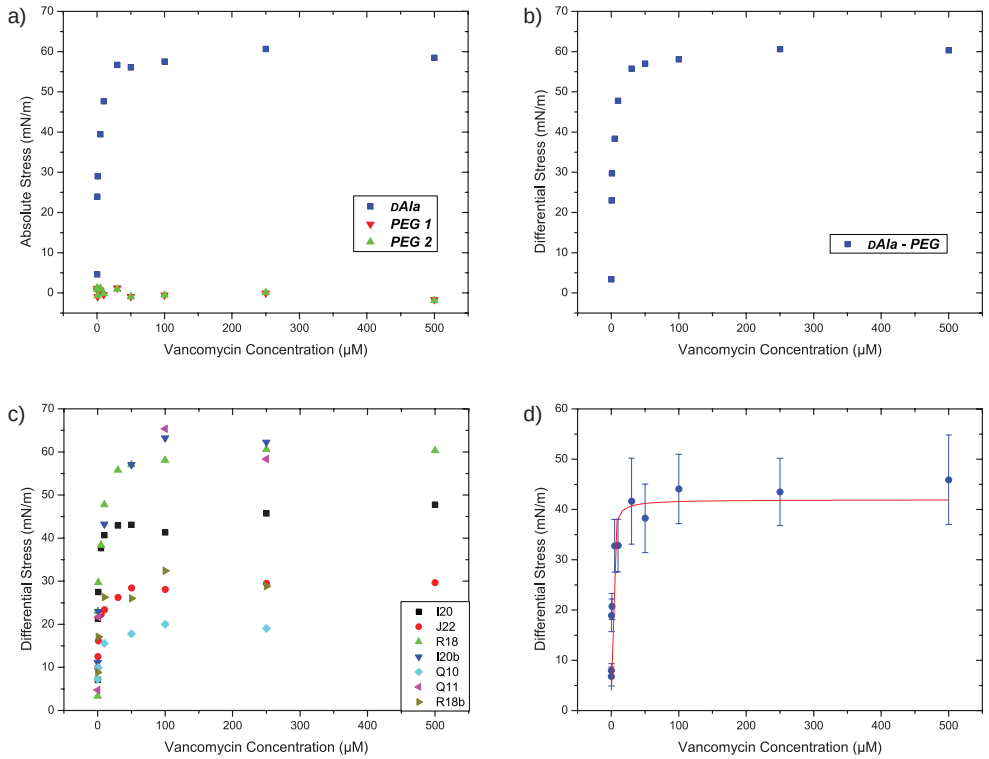

Figure 6.9: Cantilever surface stress measurements with different vancomycin concentrations to investigate the drug-target binding affinity. ***(a)*** *Absolute stress signal of 1* **DAla***-coated and 2* **PEG***-coated cantilevers from chip R18 and* ***(b)*** *the corresponding differential stress signal (***DAla** *minus arithmetic mean of* **PEG** *cantilevers).* ***(c)*** *Differential stress signals for 7 different cantilever arrays.* ***(d)*** *Mean of all 7 cantilevers with standard error bars (blue). The red line shows the fit of the Langmuir adsorption isotherm.*

in our group, which is 29.7 $\pm$ 1.0 mN/m. Our experience says that, although there is a large variation in maximum stress values for different chips, K_d values are always very similar. It is likely that this difference is caused by the large variation in deflection signals for different cantilever arrays, as mentioned above.

6.7 Measurements in Serum

When drugs are introduced into the human body, they are exposed to a vast number of various proteins. Unspecific binding to these proteins (for example in blood)

Table 6.1: *Equilibrium dissociation constant K_d of vancomycin-mucopeptide interactions on cantilever arrays compared with previously reported cantilever data, as well as K_d literature values measured with surface plasmon resonance and solution-phase UV spectroscopy.*

Cantilever (this work)	Previous Cantilever	SPR	Solution
0.9 ± 0.2 μM	1.0 ± 0.3 μM[1]	1.1 ± 0.1 μM[2]	0.7 μM[4]
		0.7 μM[3]	21 μM[5]

[1] Previous data from our group [Ndieyira08].

[2] SPR assay using self-assembled monolayers [Cooper00a].

[3] SPR assay using lipid layers and Doc-KAA [Spencelayh06], no error given.

[4] Solution assay using diacetyl-L-Lys-D-Ala-D-Ala [Nieto71], no error given.

[5] Solution assay using diacetyl-L-Lys-D-Ala-D-Ala [Bugg91], no error given.

reduces the free concentration of the drug and thereby its activity. The assessment of these interactions and the free drug concentration is crucial for the design of a new drug. Therefore, the potency of cantilever sensors to detect vancomycin in serum was investigated within in the clinically relevant concentration range of 3-27 μM [Rotschafer82]. Figure 6.10 shows the deflection signal for **D*Ala***- and **D*Lac***-coated cantilevers upon injection of 7 μM vancomycin in serum (90% fetal calf serum plus 10% sodium phosphate buffer pH 7.4). The differential signal for **D*Ala*** in serum was 105 ± 4 nm, and no significant bending was detected for **D*Lac***. This proves that cantilever sensors are still sensitive to the vancomycin-mucopeptide interaction in a complex background of serum. However, this signal is significantly smaller compared to the measurement in buffer solution with the same vancomycin concentration and on the same chip, which was 143 ± 5 nm (see fig. 6.3b). We therefore presume that the free vancomycin concentration is smaller in serum, as a certain amount of vancomycin

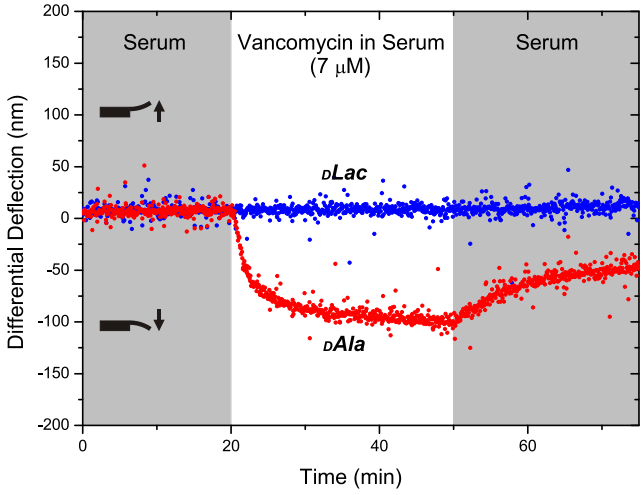

Figure 6.10: Detection of vancomycin in blood serum at clinically relevant concentration. *Differential bending signal of* **DAla** *(red) and* **DLac** *(blue) upon injection of 7 μM vancomycin in a mixture of 90% fetal calf serum and 10% sodium phosphate buffer is shown.*

molecules are bound to serum proteins (continuing work on this topic was done by Ndieyira *et al.*, manuscript in preparation).

6.8 Discussion

The experiments presented in this chapter confirm and support previous results in our group, which described for the first time the investigation of drug-target binding interactions using cantilever array sensors. The results show that cantilever sensors have the sensitivity to detect and quantify the binding affinity of the antibiotic vancomycin to mucopeptide analogues. Thereby we could discriminate between mucopeptide precursors found in vancomycin-sensitive (**D*Ala***) and vancomycin-resistant bacteria (**D*Lac***), and detect the deletion of a single hydrogen bond which is associated with the bacteria's drug resistance. This work particularly showed (1) that the detection limit of the vancomycin-mucopeptide interaction with the current set-up is $\sim$ 10 nM, (2) that cantilever chips can be reused and recycled for multiple measurement cycles and (3) that the set-up is still able to specifically detect the drug-target interaction in

a complex background of serum. The latter is particularly important to investigate promising drug candidates in relation with its tendency to bind to serum proteins which reduce the concentration of free drug that is available to bind to its target. Further work on this topic was done by Ndieyira (manuscript in preparation, 2011).

When antibiotic molecules are binding to the mucopeptide analogues on the cantilever surface, a local strain is generated. In all antibiotic binding experiments a downward bending of the cantilever was observed that is caused by a compressive surface stress on the upper side of the cantilever. The reasons for this surface stress include steric crowding, electrostatic repulsion (vancomycin carries an overall charge of +1 at pH 7.4) and other changes in surface energy (this will be discussed in more detail in chapter 8). Furthermore, the fact that the deflection signal is not going back to the baseline when injecting buffer solution after the antibiotic injection, and the fact that an HCl washing step of at least 30 min is needed to regenerate the cantilever surface, indicate that the vancomycin-mucopeptide interaction is fairly strong.

The experiments also confirmed the need for a suitable coating for *in-situ* reference cantilevers. Polyethylene glycol has proven to be a good choice, as our ***PEG***-coated cantilevers showed no significant response to the antibiotic solution for any antibiotic concentration measured. Differential deflection measurements help eliminate unspecific effects such as changes in temperature or changes in refractive index of the liquid, and non-specific interactions with the underside of the cantilevers. They also remove spikes and changes in cantilever deflection caused by changes in flow rate and liquid pressure when a new liquid is injected.

All data sets recorded using a dilution series of vancomycin followed nicely the Langmuir adsorption isotherm. Although the results from different arrays gave very similar K_d values, there was a large variance in the maximum surface stress (a value). The large variance of between-array measurements compared to within-array measurements agrees with previous findings in our group [Watari07b, Barrera08], however this may have various reasons which are difficult to identify. Possible reasons are mechanical differences of the cantilevers themselves (spring constant) due to irregular-

ities in the microfabrication process, differences in the gold layer or inhomogeneities in the thiol layers. However it is difficult to detect mechanical effects because mechanical differences are convoluted with the laser alignment. Furthermore, differences in a values did not correlate with differences in heating test signals nor resonance frequencies (fig. 6.11), which would be the case for a mechanical origin. It is sometimes observed that cantilevers are bent after the gold evaporation. Because we only measure the change in cantilever deflection upon analyte binding and not the absolute bending of the cantilevers, the initial bending might also have an influence on the measured deflection signal. We also observed that small changes in the solution concentrations of the D***Ala*** thiols (and maybe also variations in the incubation time) give rise to significant variations in the deflection signal due to different structural arrangements of the monolayer (this will be covered in chapter 8). Cross-contamination of neighbouring cantilevers through drops that are spreading onto the chip body during functionalization is also possible but we always took care that this did not happen. Nevertheless, thiols might also migrate through the vapour phase from one cantilever to another during the functionalization process, especially if high concentrations of thiol solutions are used.

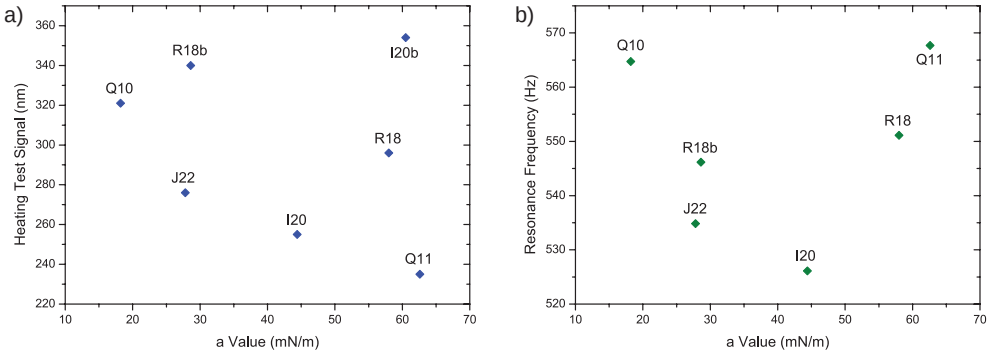

Figure 6.11: Relation of mechanical properties of cantilevers with maximum stress values. ***(a)*** *Heating test signals and* ***(b)*** *resonance frequencies plotted against a values for the cantilevers mentioned in section 6.6. No correlation is observed for these parameters.*

To sum up, functionalization of cantilever arrays seems to a crucial process and the main contribution to the variation of deflection signals between different arrays. The capillary method is a simple way to coat each cantilever of an array differently. However, it is not performed in a very well controlled environment and is also dependant on the operator. For the future progress of the cantilever technology alternative and more reliable functionalization procedures have to be considered.

6.9 Conclusion

This chapter demonstrates the ability of cantilever sensors to detect and quantify the binding interactions of the glycopeptide antibiotic vancomycin to cell wall peptide analogues. Thereby the setup is able to discriminate between cell wall peptides occurring in vancomycin-sensitive and vancomycin-resistant bacteria. Furthermore, I showed that the sensing layers and cantilever chips can be regenerated to allow for multiple consecutive binding experiments and multiple usage of sensor chips, which is essential for drug screening applications. Moreover, it has been shown that the antibiotic-mucopeptide interactions can even be detected in a complex background of serum proteins. This opens up radically new possibilities for the study and prediction of drug activities in the human body. However, functionalization of cantilever arrays seems to be a crucial process and significantly contributes to the variation of deflection signals between different arrays. The role of surface coatings will be investigated further in the following chapters.

CHAPTER 7

Percolation of Drug-Target Interactions

7.1 Introduction

The previous chapter illustrates that cantilevers are a promising technology to investigate drug-target interactions – able to measure binding constants with nanomolar sensitivity and high specificity to drug-susceptible and resistant phenotypes, even in blood serum. However the mechanism by which local drug-target binding at the cell wall actually kills a bacterium remains the subject of much debate and interest. Recently our group has proposed a percolation model to describe the generation of surface stress on cantilevers and speculate that it may also be applicable to forces on real bacteria [Ndieyira08]. The model proposes that stress is dependent on two factors: a chemical factor that describes the local drug-target interaction and a geometric factor that describes the large scale connectivity that arises from a stressed network formation (fig. 7.1). The model was tested using cantilevers coated with different amounts of **D*Ala*** using mixed monolayers of **D*Ala*** and ***PEG***.

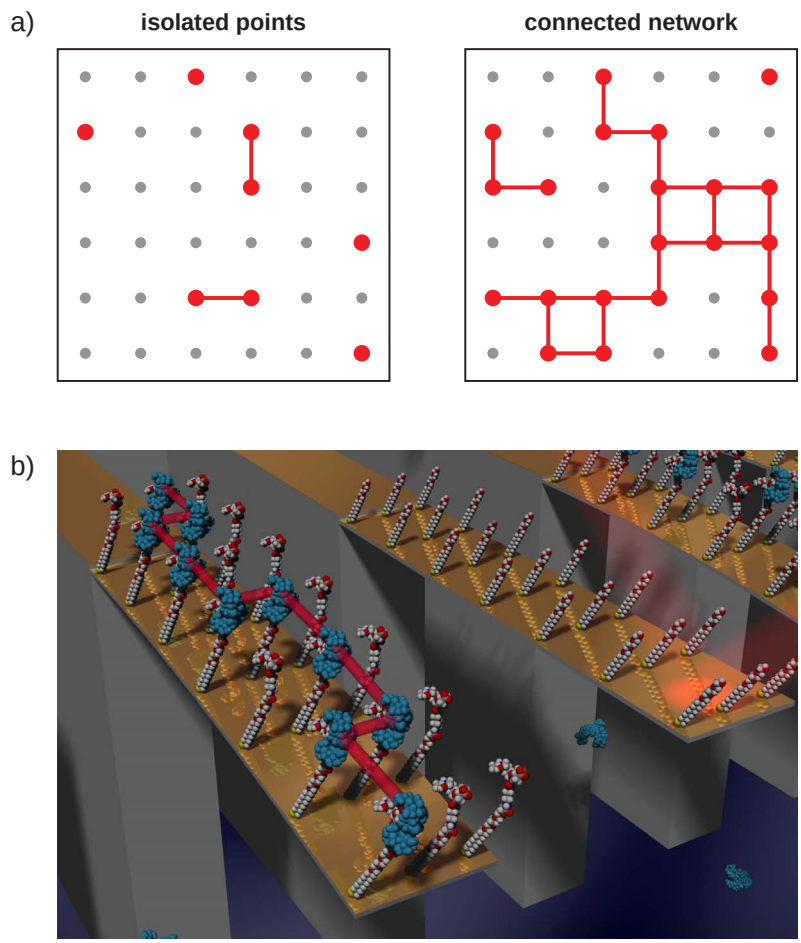

Figure 7.1: Principle of percolation. *(a) Schematic to show the concept of percolation. If only a small number of sites are occupied (left), the points are isolated from each other (grey dots = unoccupied; red dots = occupied). When the number of occupied sites increases (right), a percolating network is formed that connects the binding sites (red lines).* ***(b)*** *Illustration of percolation on cantilevers. The blue objects represent vancomycin molecules bound to* **DAla** *on the cantilever (or free floating in solution). The red line symbolises the percolation effect, i.e. the connectivity of the vancomycin-mucopeptide binding sites.*

The aim of my work was to further investigate this work and examine the role of different drugs, particularly dimerising analogues of vancomycin that have been shown to be effective against resistant phenotypes. Therefore, in this chapter I will first review the concept of percolation and the findings of previous work. In this context I will highlight my contribution to this work in the form of XPS analysis of surface coatings to determine the true density of **D*Ala*** on a surface. I will then describe my attempts to subsequently repeat the cantilever experiments on vancomycin binding to mixed **D*Ala*/*PEG*** monolayers and the challenges encountered, followed by preliminary work using the dimerising antibiotic chloroeremomycin.

7.2 Concept of Percolation on Cantilevers and Bacteria

The background of this work comes from experimental measurements previously done in our group which investigated the mechanical response of cantilevers to different **D*Ala*** densities using mixed monolayers [Ndieyira08]. This was achieved by mixing **D*Ala*** thiols with ***PEG*** thiols in different ratios prior to the formation of the SAMs. The **D*Ala*** surface coverage fraction was defined as p, with $p = 1$ for a pure **D*Ala*** layer and $p = 0$ for a pure ***PEG*** layer. Experiments showed that for fixed vancomycin concentration, no detectable nanomechanical signal was measured for $p = 0$ to $p = 0.1$, whereas from $p = 0.1$ to $p = 1$ there is a steady increase following an approximately linear shape. This suggests that the surface stress transduction is a collective phenomenon that requires connectivity of the occupied binding sites by short-range interactions. This in turn is only possible if a relatively large fraction of the surface is covered and the binding sides are close enough. Assuming that the local chemical events and geometric effects responsible for the collective build-up of strain are separable, a percolation model was developed for the description of cantilever surface stress

$$\Delta\sigma_{eq} = \frac{a \cdot [Van]}{K_d + [Van]} \left(\frac{p - p_c}{1 - p_c}\right)^{\alpha} \qquad \text{for} \quad p > p_c \tag{7.1}$$

and zero otherwise, where p_c is the critical percolation threshold. The first term is the Langmuir adsorption isotherm, which has been used previously to describe drug-target binding events (equation 6.1), and the second term describes the large-scale mechanical connectivity of the binding sites and the resulting formation of a network of interactions (percolation) [Stauffer94]. The exponent of the power law α accounts for elastic interactions between binding sites upon vancomycin binding. For short-range interactions, such as steric neighbour-neighbour repulsive interactions, there will be a finite percolation threshold p_c above which there will be a connected network that can produce an apparent bending of the cantilever.

The fit of the equation above to the data that was measured previously in our group revealed a percolation threshold $p_c = 0.075$ and a power law $\alpha = 1.3$ (fig. 7.2). This indicates that the generation of cantilever surface stress due to a drug-target binding reaction is indeed a collective phenomenon where a certain number of binding sites

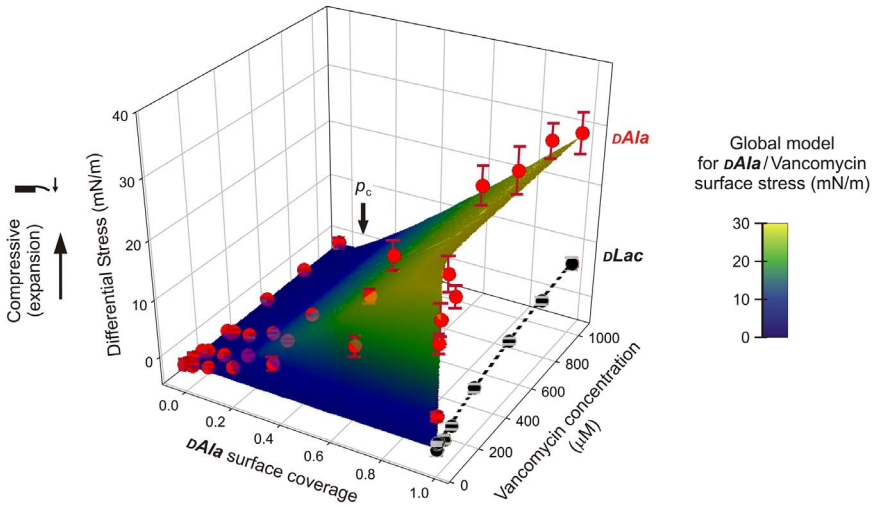

Figure 7.2: Nanomechanical drug-target percolation on cantilever arrays. *A three-dimensional graph showing the measured differential surface stress response for* **DAla***- (red circles) and* **DLac***-coated cantilevers (black circles) as a function of vancomycin concentration in solution [Van] and* **DAla** *surface coverage p, superimposed with the results of the global fit according to equation 7.1. (Figure from [Ndieyira08].)*

need to be occupied in order to form a network of interactions and thus large-scale repulsive forces.

7.3 Analysis of Mixed Monolayers using XPS

The ratio of two different thiols in a mixed monolayer is not always linearly proportional to their molar fraction in the solution used to prepare the SAM because often one component preferentially adsorbs onto the gold substrate [Whitesides90]. For the quantitative analysis of the stress signals in [Ndieyira08], we therefore investigated the relation between solution molar fraction and surface coverage fraction of a mixture of **D*Ala*** and ***PEG*** thiols using X-ray photoelectron spectroscopy (XPS). The corresponding SAMs were prepared by mixed **D*Ala*/*PEG*** solutions with a **D*Ala*** molar fraction of 0.0, 0.05, 0.1, 0.3, 0.5, 0.7, 0.9 and 1.0, respectively (a ratio of 0.0 indicates a pure ***PEG*** solution and a ratio of 1.0 a pure **D*Ala*** solution). High resolution scans of the N (1s), S (2p) and Au (4f) peaks were recorded using an analyser pass energy of 20 eV (fig. 7.3). The graphs show that there is no visible nitrogen signal for ratios below 0.3 **D*Ala*** and the highest nitrogen intensity is measured for a pure **D*Ala*** monolayer. The sulphur signals look very similar for all samples except for the pure **D*Ala*** monolayer where a clearly lower sulphur signal was detected. However, there is a very low signal-to-noise ratio for the sulphur peak because there is only one sulphur atom per thiol molecule, hence we have to be careful when interpreting this data. The intensity of the gold signal decreased for samples with a **D*Ala*** molar fraction above 0.7 and was lowest for a pure **D*Ala*** layer.

The N (1s) intensity can be directly correlated with the **D*Ala*** surface coverage as nitrogen is present only in **D*Ala*** peptides and not in ***PEG***. The overall coverage of thiols is proportional to the sulphur intensity because only one sulphur atom occurs in each thiol. However, because the sulphur atoms are located at the interface between the thiol layer and the gold surface, the sulphur photoemission electrons are attenuated by the overlying layer. Furthermore, **D*Ala*** molecules are longer and bulkier than ***PEG***

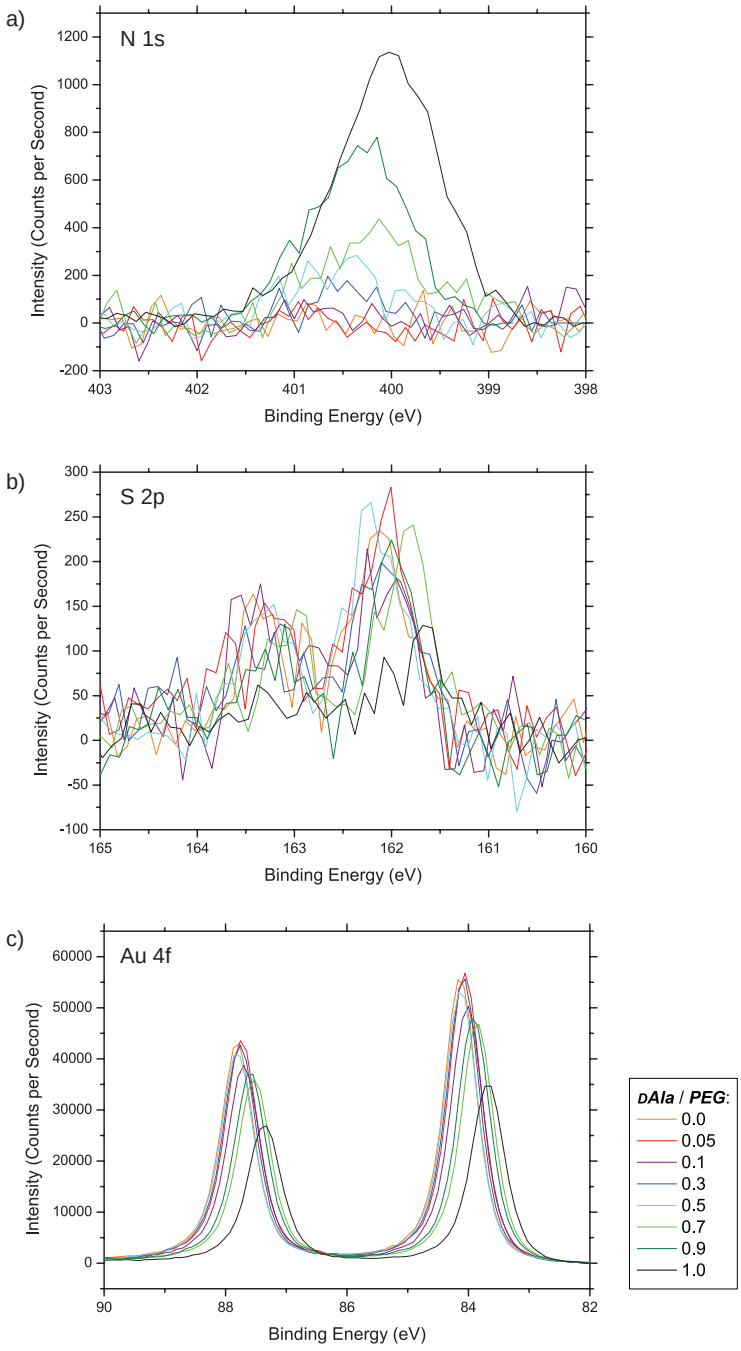

Figure 7.3: X-ray photoelectron spectroscopy raw data for mixed monolayers. *Curves are overlaid for mixed monolayers prepared by different* **DAla/PEG** *solution molar ratios.* ***(a)*** *N (1s),* ***(b)*** *S (2p) and* ***(c)*** *Au (4f) signal.*

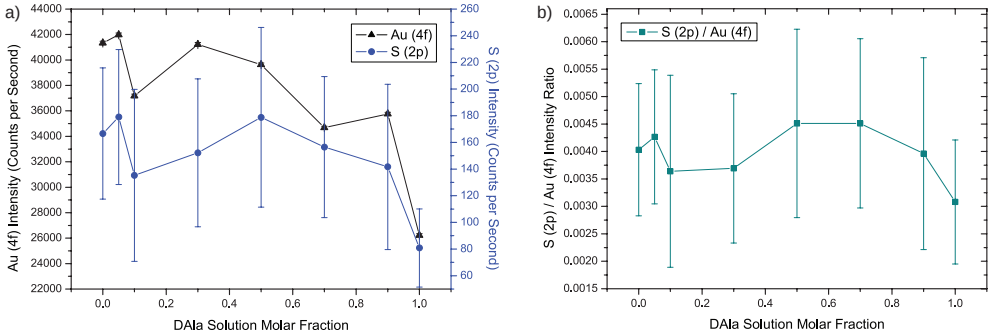

Figure 7.4: XPS analysis of sulphur and gold intensities to account for monolayer thickness and photoelectron attenuation. ***(a)*** *Intensities of the S (2p) (blue circles) and Au (4f) signal (black triangles) for mixed monolayers from different* **DAla/PEG** *solution molar ratios.* ***(b)*** *Ratio of the the S (2p) and Au (4f) intensities.*

and therefore we expect differences in monolayer thickness for different **D*Ala*/*PEG*** ratios. This has an impact on the sulphur intensities so that the S (2p) peak cannot be correlated directly with the overall thiol density. This problem can be avoided by calculating the ratio of the S (2p) and Au (4f) intensities because both intensities will be attenuated by a very similar extent by the overlying layer. Figure 7.4 shows the intensities of the S (2p) and Au (4f) and their ratio which is a measure for the total thiol surface coverage.

Figure 7.5 shows the results for the N (1s) intensities and the the ratio of the S (2p) and Au (4f) intensities as a function of **D*Ala*** solution molar fraction, both normalised to 100% **D*Ala***. It is obvious from this graph that the ratio of **D*Ala*** solution molar fraction and surface coverage does not follow a linear relation but that the adsorption of ***PEG*** is preferred over adsorption of **D*Ala***. This finding is crucial for the quantitative analysis of the cantilever experiments with mixed monolayers and the resulting surface stress upon antibiotic binding. Furthermore, this data showed that the overall thiol density is lower for pure **D*Ala*** monolayers compared to ***PEG*** SAMs. This finding is intuitive because **D*Ala*** molecules are longer and have bulky end groups, giving rise to greater steric effects and hence to a lower surface coverage. We can estimate the surface area occupied by one **D*Ala*** peptide molecule by comparing

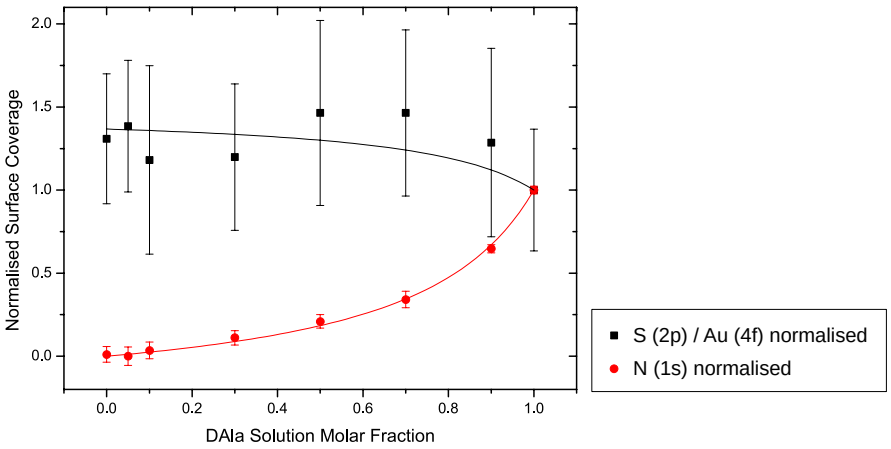

Figure 7.5: XPS analysis of mixed monolayers. *The N (1s) signal (red) and the ratio of the S (2p) and Au (4f) signals (black) are plotted versus the* **DAla** *solution molar fraction (both normalised to 100%* **DAla***). Fits of equations 7.2 and 7.3 to the data are shown.*

the S (2p) / Au (4f) ratio for pure ***PEG*** and **D*Ala*** monolayers. By referring to the literature value of 0.27 nm^2 per thiolate reported for ***PEG*** SAMs [Schwendel03], this translates into a molecular area of 0.35 nm^2 in the 100% **D*Ala*** SAM.

A model was developed by Moyu Watari to describe the competitive adsorption of ***PEG*** and **D*Ala*** thiols onto a gold surface (see [Ndieyira08] supplementary material). According to this model the surface coverage fraction of **D*Ala*** $\chi_{DAla}^{surface}$ and ***PEG*** $\chi_{PEG}^{surface}$ can be calculated using the following equations

$$\chi_{DAla}^{surface} = \frac{K_{DAla}\ \chi_{DAla}^{solution}}{1 + \chi_{DAla}^{solution}\ (K_{DAla} - 1)} \tag{7.2}$$

$$\chi_{PEG}^{surface} = \frac{K_{DAla}\ (1 - \chi_{DAla}^{solution})}{K_{thiol}\ (1 + \chi_{DAla}^{solution}\ (K_{DAla} - 1))} \tag{7.3}$$

where $\chi_{DAla}^{solution}$ is the **D*Ala*** solution molar fraction, K_{DAla} is the surface binding constant of **D*Ala*** and K_{thiol} is the overall thiol binding constant. When fitting these equations to the data in figure 7.5, we found the values $K_{DAla} = 0.23 \pm 0.01$ and $K_{thiol} = 0.16 \pm 0.01$, suggesting that the adsorption on ***PEG*** is preferred compared to **D*Ala***.

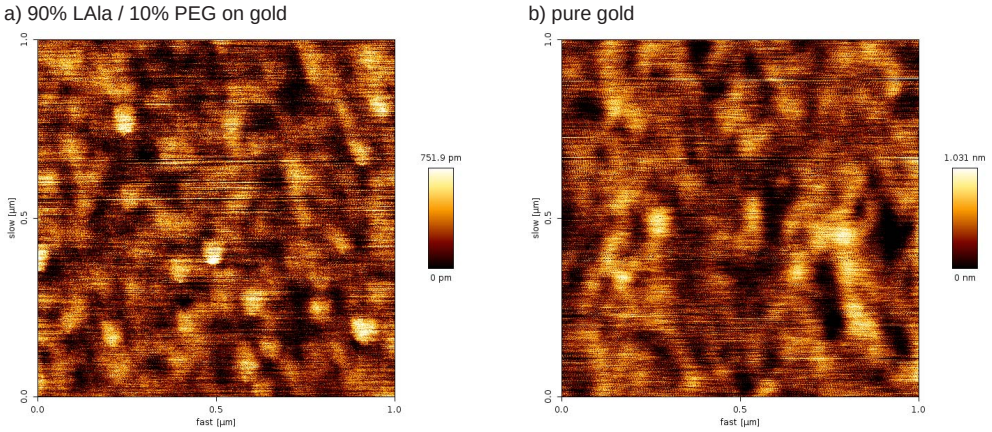

Figure 7.6: Investigation of mixed monolayers using atomic force microscopy. *AFM images of* ***(a)*** *a mixed monolayer of* **LAla** *and* **PEG** *in a solution molar ratio of 9:1 on a gold substrate and* ***(b)*** *a bare gold substrate.*

7.4 Investigation of Mixed Monolayers using AFM

Besides the challenges with the mixing ratios in mixed monolayers, which was addressed in the section above, it is also unclear if the different thiols aggregate into separated islands or are randomly distributed. AFM was therefore used in an attempt to image mixed monolayers. From these measurements I hoped to get an insight into the arrangement of the monolayers and whether phase separation occurs or not.

However, due to limited supplies of **D*Ala***, these experiments had to focus on the enantiomer **L*Ala***. **L*Ala*** is the stereoisomer of **D*Ala***, i.e. they have the same chemical structure but **L*Ala*** has two terminal L-Alanine residues instead of D-Alanine. **L*Ala*** was used instead of **D*Ala*** because our **D*Ala*** stock solution was almost used up and I expected a very similar arrangement of the monolayers for both thiols. A piece of gold-coated silicon wafer (see section 5.4.1) was coated with a mixture of **L*Ala*** and ***PEG*** in a solution molar ratio of 9:1. Figure 7.6 shows an AFM image of those mixed monolayers and a bare gold sample. Both samples look very similar and the topology of the images arises mainly from the roughness of the gold surface. The gold grains are fairly small because I did not have the equipment to anneal the gold

layer during evaporation, and thus the thiol monolayer was not observable with AFM. Future experiments will use annealed gold surfaces with large crystalline gold terraces and hopefully I will be able to image the monolayers using those substrates. An option would also be to bind antibiotics to the D***Ala*** peptides on the surface, which makes them more distinguishable from the shorter ***PEG*** thiols. However, in order to make the antibiotic stick to the surface, it is likely that the monolayers have to be imaged in liquid in the presence of a high antibiotic concentration, which would be very difficult to accomplish.

7.5 Binding Experiments with Mixed Monolayers

I repeated the mixed monolayer experiments that have previously been done in our group [Ndieyira08] (see above) and performed vancomycin binding experiments where the cantilever response was investigated for varying vancomycin concentrations and varying D***Ala*** densities on the cantilever. An important point to emphasise upfront is that new mixed D***Ala/PEG*** solutions were prepared for the experiments described in this and the next section because the previous solutions were used up after the XPS experiments described in section 7.3. Furthermore, there was only a very small amount of D***Ala*** stock left (which was kept in a 2 mM stock solution) so that the XPS analysis could not be repeated with the new mixed solutions. Therefore, we had to assume that the solution molar fractions and the resulting surface coverage fractions were identical for both sets of samples. As it will be seen in this section, this assumption poses a challenge for the interpretation of the cantilever data. Therefore, these results must be interpreted with caution. However, the findings and methodologies developed in this chapter were deemed important for the cantilever field and highlight the challenges and need to fully characterise the properties of the sensing layers.

For the experiments presented in this section, all eight cantilevers of a chip were coated with different mixed monolayers ranging from 0% to 100% D***Ala***. Figure 7.7a-e shows the results for four different cantilever arrays and their average, where the dif-

ferential surface stress was plotted against the vancomycin concentration for different **D*Ala*** solution molar ratios. Upon fit of the Langmuir adsorption isotherm (equation 6.1), the average graph reveals a saturation stress value of 39.5 mN/m for pure **D*Ala*** monolayers and a K_d of 1.40 $\pm$0.87 μM. The saturation stress drops by a factor of 6.5 for 90% **D*Ala*** (solution molar fraction), giving a value of only 6.1 mN/m and almost undetectable values for lower **D*Ala*** coverage. These results are different to previously measured data in our group [Ndieyira08] where a surface stress of $\sim$ 20 mN/m was detected on cantilevers that were prepared with 90% **D*Ala*** solution, and still $\sim$ 5 mN/m with 70% **D*Ala***. The mismatch between these two sets of experiments can be due the differences in the mixed thiol solutions used to prepare the SAMs or due to differences during the functionalization process, and will be discussed at the end of this chapter.

This surface stress data was then also plotted versus the **D*Ala*** surface coverage fraction (fig. 7.7f), which was determined from the solution molar fractions and the XPS measurements presented in the previous section.[1] The plots in figure 7.7f show a strong non-linear dependence of the surface stress on the **D*Ala*** surface molar fraction, and a rapid drop of surface stress in the range of a **D*Ala*** surface coverage fraction $p = 1$ to $p \approx 0.7$. A series of least-square fits of equation 7.1 to this data was carried out in order to find values for the percolation threshold p_c and the power law α. Because the parameters p_c and α describe a collective phenomenon and are thus coupled in a statistical sense, not only multiparameter fits were performed but I also examined how the fit changes as a function of p_c. Figure 7.8 shows the resulting α for different p_c and the corresponding squared deviation, which revealed a percolation threshold of $p_c = 0.0$ and a corresponding power $\alpha = 4.03 \pm 0.42$. These results are in contradiction with previous results in our group that showed a $p_c > 0$ (see introduction of this chapter), however this discrepancy is not very surprising as I

[1] Note again that the mixed **D*Ala*** and ***PEG*** solutions were prepared freshly for the new experiments mentioned in this section as the old stock solutions were used up after the XPS measurements. Therefore, the total concentrations and ratios of the two compounds might not be exactly identical. Nevertheless, I had to assume that solution and surface molar fractions were the same for both sets of solutions as I did not have enough **D*Ala*** left to perform another XPS run.

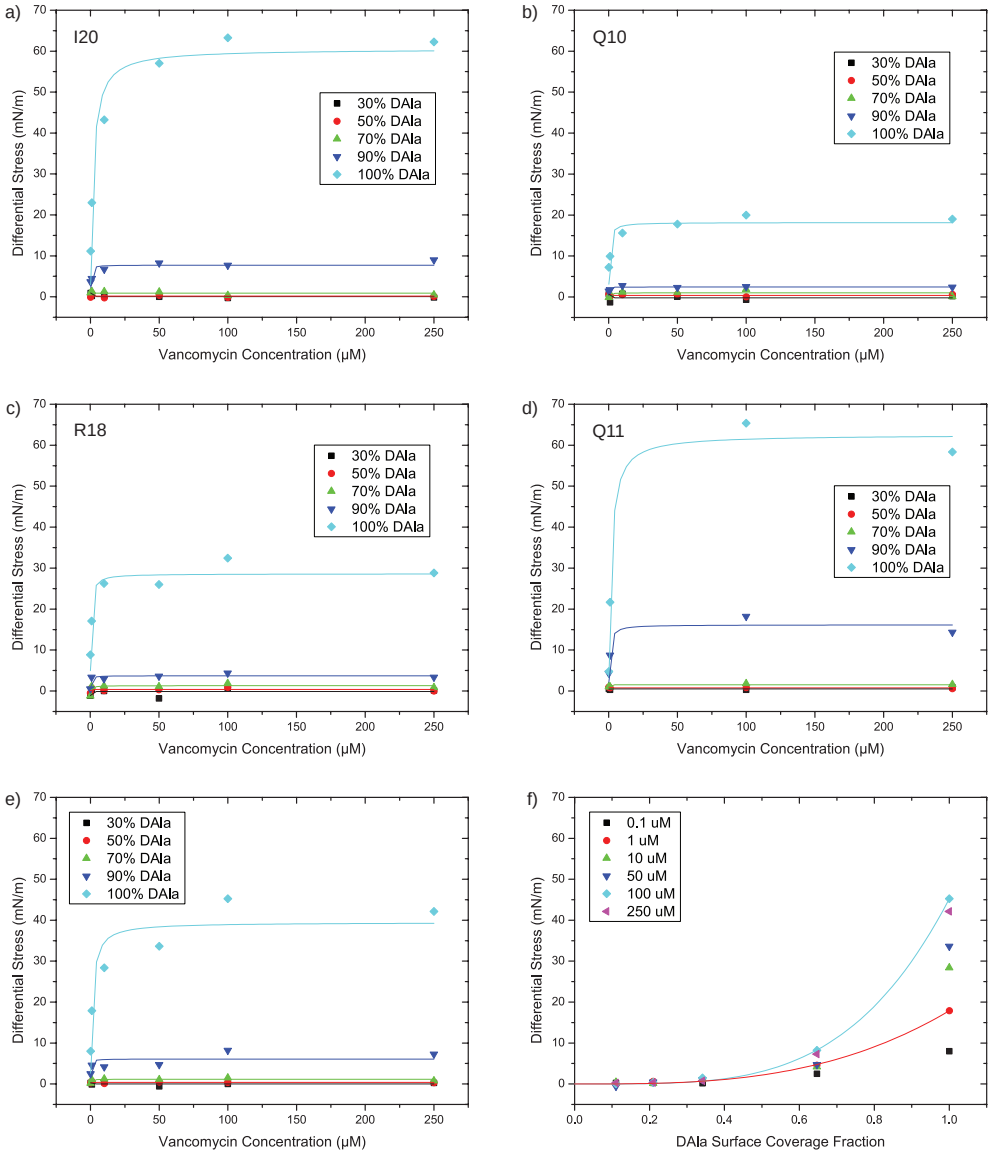

Figure 7.7: Nanomechanical drug-target percolation on cantilever arrays using vancomycin. *Differential surface stress values for varying vancomycin concentrations and varying* **DAla** *solution molar fractions for* ***(a)*** *chip I20,* ***(b)*** *chip Q10,* ***(c)*** *chip R18 and* ***(d)*** *chip Q11.* ***(e)*** *Average stress signal from those four chips. Fits of the Langmuir adsorption isotherm (equation 6.1) are shown for all data points in (a)-(e).* ***(f)*** *Average stress signal plotted versus the* **DAla** *surface coverage fraction (estimated from the previous XPS analysis) for different vancomycin concentrations to show the nanomechanical percolation. Fits of equation 7.1 are shown for 1 and 100 μM vancomycin only for clarity.*

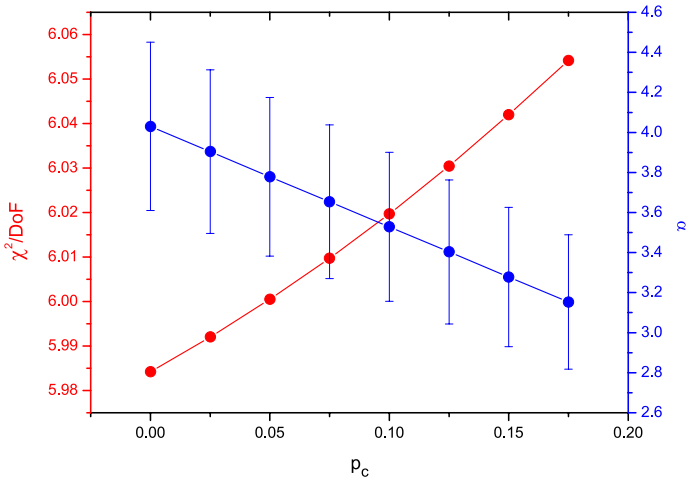

Figure 7.8: Least-square analysis of vancomycin data to determine the best values for p_c and α. *The plot shows the χ^2 values divided by the degrees of freedom (DoF) for each p_c (red) and the corresponding α values (blue).*

measured very low cantilever deflection signals for D***Ala*** surface coverage fractions smaller than 1, as explained above. A percolation threshold of zero would suggest the presence of long-range interactions, where no critical density of interaction sites is needed to form repulsive forces and a compressive surface stress.

Multiparameter least-square fits were also applied to the whole data and subsets of the data in the form of constant p or constant $[Van]$ cuts through the data (table 7.1). The results show that all the values are consistent within the experimental errors, although very large errors were calculated for some fits. Therefore, it can be concluded that equation 7.1 is valid and that the chemical and geometrical factors are separable.

7.6 Binding Experiments using Chloroeremomycin

Two of the arrays with mixed monolayers from the previous section were also used to perform binding experiments using the glycopeptide antibiotic chloroeremomycin. Chloroeremomycin is a derivative of vancomycin and has a higher binding affinity to mucopeptides [Allen03]. Both antibiotics share the same backbone but chloroere-

Table 7.1: *Least square fits of equation 7.1 to vancomycin data subsets. [Van] denotes the vancomycin solution concentration. The term 'all' means that all the values measured in these experiments were considered for the fit. If no error is given, the value was fixed during the fitting procedure.*

p	[Van] (μM)	a (mN/m)	K_d (μM)	p_c	α
all	all	39.34 $\pm$ 1.41	1.35 $\pm$ 0.34	0.0 $\pm$ 0.96	4.03 $\pm$ 4.96
all	0.1	39.34	1.35	0.096 $\pm$ 1.11	1.0 $\pm$ 3.55
all	1	39.34	1.35	0.0 $\pm$ 0.48	2.89 $\pm$ 1.89
all	10	39.34	1.35	0.0 $\pm$ 6.26	4.79 $\pm$ 38.06
all	50	39.34	1.35	0.0 $\pm$ 4.10	4.75 $\pm$ 24.72
all	100	39.34	1.35	0.0 $\pm$ 1.85	3.54 $\pm$ 8.55
all	250	39.34	1.35	0.0 $\pm$ 1.20	3.91 $\pm$ 6.02
1.0	all	39.46 $\pm$ 3.40	1.40 $\pm$ 0.87	—	—

momycin has an additional sugar group at residue 6 (see figure 2.4) and it is known that chloroeremomycin has a higher tendency to form homo-dimers than vancomycin, which is believed to be the reason for the higher binding affinity to **D*Ala*** on surfaces [Allen97].

Cantilever binding experiments for varying chloroeremomycin concentrations and varying **D*Ala*** densities were performed in exactly the same way as for vancomycin, except that lower antibiotic concentrations were used (because of the higher binding affinity of chloroeremomycin saturation of the surface stress is reached at lower antibiotic concentrations). Figure 7.9a-c shows the results for two arrays and their average. The average graph revealed a saturation surface stress value of 41.6 mN/m and a K_d of 0.13 $\pm$ 0.05 μM for 100% **D*Ala***, whereas it the deflection signal dropped to 5.7 mN/m for 90% **D*Ala*** solution molar fraction. This is again a large decrease of stress signal for **D*Ala*** coverage fractions lower than 1, similar to what was observed for vancomycin.

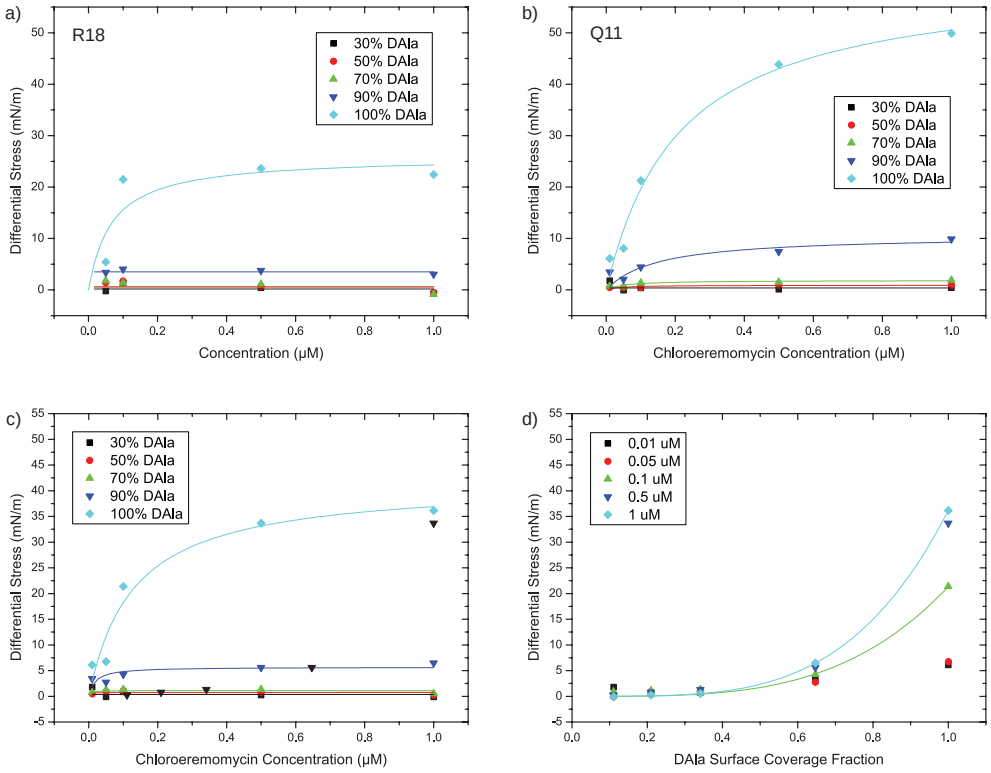

Figure 7.9: Nanomechanical drug-target percolation on cantilever arrays using chloroeremomycin. *Differential surface stress values for varying chloroeremomycin concentrations and varying* **DAla** *solution molar fractions for* ***(a)*** *chip R18 and* ***(b)*** *chip Q11.* ***(c)*** *Average stress signal from those two chips. Fits of the Langmuir adsorption isotherm (equation 6.1) are shown for all data points in (a)-(c).* ***(d)*** *Average stress signal plotted versus the* **DAla** *surface coverage fraction for different chloroeremomycin concentrations to show the nanomechanical percolation. Fits of equation 7.1 are shown for 0.1 and 1 μM chloroeremomycin only for clarity.*

The surface stress data was also plotted versus **D*Ala*** surface coverage fraction determined from previous XPS measurements (fig. 7.9d). Again these results look similar to the vancomycin data with a strong non-linear relationship. A series of least-square fits of equation 7.1 was carried out in order to find values for the percolation threshold p_c and the power law α. Figure 7.10 shows α values for different fixed p_c and the corresponding squared deviation, which revealed a percolation threshold of

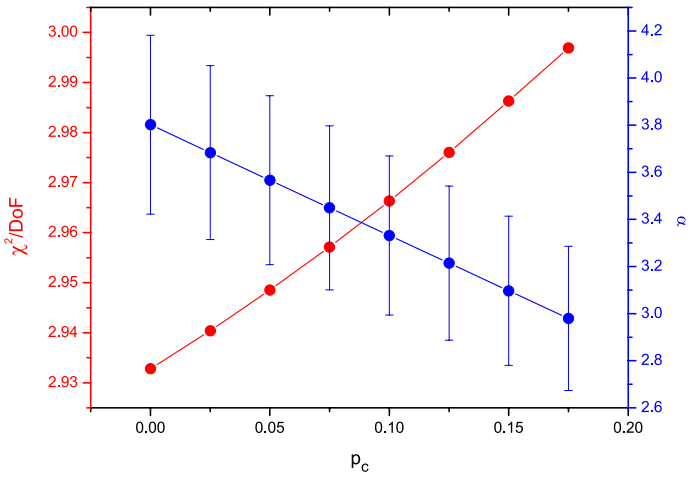

Figure 7.10: Least-square analysis of chloroeremomycin data to determine the best values for p_c and α. *The plot shows the χ^2 values divided by the degrees of freedom (DoF) for each p_c (red) and the corresponding α values (blue).*

$p_c = 0.0$ and a corresponding power $\alpha = 3.80 \pm 0.38$. These results reveal the same p_c compared to the vancomycin experiments, but a slightly smaller α value (although they are within the error limits).

Additionally, multiparameter least-square fits were applied to the whole chloroeremomycin data and subsets of the data in the form of constant p or constant $[CE]$ cuts through the data (table 7.2). The results show again that all the values are consistent within the experimental errors and thus confirm the validity of equation 7.1.

7.7 Discussion

This chapter takes the investigation of antibiotic drug-target interactions one step further by observing the cantilever's response due to varying peptide densities on the surface. When antibiotics bind to a **D*Ala***-coated cantilever surface, molecular binding events occur which generate a repulsive compressive surface stress, the origin of which has been of much scientific interest and debate [Fritz00, McKendry02, Shu07, Watari07b]. The percolation model proposed by Ndieyira *et al.* [Ndieyira08] provides

Table 7.2: *Least square fits of equation 7.1 to chloroeremomycin data subsets. [CE] denotes the chloroeremomycin solution concentration. The term 'all' means that all the values measured in these experiments were considered for the fit. If no error is given, the value was fixed during the fitting procedure.*

p	[CE] (μM)	a (mN/m)	K_d (μM)	p_c	α
all	all	41.29 ± 2.14	0.124 ± 0.022	0.0 ± 0.78	3.80 ± 3.85
all	0.01	41.29	0.124	0.0 ± 1.46	1.00 ± 3.34
all	0.05	41.29	0.124	0.0 ± 3.30	3.09 ± 13.69
all	0.1	41.29	0.124	0.0 ± 1.47	3.19 ± 6.24
all	0.5	41.29	0.124	0.0 ± 0.66	3.99 ± 3.41
all	1.0	41.29	0.124	0.0 ± 0.28	3.99 ± 1.41
1.0	all	41.63 ± 4.83	0.128 ± 0.051	—	—

a useful theoretical framework for the understanding of the surface stress and the mechanical properties of the antibiotic-mucopeptide interaction.

A main achievement of this chapter are the XPS experiments that show the relation between the solution molar fraction and surface coverage fraction of a mixture of two different thiols. It was found the ***PEG*** preferable adsorbs onto the gold substrate compared to **D*Ala***. The tripeptide end group of **D*Ala*** is fairly bulky and hinders the formation of a compact SAM, therefore ***PEG*** will have a higher packing density and more favourable lateral interactions, which might lead to a preferred adsorption and SAM formation.

Another aim of this chapter was to repeat previously reported experiments to investigate the binding of vancomycin to mixed **D*Ala*** monolayers and then expand this method to different vancomycin-related antibiotics. However, my experiments revealed results that are not consistent with the results reported in [Ndieyira08], as I measured much lower cantilever deflection signals at intermediate **D*Ala*** surface coverage fractions, which is exemplarily displayed in figure 7.11. Due to these differences, my cantilever experiments led to fundamentally different values for p_c

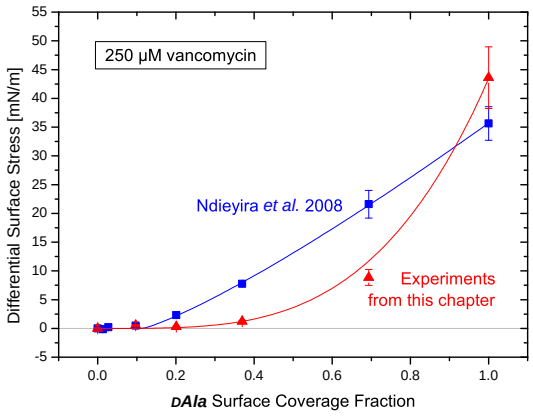

Figure 7.11: Comparison of percolation experiments. *The cantilever surface stress signal upon injection of 250 μM vancomycin is shown for different* **DAla** *surface coverage fractions. The results from [Ndieyira08] are displayed with blue squares and the results from this chapter are displayed with red triangles. Note that the* **DAla** *surface coverage values were assumed to be the same for both set of experiments although different* **DAla** *samples were used.*

and α compared to previous results. The origin of this mismatch can be various and possible reasons are given in the following:

- Chemical change in the stock solution. We assumed that the ***DAla*** solution fraction of the mixed ***DAla/PEG*** solutions was the same as for the samples used for the XPS analysis but it is likely that the ***DAla*** solution fraction was smaller than expected, therefore leading to a lower ***DAla*** surface fraction than the previous XPS measurements suggested. As mentioned earlier, the ***DAla*** stock solution used to prepare those mixed solutions was almost used up and therefore it is possible that the active concentration gradually decreased over time or impurities were added. A lower activity could be explained by the formation of disulphides by the coupling of two thiols. Disulphides (***DAla***$_2$) might adsorb slower to the substrate compared to monomeric ***DAla*** and therefore decrease the surface fraction of ***DAla*** in mixed monolayers. It might also be

possible that **D*Ala*** sticks to plastic pipette tips, so that the overall concentration of the stock solution decreases slightly every time a fraction is removed.

- Temperature effect. The functionalization of cantilever arrays was performed using small glass capillaries on a special stage. However, this process was not temperature-controlled. Different room temperatures might therefore lead to significantly different relative adsorption ratios of **D*Ala*** and ***PEG***, as binding constants K have an exponential dependence on temperature ($K = e^{-\Delta G/RT}$).

- Cantilever properties. The mechanical properties of the cantilever arrays might have changed. However, this is unlikely to have such a big impact, as the chips for the two sets of experiments where taken from the same batch of cantilevers (from the same wafer).

- Gold layer. A different metal deposition system was used in the two sets of experiments for the deposition of the gold layers on cantilevers. This might lead to different gold layers with different grain sizes, which might have an influence on the percolation effects on the cantilever surface.

From these results we learned that the formation of **D*Ala*** SAMs and its effect on the generation of surface stress upon antibiotic binding is still poorly understood. More work on these processes had to be done, which will be reported in the following chapter of this thesis.

Despite the poor repeatability of the percolation experiments in this chapter, a data analysis for the calculation of the p_c and α values was performed. I found a percolation threshold of zero for both vancomycin and chloroeremomycin and very similar α values that were in the error range of each other. While one could argue that the small differences in α values might be due to different modes of action and mechanical properties of the two antibiotics (monomer vs. dimer), we think that the similarity of the α values actually prove the validity of equation 7.1, i.e. that the geometric effects and the chemical binding effects are decoupled.

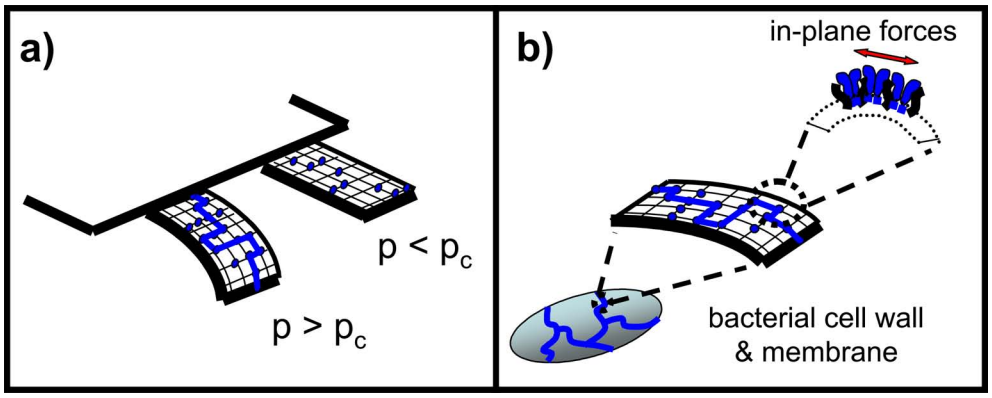

Figure 7.12: ***Concepts underpinning nanomechanical antibiotic transduction.*** ***(a)*** *Schematic showing the concept of percolation on a cantilever array.* ***(b)*** *Schematic illustrating nanomechanical drug-target percolation on a bacterial membrane and cell wall. (Figure from [Ndieyira08].)*

Nevertheless, the studies presented in this chapter have to be repeated to assess the validity of these findings. Recent studies in our group also suggested that the dimerisation of antibiotics plays a larger role when binding to vancomycin-resistant peptides **D*Lac*** (Ndieyira *et al.*, manuscript in preparation, 2011), therefore future work will also use mixed monolayers with the **D*Lac*** instead of **D*Ala***.

7.8 Conclusion

This chapter focused on the understanding of the mechanics involved in the mode of action of glycopeptide antibiotics. It was found that the **D*Ala*** surface density plays a major role in mechanotransduction of binding events, however the experiments were subject to some challenges and the interpretation of the data was not straightforward. Nevertheless, we can speculate that nanomechanical percolation may play an important role not only in cantilever sensor response but also in the glycopeptide antibiotic mode of action in real bacteria (fig. 7.12). Drug-target binding events may act collectively to disrupt the mechanical properties of the bacterial peptidoglycan cell wall and plasma membrane. The results presented in this chapter should therefore clearly

motivate future work to investigate the percolation of drug action in the cell wall and lipid membranes, including eventually those of living bacteria, and also test the nanomechanical mode of action of dimerising antibiotics.

Before the experiments with mixed monolayers can be repeated and tested for different antibiotics, we need to gain a better understanding of the formation of these SAMs. The next chapter therefore focuses on the structure and orientation of pure D***Ala*** SAMs and their impact on the cantilever surface stress. Moreover, the following experiments were performed with a new batch of D***Ala*** peptides, which had to be tested first and compared to results from experiments with the old batch. An improved understanding of these thiols and their SAMs will pave to way for further studies of the mechanics of the antibiotic-mucopeptide interaction using sensing layers with a controlled density of D***Ala*** peptides.

CHAPTER 8

Influence of SAM Structure on Surface Stress

8.1 Introduction

In chapters 6 and 7 it was shown that cantilever sensors are uniquely suited to detect the nanomechanics of antibiotic-mucopeptide interactions and that the magnitude of the surface stress signal strongly depends on the composition of the sensing film. Contrary to other sensing methods such as SPR, our cantilever percolation studies suggested that the highest surface stress signal was generated by relatively high density 'pure' D***Ala*** SAMs. However, these studies investigated only mixed D***Ala/PEG***monolayers using one concentration of D***Ala*** thiol. Moreover, as discussed previously the use of mixed SAMs raises issues of phase separation, which is challenging to characterise at the nanoscale. Therefore the key objective of this chapter was to further investigate the role of the SAM structure on surface stress in order to unravel the fundamental mechanical transduction mechanism and ultimately to significantly amplify the surface stress enabling much lower antibiotic concentrations to be detected. Rather than use mixed monolayers, I simply tuned the concentration of the D***Ala*** thiol solution that

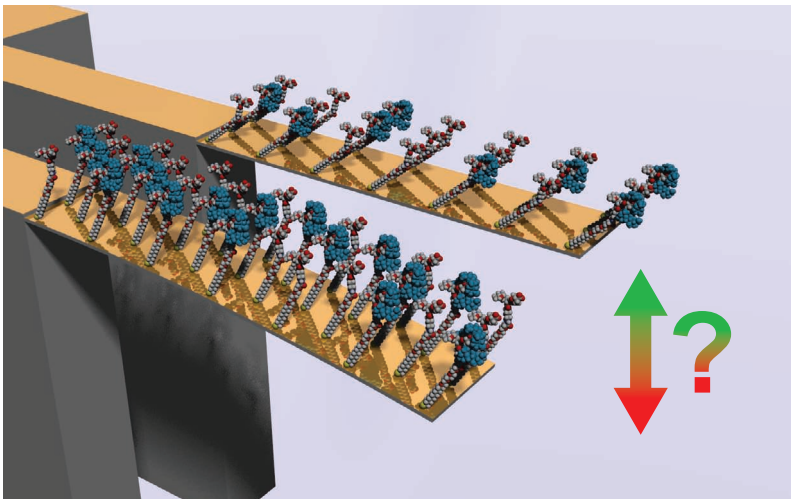

Figure 8.1: Relation between SAM structure and surface stress. *Illustration to depict the question of how the SAM structure can influence the surface stress upon antibiotic binding.*

was used to prepare the SAMs, keeping all other parameters constant, including the incubation time (fig. 8.1). To investigate this effect I characterise the density, orientation and wetting properties of the underlying SAM and deconvolve the influence of the bound vancomycin molecules using complementary surface plasmon resonance measurements. Finally, the findings from these model SAMs are compared to structural studies of Lipid II in real bacteria.

8.2 Effect of Thiol Concentration on Surface Stress

A set of surface stress experiments were performed using cantilevers functionalized with different **D*Ala*** concentrations to determine the optimal **D*Ala*** solution concentration that yields the highest surface stress upon antibiotic binding. Previous models on the function of cantilever sensors suggested that the generation of surface stress depends on steric and electrostatic interactions between bound molecules on the cantilever surface. From these theories and the percolation experiments presented in chapter 7 of this manuscript we expected the surface stress to be proportional to the amount of bound analyte and the density of ligands on the sensor surface (as illustrated

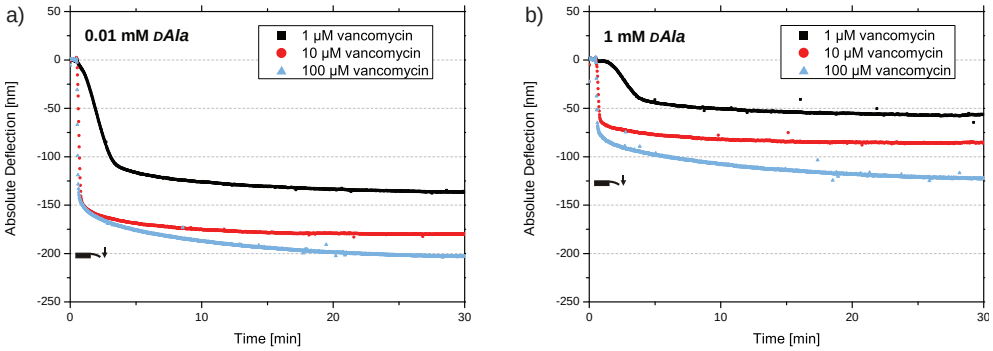

Figure 8.2: *Raw data for the injection of different vancomycin solutions on two different* **DAla** *sensing layers.* ***(a)*** *Bending signal of a cantilever functionalized with a 0.01 mM* **DAla** *solution and* ***(b)*** *with a 1 mM* **DAla** *solution.*

in fig. 8.1). It is therefore commonly suggested to use thiol concentrations in the millimolar range which are known to form nicely packed monolayers within tens of minutes.

The results from my experiments however do not support this convention. Figure 8.2 shows a representative selection of cantilever bending raw data for two different **D*Ala*** concentrations and three different vancomycin injections. I found a downwards bending (compressive stress) upon vancomycin binding for both of these sensor coatings but the cantilever functionalized with 0.01 mM **D*Ala*** gave a signal of 200 nm, almost double that generated by a cantilever functionalized with 1 mM **D*Ala*** (120 nm).

We then expanded this study by using arrays of eight cantilevers coated with different **D*Ala*** concentrations ranging from 10^{-4} to 4 mM. In total 36 measurements were acquired on 40 cantilevers, on 5 individual arrays. When plotting the cantilever saturation deflection against all **D*Ala*** solution concentrations we investigated, the data revealed a sharp peak in the range between 10^{-3} and 0.1 mM **D*Ala*** (yellow area in fig. 8.3), with low signals generated above and below these concentrations. We found the largest deflection at 0.05 mM **D*Ala***. Although we see a fairly large variation between different chips at some **D*Ala*** concentrations, there is a clear amplification

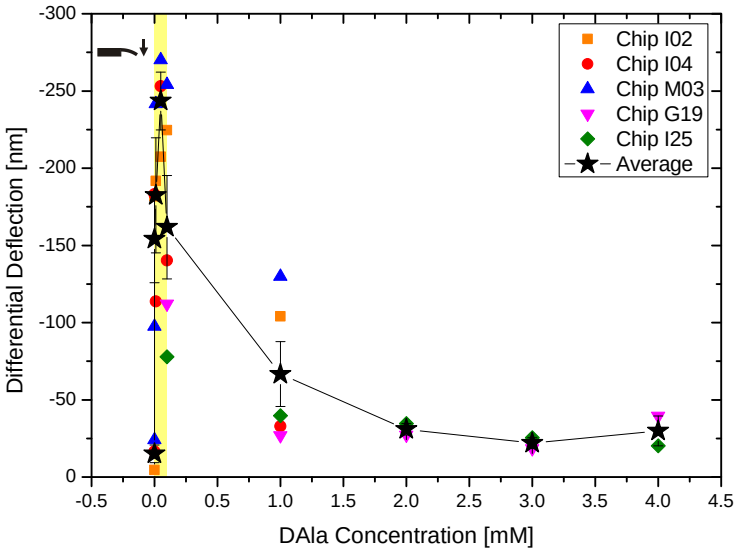

Figure 8.3: Cantilever deflection for different* DAla *layers upon injection of 250 μM vancomycin. *Differential deflection data from 5 different cantilever array chips and arithmetic mean of differential deflection. Error bars are standard errors.*

of cantilever deflection observable in this low concentration range. These results tell us that there must be a significant difference in the arrangement of thiols within the SAMs which have a large impact on the generation of surface stress. The variation in deflection signal between some chips also indicates that the functionalization is a crucial and very delicate step.

In order to understand this striking amplification of surface stress, I used several surface analysis techniques to investigate the structure of the SAMs. Figure 8.4 compares the cantilever deflection and binding strength with the sensing layer thickness and wetting properties.

The dependence of the cantilever deflection on the ***DAla*** concentration can be seen more clearly when plotted on a logarithmic scale (fig. 8.4a) The equilibrium dissociation constant K_d was calculated from deflection measurements with different vancomycin concentrations. I found K_d values around 1 μM for ***DAla*** concentrations between 10^{-3} and 1 mM which are consistent with previously measured binding

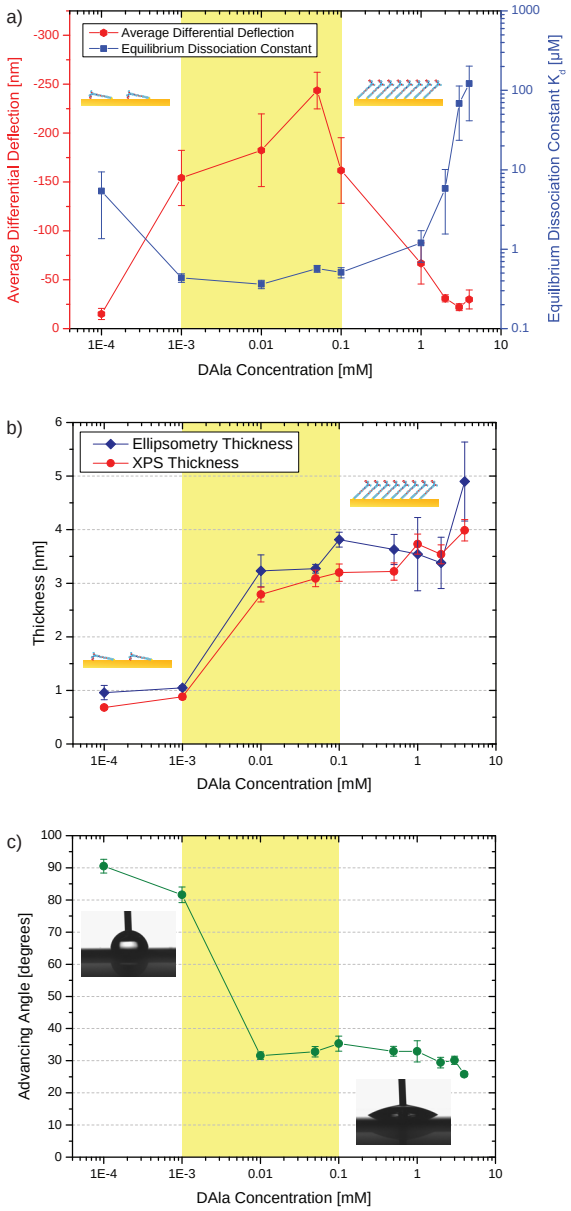

Figure 8.4: Comparison of cantilever deflection and K_d with sensing layer thickness and wetting properties. ***(a)*** *Average differential deflection upon injection of 250 μM vancomycin solution from five different cantilever arrays (red) and equilibrium dissociation constant K_d (blue).* ***(b)*** *Thickness of* **DAla** *layers measured using ellipsometry and ARXPS.* ***(c)*** *Wetting properties of* **DAla** *layers measured using contact angle goniometry. Advancing angles are shown for DI water on* **DAla** *samples. A bare gold sample revealed an advancing angle of 87° (not shown). The yellow area indicated the transition between lying and standing SAMs.*

affinities [Cooper00a, Ndieyira08]. However, K_d values for **D*Ala*** concentration above or below that range were 1–2 orders of magnitude larger.

The thickness of the SAMs were investigated using two methods: (i) ellipsometry and (ii) angle-resolved XPS (details about the ARXPS data is given later in section 8.4). Figure 8.4b shows the measured thicknesses of SAMs formed by different **D*Ala*** solution concentrations. The results from the two different techniques agree very well. For **D*Ala*** concentrations below 0.01 mM, a SAM thickness of 0.7 – 1.0 nm was measured, indicating that no upright monolayer was formed but thiols were lying flat on the gold surface. At a **D*Ala*** concentration of 0.01 mM I measured a thickness of 2.8 ± 0.2 nm, which can be interpreted as a standing-up monolayer. The thickness then increased monotonically for higher **D*Ala*** concentrations reaching a thickness of 4.0 ± 0.2 nm for the 4 mM **D*Ala*** sample.

Contact angle measurements were performed to investigate the wetting properties of SAMs. The advancing angles of DI water were determined on the same samples used for XPS and ellipsometry measurements (fig. 8.4c). The outcome is comparable to the thickness measurements. I found a rapid change in contact angle for **D*Ala*** solution concentrations between 10^{-4} and 0.01 mM (from hydrophobic towards more hydrophilic surfaces) and an almost invariable contact angle of $\sim 30^{\circ}$ above this point. We may simply rationalise the wetting properties in terms of the amphiphilic composition of the **D*Ala*** molecule with a long C_{11} hydrophobic alkyl chain and hydrophilic polar head group. In the lying down phase we might expect that exposure to the alkyl chain generates a hydrophobic surface. By contrast, as the molecules begin to stand up and pack more densely, the hydrophobic chains become buried, meaning that the surface wetting properties become dominated by the hydrophilic polar head groups. Though this simple interpretation is in agreement with the measurements we must also consider the role of the underlying gold surface. On a 'bare' gold surface (3 days after the samples were removed from the metal deposition chamber) I measured an advancing angle of $87 \pm 4^{\circ}$. The wetting properties of gold surfaces are the subject of much debate in the scientific literature. Clean gold surfaces are

known to be strongly hydrophilic and are completely wetting (contact angle of $\sim 0°$), however when exposed to air they quickly absorb carbonaceous contaminations from the environment and thus become hydrophobic within minutes [Smith80]. I therefore attribute the rather high contact angle in my experiments with contaminated gold surfaces. The contact angles of the 10^{-4} and 10^{-3} mM **D*Ala*** samples are similar to the one of the gold surface. In these samples the thiols only cover the gold substrate incompletely and the wetting properties of the underlying gold dominate.

The results presented so far show clearly that the structure of the **D*Ala*** SAMs have a big impact on the generation of surface stress upon vancomycin binding. Thereby, the highest surface stress is generated on SAMs that are in the transition between lying-down and standing-up layers, as indicated by the yellow area in figure 8.4. The following section will look in more detail into the density and orientation of the monolayers in order to understand these effects.

8.3 Density of Sensing Layers

X-ray photoelectron spectroscopy (XPS) is a useful tool to investigate the elemental composition of a surface. For the measurements described in this chapter, a Thermo Scientific Theta Probe XPS system was used, a very powerful instrument that also allows angle-resolved XPS (ARXPS). High resolution spectra were recorded for the Au 4f, S 2p, N 1s, O 1s and C 1s peaks on nine **D*Ala*** samples (10^{-4} – 4 mM) and two reference samples (2 mM HDT and 2 mM ***PEG***). For more details see appendix B.

Figures 8.5a+b show the evolution of the elemental composition with **D*Ala*** concentration for the Au 4f and S 2p peaks. In order to maximise the sulphur signal, I summed up the spectra from all detection angles on each sample. The gold peak reveals large intensities for two lowest concentrated samples and significantly lower intensities for $\geq$0.01 mM **D*Ala***. There is a continuous decrease of gold intensity for higher **D*Ala*** concentrations due to increased attenuation of the photoemission electrons by the overlying SAM. The intensity of the sulphur signal is almost concentration-independent

except for two lowest **D*Ala*** concentrations. The issue here is that this signal is very low and is also attenuated by the overlying layer. Therefore the sulphur signal on its own is not very meaningful. To overcome the problems of signal attenuation, the ratio of S 2p / Au 4f intensities were calculated (fig. 8.5c). Because the sulphur atoms are always attached to the gold substrate in these SAMs, the sulphur and gold signals are equally affected by the attenuation of photoemission electrons. Therefore, their ratio will account for the reduction of intensity and is also a measure for the number of thiol molecules on the surface (because every **D*Ala*** molecules contains only one sulphur atom). The S / Au curve shows a direct correlation with **D*Ala*** concentration, meaning that the number of **D*Ala*** molecules per unit area increases with its solution concentration.

In order to estimate the thiol density on the gold substrate, I took advantage of the extensive research that has been done on simple alkanethiol monolayers on gold. It is known that an ideally packed alkanethiol SAM on a Au(111) surface has a theoretical packing density of 0.214 nm^2 per thiol molecule [Strong88]. It is also known from experimental values that a ***PEG*** monolayer has a grafting density of 0.27 nm^2 per molecule [Schwendel03]. By comparing the ratio of the S 2p / Au 4f signal of the **D*Ala*** and HDT/***PEG*** reference samples, I calculated the coverage on other samples.

The results of the thiol density calculations are displayed in figure 8.5d and they show the same trend as the SAM thickness measurements mentioned above. Generally, the area values calculated from the HDT reference are 22% smaller compared to the values from the ***PEG*** reference although deviations from theoretical values may occur due to sample defects.

According to these calculations, the highest concentrated **D*Ala*** sample also gave the most dense SAM, that is an area of 0.41 nm^2 per **D*Ala*** molecule (calculated using the ***PEG*** reference). For lower concentrations the area per **D*Ala*** increases marginally but consistently and reaches 0.54 nm^2 per thiol for 0.05 mM **D*Ala***. For **D*Ala*** concentrations <0.01 mM the density is decreasing rapidly, leading to a **D*Ala***

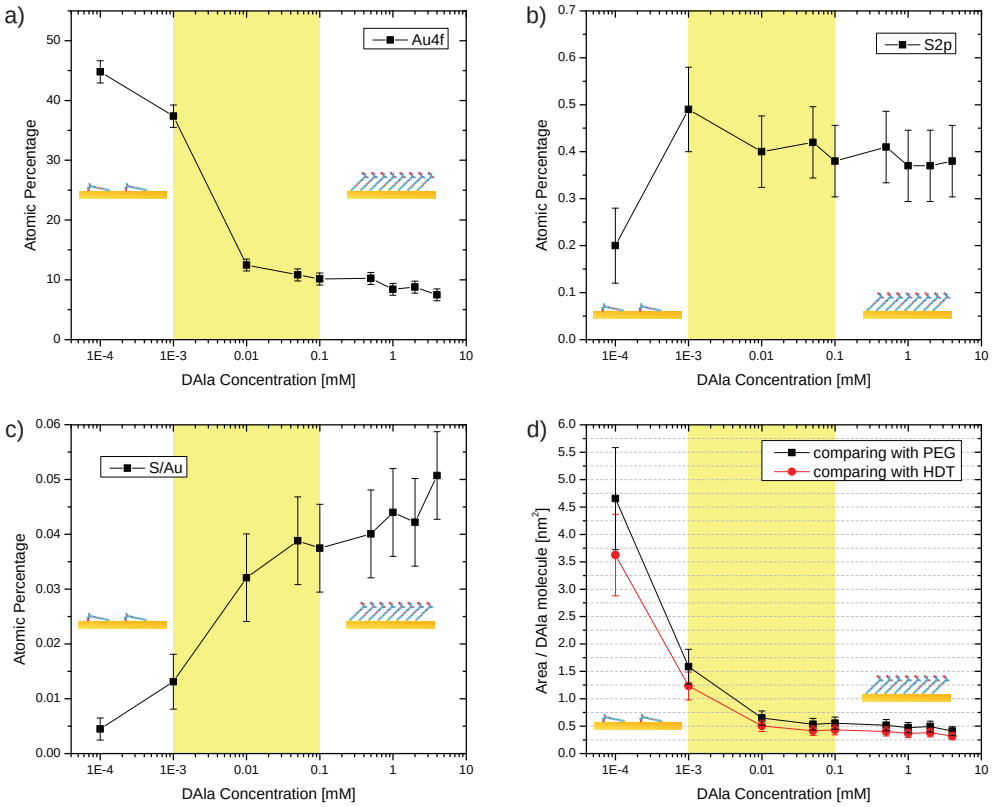

Figure 8.5: Density estimation of* DAla *layers. ***(a)*** *Atomic percentage of the Au 4f peak and* ***(b)*** *of the S 2p peak measured by XPS.* ***(c)*** *Ratio of the S 2p / Au 4f peaks, which is proportional to the thiol density on the surface.* ***(d)*** *Area per* **DAla** *molecule, calculated by comparing the S/Au ratio with* **PEG** *and HDT reference samples.*

area as large as 4.65 nm^2 for the lowest concentrated sample I measured, which corresponds clearly to a widely dispersed D*Ala* layer.

I estimate that a D*Ala* molecule which is lying flat on the surface covers a surface area of $\sim$1.3 nm^2 on the gold substrate. This means that the D*Ala* coverage is 80–100% on the 10^{-3} mM D*Ala* sample and roughly 30% on the 10^{-4} mM sample, which agrees with observations that these two samples contain carbonaceous contamination, as seen in the contact angle measurements.

8.4 Orientation of Sensing Layers

Besides the potential to analyse the elemental composition of a surface layer, angle-resolved XPS (ARXPS) offers the much more powerful option to generate depth profiles of samples. ARXPS follows a simple principle: the deeper inside the surface an element occurs, the lower its intensity at large take-off angles due to inelastic scattering of the photoelectrons (see also appendix B). This method allowed to determine the orientation of the **D*Ala*** chains in the SAMs and to assess if multilayer structures were formed. Nevertheless, we have to keep in mind that XPS measurements are performed in ultra-high vacuum and therefore the SAMs can have different conformations compared to SAMs immersed into liquid.

The structure of the **D*Ala*** molecule is shown in figure 8.6 and the atoms are colour-coded in respect of the distinct peaks they give in the XPS data. SAMs formed by **D*Ala*** consist of four different elements – sulphur, carbon, oxygen and nitrogen – as well as the gold substrate. Thereby the carbon signal can split up into three different peaks depending if the carbon atom is bound to none, one or two strongly electronegative neighbours (O or N). Similarly, the oxygen signal splits up into two peaks depending if the oxygen atom occurs within an ethylene glycol group or within a peptide bond. The oxygen atoms in the terminal carboxyl group give a similar signal as the ones from the peptide bond and are included in this group for simplicity.

I used **D*Ala*** solution concentrations between 10^{-4} and 4 mM to prepare the samples for angle-resolved XPS measurements. The depth profiles of the 10^{-3} and 1 mM **D*Ala*** samples, the two most representative samples, are displayed in figure 8.7a+b (the complete set of depth profiles are collected in appendix B). I consider the sample that was prepared with 1 mM **D*Ala*** first. According to theory this concentration should lead to dense and ordered monolayers where the thiol molecules are standing up on the surface. Indeed, we can find the S 2p signal very close to the gold substrate and deeper within the surface than any other signals (arrow 1 in fig. 8.7b). The C 1s CC signal has a peak slightly higher up in the surface layer (arrow 2) which coincides with the C11 linker in the molecule. Next higher in the layer we find the C 1s COC

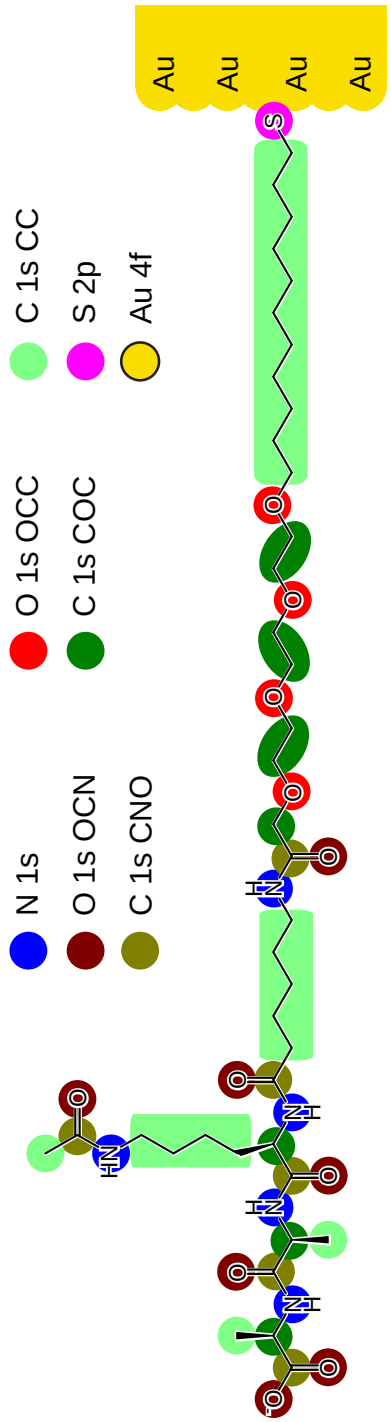

Figure 8.6: Structure of* DAla *with elements colour-coded corresponding to XPS signals. *Eight different atoms or chemical states can be identified using XPS: gold (Au 4f), sulpur (S 2p), nitrogen (N 1s), two different oxygens (O 1s OCC and O 1s OCN), and three different carbons (C 1s CC, C 1s COC and C 1s CNO).*

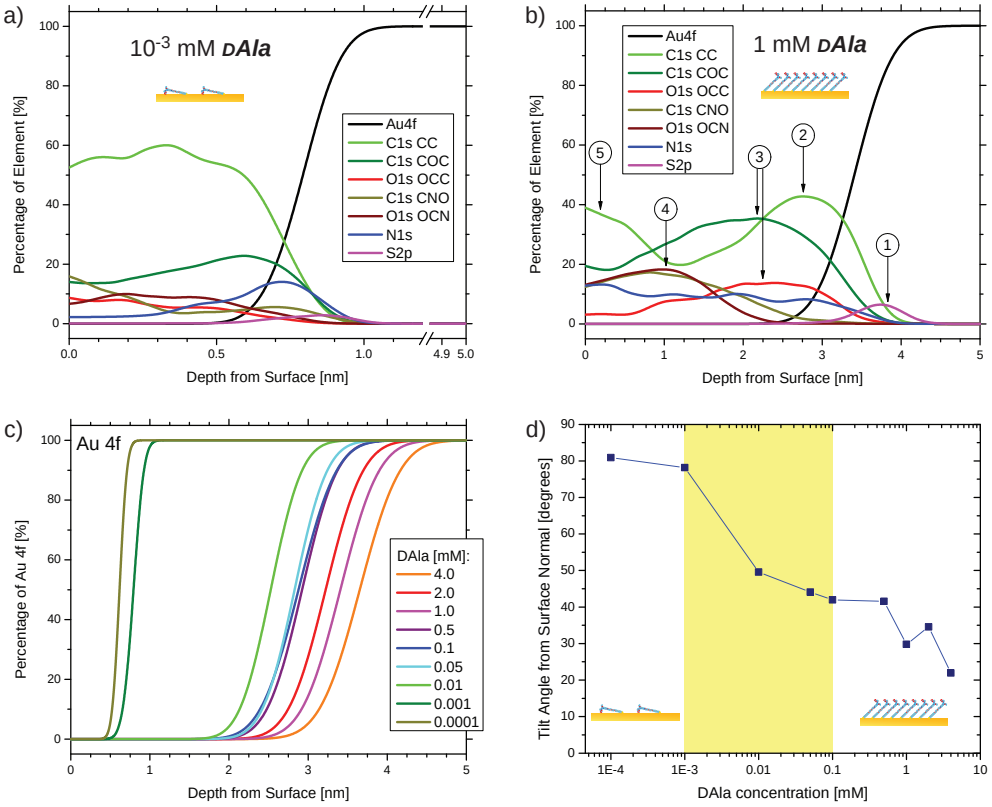

Figure 8.7: Depth profiles and orientation of* DAla *layers. ***(a)+(b)*** *ARXPS depth profiles for* 10^{-3} *and 1 mM* **DAla** *samples. The numbered arrows in (b) indicate different elements and their position within the layer (see text).* ***(c)*** *Comparison of the depth profiles of the Au 4f signal for all* **DAla** *samples which is a direct measure for the SAM thickness.* ***(d)*** *Tilt angles from the surface normal of the* **DAla** *molecules.*

and O 1s OCC signals from the triethylene glycol group (arrow 3). The ratio of the percentage values for these two elements also roughly agrees with the stoichiometry (2:1) within the **D*Ala*** molecule. Very close to the surface we finally see the C 1s CNO, O 1s OCN and N 1s signals for the atoms in the tri-peptide (arrow 4). Interestingly, the C 1s CC signal exhibits again a peak at the very top of the surface which might indicate that the carbon side chine of the lysine group is pointing out of the layer. However, the exact conformation of the fairly bulky tri-peptide headgroup remains unclear.

The situation changes radically for the sample prepared using 10^{-3} mM **D*Ala*** solution (8.7a). The thickness of the monolayer decreased significantly and the elements are distributed more equally over the depth of the layer, which suggests that an incomplete SAM is formed where the thiol molecules are adopting a lying-down conformation. Another special feature is that the nitrogen signal occurs very close to the gold substrate whereas it was located at the very top of the surface for the 1 mM **D*Ala*** sample. This might indicate that the nitrogen atoms from the tri-peptide tend to stick to the gold surface due to favourable charge interactions (comparable effects have been observed with DNA adsorbing to gold surfaces [Herne97] or gold nanoparticles attaching to nitrogen-doped carbon nanotubes [Jiang03]). Furthermore, it is striking that the C 1s CC signal is much larger than suggested by the **D*Ala*** stoichiometry. I suppose that in this case there is an incomplete coverage of the gold surface and that carbonaceous contaminants adsorbed onto the uncovered parts of the gold surface (see also XPS raw data of C 1s peak in figure B.1).

In order to follow the changes of the different elements within the SAMs, it is more convenient to plot in one graph the depth profile of a single element for all samples. For example the Au 4f signal is plotted for all samples in figure 8.7c. It can be seen that the depth of the gold interface increases monotonically with **D*Ala*** concentration which is a measure for the thickness of the SAM. Apparently the two lowest **D*Ala*** concentrations form much thinner layers than all the other samples. The steepness of the curve at the gold interface is higher for these two samples compared to the other samples. I attribute these differences to an artefact of the computer model for the calculation of the depth profile and not to different roughness of the gold substrates.

The depth profiles of the S 2p signals would be a direct measure for the thickness of the monolayers, as the sulphur atom is located at the interface to the gold substrate. Unfortunately the signal-to-noise ratio for the S 2p raw signals is rather low, so that the calculation of the thickness from the sulphur intensities is not very reliable. I therefore calculated the SAM thickness as the depth from the surface at which the Au 4f signal reaches 80%. The thickness data calculated in this way was already shown earlier in

figure 8.4 and was compared to the ellipsometry data. It is apparent that the SAM thickness increases continuously with **D*Ala*** concentration and there is no complete saturation above 0.01 mM **D*Ala***. This suggests that a densely packed monolayer is only formed at high **D*Ala*** concentrations or for longer incubation times than were used here. I attribute the growth of the SAM thickness with an increase in thiol density and therefore a decrease in the tilting angle from the surface normal. The tilting angle ω can be calculated using the simple formula

$$\cos(\omega) = \frac{t}{l} \tag{8.1}$$

where l is the length of the **D*Ala*** molecule and t is the thickness of the SAM. I estimated a length of 4.5 nm for the **D*Ala*** molecule using the ChemDraw software and I used the XPS thickness measurements for the calculation of the tilting angles. The angles vary between 27° for the 4 mM **D*Ala*** sample and 52° for the 0.01 mM **D*Ala*** sample (fig. 8.7d). I calculated tilting angles close to 90° for the two lowest **D*Ala*** concentration (79° for 10^{-3} mM **D*Ala*** and 81° for 10^{-4} mM **D*Ala***). However, the simple equation 8.1 fails for lying-down layers because in these cases the width of the molecules (rather than its length) is the determining factor for the SAM's thickness.

8.5 Comparison with Surface Plasmon Resonance and Estimation of Binding Efficiency

Surface plasmon resonance (SPR) measures mass-related adsorption of molecules due to changes in dielectric constant. I therefore wanted to check if the surface stress effects that were seen on cantilevers are specific to the cantilever method or if it is a general binding interaction phenomenon. More precisely, I wanted to investigate if the change in surface stress for different **D*Ala*** coverages is due to different amounts of adsorbed antibiotic molecules or due to a fundamental effect in the surface stress generation on the cantilever.

Bare gold chips were used for the SPR measurements in order to have comparable conditions to the cantilever experiments. The SPR chips were coated *ex-situ* with

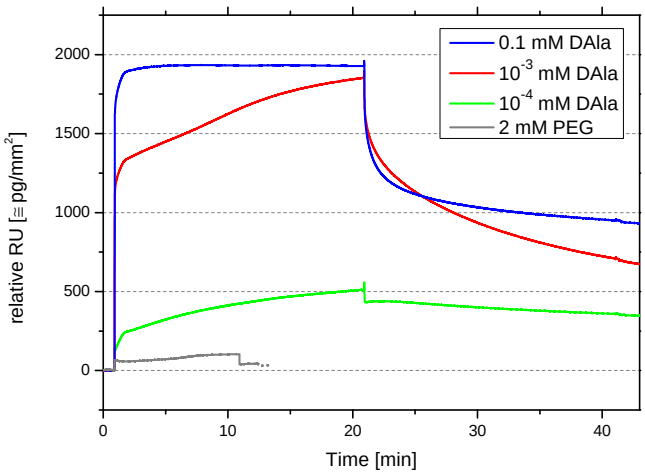

Figure 8.8: SPR signal upon injection of 250 μM vancomycin for different* DAla *coatings. *Solid lines show the absolute SPR signal for gold chips functionalized with 10^{-4}, 10^{-3} and 0.1 mM* **DAla**, *and 2 mM* **PEG**. *All curves are shifted vertically to overlay them. The curves represent the absolute SPR signal which is not adjusted for changes in refractive index of the injected solution. Injection times were 20 min on* **DAla** *sample and 10 min on the* **PEG** *sample.*

different concentrations of ***DAla*** molecules in the same way as the XPS and cantilever samples. The solid lines in figure 8.8 show the absolute SPR data upon a 20 min injection of 250 μM vancomyin for three different ***DAla*** substrates (10^{-4}, 10^{-3} and 0.1 mM ***DAla***). The graphs reveal that the SPR signal scales with ***DAla*** concentration, however the kinetics of the reaction seems to be considerably different for some samples. For the chip prepared with 0.1 mM ***DAla*** the SPR signal reaches saturation after less than 5 min with a plateau at around 2000 RU (response units). The 10^{-3} mM ***DAla*** sample also exhibits a very fast initial binding reaction, reaching 1400 RU after only 1 min. However, this sample does not show saturation but the signal kept increasing by about 33 RU/min and reached 1916 RU after 20 min, when the reaction was stopped with a buffer wash. The buffer wash again showed different kinetics for those two chips. The chip prepared with 10^{-4} mM ***DAla*** reveals similar results as the

10^{-3} mM sample but gives a roughly 4 times lower signal, only the washing step seems to be considerably slower. The change in refractive index for a 250 μM vancomyin solution was determined as 63 RU on a ***PEG*** sample which is small compared to the measured signals on the **D*Ala*** samples (short injection in fig. 8.8, grey line).

I then compared the SPR saturation signals for a larger range of **D*Ala*** concentrations (fig. 8.9a). The SPR response reveals a fast increase for samples below 0.01 mM **D*Ala*** and plateaus at higher concentrations, suggesting that the amount of bound antibiotic is constant above 0.01 mM. This is clearly different than the cantilever data mentioned in the beginning of this chapter, which raises the key question why the response at higher **D*Ala*** concentrations drops on the cantilever sensors but not on SPR, and clearly suggests that the signal generation of the two technologies are fundamentally different.

To test the validity of these findings, I also measured values for the equilibrium dissociation constant K_d using SPR (fig. 8.9b). The results are comparable to the binding affinities measured on cantilevers, revealing K_d values around 1 μM for **D*Ala*** concentration between 10^{-3} and 1 mM and a significant higher value for lower concentrations.

The SPR data allows to calculate the absolute number of vancomycin molecules bound to the **D*Ala*** sensing layers, as 1 RU generally corresponds to 1 pg of adsorbate per mm^2 (note that these values are determined for a CM5 sensor chip and the adsorption of proteins, and can therefore be slightly different for the surfaces and analytes used here). By comparing this number to the density of **D*Ala*** molecules I could then estimate the fraction of bound **D*Ala*** molecules, i.e. the percentage of bound versus total number of **D*Ala*** molecules (table 8.1). I found the highest fraction bound (91%) for the 10^{-3} mM **D*Ala*** sample.

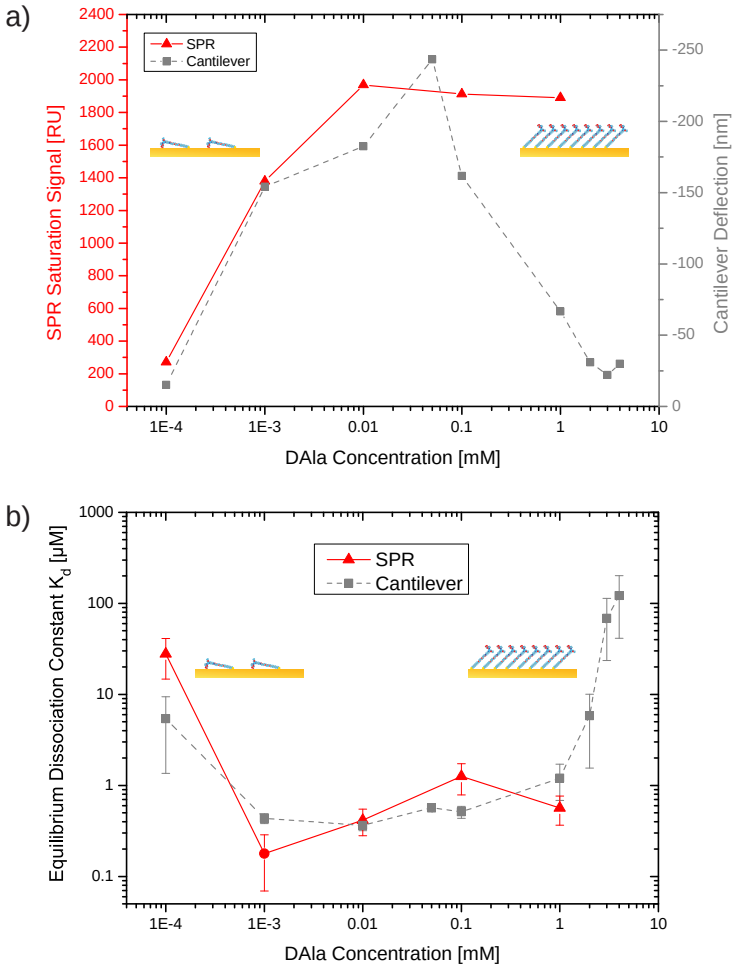

Figure 8.9: SPR saturation signal and K_d values. ***(a)*** *SPR saturation signal for different* **DAla** *samples. The saturation signal was calculated as the change in RU 2 min after the injection of 250 μM vancomycin solution and the value was corrected for the change in refractive index of the vancomycin solution. The cantilever data from figure 8.4a is shown with a dashed line for comparison.* ***(b)*** *Equilibrium dissociation constants K_d measured on the same* **DAla** *samples by injecting different concentrations of vancomycin.*

Table 8.1: Fraction of bound* DAla *molecules for different densities. *The percentage of* **DAla** *molecules occupied by vancomycin upon injection of 250 μM vancomycin was calculated by comparing the density of* **DAla** *molecules on the surface (from XPS data) and the amount of bound vancomycin (from SPR data).*

D*Ala* concentration mM	D*Ala* density nm^{-2}	Vancomycin density nm^{-2}	Fraction bound %
10^{-4}	0.215	0.112	52
10^{-3}	0.631	0.573	91
0.01	1.544	0.817	53
0.1	1.803	0.794	44
1	2.117	0.785	37

8.6 Discussion

In this chapter we reveal that the structure of the underlying SAM has a striking effect on the magnitude of surface stress, allowing it to be amplified by up to 1 order of magnitude. By simply tuning the concentration of the D*Ala* thiol I have investigated the influence of SAM density, orientation and the fraction of drug-bound peptide on surface stress. My findings identify three distinct regimes of stress generation: (i) low concentration regime $\leq 10^{-4}$ mM, where the thiols are predominantly in the lying down phase and the stress signal is very weak; (ii) an intermediate concentration regime around 10^{-3} – 0.1 mM, where thiols undergo the lying down to standing up phase transition and stress is maximised; and (iii) a high concentration regime ≥ 1 mM, the range where SAMs typically form well-defined high density layers but where the surface stress signal drops to a negligible value. Each phase is illustrated in figure 8.10 and will be considered individually in the section below.

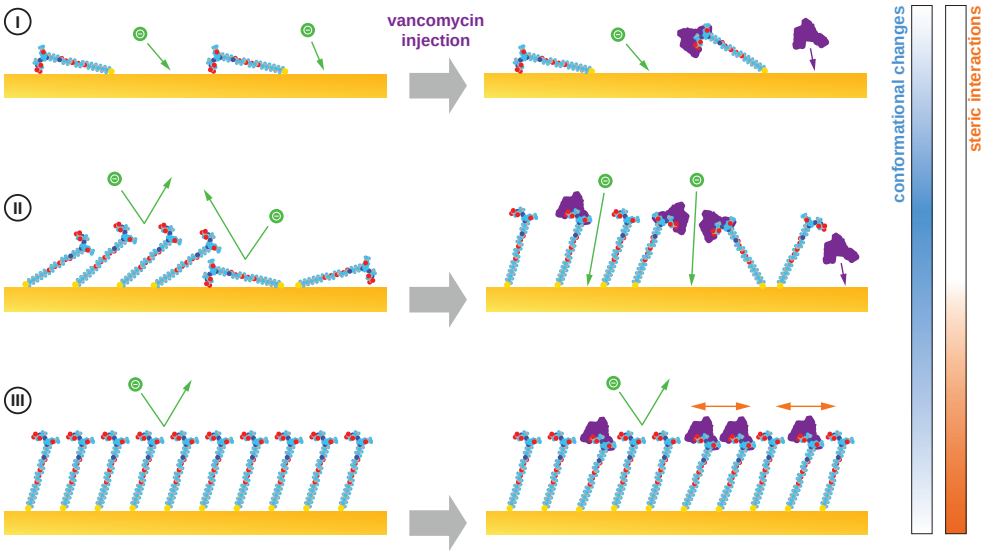

Figure 8.10: Model for generation of surface stress at different* DAla *densities. *The illustration shows the effects of vancomycin binding to different* **DAla** *sensing layers. The green circles indicate ions of the buffer solution that can interact with the gold surface and lead to charge redistributions. The gradient bars on the right hand side indicate the role of conformational and steric effects for the relevant layers.*

(i) Low concentration range $\leq 10^{-4}$ mM D*Ala*

At low **D*Ala*** concentrations the cantilever signal upon exposure to vancomycin was found to be very small ($\sim$ 15 nm), indeed close to detection limit with a weak K_d of $\sim$ 10 μM. Complementary XPS and ellipsometry both showed that the thiols are in the lying down phase, in agreement with the hydrophobic contact angle measurements, which I attribute to the exposure of the C_{11} alkyl chain. More detailed XPS analysis confirmed that the thiols form a low density film where a significant fraction of gold surface remains bare and SPR measurements indicate very low fraction of drug binding.

(ii) Intermediate concentration range 10^{-3} – 0.01 mM D*Ala*

At intermediate thiol concentrations between 10^{-3} and 0.1 mM **D*Ala*** I observed a dramatic increase in the cantilever bending signal up to 270 nm and a low K_d of 1 μM which is characteristic of the relatively strong vancomycin-**D*Ala*** interaction formed by 5 hydrogen bonds. XPS, ellipsometry and contact angle measurements are all consistent with the underlying monolayer transition from the lying down to standing up phase. As figure 8.10 illustrates this is a relatively disordered phase compared to (i) and (iii). The SPR measurements indicate that the fraction of drug bound to peptide increases and results in a K_d of 1 μM, again in agreement with the cantilever data.

(iii) High concentration range $\geq$ 1 mM D*Ala*

In the third regime of high thiol concentrations above 1 mM, the cantilever signal is observed to drop significantly to $\sim$ 30 nm, with a correspondingly weak K_d of up to 100 μM for 4 mM **D*Ala***. XPS, ellipsometry and contact angle measurements all confirm that the monolayer is in the standing up phase with a packing density close to theoretical packing limit of **D*Ala***. Intriguingly, SPR measurements indicate that the fraction of drug bound to the peptide remains nearly constant in the high and intermediate regimes and K_d is $\sim$ 1 μM, again consistent with a specific drug-target interaction.

These findings appear to suggest that stress is strongly associated with the conformational change associated with the lying down to standing up phase of SAMs. This is the most disordered of the three different regimes illustrated in figure 8.10. To rationalise this effect I now consider the different factors which are thought to contribute to stress generation — electrostatic, steric and conformational effects.

8.6.1 Model for the Generation of Surface Stress on Cantilevers

The origins of surface stress on cantilever sensors are still the subject of much scientific interest and debate and are known to depend strongly on the chemical or biological interactions that are investigated. Several repulsion effects have been proposed such

as electrostatic interactions, Lennard-Jones interactions, conformational changes or interactions with the gold substrate (for more details see introduction chapter, section 3.9). I now apply this knowledge to my system and try to find out which of the mentioned interactions is most likely to produce a surface stress.

Electrostatic interactions

The surface stress of a charged layer on a cantilever can be calculated using the equation

$$\sigma = -\frac{1}{2}\frac{4\pi l_B}{\kappa_3 d}\frac{Q^2}{A^2} \tag{8.2}$$

where l_B is the Bjerrum length, κ_3 is the inverse screening length of the solvent, d is the distance of the charge above the gold substrate (thickness of the layer) and Q/A is the surface charge density [Sushko09]. Sushko *et al.* calculated a surface stress of $\sim$25 mN/m for a fully deprotonated layer of mercaptohexadecanoic acid. In my case the SAM is thicker and the charge density is lower. Even if we assume that vancomycin has a charge of -1e and that every **D*Ala*** molecule on the surface is bound to a vancomycin molecule, the surface stress would only amount to 2.4 mN/m. However, in reality the binding efficiency is less than 100%, so that I expect the contribution of the electrostatic repulsion to the surface stress to be less than 1 mN/m and therefore negligible.

Steric repulsion (Lennard-Jones interactions)

I estimate the area that is occupied by the **D*Ala*** headgroup as $\sim$0.5 nm^2 (using crystallographic data and the modelling software ChemBioOffice). This value corresponds to the density of high concentrated **D*Ala*** layers ($\geq$0.1 mM **D*Ala***) which I have measured experimentally. We can therefore assume that for these samples the surface is saturated with molecules. The area occupied by a vancomycin molecule when bound to **D*Ala*** is around 1.3 nm^2 (also estimated using crystallographic data and the modelling software ChemBioOffice). It is obvious that a structural rearrangement is necessary for saturated **D*Ala*** layers to accommodate the vancomycin binding, which might very

well lead to an in-plane surface stress. Furthermore, structural water molecules or a water shell around the vancomycin molecules might also contribute to the generation of surface stress. Steric repulsion is less likely for low density **D*Ala*** layers. In the case of the 10^{-3} mM **D*Ala*** sample the area per **D*Ala*** molecules is 1.6 nm^2, that is slightly larger than the vancomycin area. Nevertheless I still measure a surface stress signal of 150 mN/m on these cantilevers upon vancomycin binding. Furthermore, the steric repulsion theory does not support the fact that low surface stress values were measured for **D*Ala*** concentrations $\geq$1 mM. One could argue that accessibility of the **D*Ala*** molecules for vancomycin plays a role when the SAM is becoming too dense. However, SPR measurements rule out a major accessibility issue, as I measured very similar RU values ($\sim$ 2000 RU) for samples prepared with 0.01, 0.1, as well as 1 mM **D*Ala***, meaning that the same amount of vancomycin molecules binds to these sensing layers. Taking all these facts together we can argue that steric repulsion might indeed be a factor in the generation of surface stress at high **D*Ala*** densities but it does not seem to be the only effect involved. The quantitative estimation of these forces would require complex calculations and computer modelling and goes beyond the scope of this thesis. That said, initial simulations have shown that the energetically most favourable distance between two **D*Ala*** molecules on a surface is 7.1 Å (personal communication with Anna Dejardin), which is consistent with my experimental results of $\sim$0.5 nm^2 per **D*Ala*** molecule.

Conformational Changes

Stachowiak *et al.* [Stachowiak06] first proposed that conformational changes play an important role in stress generation using model DNA SAMs. Herein we also find strong evidence to support the hypothesis that the conformational change associated with the lying down to standing up phase of SAMs generates a large surface stress. Figure 8.10 illustrates that the conformational change of the SAM can have several different roles: the disorder in the film may improve steric accessibility of the peptides, drug binding may itself induce further conformational changes, that may result in an increase in

entropy of the system. In addition this would expose additional 'bare' gold sites on the surface of the cantilever. This was investigated further in two control experiments: Contact angle measurements of different **D*Ala*** films in the presence and absence of vancomycin showed a pronounced 30° increase in hydrophilicity for 10^{-3} mM SAMs upon vancomycin binding, in agreement with the hypothesis that the polar head groups stand up making the surface more hydrophilic (fig. 8.11). Secondly, studies on bare gold cantilevers showed markedly different bending signals compared to **D*Ala*** coated cantilevers indicating non-specific interactions with a high degree of drift (fig. 8.12). However, further work is needed as bare gold surface are notoriously problematic due to contamination artefacts and contact angle measurements are performed in the dry state and therefore suffer from drying effects. Nevertheless, my findings strongly support the hypothesis that conformational changes associated with drug-target binding induce large changes in surface stress.

8.6.2 Theoretical Considerations

Future work should combine the experimental observations from this chapter with further theoretical work. The theoretical relations between surface stress σ and surface free energy F was first described by Shuttleworth in 1950 [Shuttleworth50] and already introduced in section 3.4 (equation 3.5). For isotropic surfaces ($\epsilon_{12} = \epsilon_{21} = 0$ and $\epsilon_{11} = \epsilon_{22} = \epsilon$) Shuttleworth equation simplifies to

$$\sigma = F + \frac{dF}{d\epsilon} = F + A\frac{dF}{dA} \tag{8.3}$$

where $\epsilon = dA/A$ and A is the surface area. Shuttleworth equation describes an ideal metal surface which is strained *elastically*. It could be applied to the bending of a simple silicon cantilever but it is oversimplified to take into account a biological sensing layer or the binding of molecules from the environment.

Couchman took a slightly different approach [Couchman72]. He described the surface layer in terms of the number N of surface atoms in the surface area A with the average area per surface atom $a = A/N$. Hence, the excess free energy per surface

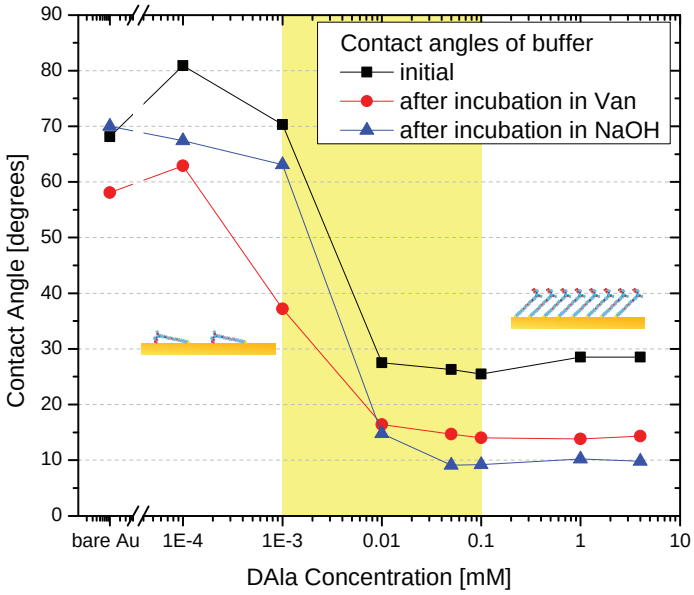

Figure 8.11: Contact angles upon vancomycin binding. *Comparison of contact angles of buffer on* **DAla** *layers before and after binding of vancomycin. The following procedure was used: A 10 μl drop of PBS buffer was deposited onto the sample surface to measure the initial contact angle (black squares). Buffer was used instead of water in order to keep similar conditions compared to the measurements on the cantilevers. The sample was then immersed into a 250 μM vancomycin solution for 5 min, dried under a nitrogen stream and the contact angle of a buffer drop was measured again (red circles). Subsequently, the sample was immersed into a 10 mM NaOH solution for 3 min to wash of the antibiotic, and the contact angle of a buffer drop was measured a last time (blue triangles).*

atom becomes $\Delta E = aF$ which then allows to relate the atomic behaviour of the surface with the surface stress. One can then derive an equation for the *effective* surface stress g (see ref. [Couchman72] for details):

$$g = \Delta E \frac{\partial N}{\partial A} + N \frac{\partial \Delta E}{\partial A} \tag{8.4}$$

If we consider purely plastic deformations (liquids), the density of surface atoms does not change and therefore the second term of equation 8.4 becomes zero, and $g_{liquids} = F$. In contrast, if we consider purely elastic deformations, the number of surface atoms does not change and therefore the first term of equation 8.4 becomes zero,

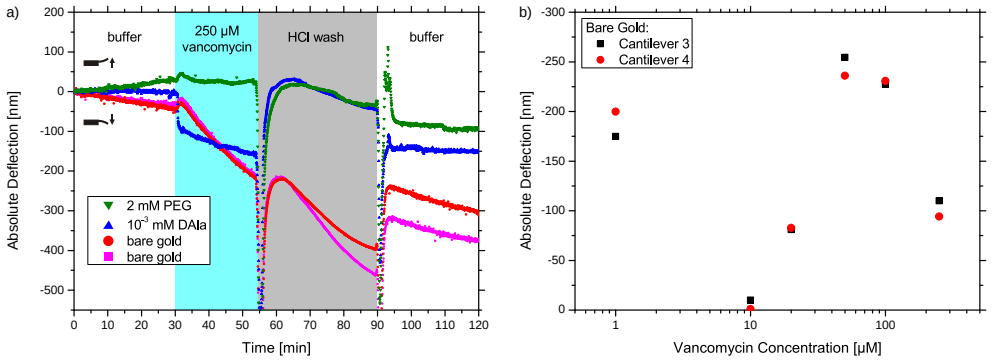

Figure 8.12: Surface stress on bare gold cantilevers. ***(a)*** *The graph compares the absolute bending signal of four cantilevers from a single chip upon injection of 250 μM vancomycin. Cantilevers were either non-coated (bare gold), coated with low concentrated* **DAla** *solution (10^{-3} mM) or coated with* **PEG** *(2 mM).* ***(b)*** *Comparison of deflections of two bare gold cantilevers for different vancomycin injections (measurements were performed in order of increasing vancomycin concentration, lowest first). The signal does not only scale with vancomycin concentration but also with the order of injection, suggesting that vancomycin has a high tendency to adsorb onto gold surfaces or the organic contamination layer.*

leading to $g_{elastic} = \partial\Delta E/\partial a$. This equation can be rewritten to give Shuttleworth equation because per definition $\Delta E = aF$. For complex systems however, both terms in equation 8.4 are finite and the whole equation has to be considered.

In the case of our vancomycin-**D*Ala*** system we can make use of Couchman's equation and interpret ΔE as the change in surface energy per binding event. Thereby the first (plastic) term $\Delta E \frac{\partial N}{\partial A}$ accounts for the actual binding events, i.e. the addition of the the vancomycin molecules to the surface. The second (elastic) term $N \frac{\partial \Delta E}{\partial A}$ can be treated as the change in surface energy associated with the surface expansion. Unfortunately, in this particular case both terms are finite and cannot be determined experimentally. Nevertheless, we can assume that the ratio and magnitude of these terms vary with the **D*Ala*** density on cantilevers and hence lead to the large differences in surface stress which I have observed experimentally.

Finally, the vancomycin-D*Ala* surface can also be approximated by a thermodynamic system with free energy F as a function of D*Ala* concentration $[\text{D}\textit{Ala}]$ and vancomycin concentration $[van]$:

$$F([\text{D}\textit{Ala}], [van]) \approx F([\text{D}\textit{Ala}]) + [van]\frac{dF}{d[van]} \tag{8.5}$$

Thereby, $\frac{dF}{d[van]}$ is singular at the conformational phase transition for $[\text{D}\textit{Ala}] = [\text{D}\textit{Ala}]_{critical}$ which can explain the peak in surface stress at intermediate D*Ala* concentrations in a thermodynamic sense.

8.7 Conclusion

In this chapter I have demonstrated that the thiol density and orientation has an enormous effect on the magnitude of surface stress associated with the binding of vancomycin to D*Ala* sensing layers and that we can tune the density of the layer in order to amplify the sensitivity of the device. I now conclude this study by plotting the surface stress against the D*Ala* surface density (fig. 8.13). In this representation the highest surface stress values are found in the density range between 0.6 and 1.8 nm^{-2}. Below and above these densities we see a significant drop in surface stress.

These effects may be further amplified by designing sensing layers which undergo large conformational changes upon recognition or binding of an analyte molecule. This could include hairpin structures that unfold when a ligand binds to them, or hydrogels that can exhibit specific swelling behaviours due to changes in the environment. It has also been proposed to use some kind of secondary messengers or surface stress enhancers (such as charged molecules). For example, if conformational changes of SAMs reveal areas of the underlying gold substrate, these secondary molecules could interact with the gold surface which would lead to a change in surface stress due to changes of the charge distribution in the gold layer [Godin10b].

Finally, we can compare these results with the peptidoglycan densities in real bacteria. For example Zaritsky *et al.* [Zaritsky79] measured a peptidoglycan density of 1.5 – 1.8 nm^{-2}. Remarkably, this is exactly the density range where we see the

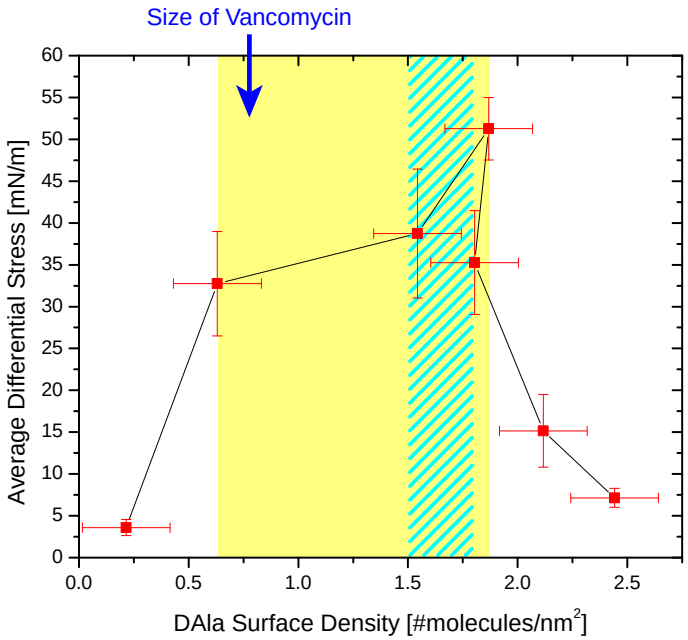

Figure 8.13: Cantilever surface stress plotted against thiol density. *The yellow area indicated the range where I measured the highest surface stress, whereas the cyan shaded area indicated the density of peptidoglycan in real bacteria [Zaritsky79]. The inverse size of vancomycin is indicated with an arrow.*

highest surfaces stress on cantilevers (shaded area in fig. 8.13). Moreover, the size of a vancomycin molecule also corresponds to the area of **D*Ala*** molecules in the range of the highest surface stress.

CHAPTER 9

Instrument Development for Drug Analysis

9.1 Introduction

The previous chapters illustrated the potential of cantilever sensors to quantify drug-target interactions using the commercial Scentris system. However, promising results with this system suffered from significant limitations: The Scentris flow system is a simple gravity flow setup and its standard liquid cell has a very large volume of 80 μl. The consequences of this design are that drug analysis is expensive as large volumes and long equilibration times are needed, making the analysis not only costly but also time-consuming. Moreover, it does not allow kinetic analysis, which would provide important information on drug-binding interactions.

Therefore, a significant part of my work was dedicated to the modification and optimization of a cantilever sensor system to address the issues above (fig. 9.1). This setup was originally built as a gas sensing device and was modified for sensing applications in liquid in collaboration with Hans Peter Lang and Christoph Gerber from the University of Basel.

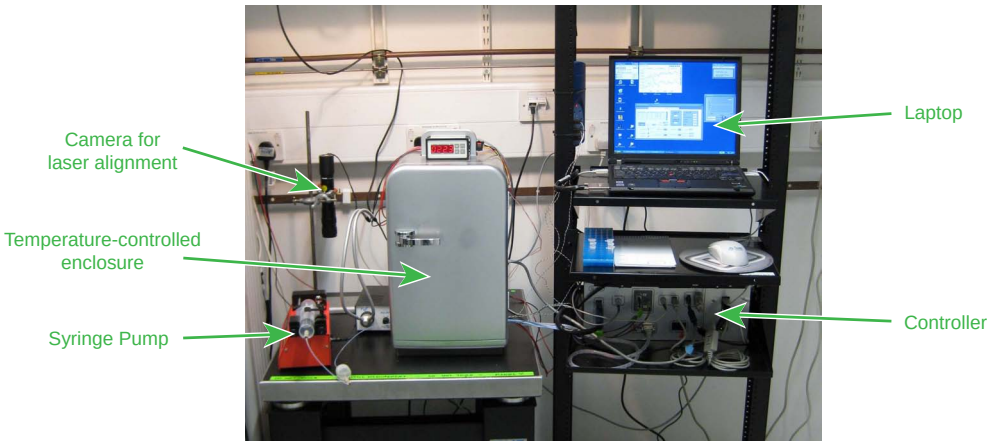

Figure 9.1: Overview of NOSE system. *A temperature-controlled enclosure holds all the liquid samples, the running buffer, the fluidics system and the actual cantilever sensing unit. The syringe pump generates a steady flow rate and acts as waste collector outside the box. A camera for the laser alignment can be placed in the box when opened. Electronics controller and laptop (user interface and data acquisition) are placed on a separate rack next to the instrument to prevent mechanical vibrations.*

In this Chapter I will describe the original system (the so-called NOSE system), the development of microfluidics using a miniaturised flow cell, automated injections using a syringe pump, a noise reducer, mirror coatings, and an isolation box with temperature controller. Finally, the optimised system is tested using the model vancomycin-D***Ala*** system and the first kinetic measurements are reported. These developments mark important milestones for the technology since an improved liquid handling system allows smaller sample volumes and shorter measurement times compared to the Scentris system. Therefore, these improvements made the cantilever technology more useful and reliable for drug screening applications.

9.2 Original Gas Detection System

The SG-NOSE gas sensing device was designed and built by a research group of the Institute of Physics at the University of Basel, Switzerland (SG stands for static mode

in gaseous environment). It was designed to detect chemical vapours, odours and breath samples by recording the swelling behaviour of different polymer films on cantilevers [Lang07]. I used this set-up in some experiments to study the formation of alkanethiol SAM from gas phase on cantilevers (see appendix C).

The gas measurement chamber was made of polyether ether ketone (PEEK) and has a volume of $\sim$200 μl . It was designed to hold a standard IBM cantilever array chip and allows easy and reproducible mounting. Initial measurements showed that this chamber was not suitable for experiments in liquid due to the large volume, insufficient mixing of injected samples and leakage problems, and therefore had to be replaced.

9.3 Fluid Cell and Flow System

Because the measurement chamber which was delivered with the SG-NOSE system was not suitable for measurements in liquids, I had to obtain an appropriate liquid cell. A suitable measurement chamber was provided by the instrument developers from the University of Basel which was designed to fit the NOSE system. This cell has a very small volume (8 μl) and only the the cantilever beams themselves are sticking out into a liquid channel, therefore allowing very fast exchange of sample solution even at low flow rates (fig. 9.2). Moreover, the cell is fitted with a groove that carries the cantilever array perfectly and makes the loading of the chip quick and reproducible. Because of this easy mounting the position between different chips changes only marginally and hence permits a much faster alignment of the read-out lasers.

9.3.1 Fluidics System

Due to the small volume of the new liquid cell, measurements at low flow rates and therefore with low sample consumption could be performed. However, as a prerequisite the fluid handling system around the measurement chamber had to be built first.

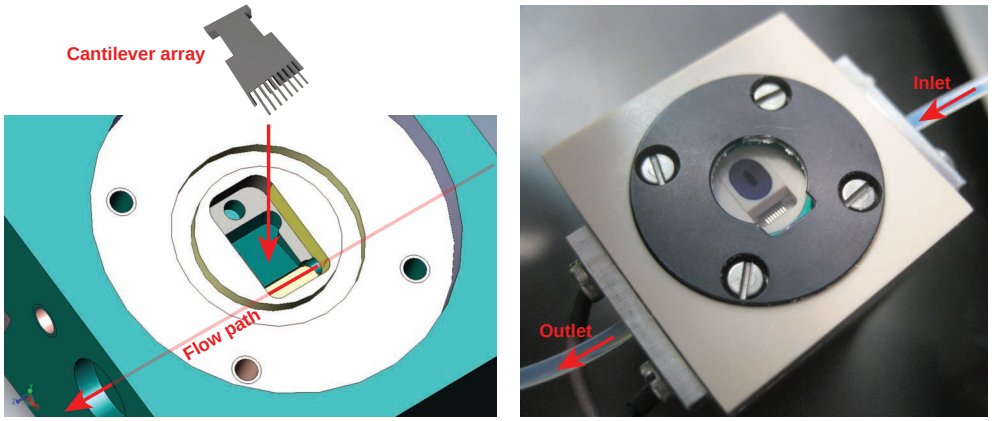

Figure 9.2: Illustration of the NOSE liquid cell. *On the left a schematic is displayed which shows the groove for the cantilever chip and the path of the liquid flow. The right side shows a photograph of the closed liquid cell. The cantilevers sticking into the liquid chamber can be seen.*

I designed a sample holder that can hold up to 10 standard 1.5–2.0 ml plastic vials and allows a quick and easy exchange of vials (fig. 9.3a). This has the advantage that the solutions can be prepared in the same vial that is used for the cantilever measurement and no transfer step is needed. Larger plastic tubes can be used for the running buffer and are also easily inserted into a sample rack.

The sample vials are connected to the liquid cell through an automatic 10-way valve switch which allows the computer-controlled exchange of liquid samples (fig. 9.3a/b). An additional T-valve allows to bypass the solutions so that they do not flow through the measurement chamber (for example for cleaning purposes).

A constant flow rate is achieved using a syringe pump that is connected to the outlet of the liquid cell (fig. 9.3c). This pump pulls the solutions through the fluidics system and also acts as a waste container. The syringe pump allows a large range of flow rates from less than 1 μl/min to several 100 μl/min as well as long measurement durations that permit overnight experiments.

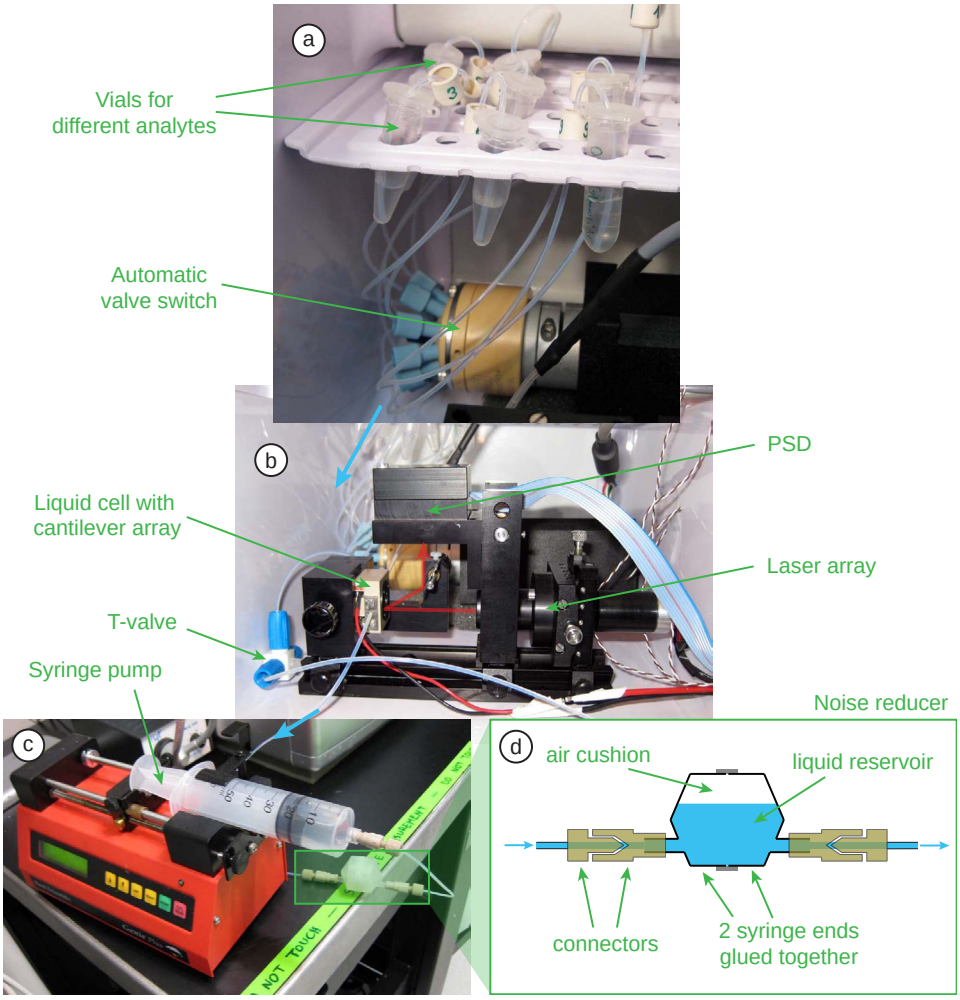

Figure 9.3: Overview of the fluidics system of the NOSE system. *(**a**) Standard 1.5–2.0 ml plastic vials can be used to place the sample solutions into the system and they are connected to the measurement chamber via a 10-way automatic valve switch. (**b**) The actual measurement unit consist of the liquid cell, a laser array and a PSD. A T-valve allows to bypass the liquid so that it is not flowing through the cell. (**c**) A syringe pump is used to provide constant flow over several hours. (**d**) A self-made noise reducer provides a smoother flow and eliminates mechanical noise from the syringe pump.*

9.3.2 Noise Reducer

The syringe pump can provide very accurate and low flow rates. Nevertheless, it is a mechanical pump which is moving in small steps and hence the pump can introduce mechanical noise in the cantilever system. To prevent this issue, I developed a simple but effective noise reducer. It consists of a small liquid reservoir located between the syringe pump and the liquid cell where an air bubble was introduced that acts as a cushion and dampens mechanical noise from the pump. This noise reducer was fabricated by cutting off the ends of two 50 ml plastic syringes and glueing them together to form a small chamber with an inlet and outlet (fig. 9.3d). Using this tool I did not observe any influence of the syringe pump on noise level of the instrument.

9.3.3 Choice of Mirror

The NOSE liquid cell requires a small mirror that reflects the laser beam from the cantilevers onto the PSD (see fig. 9.3b). The mirror that was delivered with the liquid cell was produced by evaporating a layer of silver onto a piece of silicon wafer, which has a very high reflectance. However, silver oxidises after a while when it is exposed to air. This made the mirror less reflective and even brown spots appeared after some months, which in turn increased the noise level of the cantilever readout.

Hence, I searched for a better solution. Protected silver mirrors that do not oxidise are available commercially but those are usually too thick to mount into our setup. Therefore I looked into other materials that have a high reflectance and are readily available. At 760 nm, the wavelength of the lasers that were used to readout the cantilever deflection, gold has an even higher reflectance than silver (Au 0.98, Ag 0.96, see fig. 9.4)). Aluminium has a slightly lower reflectance at this wavelength (Al 0.88) but is still suitable. Moreover, both Al and Au is readily available and could be evaporated into Si wafer pieces in-house. Therefore, either Au or Al mirrors were used which remained clean over a long period of time. I did not observe significant differences in signal-to-noise ratio for these two mirror coatings.

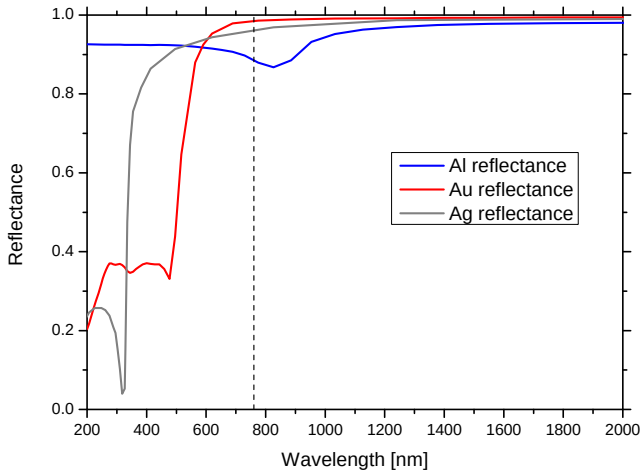

Figure 9.4: Reflectance of Ag, Au and Al for different wavelengths. *The dashed line is at 760 nm, the wavelength of the laser that is used to readout the cantilever deflections.*

9.4 Isolation Box and Temperature Control

Due to the mechanical nature of cantilever sensors and the bimetallic effect of gold-coated cantilevers, experiments should be performed in an isolated environment with constant temperature. Furthermore, light does disturb the optical readout so that the cantilever system should ideally be operated in darkness.

A simple and effective solution for these issues is provided by a commercially available mini-fridge. Not only does this enclosure shield light and acoustic noise but the built-in peltier element allows the adjustment of the temperature inside the box. I equipped the enclosure with a temperature controller to regulate the fridge's peltier cooler/heater and therefore set the temperature inside the box to a constant level (fig. 9.5). The temperature sensor that provided feedback to the controller was placed $\sim$ 1 cm in front of the back of the fridge where the peltier element is located. To improve the temperature circulation within the enclosure, a small fan was placed next to the heating/cooling unit. This fan was mounted using rubber washers that

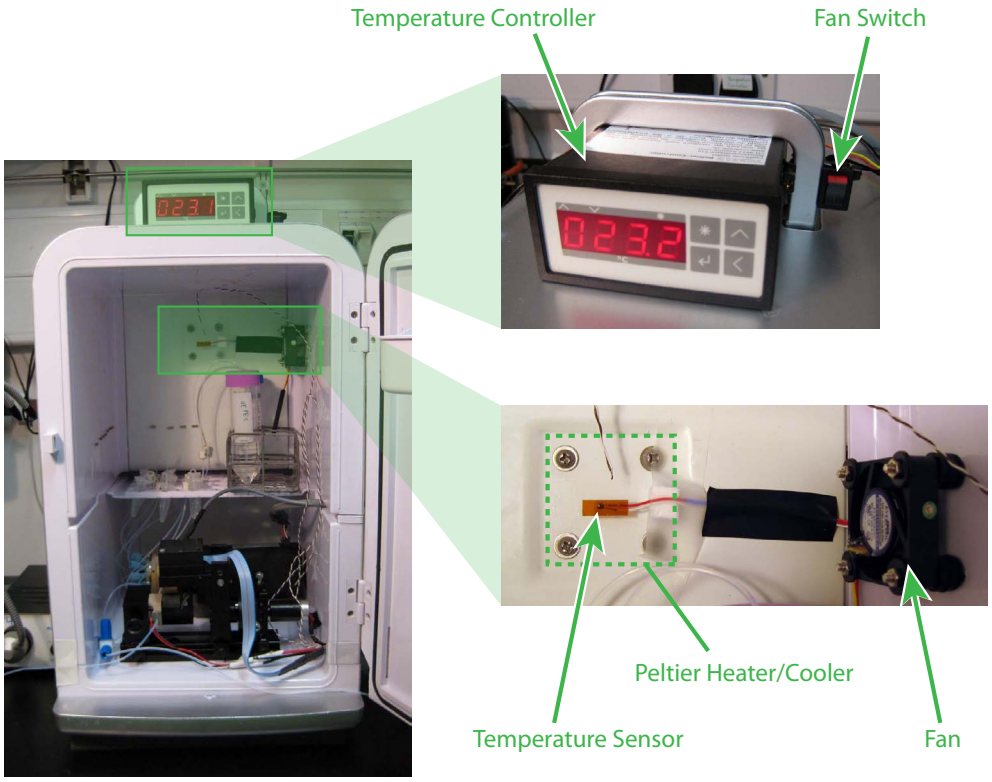

Figure 9.5: System enclosure with temperature control. *A mini-fridge provides a simple but effective aid to isolate the measurement unit from the environment. The built-in peltier heater/cooler is used to regulate the temperature inside the enclosure with the help of an external temperature controller. A small fan circulates the air inside the box and thereby improves the temperature control. The fan can be switched on/off using a switch on the outside of the enclosure if needed.*

reduce mechanical noise. In addition, the fan could be turned off with a switch on the outside of the box if needed.

Figure 9.6 demonstrates the capabilities of the temperature controlled enclosure. After the box is closed and the controller is switched on, it takes usually about 60 min until the setpoint is reached. The temperature is then stable for several hours (e.g. for overnight measurement) with a variance of about ± 0.05°C.

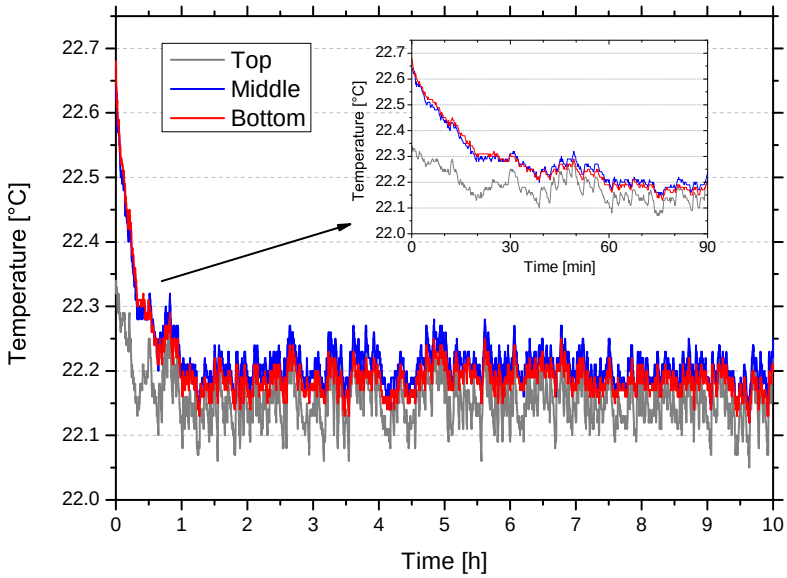

Figure 9.6: Demonstration of the temperature controller. *The temperature data for three temperature sensors within the enclosure are shown. Top: next to the peltier cooler/heater. Middle: in the middle of the box. Bottom: at the bottom of the box close to the liquid cell. The inset shows the first 90 min after the box was closed and the controller was switched on.*

9.5 Effect of Flow Rate

Previously we used gravity flow to inject different samples into the measurement chamber. Gravity flow has the advantage that it does not require any mechanical parts and therefore does not introduce additional noise into the system. However, the disadvantage is that it only works reliably at relatively high flow rates (~ 200 μl/min). Moreover, the flow rate has a large variance as it depends on the height difference between the inlet and outlet and thereby decreases while the sample solutions are consumed during an experiment.

The use of a syringe pump allows a constant flow rate over a long period of time and hence allows the realization of experiments in a more controlled environment. Due to the small cell volume and the controlled flow rate I could study the effect of the flow rate on the binding kinetics and affinity. Obviously, a lower flow rate requires less sample per time but on the other had it makes the reaction slower and

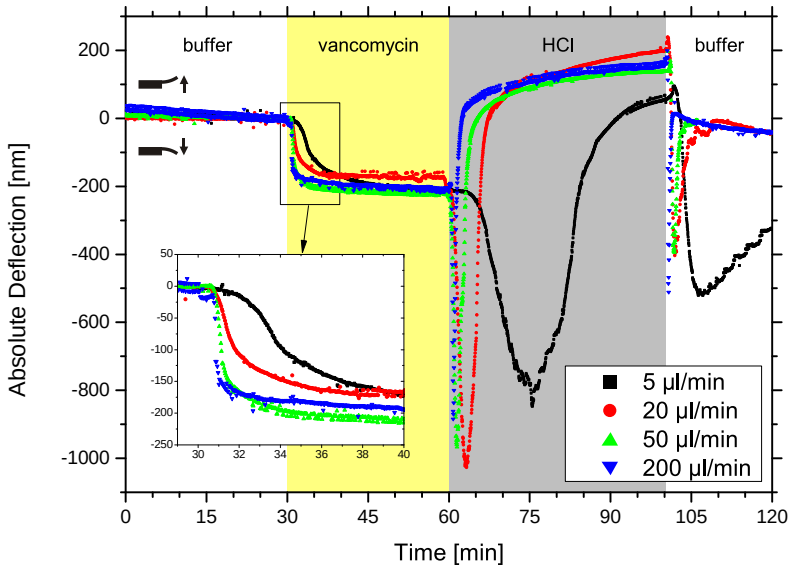

Figure 9.7: Effect of flow rate on vancomycin-*D*Ala binding reaction. *The experiment shows an injection of buffer, 100 μM vancomycin, 10 mM HCl and again buffer. The inset shows the first 10 min of the vancomycin injection in more detail.*

hence requires longer contact times. I therefore compared the binding of 100 μM vancomycin to **D*Ala***-coated cantilevers at four different flow rates: 5, 20, 50 and 200 μl/min. Figure 9.7 clearly shows that the binding kinetics scale with the flow rate, as expected. For the high flow rate (200 μl/min) saturation of the cantilever deflection is reached very quickly within $\sim$ 2 min. At flow rates of 20 and 50 μl/min it takes slightly longer but still less than 10 min to reach saturation, whereas at a very low flow rate (5 μl/min) saturation is only reached after 20 min. The absolute saturations deflections are slightly different for different flow rates, however this variation is within the experimental error and does not seem to correlate with the flow rate. The effects of the flow rates also appear in the subsequent washing step. For flow rates above 20 μl/min an HCl washing step of 40 min seems to be very efficient and the signal goes back to the initial deflection upon injection of buffer. In contrast, at a rate of 5 μl/min the antibiotic is not washed off efficiently and a long washing time would be required to regenerate the chip for further measurements.

The binding reactions of a full vancomycin dilution series was measured at a flow rate of 50 μl/min. With this I calculated a value for the equilibrium dissociation constant K_d = 1.49 $\pm$ 0.44 μM, which is very similar to binding affinities measured on the Scentris system (see also chapter 6). Furthermore, I did not observe a significant dependence of equilibrium signal with flow rate, i.e. the binding affinities should be independent of the flow rate. Therefore, flow rates between 20 and 50 μl/min were used for future experiments, which is a good compromise between sample consumption and binding kinetics.

9.6 Kinetics Experiments

Due to the small volume of the liquid cell and the controlled flow rate I could not only investigate the binding affinity (using the equilibrium signals and the Langmuir adsorption isotherm) but also the binding kinetics. I could fit binding kinetics models to the time-dependant deflection data and therewith calculate association and dissociation rates.

A first order binding reaction on a surface can be described as [Nieba96]

$$\frac{dR_t}{dt} = k_{on} \cdot C \cdot (R_{max} - R_t) - k_{off} \cdot R_t \tag{9.1}$$

where R_t is the measured response (cantilever deflection) at time t, R_{max} is the maximal response at saturation, C is the analyte (antibiotic) concentration, and k_{on} and k_{off} are the rate constant for the association and dissociation, respectively. When integrated, this can be written as

$$R_t = \frac{r_0}{k_{obs}} \cdot (1 - e^{-k_{obs} \cdot t}) \tag{9.2}$$

with

$$r_0 = k_{on} \cdot C \cdot R_{max} \tag{9.3}$$

$$k_{obs} = k_{on} \cdot C + k_{off} \tag{9.4}$$

For practical purposes I added to equation 9.2 the parameters t_0 which is the time of analyte injection and R_0 which is the deflection at the time of analyte injection:

$$R_t = R_0 + \frac{r_0}{k_{obs}} \cdot (1 - e^{-k_{obs} \cdot (t - t_0)}) \tag{9.5}$$

With these corrections the equations could be fitted to the measured raw data without the need of adjusting the data.

Similarly, the dissociation reaction can be described as

$$\frac{dR_t}{dt} = -k_{off} \cdot R_t \tag{9.6}$$

which upon integration can be written as

$$R_t = R_0 + R_1 \cdot e^{-k_{off} \cdot (t - t_1)} \tag{9.7}$$

where R_0 is again the response of the baseline before the analyte injection, R_1 is the response with respect to the baseline at the beginning of the dissociation process and t_1 the time at the beginning of the dissociation process.

I measured a series of vancomycin binding reactions and let the antibiotic dissociate before the washing step. Equations 9.5 and 9.7 were then fitted to the first minute of the association and dissociation reaction, respectively. The dissociation rate can be directly determined from the fit to the dissociation reaction. Using the fit to the association reaction and equation 9.4 I could then calculate the association rate. Finally, the equilibrium dissociation constant can the easily determined by the relation $K_d = \frac{k_{off}}{k_{on}}$.

The response of three different cantilevers from the same chip was compared upon injection of four different vancomycin concentrations (1, 10, 50 and 250 μM). Using the kinetics methods described herein I calculated a K_d value of 1.9 $\pm$ 1.5 μM, which agrees very well with the method using the Langmuir adsorption isotherm. I found k_{off} = (1.84 $\pm$ 0.32) $\times$ 10^{-3} s^{-1} and k_{on} = (2700 $\pm$ 2900) $M^{-1}s^{-1}$. Whereas k_{off} was very constant for all samples, k_{on} varied a little with vancomycin concentration (hence the larger error) which might be due to mass transport limitations during the injection.

I can summarise that this optimised cantilever system does not only allow the measurement of binding affinities but also binding kinetics which is an important factor for the screening of drug-target interactions. Moreover, the kinetics method requires fewer injections of different antibiotic concentrations to determine the binding affinity compared to the Langmuir method.

9.7 Single-Cycle Experiment

So far I always reported multi-cycle binding reactions where the sensor surface was washed and regenerated after every antibiotic injection step. This has the advantage that all experiments are very easily comparable and it is presumed that the binding reaction is performed at the same conditions for all injections. Nevertheless, this method is time-consuming and is prone to errors if the sensing layers are not completely regenerated after the previous binding experiment. In addition, the quality of the sensing layers is decreasing if a large number of washing steps are performed which is limiting the lifetime of a sensor chip.

I therefore performed so-called single-cycle experiments where increasing analyte concentrations are injected successively without washing steps in between. These binding experiments are already routinely used on SPR systems and require a much shorter analysis time, thereby allowing a quick and reliable determination of the binding affinity.

Figure 9.8a shows a typical single-cycle experiment for the measurement of the vancomycin-D***Ala*** binding affinity. The curve can simply be baseline-corrected (if required) and the response can be determined from the deflections at the end of each analyte injection step. These reporting points can then be plotted against the vancomycin concentration and fitted with the Langmuir adsorption isotherm (fig. 9.8b) in the same way as for the multi-cycle experiments. Using this method I determined a K_d value of 1.25 ± 0.41 μM which agrees very well with other ways of calculating the binding affinity.

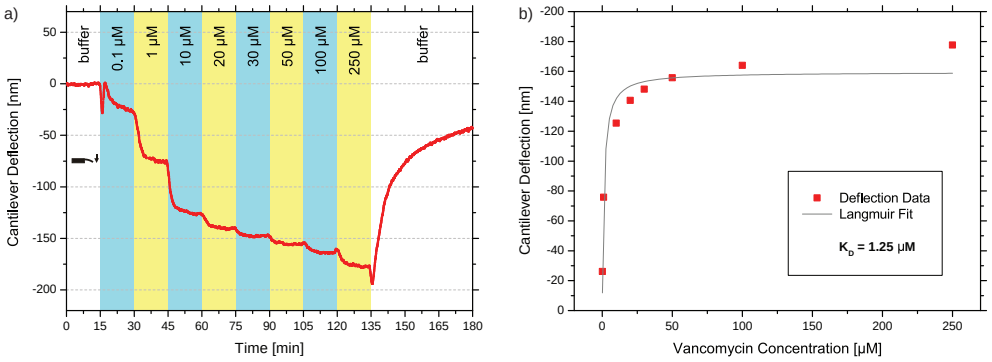

Figure 9.8: Single-cycle binding experiment on cantilevers. ***(a)*** *Consecutive injection of 8 different vancomycin concentrations over* **DAla** *coated cantilevers. The average deflection of three different cantilevers from the same chip is displayed.* ***(b)*** *Fit of the Langmuir adsorption isotherm against the cantilever deflection for different vancomycin concentrations.*

9.8 Discussion

The instrument improvements described in this chapter allowed better control of experiments, shorter injection times and lower sample consumption. A good example of these achievements is given by the single-cycle experiment in figure 9.8, where a sample injection time of 15 min at a flow rate of 50 μl/min was used, resulting in a total sample consumption of 750 μl and a total measurement time of 3 hours. This could be further optimized by using shorter injection times and lower flow rates. These are huge improvements compared to the Scentris instrument, where sample volumes of about 15 ml have to be used in order for the gravity flow system to work properly, and the measurement of a full dilution series takes usually two working days.

Table 9.1 gives a comparison between the technical features of the Scentris and NOSE systems. The table also contains the specifications of a commercial SPR system with an extremely small cell volume and fully automated liquid handling and operation, which admittedly is the benchmark for cantilever systems.

Table 9.1: *Comparison of the technical specifications of the NOSE cantilever instrument (as described in this chapter), the Scentris cantilever instrument (as used in chapters 6-8 with gravity flow system), and a commercial SPR instrument (Biacore T100). Typical values from my own experience are given for the cantilever systems, whereas the data for the SPR system is taken from a Biacore product information brochure.*

Feature	**Scentris**	**NOSE**	**Biacore T100**
Analysis time per cycle	$\geq$ 10 min	$\geq$ 3 min	$\geq$ 2 min
Affinity measurement	Yes	Yes	Yes
Kinetics measurement	No	Yes	Yes
Automation	Few hours (gravity flow is not very robust and should be watched regularly)	Up to 30 h unattended operation (depending on flow rate and syringe volume)	48 h unattended operation
Required sample volume	$\sim$ 15 ml	500 μl	50-400 μl
Flow rate range	150-300 μl/min	5-200 μl/min	1-100 μl/min
Flow cell volume	80 μl	8 μl	0.06 μl
Number of samples	6	10	Up to 384

9.9 Conclusion

This chapter showed the further development of an existing cantilever system for applications in drug-screening. This involved the use of a new liquid cell with a very small volume, the implementation of a fluidics system that allows the handling of small sample volumes and the customisation of an enclosure for a controlled environment.

Using this system, I showed that measurements at low flow rates give comparable results to previous experiments but require significantly less sample volume. Furthermore, I demonstrated that kinetics experiments are feasible due the small cell volume and constant flow rate. Finally, single-cycle binding experiments allow the quick and reliable determination of binding affinities. Thanks to this optimization, the NOSE cantilever system has some features that are almost comparable to modern SPR systems. Moreover, the instrument was now amenable to the analysis of complex lipid membranes which will be described in the next chapter.

CHAPTER 10

Supported Lipid Layers on Cantilevers

10.1 Introduction

The cantilever experiments described in chapters 6-9 used surface coatings based on model SAMs where thiolated model peptides were attached to a gold surface. Although these sensing layers produced good results in binding antibiotic molecules and quantifying their binding affinities, they are model systems where the cell wall peptide analogues are coupled rigidly to the surface with little possibility for surface diffusion. Therefore, it is questionable how well these rigid synthetic layers mimic the nature of a real bacterial cell wall where Lipid II is anchored to the membrane via a C_{55} tail and hence free to diffuse in a 2D plane.

In this chapter I describe an approach to coat one side of the cantilevers with a lipid layer where membrane-anchored receptor molecules can be inserted (fig. 10.1). Given that more than 50% of all drug targets are membrane bound, this would open up a significant range of applications for the study of drug-target interactions in a more natural environment. The ultimate goal is to immobilize trans-membrane

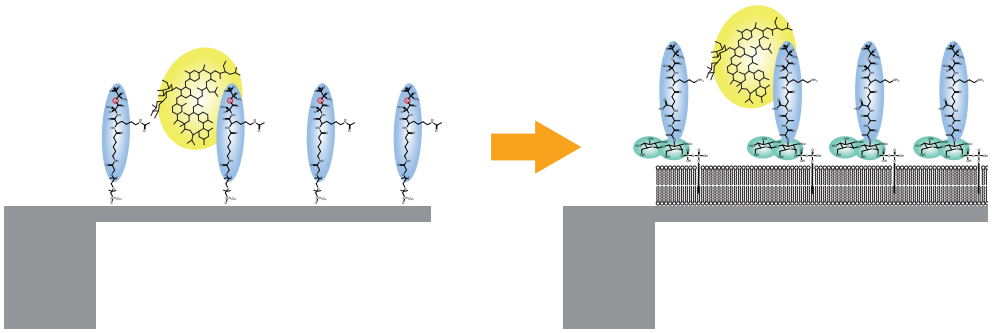

Figure 10.1: From SAMs to lipid layers. *Schematic to show the differences between self-assembled monolayers and more natural supported lipid layers on cantilevers.*

proteins on the cantilever surface in order to study drug-target binding that closely mimic the environment on the cell surface. Previous experiments with the model protein bacteriorhodopsin already showed potential of cantilever sensors to measure the surface stress associated with conformational changes of this membrane protein [Braun06].

In the context of the antibiotic experiments, the use of lipid layers on cantilevers would also allow to study additional features of the class of glycopeptide antibiotics. In the future, some semi-synthetic glycopeptide antibiotics such as oritavancin will have a hydrophobic chain which anchors the antibiotic molecule in the lipid membrane and hence improve the binding strength to the cell wall precursors. Cantilevers coated with lipid layers where mucopeptides can be inserted would allow to study this anchoring or other effects associated with the bacterial cell membrane.

Here, I describe the application of lipid layer coatings to cantilever sensors and compare different strategies for the formation of hybrid lipid bilayers. Prior to antibiotic analysis, a model membrane-associated system was tested by introducing the receptor molecules ganglioside GM1 into the lipid layers which can selectively bind the B subunit of cholera toxin. Using this approach I demonstrated first proof-of-principle experiments for the specific detection of receptor-ligand interactions on lipid layers using cantilever sensors. These experiments open possibilities for radically

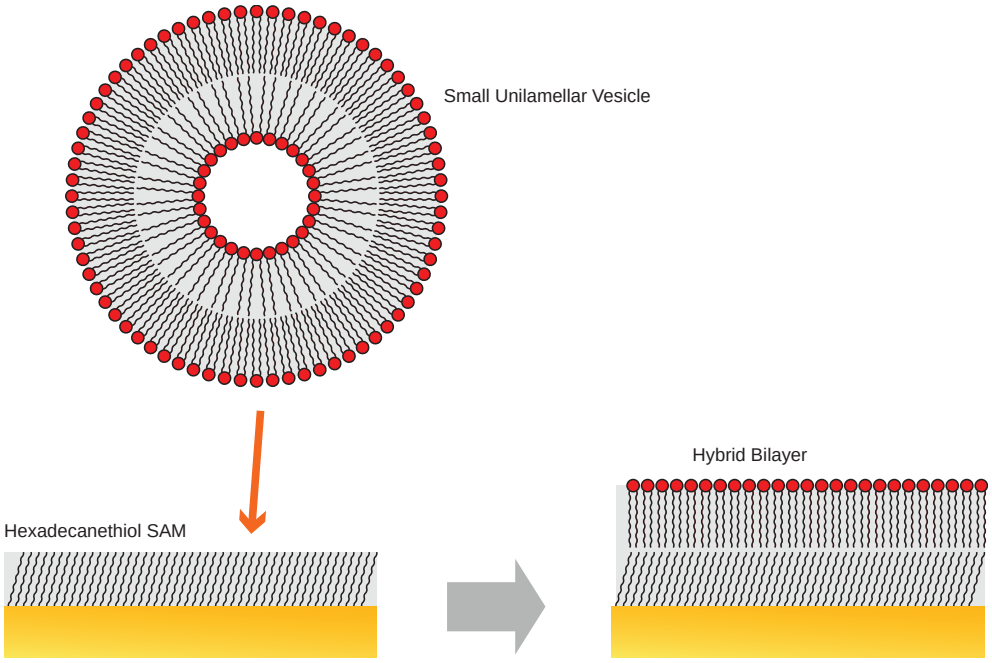

Figure 10.2: Schematic to illustrate the formation of a hybrid bilayer. *Small unilamellar vesicles (SUV) fuse with the hydrophobic substrate made up by a hexadecanethiol SAM. Thereby they form a hybrid bilayer where the hydrophobic tail groups of the lipids point towards the HDT substrate.*

new applications of cantilevers for the screening of membrane-tethered drug-target interactions.

10.2 Loading of Cantilevers with Lipid Layers

One of the simplest ways to prepare artificial lipid layers on a surface are so-called *hybrid bilayers* [Richter06] (another name in use is *supported lipid monolayer*). First, the substrate is rendered hydrophobic by the application of a self-assembled monolayer of alkanethiols. If small unilamellar vesicles (SUV) then come into contact with this hydrophobic layer, they unfold and thereby form a lipid monolayer with the hydrophobic tails pointing towards the alkane SAM (fig. 10.2).

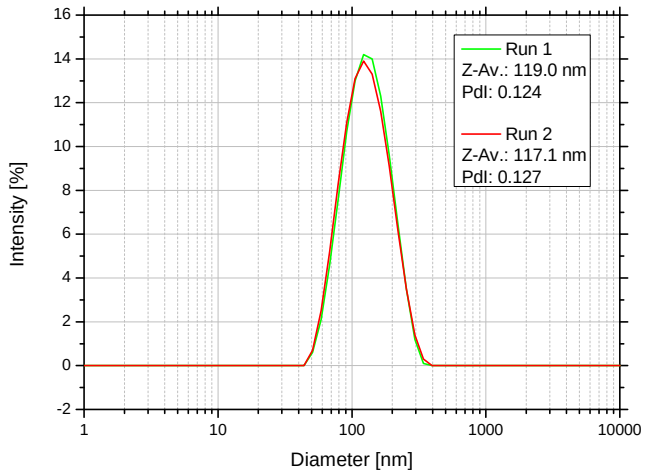

Figure 10.3: Size distribution of SUV measured by dynamic light scattering. *Two independent runs using the same sample solution agree very well, giving a z-average (mean hydrodynamic diameter) of 117 – 119 nm. PdI = polydispersity index.*

I used gold-coated cantilever arrays and coated the upper side of the cantilevers with a monolayer of hexadecanethiol (HDT). A suspension of phosphatidylcholine (PC) was prepared and then extruded with a 50 nm membrane to give SUV (see methods, section 5.6.1). During the extrusion process the PC suspension became visibly less cloudy, suggesting that small vesicles were formed. Nevertheless, dynamic light scattering (DLS) was performed with a SUV sample suspension in order to identify the size distribution of the vesicles. I measured two independent runs using the same SUV sample solution (diluted to 0.002% w/v) as shown in figure 10.3. The z-average (mean hydrodynamic diameter) was identical for both runs (117 – 119 nm) with a size distribution of around 50 nm. Although this vesicle size is considerably larger than the nominal pore size of the extrusion membrane, the extrusion process yielded a monodisperse solution. I presume that the lipid vesicles become deformed when they are pressed through the membrane and therefore adopt a larger size when they are free in solution.

I tested the feasibility of forming a hybrid lipid bilayer on cantilevers directly in the cantilever sensor device (*in-situ*). To achieve this, the cantilevers of a single chip were coated with HDT or PEG using the capillary method and then inserted into the liquid cell where PC vesicles were injected *in-situ*. Figure 10.4 shows a typical bending behaviour for these cantilevers for two consecutive injections of SUVs (overall 1 mM PC in the suspension), followed by a 20 mM CHAPS[1] washing step. Cantilevers pre-functionalized with hydrophobic HDT revealed a downwards bending of typically 50 – 100 nm upon the first SUV injection. The deflection was stable during the subsequent buffer injection, showing that the lipid layer remained intact for 1 h (and likely longer). A second SUV injection changed the deflection only slightly, confirming that a stable lipid layer was formed during the first SUV injection. After a washing step with the detergent CHAPS the cantilever bending is going back to the original state, indicating that the lipid layer is removed. In contrast, cantilevers coated with PEG do not show any significant deflections upon injection of SUV or detergent. I can therefore conclude that the observed cantilever bending is due to the formation of a hybrid bilayer on the HDT coating.

To investigate if the sensor chips can be reused and coated again with a lipid layer, I performed several consecutive SUV and detergent injections. Figure 10.5 shows the response of a HDT-coated cantilever for three cycles of SUV injections. I observed cantilever deflections of around 70 – 100 nm after all three SUV injections and the response was going back to the zero baseline after each detergent wash. Even after the last washing step, which was 12 hours after the start of the experiment, the signal went back to the initial value and did not drift much. In this experiment, vesicles were injected for a duration of 2 hours each, which is twice as long as in the previous experiment (compare fig. 10.4 and 10.5). Nevertheless, I measured similar deflection values for both experiments, suggesting that saturation of the lipid coverage is reached after 1 hour. Furthermore, the detergent octyl β-D-glucopyranoside (OGP, 40 mM) was used in the latter experiment instead of CHAPS. OGP has a higher critical micellar

[1] CHAPS = 3-[(3-cholamidopropyl)dimethylammonio]-1-propanesulfonate

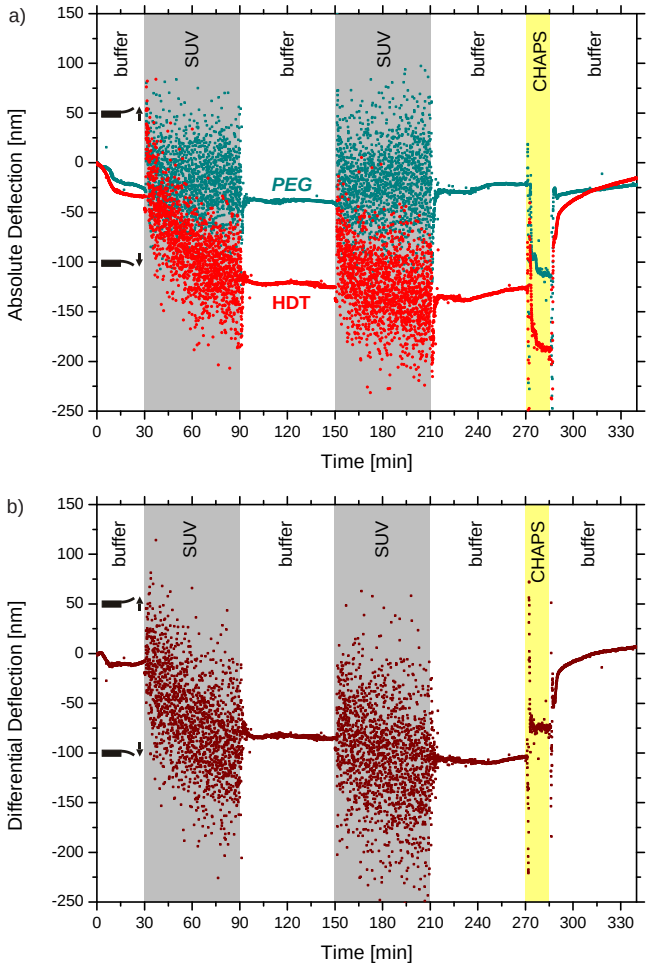

Figure 10.4: Formation of hybrid bilayers on cantilevers. *(**a**) Absolute signals of cantilevers coated with HDT and PEG and (**b**) differential signal HDT minus PEG. The large noise during the vesicle injections (grey boxes) is due to light scattering of the read-out laser. The PC concentration in the SUV suspensions was 1 mM.*

concentration (CMC) compared to CHAPS (OGP = 24–26 mM; CHAPS = 6–10 mM; values from Sigma Aldrich). Hence, OGP removes the lipid layer more efficiently and a stable baseline is reached quicker after the washing step, as can be seen in figure 10.5.

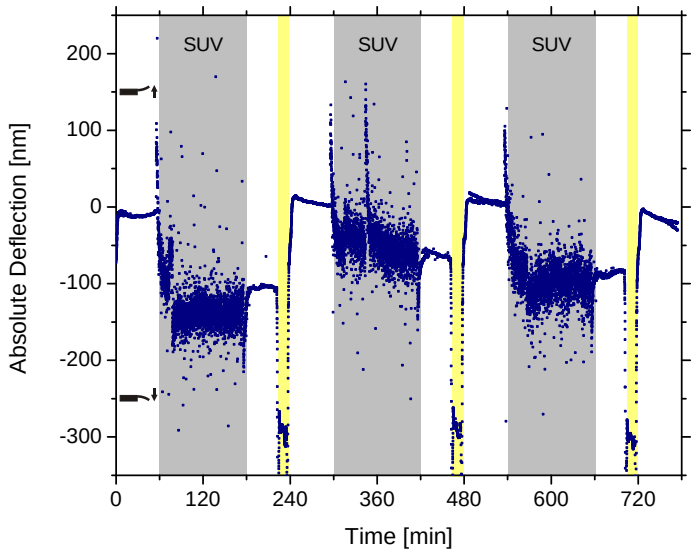

Figure 10.5: Cycles of formation and removing lipid layers on cantilevers. *SUV injections (1 mM PC) are indicated with a grey background, the washing step with the detergent octyl β-D-glucopyranoside (OGP, 40 mM) with a yellow background and buffer injections with a white background.*

10.3 Cholera Toxin - Ganglioside GM1 Binding Interaction

Cholera toxin (CT) is an enterotoxin released by the bacterium *Vibrio cholerae* and is responsible for the harmful effects of the cholera infection [Holmgren73]. CT forms a heterohexameric complex of the subunits A (27 kDa) and B (11.6 kDa) with the stoichiometry AB_5 (fig. 10.6a). Whereas the A subunit is responsible for the enzymatic activity of the toxin, each of the B subunits can bind to ganglioside GM1 receptors on cell surfaces (fig. 10.6b). This binding interaction is stabilised by several hydrogen bonds within the binding pocket, mainly involving the two terminal sugar groups of ganglioside GM1 [Merritt94]. The CT-GM1 interaction has a very strong binding affinity and K_d values in the range of 0.2 – 0.7 nM were reported by previous studies using SPR [Cooper00b].

I used the binding of cholera toxin B subunit to ganglioside GM1 as a test system to investigate the feasibility of detecting specific interactions of proteins with membrane-

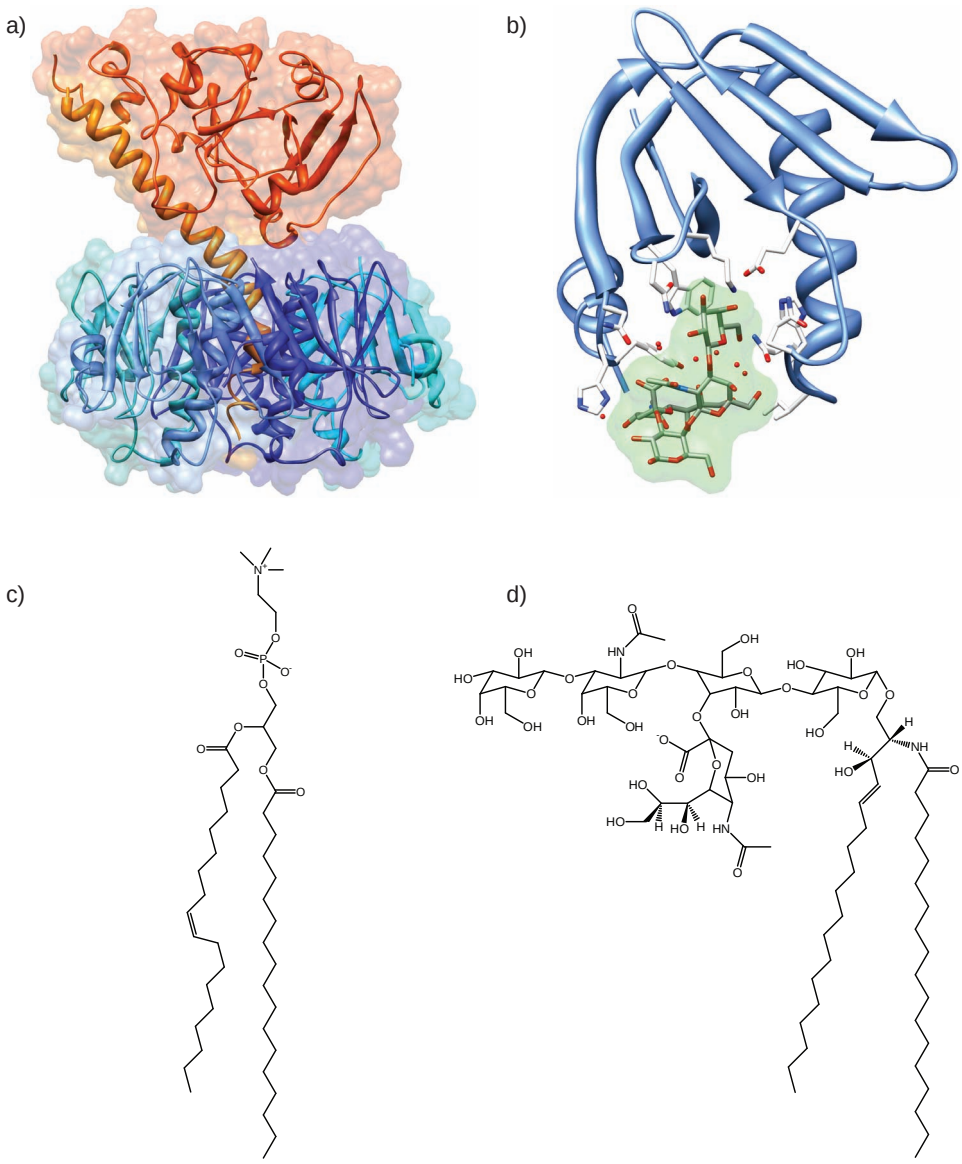

Figure 10.6: Structures of cholera toxin and ganglioside GM1. *(**a**) Illustration of the cholera toxin complex (from PDB ID: 1XTC, [Zhang95]). The A subunit is shown in orange and the five B subunits in different shades of blue. (**b**) Illustration of one CT B subunit (blue) bound to the four terminal sugar groups of ganglioside GM1 (green) to show the molecular interaction occurring in the binding pocket (from PDB ID: 3CHB, [Merritt98]. (**c**) Chemical structure of phosphatidylcholine with one stearic and oleic acid chain. Typical lots have fatty acid contents of approximately 33% palmitic, 13% stearic, 31% oleic, 15% linoleic and minor amounts of other acids. (**d**) Chemical structure of ganglioside GM1 pentasaccharide.*

anchored receptors using cantilever sensors. Both components, ganglioside GM1 and CT B subunit, are easily available which made this interaction a good test system. Moreover, ganglioside GM1 has two long hydrophobic chain and can be easily inserted into an artificial PC membrane (fig. 10.6c/d).

In initial experiments cantilevers were coated with lipid layers consisting of either PC containing 2% w/w ganglioside GM1 (active cantilevers) or pure PC (reference cantilevers). The coating was achieved with the capillary method, i.e. by introducing the cantilevers into capillaries filled with a SUV suspension. Vesicles containing GM1 were prepared by mixing GM1 with PC in the desired ratio at the beginning of the SUV preparation process (see methods, section 5.6.1).

Figure 10.7 shows the cantilever deflection data for the injection of 100 nM cholera toxin B subunit. Although there is significant drift of the signal at the beginning of the experiment (the temperature was not yet equilibrated), I observed a clear deflection of $\sim$ 30 nm for the cantilever coated with 2% GM1 upon injection of CT (between 10 and 30 min in fig. 10.7a). The reference cantilever did not show a significant response which supports the specificity of the detected signal. I then tried to recover the sensor surface by injecting a solution of 10 mM Glycine HCl (pH 2), followed by a second CT injection. However, this second CT injection did not induce a cantilever response anymore (between 70 and 75 min in fig. 10.7a). The differential data (fig. 10.7b) clearly reveals a specific response upon the first CT injection. Within 10 min of the injection a plateau is reached with a differential deflection of $\sim$ 30 nm. This is a fairly small deflection signal but still within the detectable range of the system. However, a very quick dissociation was observed when buffer was injected (after 30 min in fig. 10.7b), although the CT-GM1 binding interaction is known to be very strong. This raises questions about the specificity of the measured cantilever response. Nevertheless, the differential signal does not go completely back to zero but remains at a deflection of $\sim$ 6 nm, which might indicate that CT is not completely washed off. These specificity issues will be discussed later in this chapter.

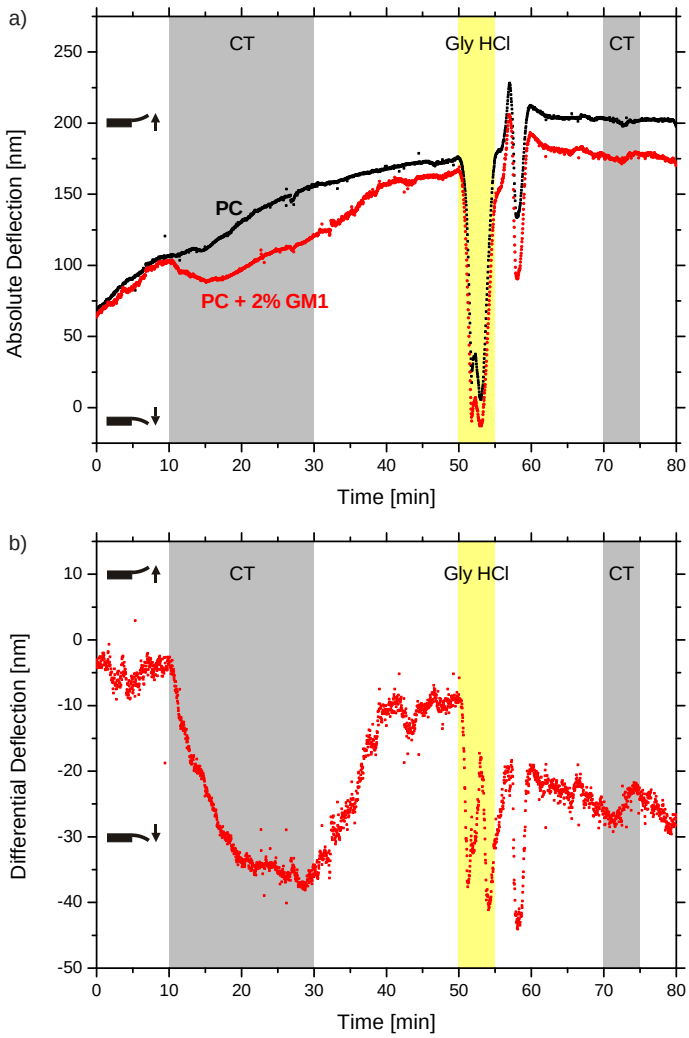

Figure 10.7: Binding of cholera toxin B subunit to hybrid bilayers containing ganglioside GM1. ***(a)*** *Absolute deflection signal and* ***(b)*** *differential signal. The mean of 2 cantilevers from the same chip is shown for each curve. The injection of 100 nM cholera toxin B subunit (CT) is marked in grey and the washing step with Gly HCl is marked in yellow. The flow rate was 30 μl/min throughout the whole experiment.*

Because the signal upon CT injection was fairly low and because the experiment raised questions about the specificity of the detected deflection, I tried to improve the sensitivity and specificity of the system. In a first attempt, I increased the percentage of GM1 in the hybrid bilayers. However, these experiments did not give any satisfying results within the time frame of this thesis. I cannot explain at this stage if the failure of these experiments is due to the changed density of GM1 receptors in the sensing layers or due to other factors.

I also tried to improve the quality of the lipid layers by using other preparation methods than the capillary method. Capillaries have the advantage that they allow each cantilever to be coated individually. The drawback however is that long incubation times (> 1 h) are impossible which might be needed for a high coverage of the cantilevers (the solution in the capillaries is evaporating during the functionalization process which can lead blockages of the capillaries). Three other functionalization procedures were therefore tested (see methods, section 5.6.3 for more details):

- **Injection method:** SUV were injected directly *in-situ* over the cantilevers, i.e. in the measurement chamber.
- **Incubation method:** The whole cantilever chip was immersed in a suspension of SUV for a period of several hours.
- **Detergent method:** The cantilever chip was immersed into a mixture of PC, GM1 and the detergent OGP. This solution was then stepwise diluted which gives a hybrid bilayer as the detergent is removed.

The disadvantage of these methods is that they can only be performed in batch, meaning that all cantilevers of one chip are exposed to the same solution during the coating process. One way to still get reference cantilevers is by initially coating some cantilevers with ***PEG*** and some with HDT using the capillary method, as there should be no hybrid bilayer be formed on ***PEG***-coated cantilevers.

I performed a small number of experiment for all three methods. Unfortunately, the injection and incubation method did not give any useful results for the set of

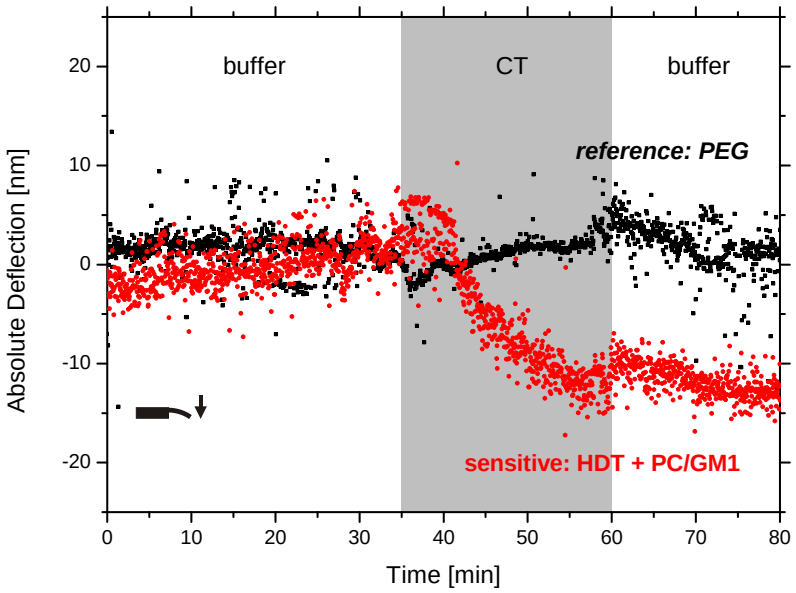

Figure 10.8: Binding of CT to GM1 prepared by the detergent method. *The black curve is the response of a cantilever coated with* **PEG**, *whereas the red curve is the mean response of two cantilevers coated with a hybrid bilayer containing GM1. The grey box indicates the injection of 200 nM CT leading to a deflection of 15 nm. The flow rate was 30 μl/min.*

experiments that were performed here. The detergent method on the other hand appeared to be promising. Figure 10.8 shows the result from a injection of 200 nM CT over a chip that was prepared with the detergent method. Although the signal is quite noisy, I observed that upon injection of CT the active cantilever bends downwards by 15 nm, whereas the reference cantilever does not show a significant deflection. This is similar to the graph shown before for the capillary method, only that the deflection has now half the value (compare fig. 10.7 and 10.8). In contrast to the measurement with the capillary method, here the response remains constant during the following buffer injection, suggesting that the analyte remains bound to the cantilever.

The experiment above (fig. 10.8) was then continued. After the first CT injection, the chip was exposed to a Gly HCl washing step to recover the sensor surface, followed by a second CT injection (fig. 10.9). The cantilevers reveal large deflections of more than 100 nm after the washing step and thereafter the signal is drifting for more

than 1 h. Moreover, the ***PEG***-coated cantilever seems to be more affected by this phenomenon which might have to do with molecular rearrangements on the surface. Although the second CT injection is convoluted with drift, it generates another specific binding response of $\sim$ 10 nm which becomes particularly apparent in the differential signal (between 160 and 190 min in fig. 10.9b). I then performed another Gly HCl washing step and finally injected a solution of 0.1 mg/ml BSA as a negative control. This BSA injected resulted in a small deflection of $\sim$ 20 nm on both active and reference cantilevers. Although this signal is larger than both CT injections it does not seem to be specific to any cantilever coating. Therefore it does not show up in the differential deflection signal, which (once again) urges the need for differential measurements and suitable reference coatings.

10.4 Discussion

This chapter reports the first proof-of-principle experiments for receptor-ligand analysis on supported lipid layers using multiple cantilever array technology. In particular, I demonstrated the formation of hybrid bilayers on the cantilever surface and the binding of cholera toxin B subunit to ganglioside GM1 embedded in a lipid layer.

The CT-GM1 interaction has previously been studied on hybrid lipid bilayers using SPR [Cooper00b, Terrettaz93] and hence provides a good test system for the cantilever sensor. These SPR experiments were highly reproducible and showed that the amount of bound CT scales with the percentage of GM1 within the lipid layer. They also allowed the measurement of a CT dilution series in order to calculate the binding affinity. My cantilever experiments were able to detect the CT-GM1 binding interaction, however they did not yet allow such detailed investigations due to low signals and relatively poor reproducibility. Nevertheless, future experiments will be guided into this direction.

In order to overcome these limitations, I varied the protocol for the preparation of the GM1-containing hybrid bilayers. However, the variation of the GM1 percentage in

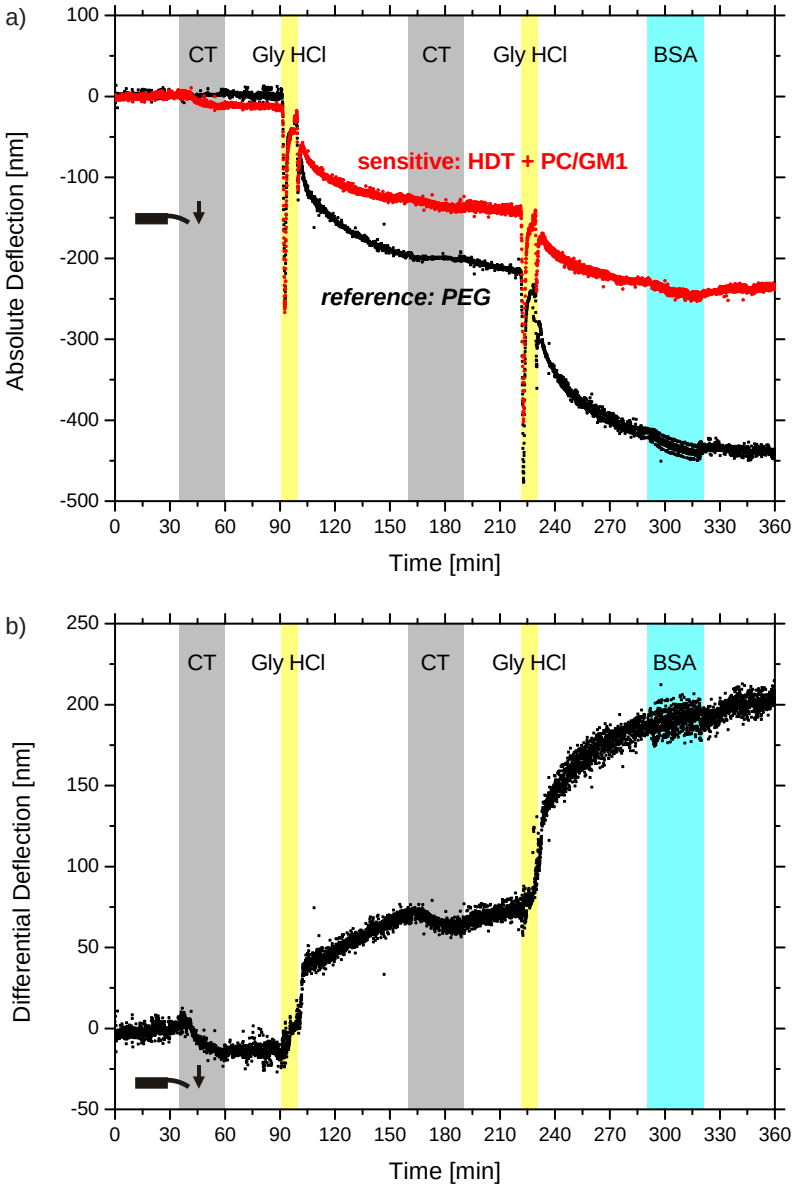

Figure 10.9: Continued binding experiment of CT to GM1 prepared by the detergent method. ***(a)*** *Absolute deflection signal and* ***(b)*** *differential signal. The response of the active cantilever is shown in red and the reference cantilever in black. The grey boxes indicates an injection of 200 nM CT, the yellow boxes indicate a washing step with 10 mM Gly HCl pH 2 and the the blue box indicates an injection of 0.1 mg/ml BSA. The flow rate was 30 µl/min. The two CT injections reveal a specific signal on the active cantilever whereas the BSA binding is unspecific and thus generates no response in the differential signal.*

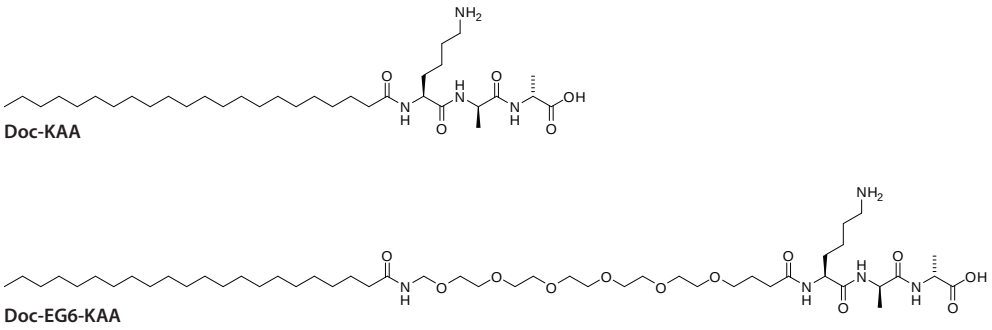

Figure 10.10: Chemical structures of mucopeptide analogues for the insertion into lipid layers. *Doc-KAA = docosanoyl-acetyllysyl-*D*-alanyl-*D*-alanine; Doc-EG6-KAA = docosanoyl-hexaethylene glycol-acetyllysyl-*D*-alanyl-*D*-alanine.*

the sensing layer and the application of different methods for the formation of the lipid layers produced only a limited success. The preparation using the detergent method revealed the best results so far, as it gave reproducible results for the binding of CT and fairly low unspecific binding signals of BSA.

The unspecific binding of BSA to the sensor surface seems to be a general problem with hybrid bilayers on cantilever. If an incomplete lipid layer is formed on the HDT monolayer, BSA binds to 'hydrophobic holes' in the layer which leads to an unspecific response. I performed some initial experiments using different methods and incubation times for the formation of lipid layers and investigated their susceptibility for unspecific BSA signals. These measurements suggest that the incubation time does influence the specificity. For example a chip that was immersed into a SUV suspension for 1 h revealed a deflection of 30-40 nm upon a BSA injection, whereas a chip that was incubated overnight (20 h) did not show a measurable deflection upon BSA injection. Furthermore, chips prepared using the detergent method usually showed smaller unspecific BSA signals compared to chips that were coated with lipids *in-situ* (injection method).

The original objective of this chapter was the study of antibiotic-mucopeptide interactions on supported lipid layers [Cooper99]. I performed a few preliminary experiments where Doc-KAA (fig. 10.10), a synthetic peptide that mimics Lipid II,

was inserted into hybrid lipid bilayers on cantilevers. Unfortunately, I did not manage to detect a specific binding signal of vancomycin in these experiments so far. Future experiments will use the improved model peptide Doc-EG6-KAA (fig. 10.10) where the tripeptide is placed further away from the lipid surface which mimics to the structure of Lipid II better. These experiments will allow to study the drug-target interactions of glycopeptide antibiotics in a more natural environment and would also allow an convenient model to vary the mucopeptide density for the investigation of the mechanical properties of the antibiotic action.

Future experiments will also include a general assessment of the formation of lipid layers on cantilevers. Because cantilever sensors rely on an asymmetry effect (i.e. a differential change of surface stress between the upper and lower side of the cantilever) it is important that only one side is coated with a lipid layer. However, with the current protocols I cannot exclude that vesicles also adsorb on the lower side of the cantilever (bare silicon). Future work therefore has to consider blocking the backside using silane surface chemistry. Furthermore, I have to identify if hybrid bilayers are really suitable for measurements on cantilever, as the hydrophobic HDT layer will always be susceptible to unspecific adsorption of proteins from the analyte solution. Other types of supported lipid layers, where an intact lipid bilayers are attached to the sensor surface [Cooper04] should also be considered for future experiments.

10.5 Conclusion

In this chapter I took the cantilever technology one step further by the first application of tethered lipid layers as sensor coatings on cantilevers for the analysis of specific ligand-receptor interactions. Preliminary experiments with a biological test system show the feasibility of such strategies, however further improvements are needed for the robust and specific detection of drug-target interactions. This method would generate radically new possibilities of cantilever sensors for membrane-associated drug screening.

CHAPTER 11

Conclusion and Future Work

This thesis shows that cantilever sensors are a promising new technology for the rapid and label-free analysis of drug-target interactions. Three milestones for the development and optimization of this sensor platform for drug analysis were reported: (i) Study antibiotic-mucopeptide interactions on cantilevers and understand the impact of the structure of the sensing layer on the sensor response. (ii) Further development of a cantilever instrument for the robust performance and low sample consumption. (iii) Implementation of new approaches for sensing layers by the application of tethered lipid layers.

In the next sections I will summarise the key findings in chapters 6-10 of my thesis and then describe key future experiments for this technology.

Nanomechanical Detection of Vancomycin

It was demonstrated that cantilever sensors are able to detect antibiotic drug-target interactions and discriminate between mucopeptide precursors from vancomycin-

sensitive (D***Ala***) and vancomycin-resistant bacteria (D***Lac***). The smallest vancomycin concentration that could be detected reproducibly was 10 nM, a sensitivity that is comparable to SPR [Rao99]. When using antibiotics with a stronger binding affinity, the sensitivity was even smaller, reaching values in the picomolar range for oritavancin (data not shown). The equilibrium dissociation constant that was determined for vancomycin was comparable to previously reported values, which is a good benchmark for the cantilever system. It was also shown that the vancomycin-D***Ala*** binding interaction formed a uniform surface stress along the cantilever axis. Furthermore, our set-up was able to detect the specific drug-target interaction in a complex protein background of blood serum. The latter positions cantilever sensors as a useful tool for the detection of a drug's free concentration and for the prediction of a drug's activity in human blood (Ndieyira *et al.*, manuscript in preparation, 2011).

Reference cantilevers coated with ***PEG*** did not show any specific interactions with antibiotics, hence unspecific effects and temperature drifts could be eliminated successfully in the differential signal. We were also able to regenerate the sensing layers on the cantilevers. This was achieved by flushing the measuring chamber with low concentrated HCl, leading to the unbinding of antibiotic molecules. It was found that the duration of the washing step had to be at least 30 min, so that the same array gave repeatable results. The cantilever arrays can even be recycled completely using a cleaning procedure with *aqua regia* and *piranha solution*. This process removed any metallic or organic layers so that the chip could be functionalized freshly and used for a new set of experiments.

Percolation Model for Stress Generation

Antibiotic binding experiments have been preformed where the density of the mucopeptide analogues D***Ala*** on the cantilever was varied systematically by the use of mixed monolayers with ***PEG***. From those experiments we hoped to improve our understanding of the generation of surface stress upon drug-target binding on the cantilever and get an insight into the mode of action of the antibiotics. It was found

that the cantilever surface stress can be described by a percolation model, where local chemical events and geometrical effects that build up the surface stress are separable. In this model, a percolation threshold above zero suggests that short range steric interactions lead to the generation of surface stress, whereas a percolation threshold of zero suggests long range elastic forces.

X-ray photoelectron spectroscopy showed that for a mixture of **D*Ala*** and ***PEG*** the solution molar fraction does not correspond linearly to the surface coverage fraction in a SAM, but that ***PEG*** adsorbs preferably onto the surface. These results were absolutely crucial for the correct analysis of the cantilever deflection data with mixed monolayers. Although the results from cantilever experiments with mixed monolayers that were performed as part of this thesis differed significantly from previous results in our group, they still indicate a collective phenomenon for the generation of surface stress. When comparing the cantilever data for the two antibiotics vancomycin and chloroeremomycin, I found very similar p_c and α values and could therefore not discriminate between these two antibiotics. The main conclusion from this chapter however was that the formation of the sensing layers on cantilevers is a crucial process and it highlighted the need to characterise these SAMs for every set of experiments.

Influence of SAM Structure on Surface Stress

In addition to the experiments with mixed monolayers, I tuned the **D*Ala*** sensing layers by simply varying the total thiol density on the sensor surface. We have already seen in the percolation experiments that small changes in **D*Ala*** solution concentration can have a huge impact on the cantilever response upon antibiotic binding, a phenomenon that was then studied in more detail. In summary, I diluted the **D*Ala*** solution that was used to coat the cantilevers over a range of almost five orders of magnitude. Thereby, I produced pure **D*Ala*** monolayers with different densities and conformations, which was confirmed by ARXPS, ellipsometry and contact angle measurements.

The structure and density of the underlying SAM was shown to have a striking effect on the surface stress generated upon vancomycin binding. Thereby, I did not

measure the highest surface stress on the most dense monolayers, which intuitively would be the case for purely steric interactions for the generation of surface stress. In contrast, I found an enhancement of surface stress at unexpectedly low D*Ala* densities, i.e. for surfaces that were prepared with solution concentrations between 10^{-3} and 0.1 mM D*Ala*. In this concentration range the transition between lying-down and standing-up SAMs occurs which is associated with high disorder in the layer. Moreover, monolayers with a low D*Ala* density have larger intermolecular separations and hence more structural flexibility. We therefore propose that, due to this disordered state, drug binding can introduce conformational changes that increase the entropy of the system. This may also expose 'bare' gold sites between the D*Ala* molecules and should be investigated further. In addition, at lower receptor densities the accessibility of the D*Ala* peptides may be improved resulting in a more efficient and stronger binding of vancomycin, and it was found that the D*Ala* density giving rise to the highest surface stress on cantilevers corresponds to the peptidoglycan density in real bacteria.

Owing to these new findings for the amplification of surface stress, this effect can be applied to the design of novel sensing layers. One could use surface coatings that trigger a conformational change upon analyte binding and therefore enhance the cantilever response. These findings are crucial for the development of the technology and may hold the key to the detection of very low antibiotic concentrations for drug-target analysis and also other medical applications such as therapeutic drug monitoring or forensics.

The results from this chapter also highlight the importance of a good reference coating in order to assure the specificity of the measured signal. Furthermore, it is crucial to understand the structure of the sensing layers, a challenge that probably has been underestimated in the field of cantilever research so far. Therefore, it would be desirable to have a surface analysis method such as XPS, that can perform characterisation of sensing layers directly on functionalized cantilevers for every set of experiments.

Instrument Development for Drug Analysis

A major aim of this thesis was to obtain a better understanding of the generation of surface stress on cantilevers, which is doubtlessly crucial for the design of improved sensing layers and the further development of this technology. Nevertheless, for the success of biochemical applications the whole system around the cantilever chips needs to be optimised, too. A part of this work was therefore dedicated to the improvement of an existing cantilever sensor device for robust performance and low sample consumption.

I implemented a fluidics system using a low-volume liquid cell, a syringe pump and a 10-way valve switch, which allowed automated overnight experiments with constant and low flow rate, as well as low sample consumption. This system was then applied to measure binding interactions of vancomycin to **D*Ala*** SAMs. Using this improved set-up I was able to perform kinetics experiments to study the rates of association and dissociation, a feature that was unique to SPR systems in the past. I also conducted single-cycle experiments which allowed to measure a full vancomycin dilution series for the determination of K_d within three hours.

Supported Lipid Layers on Cantilevers

I demonstrated proof-of-principle experiments for the application of tethered lipid layers on cantilever arrays. Supported lipid layers have the advantage that they mimic the nature of cellular surfaces much better than SAMs on gold and they can resemble the actual bacterial cell walls very closely. Hence, they allow radically new ways to study drug-target interactions on cantilevers.

The deposition of hybrid bilayers on the cantilever surface has been shown which served as a platform for the insertion of membrane-anchored receptor molecules. I used the binding interaction of cholera toxin B subunit with ganglioside GM1 as a test system to detect specific molecular interaction on cantilevers coated with lipid layers. Initial experiment demonstrated the feasibility of this approach although I discovered some issues with the magnitude and specificity of the cantilever response.

Future work will be aimed at optimising these problems. However, taking into account the insights about D***Ala*** SAMs I gained from chapter 8, it is questionable if the bending signal can be improved substantially. For SAMs I saw that the highest surface stress is achieved a fairly low D***Ala*** coverage which allows conformational changes and exposure of the gold substrate upon analyte binding. Such features are not possible with lipid layers by virtue of their constitution, as lipid membranes always form fluid-like and densely packed layers (see also fig. 10.1).

11.1 Future Work

SAMs for Antibiotic Sensing

Future work will keep using self-assembled monolayers on cantilevers for the detection of antibiotics, as SAMs have proven to be a very simple and robust way to coat sensor surfaces. Experiments with mixed monolayers for antibiotic sensing (chapter 7) will be repeated in order to vary the receptor density in a controlled way. Because cantilever sensors are unique in the way they can sense in-plane surface stress, we envisage a systematic study to investigate the mechanical properties of different antibiotics, concretely concerning their mode of action as a monomer or dimer. Moreover, we will not only study antibiotic binding to D***Ala*** but also to the resistant peptide D***Lac***, as recent studies suggested that the ratio of antibiotic monomer to dimer on the surface depends not only in the antibiotic itself but also mucopeptide analogue present on the surface (Ndieyira *et al.*, manuscript in preparation, 2011). In addition, monolayers will be blended with L***Ala*** instead of ***PEG***. L***Ala*** is the stereoisomer of D***Ala*** and therefore has the same chemical properties, however glycopeptide antibiotics do not bind to L***Ala***, which makes it an ideal reference coating.

Following the experiments with pure D***Ala*** monolayers formed by different solution concentrations (chapter 8), the effects of gold on the generation of surface stress will be further studied. An initial experiment showed that cantilevers coated with diluted ***PEG*** layers and bare gold cantilevers give rise to large deflections upon injection

of a vancomycin solution. Such kind of experiments have to be complemented with electrochemical methods in future. In addition, computer simulations and theoretical models of organic SAMs on gold surfaces will be needed for a better understanding of these processes.

Lipid Layers for Antibiotic Sensing

Although initial experiments with hybrid bilayers on cantilevers were successful and promising, they also identified some issues. The main challenges that need to be addressed are the specificity of the cantilever response and the magnitude of the deflection signals. In order to resolve these problems, we will investigate different coating methods and also try to use supported lipid bilayers instead of hybrid layers. Finally, bacterial cell wall peptide analogues and eventually real Lipid II will be inserted into these lipid layers, in order to investigate the binding of different antibiotic molecules. This assay would be particularly interesting to study antibiotics like oritavancin or teicoplanin which have a hydrophobic chain that is thought to attach the antibiotic to the bacteria's cell membrane and therefore facilitating the antibiotic's action.

Functionalization of Cantilever Arrays

In the work presented here, I functionalized the cantilever arrays using small glass capillaries. This capillary method is simple to accomplish and does not require sophisticated and expensive technical equipment. However, it is also subject to some drawbacks and can be problematic in some cases (as experienced for example in chapter 7). Capillaries are an open system where the solvent can evaporate at both ends. The temperature of the stage is not controlled so that the evaporation rate can vary significantly at different times of the year (especially if ethanol or another volatile solvent is used). Furthermore, the incubation time can vary slightly from one cantilever to another as the liquid has to be loaded consecutively into the capillaries. The speed of this process can also be user dependent. Finally, the cantilevers are

not always inserted into the capillaries in exactly the same way (only tip inserted versus completely inserted). This again can be user dependent. In addition, sometimes the cantilevers have to be pulled out a little from the capillaries in order to prevent cross-contamination as the liquid can flow onto the chip body. In the end, all these factors influence the exposure of the cantilevers to the functionalization solution, and we have seen in chapter 8 that only small variances in thiol density can have a large impact on the cantilever response.

Other research groups have used inkjet spotters to coat cantilevers. Whereas this method allows exact control over the dosage of the functionalization solution and could be scaled up for large arrays, the drawback is that the small drops that are deposited onto the cantilevers evaporate within seconds. Therefore, the incubation time can not easily be adjusted, which might be desirable for some applications.

For the future development of the cantilever technology I therefore propose the use of microfluidic channels. The idea is that special cantilever chips are designed where each cantilever is placed into its own channel (fig. 11.1). These channels can be addressed individually for *in-situ* functionalization. Thereby the coating process would be performed in a controlled and closed environment where the exposure to the solvent is controlled by the incubation time and flow rate. The same channels could then be used for the actual binding experiments where all cantilevers can be exposed to the same analyte solution.

Sensor Design and Read-Out

For the future development of the cantilever technology we also have to consider aspects of the general sensor design (e.g. cantilever geometries) and the cantilever readout.

The optical beam deflection method has been proven to be highly sensitive and is used successfully in AFM technology since years. Nevertheless, for cantilever sensor applications the optical readout has some drawbacks, for example it does not allow measurements in opaque liquids such as blood, and the alignment of an array

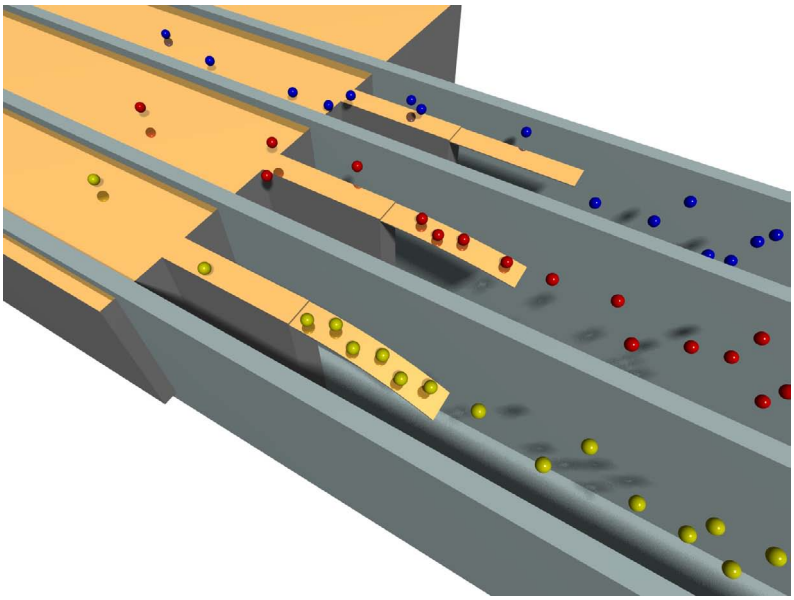

Figure 11.1: Vision of an array of cantilevers where each cantilever is embedded into its own microfluidic channel.

of lasers can be time-consuming and tedious. Researchers have therefore developed other readout methods such as piezoresistive readout, which allows the detection of cantilever bending directly on the cantilever chip, and which has recently been shown to reach a sensitivity that is suitable for biochemical applications.

In addition, the current cantilever design, where a rectangular bar is attached to the chip body, has been proven to be highly sensitive. However, it is not necessarily the most robust design, as it is susceptible to differences in flow rate or pressure, and mechanical vibrations. An example of a promising structure currently under development by Yoshikawa *et al.* are membrane-based sensors with piezoresistive readout.

11.2 Closing Remarks

This thesis presents a nice example of interdisciplinary research and includes some key concepts of nanotechnology – such as top-down approaches from microfabrication

processes, bottom-up approaches from self-assembly and the formation of biomimetic surfaces – and applies these strategies to a medical problem.

Thereby, this thesis outlines important developments in the use of cantilever technology for drug-target analysis, though much work is still needed to translate this promising technology to a commercial success. Nevertheless, future work to investigate the mechanotransduction mechanism on cantilevers and ultimately real bacteria may hold the key to the development of a new generation of antibiotics to combat drug-resistant infectious diseases.

APPENDIX A

Derivation of Langmuir Adsorption Isotherm

The Langmuir adsorption isotherm was originally developed to describe the adsorption of a gas onto a solid surface [Langmuir18] but can also be adapted to describe the adsorption of antibiotic molecules to mucopeptide analogues on cantilevers. The model is based on the following assumptions:

1. The surface containing the binding sites is a perfectly flat plane.
2. The adsorbing substance adsorbs into an immobile state.
3. All binding sites are equivalent.
4. Each binding site can hold only one molecule of the adsorbing substance.
5. There are no interactions between adsorbed molecules on adjacent sites.

If we assume this simple case, the adsorption of antibiotic molecules to mucopeptide analogues immobilised on cantilevers can be described as

$$[\mathrm{A}][\mathrm{S}] \underset{k_d}{\overset{k_a}{\rightleftharpoons}} [\mathrm{AS}]$$

where $[A]$ is the antibiotic concentration in molecules/cm^3, $[S]$ is the concentration of free surface binding sites in number/cm^2, $[AS]$ is the concentration of antibiotic molecules bound to the surface in molecules/cm^2, and k_a and k_d are adsorption and desorption constants. The rates of adsorption r_a and desorption r_d are given by

$$r_a = k_a[A][S]$$
$$r_d = k_d[AS]$$

In equilibrium the rate of adsorptions equals the rate of desorption, $r_a = r_d$, and thus

$$k_a[A][S] = k_d[AS]$$

or

$$\frac{[A][S]}{[AS]} = \frac{k_d}{k_a} = K_D$$

where K_D is the equilibrium dissociation constant. By introducing the total number of binding sites on the surface $[S_0]$ and using the equation

$$[S] = [S_0] - [AS]$$

to describe the binding site balance, this gives

$$K_D = \frac{[A][S_0]}{[AS]} - [A]$$

and rearranged

$$[S_0] = \frac{[AS](K_D + [A])}{[A]}$$

By defining θ_A, the fraction of occupied binding sites

$$\theta_A = \frac{[AS]}{[S_0]}$$

this yields the Langmuir adsorption isotherm

$$\boxed{\theta_A = \frac{[A]}{K_D + [A]}}$$

By assuming that the cantilever surface stress is proportional to the number of bound antibiotic molecules and by introducing a factor a that describes the maximum surface stress value when all binding site are occupied, the equation can be rewritten as

$$\boxed{\Delta\sigma_{eq} = \frac{a \cdot [Van]}{K_d + [Van]}}$$

where $\Delta\sigma_{eq}$ is the equilibrium signal of the cantilever surface stress.

APPENDIX B

ARXPS Raw Data and Depth Profiles

This section presents the ARXPS raw data, the data processing method and the complete set of SAM depth profiles in relation with the experiments performed in chapter 8.

B.1 ARXPS Raw Data

Figure B.1 displays the raw data overlaid for a selection of **D*Ala*** samples. The Au 4f peak reveals a decrease in intensity for higher **D*Ala*** concentrations because the signal of the gold substrate is attenuated when the adsorbed layer becomes thicker. The S 2p peaks show very low intensity overall but the intensity is increasing with higher thiol coverage. The N 1s and O 1s peaks show very low intensities for the two samples formed by the lowest **D*Ala*** solution concentrations and a rapid increase for higher concentrations. Finally, the C 1s signal not only exhibits a variation in intensity but also changes its peak shape, which means that the molecular composition of the surface layer changes, which will be discussed in the results chapter. For the N 1s, C 1

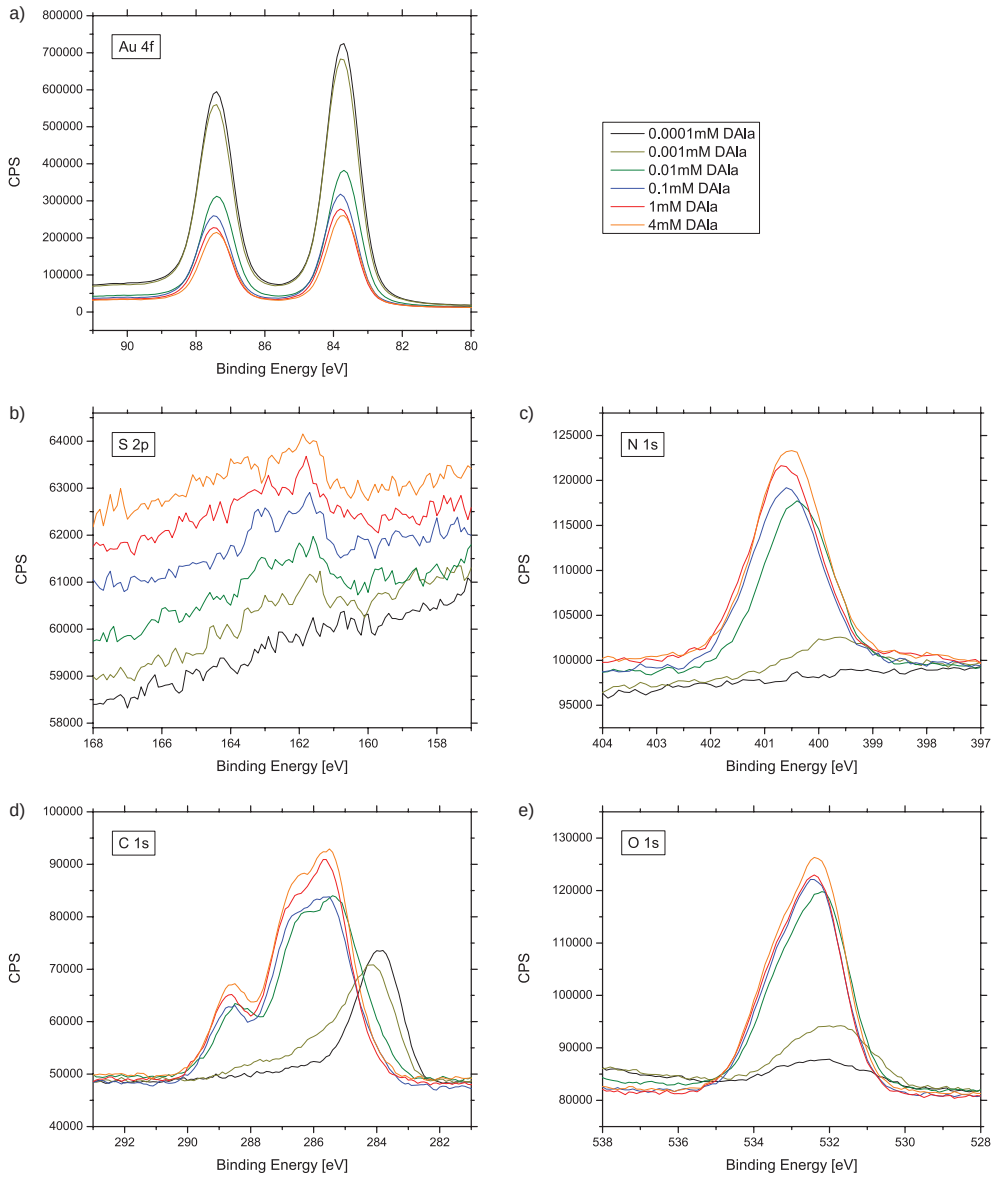

Figure B.1: XPS raw data for a selection of* DAla *samples. *Counts per second (CPS) are displayed for the Au 4f, S 2p, N 1s, C 1s and O 1s peaks. Some curves are shifted in the y-axis to make a nice overlay.*

and O 1s signal a peak shift is observed for samples $\leq 10^{-3}$ mM **D*Ala***. This is due to a charge effect, as it is known that the photoelectron energy changes when the thiols are lying flat on the surface due to interactions with the gold substrate [Duwez04].

Figure B.2 shows the collapsed raw data and fitting procedure for the 1 mM **D*Ala*** sample which is representative for all samples. For all peaks a mixed Gaussian-Lorentzian fitting function was used but depending on the element the fitting was performed with some restrictions:

- *Au 4f:* The gold signal splits up into a Au 4f and Au 4f- peak (resulting from the $4f_{5/2}$ and $4f_{7/2}$ electrons of the gold atoms). The peaks are well separated and the signal is large, thus both peaks can be fitted without any restrictions.

- *S 2p:* The sulphur signal also splits up into a S 2p and S 2p- peak. However, those peaks have very low intensity, even if all the available data from different spots and angles is collapsed. Therefore the fitting procedure was subject to strong restriction so that the results were comparable from one sample to another. We fixed the peak positions to 161.9 and 163.1 eV, respectively. Furthermore the width of the peak fit (full width at half maximum height, FWHM parameter) was set to be the same for both peaks.

- *N 1s:* The nitrogen signal occurred as a single peak with good intensity, thus the fit could be performed without restrictions.

- *C 1s:* The carbon signal splits up into three main peaks due to different chemical states of carbon atoms within the **D*Ala*** molecule. All peaks have a good intensity but overlap significantly, therefore the FWHM parameter was fixed to have the same value for all peaks within one sample but could vary from sample to sample.

- *O 1s:* The oxygen signal splits up into two peaks in a similar way as the carbon signal. The FWHM paramter was also set to be the same for both peaks within each sample.

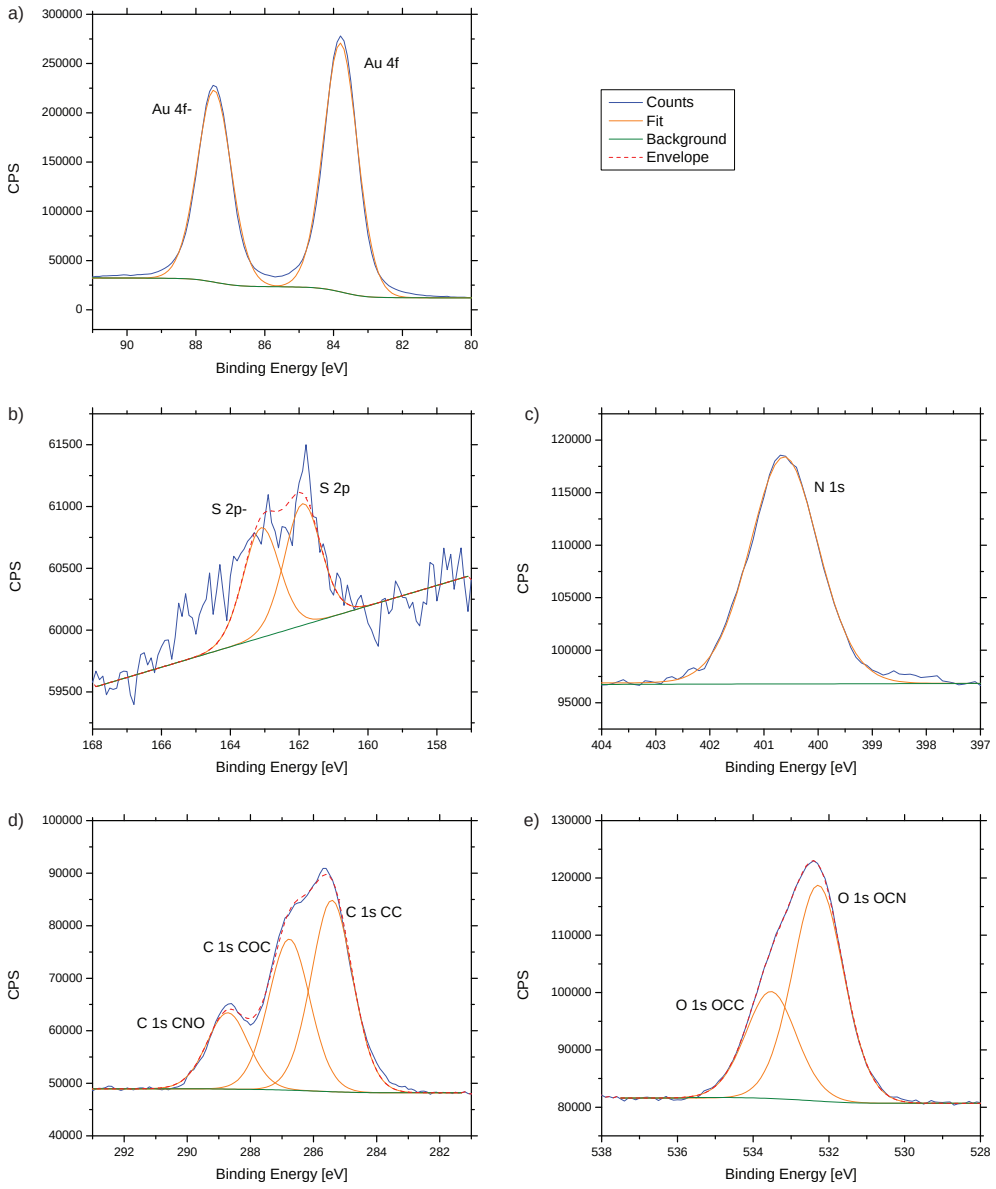

Figure B.2: Fitting of the XPS raw data. *XPS raw data for 1 mM* **DAla** *sample for* ***(a)*** *Au 4f,* ***(b)*** *S 2p,* ***(c)*** *N 1s,* ***(d)*** *C 1s and* ***(e)*** *O 1s peaks. Counts per second (CPS) are shown in blue, the background line in green, the Gaussian-Lorentzian fit in orange and the envelope of multiple fits in red.*

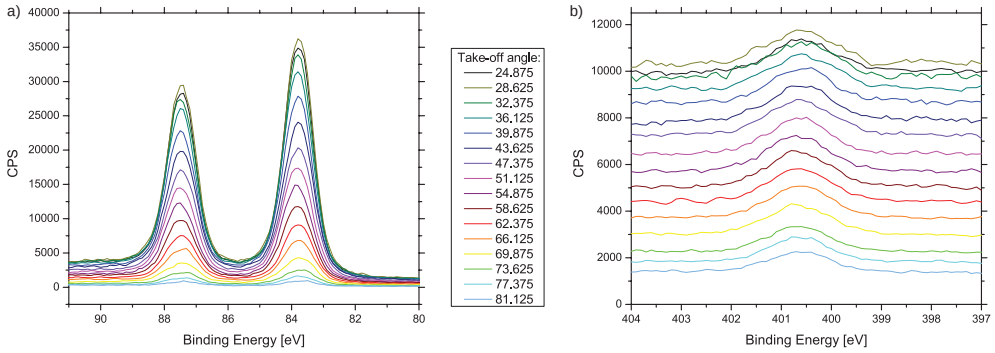

Figure B.3: Dependence of XPS signal on take-off angle. *The angle-dependence is exemplarily shown* ***(a)*** *for the Au 4f and* ***(b)*** *for the N 1s peaks of the 1 mM* **DAla** *sample.*

As shown exemplarily in figure B.3 the XPS signal was measured at 16 different take-off angles for each sample. Whereas the gold signal shows a large angle-dependence because it is buried underneath the SAM, the nitrogen signal reveals only a very small angle-dependence because the nitrogen occurs only at the very top part of the SAM. The Avantage software uses this depth information and calculates depth profiles of the surface layers with the help of iterative models (see below).

B.2 Reference Depth Profiles

I present here the depth profiles of two reference samples (HDT and ***PEG***) in order to demonstrate the power of ARXPS. The simplest sample we analysed, was a monolayer formed using a 2 mM hexadecane thiol (HDT) solution. These SAMs consist of three different elements only (neglecting the hydrogen): the gold substrate (Au 4f), one sulphur atom per molecule (S 2p) and a saturated carbon chain (C 1s CC). Figure B.4a shows the depth profile of the HDT sample which was calculated by the Avantage software. It shows a very clear transition from the carbon layer at the very top of the surface to the gold substrate, with a thin layer of sulphur in between. From this depth profile we can also easily extract the thickness of the SAM, which is $\sim$ 1.8 nm. Using this thickness and the known length of the HDT chain, we can also calculate the tilt angle of the thiol molecules within the SAM. There are two ways we can obtain a

value for the length of the HDT molecule: (i) by assuming a bond length of 154 pm per carbon-carbon bond (sp^3 hybridized orbitals) and a bond angle of 109.47° we get a value of 2.32 nm and (ii) using the ChemDraw computer software we get a length of 2.05 nm. This gives us tilt angles from the surface normal of 39.2° and 28.6° respectively, which agree with literature values of about 30° [Love05].

The other reference sample we investigated was composed of a monolayer formed by a 2 mM solution of the ***PEG*** thiol. The ***PEG*** molecules is slightly more complicated than HDT. Besides the sulphur and a C11 alkane chain, it has a terminal triethylene glycol group, which gives rise to two additional signals in the XPS measurement (C 1s COC and O 1s). The depth profile in figure B.4b again shows clearly the separation of the different elements within the SAM. The oxygen and carbon from the ethylene glycol groups are closer to the top of the surface than the carbon from alkane chain. Furthermore, the O 1s and C 1s COC occur at a ratio of about 4:7 which agrees with the stoichiometry within the ***PEG*** molecule. The thickness of the layer is 2.0 nm and by assuming a length of the ***PEG*** molecule of 2.59 nm (using ChemDraw software) we obtain a tilt angle of 39.4°. This angle is slightly larger than the one from HDT which could have to do with a less dense packing of the molecules on the surface.

From the depth profile in figure B.4 it is evident that the separation of the different elements is not perfect. We observe that the transition between the elements is not very sharp but rather follows a Gauss-like distribution. Additionally, we can see an oxygen signal very close to the sulphur and vice versa some saturation carbon signal at the very top of the surface. This can have different reasons: (i) The gold substrate is not atomically flat and therefore the peaks and zones in the depth profile are smeared out. (ii) Related to the first point, the SAM will not be perfectly ordered, especially at gold grain boundaries. (iii) The computer model for the calculation of the depth profiles uses an iterative procedure rather than direct calculations of the position of an element. This can introduce additional uncertainties and statistical errors.

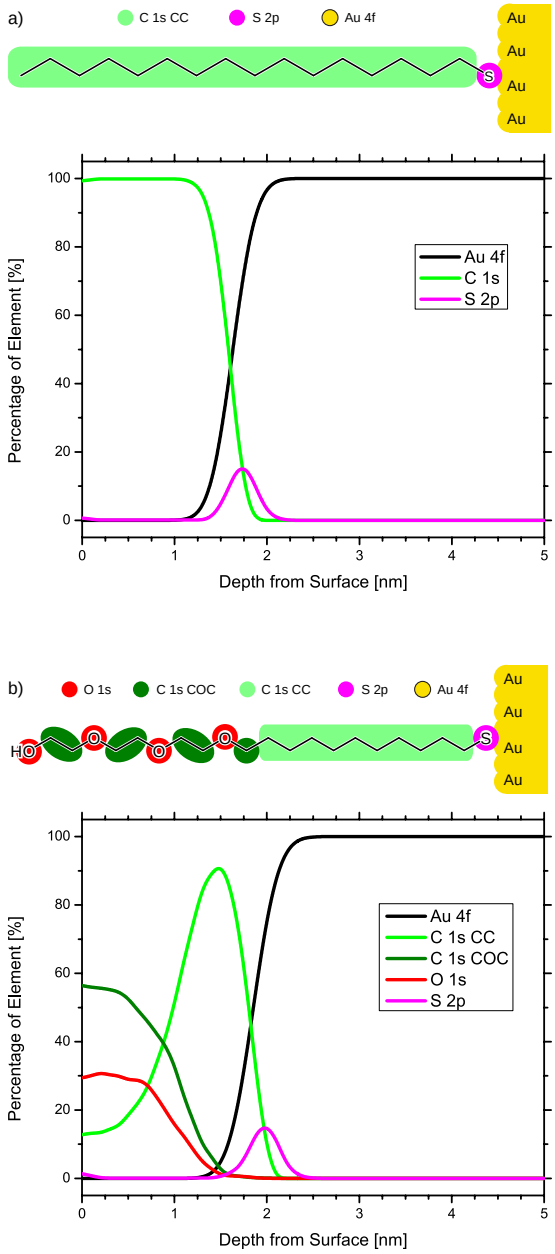

***Figure B.4: Depth profile of HDT and* PEG *layers measured by ARXPS.* (a)** *HDT and* **(b) PEG**. *The top of each subfigure shows the chemical structure of the thiol bound to a gold substrate. It is colour-coded to highlight the different elements that give rise to different XPS signals. The graph on the bottom shows the depth profile, whereby the x-axis represents the depth from the very top of the surface and the y-axis represents the occurrence of a given element within a surface layer.*

B.3 D*Ala* Depth Profiles

Figures B.5 to B.13 show the full series of depth profiles of **D*Ala*** monolayers measured by ARXPS (see section 8.4 for more information). For the colour coding of the curves refer to figure 8.6.

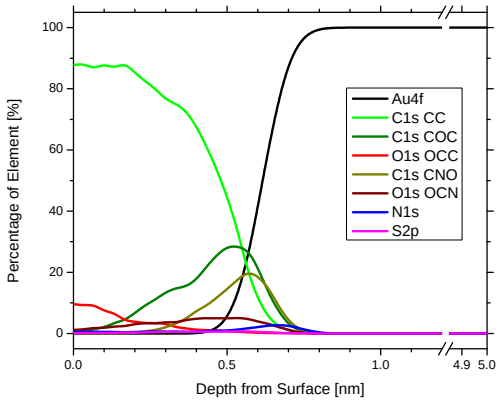

Figure B.5: *Depth profile of 10^{-4} mM* **DAla** *layer.*

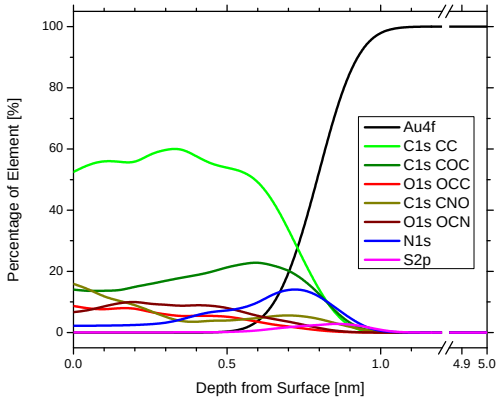

Figure B.6: *Depth profile of 10^{-3} mM* **DAla** *layer.*

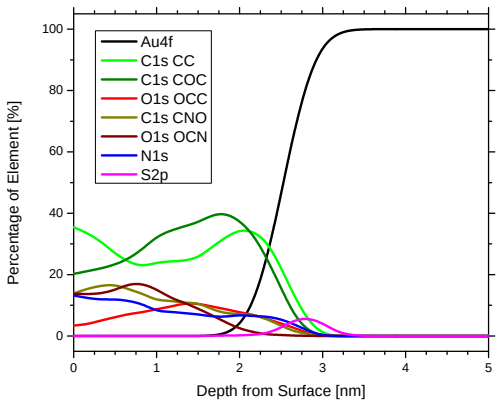

Figure B.7: *Depth profile of 0.01 mM* **DAla** *layer.*

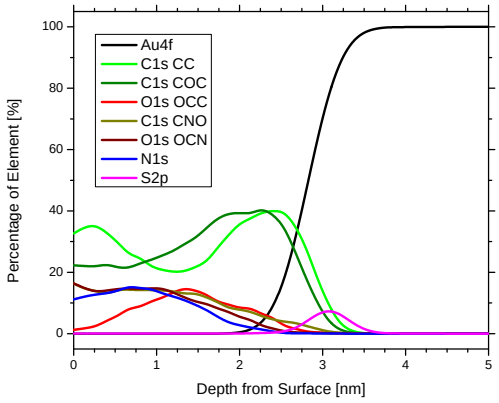

Figure B.8: *Depth profile of 0.05 mM* **DAla** *layer.*

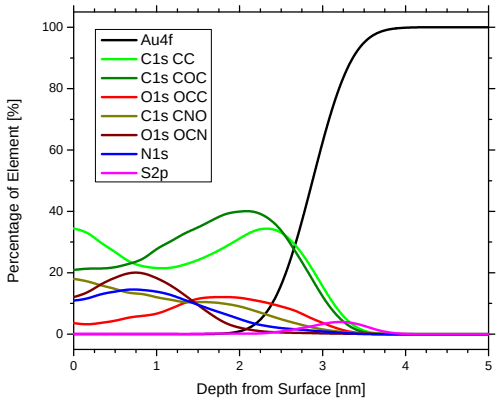

Figure B.9: *Depth profile of 0.1 mM* **DAla** *layer.*

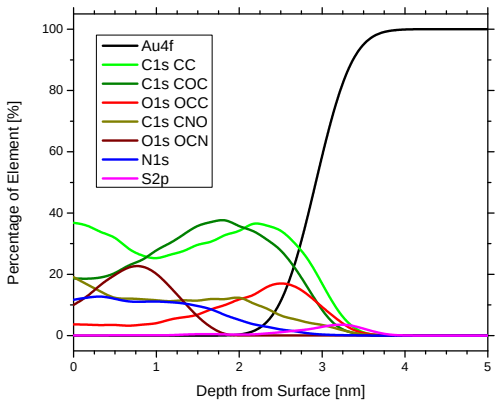

Figure B.10: *Depth profile of 0.5 mM* **DAla** *layer.*

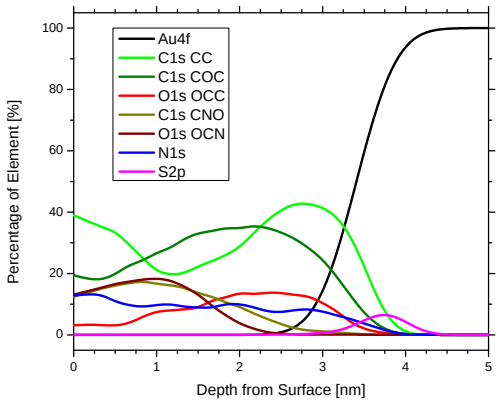

Figure B.11: *Depth profile of 1.0 mM* **DAla** *layer.*

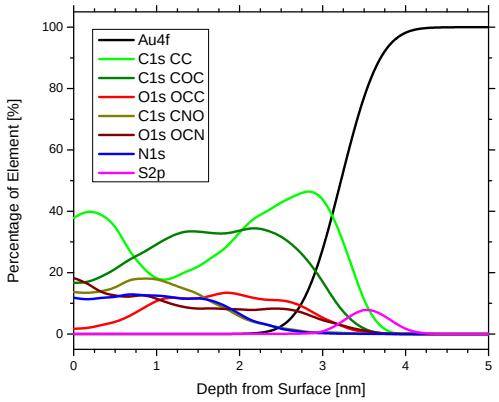

Figure B.12: *Depth profile of 2.0 mM* **DAla** *layer.*

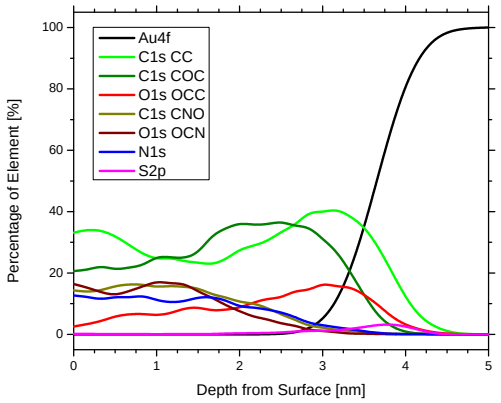

Figure B.13: *Depth profile of 4.0 mM* **DAla** *layer.*

APPENDIX C

Gas Phase Experiments

Because self-assembled monolayers are widely used nowadays, it is vital to understand the forces and interactions occurring during the formation of a SAM. The structure of the sulphur-gold interface is surprisingly complex and is still not completely understood. Researchers from the London Centre for Nanotechnology recently used a novel method to investigate the thiol-gold interactions. They coated gold nanoparticles with propane thiol (C_3H_7SH) and tracked structural changes of the nanocrystal using an X-ray diffraction method (Moyu Watara and Ian Robinson *et al.*, manuscript in preparation). To complement these experiments, I performed gas phase cantilever experiments where I measured the surface stress generated by the adsorption of a alkanethiol monolayer on gold-coated cantilevers.

The experimental setup for these measurements is schematically illustrated in figure C.1. A gold-coated cantilever array (20 nm Au) was placed into a gas cell with a volume of $\sim$ 300 μl. Reference cantilevers were left blank by applying a mask during the gold deposition process. The gas cell was connected to a syringe pump via

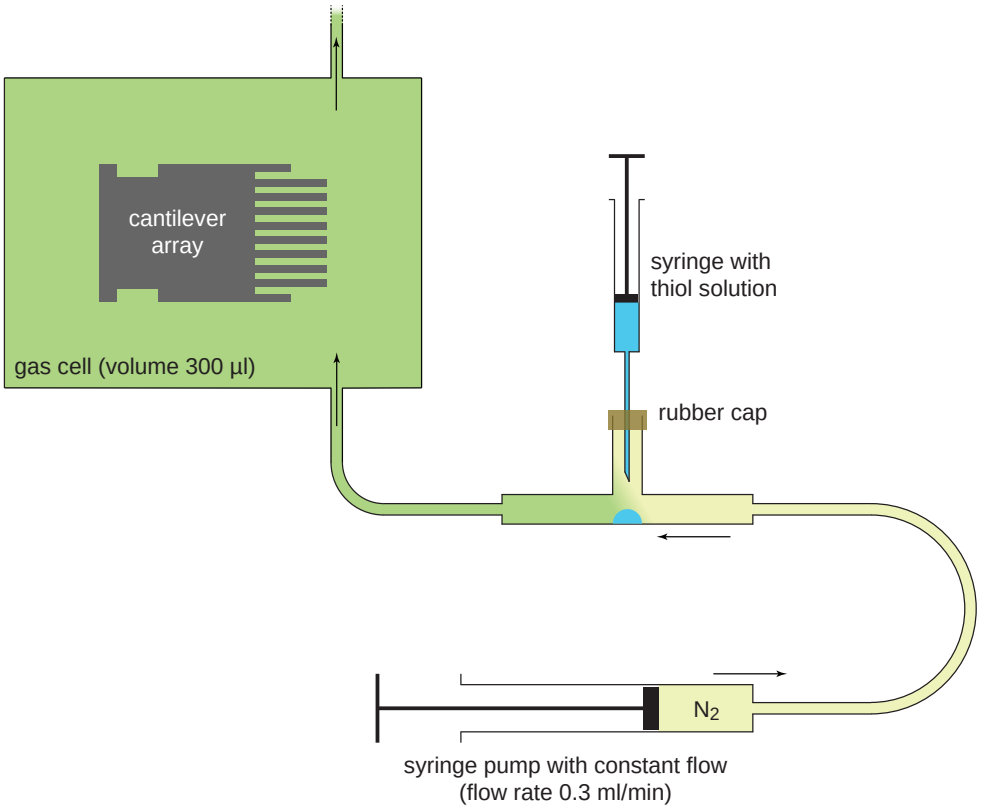

Figure C.1: Schematic illustration of gas phase experiments with alkanethiols. *A constant nitrogen stream was flown over a drop of thiol solution. The resulting thiol vapour was introduced into the gas cell with the cantilever array.*

a PTFE tubing and a T-junction. The syringe was pumping nitrogen gas through the system at a constant rate of 0.3 ml/min. A drop of the thiol solution was introduced into the T-junction using a syringe pierced through a rubber cap. Consequently, thiol vapour was carried to the gas cell via the nitrogen stream and the resulting cantilever deflection was recorded.

In an initial experiment, I added a drop of 5 mM propanethiol solution to the T-junction, whereon the gold-coated cantilevers began bending upwards, reaching a tensile surface stress of 150 mN/m (fig. C.2). After the addition of a drop of pure propanethiol, the stress increased to 240 mN/m. The higher deflection for pure thiol can be explained by a higher vapour concentration of the thiol. The bare silicon

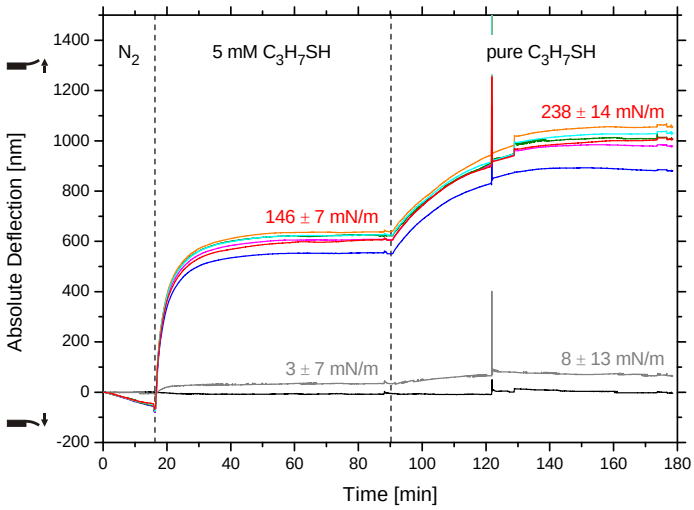

Figure C.2: Cantilever deflection upon injection of propanethiol vapour. *The response of gold-coated cantilevers is shown in colour and the response of bare silicon cantilevers (reference) is shown in black and grey. Gold-coated cantilevers bend upwards (tensile stress) upon adsorption of propanethiol.*

cantilevers did not reveal a significant bending, suggesting that the thiols are binding specifically to the gold substrate.

Astonishingly, I measured upwards bending of the cantilevers upon adsorption of propanethiol. This is fundamentally different to previously published cantilever experiments using longer alkanethiol chains which reported a downwards bending of cantilevers [Berger97, Godin04]. I therefore repeated the experiment with dodecanethiol and indeed found a downwards bending of the cantilevers upon thiol adsorption (fig. C.3). The deflections I measured were much smaller than the values reported in literature which might have to do with diffusion limitations of our setup.

The opposite cantilevers response upon adsorption of propanethiol and undecandethiol indicates that there are fundamental differences for the formation of the SAM from these thiols. We can only speculate about the reasons at this point. It might be that the propanethiol takes up a different conformation on the surface because the chain is too short for the built-up of lateral VdW interactions between the chains, which is the main contribution for the formation of standing-up layers for longer alkanethiols.

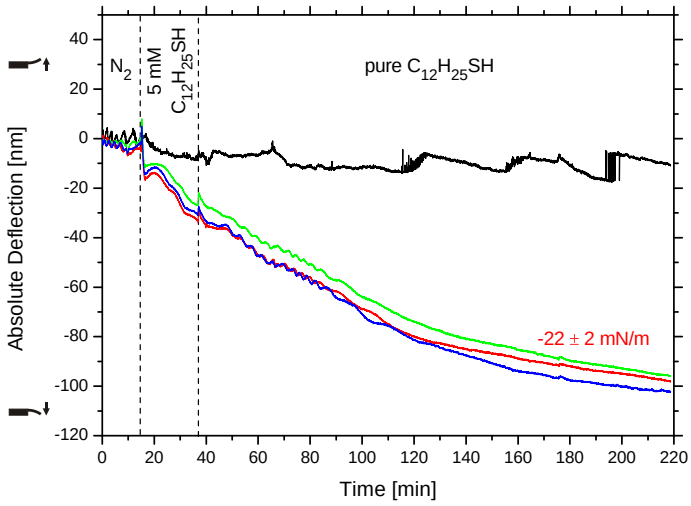

Figure C.3: Cantilever deflection upon injection of dodecanethiol vapour. *The response of gold-coated cantilevers is shown in colour and the response of a bare silicon cantilever (reference) is shown in black. Gold-coated cantilevers bend downwards (compressive stress) upon adsorption of dodecanethiol.*

This might not only influence the conformation of the thiol itself but also the structure and charge distribution of the underlying gold substrate. Further experiments and computer simulations have to be performed to gain a better understanding of this phenomenon.

Bibliography

[Allen97] N. E. Allen, D. L. LeTourneau, and J. N. Hobbs. The role of hydrophobic side chains as determinants of antibacterial activity of semisynthetic glycopeptide antibiotics. *The Journal of Antibiotics*, 50(8):677–684, 1997.

[Allen03] N. E. Allen and T. I. Nicas. Mechanism of action of oritavancin and related glycopeptide antibiotics. *FEMS Microbiology Reviews*, 26:511–532, 2003.

[Amirola05] J. Amirola, A. Rodriguez, L. Castaner, J. Santos, J. Gutierrez, and M. Horrillo. Micromachined silicon microcantilevers for gas sensing applications with capacitive read-out. *Sensors and Actuators B*, 111-112:247–253, 2005.

[Arntz03] Y. Arntz, J. D. Seelig, H. P. Lang, J. Zhang, P. Hunziker, J. P. Ramseyer, E. Meyer, M. Hegner, and C. Gerber. Label-free protein assay based on a nanomechanical cantilever array. *Nanotechnology*, 14:86–90, 2003.

[Arthur92] M. Arthur, C. Molinas, T. D. Bugg, G. D. Wright, C. T. Walsh, and P. Courvalin. Evidence for in vivo incorporation of D-lactate into peptidoglycan precursors of vancomycin-resistant enterococci. *Antimicrobial Agents and Chemotherapy*, 36(4):867–869, 1992.

[Arthur96] M. Arthur, P. E. Reynolds, F. Depardieu, S. Evers, S. Dutka-Malen, J. Quintiliani, and P. Courvalin. Mechanisms of glycopeptide resistance in enterococci. *Journal of Infection*, 32(1):11–16, 1996.

[Backmann05] N. Backmann, C. Zahnd, F. Huber, A. Bietsch, A. Plückthun, H. P. Lang, C. Gerber, and M. Hegner. A label-free immunosensor array using single-chain antibody fragments. *PNAS*, 102(41):14587–14592, 2005.

[Bain89] C. D. Bain, H. A. Biebuyck, and G. M. Whitesides. Comparison of self-assembled monolayers on gold: coadsorption of thiols and disulfides. *Langmuir*, 5:723–727, 1989.

[Baller00] M. Baller, H. P. Lang, J. Fritz, C. Gerber, J. K. Gimzewsky, U. Drechsler, H. Rothuizen, M. Despont, P. Vettiger, F. M. Battiston, J. P. Ramseyer, P. Fornaro, E. Meyer, and H.-J. Güntherodt. A cantilever array-based artificial nose. *Ultramicroscopy*, 82(1-4):1–9, 2000.

[Barna84] J. C. J. Barna and D. H. Williams. The Structure and Mode of Action of Glycopeptide Antibiotics of the Vancomycin Group. *Annual Reviews in Microbiology*, 38(1):339–357, 1984.

[Barrera08] A. D. Barrera. *Nanomechanical Sensor Arrays for Antibiotic Drug Analysis*. Ph.D. thesis, University College London, 2008.

[Berger97] R. Berger, E. Delamarche, H. P. Lang, C. Gerber, J. K. Gimzewski, E. Meyer, and H.-J. Guntherodt. Surface Stress in the Self-Assembly of Alkanethiols on Gold. *Science*, 276:2021–2024, 1997.

[Brantley73] W. A. Brantley. Calculated elastic constants for stress problems associated with semiconductor devices. *Journal of Applied Physics*, 44(1):534–535, 1973.

[Braun06] T. Braun, N. Backmann, M. Vögtli, A. Bietsch, A. Engel, H.-P. Lang, C. Gerber, and M. Hegner. Conformational Change of Bacteriorhodopsin Quantitatively Monitored by Microcantilever Sensors. *Biophysical Journal*, 90:2970–2977, 2006.

[Braun09] T. Braun, M. K. Ghatkesar, N. Backmann, W. Grange, P. Boulanger, L. Letellier, H.-P. Lang, A. Bietsch, C. Gerber, and M. Hegner. Quantitative time-resolved measurement of membrane protein-ligand interactions using microcantilever array sensors. *Nature Nanotechnology*, 4(3):179–185, 2009.

[Britton00] C. L. Britton, R. L. Jones, P. I. Oden, Z. Hu, R. J. Warmack, S. F. Smith, W. L. Bryan, and J. M. Rochelle. Multiple-input microcantilever sensors. *Ultramicroscopy*, 82(1-4):17–21, 2000.

[Brockman00] J. M. Brockman, B. P. Nelson, and R. M. Corn. Surface plasmon resonance imaging measurements of ultrathin organic films. *Annual Review of Physical Chemistry*, 51:41–63, 2000.

[Brugger92] J. Brugger, R. A. Buser, and N. F. de Rooij. Micromachined atomic force microprobe with integrated capacitive read-out. *Journal of Micromechanics and Microengineering*, 2(3):218, 1992.

[Bugg91] T. D. Bugg, G. D. Wright, S. Dutka-Malen, M. Arthur, P. Courvalin, and C. T. Walsh. Molecular basis for vancomycin resistance in Enterococcus faecium BM4147: biosynthesis of a depsipeptide peptidoglycan precursor by vancomycin resistance proteins VanH and VanA. *Biochemistry*, 30(43):10408–10415, 1991.

[Burg07] T. P. Burg, M. Godin, S. M. Knudsen, W. Shen, G. Carlson, J. S. Foster, K. Babcock, and S. R. Manalis. Weighing of biomolecules, single cells and single nanoparticles in fluid. *Nature*, 446(7139):1066–9, 2007.

[Cherian02] S. Cherian, A. Mehta, and T. Thundat. Investigating the Mechanical Effects of Adsorption of Ca2+ Ions on a Silicon Nitride Microcantilever Surface. *Langmuir*, 18(18):6935–6939, 2002.

[Christoffersen06] R. E. Christoffersen. Antibiotics – an investment worth making? *Nature Biotechnology*, 24(12):1512–1514, 2006.

[Cooper99] M. A. Cooper and D. H. Williams. Binding of glycopeptide antibiotics to a model of a vancomycin-resistant bacterium. *Chemistry & Biology*, 6:891–899, 1999.

[Cooper00a] M. A. Cooper, M. T. Fiorini, C. Abell, and D. H. Williams. Binding of vancomycin group antibiotics to -alanine and -lactate presenting self-assembled monolayers. *Bioorganic & Medicinal Chemistry*, 8:2609–2616, 2000.

[Cooper00b] M. A. Cooper, A. Hansson, S. Löfas, and D. H. Williams. A vesicle capture sensor chip for kinetic analysis of interactions with membrane-bound receptors. *Analytical Biochemistry*, 277(2):196–205, 2000.

[Cooper02] M. A. Cooper. Optical biosensors in drug discovery. *Nature Reviews Drug Discovery*, 1:515–528, 2002.

[Cooper03] M. A. Cooper. Label-free screening of bio-molecular interactions. *Analytical and Bioanalytical Chemistry*, 377(5):834–42, 2003.

[Cooper04] M. A. Cooper. Advances in membrane receptor screening and analysis. *Journal of Molecular Recognition*, 17:286–315, 2004.

[Couchman72] P. Couchman, W. Jesser, D. Kuhlmann-Wilsdorf, and J. Hirth. On the concepts of surface stress and surface strain. *Surface Science*, 33(3):429–436, 1972.

[Cox76] E. C. Cox. Bacterial mutator genes and the control of spontaneous mutation. *Annual Revue Genetics*, 10:135–156, 1976.

[deMol10] N. J. de Mol and M. J. E. Fischer. *Surface plasmon resonance: methods and protocols*. Humana Press, New York, 2010.

[Dhayal06] B. Dhayal, W. A. Henne, D. D. Doorneweerd, R. G. Reifenberger, and P. S. Low. Detection of Bacillus subtilis spores using peptide-functionalized cantilever arrays. *Journal of the Americal Chemical Society*, 128(11):3716–3721, 2006.

[Dove03] A. Dove. Screening for content – the evolution of high throughput. *Nature Biotechnology*, 21(8):859–864, 2003.

[Dubois92] L. H. Dubois and R. G. Nuzzo. Synthesis, Structure, and Properties of Model Organic Surfaces. *Annual Reviews in Physical Chemistry*, 43:437–463, 1992.

[Dubois93] L. H. Dubois, B. R. Zegarski, and R. G. Nuzzo. Molecular ordering of organosulfur compounds on Au(111) and Au(100): Adsorption from solution and in ultrahigh vacuum. *The Journal of Chemical Physics*, 98:678–688, 1993.

[Dueck10] B. Dueck. *Robust Optical Difractive Technique to Read Out Cantilever Detection*. Ph.D. thesis, University College London, 2010.

[Duwez04] A.-S. Duwez. Exploiting electron spectroscopies to probe the structure and organization of self-assembled monolayers: a review. *Journal of Electron Spectroscopy and Related Phenomena*, 134:97–138, 2004.

[Ehrlich13] P. Ehrlich. Address in Pathology, On Chemiotherapy. *British Medical Journal*, 2(2746):353–359, 1913.

[Fernandes06] P. Fernandes. Antibacterial discovery and development – the failure of success? *Nature Biotechnology*, 24(12):1497–1503, 2006.

[Fishman03] M. C. Fishman, A. R. Hoffman, R. D. Klausner, and M. S. Thaler. *Medicine*. Lippincott Williams & Wilkins, 5th edition, 2003. ISBN 978-0781725439.

[Fleming29] A. Fleming. On the antibacterial action of cultures of a Penicillium, with special reference to their use in the isolation of B. influenzae. *British Journal of Experimental Pathology*, 10:226–236, 1929.

[Fritz00] J. Fritz, M. K. Baller, H. P. Lang, H. Rothuizen, P. Vettiger, E. Meyer, H. Güntherodt, C. Gerber, and J. K. Gimzewski. Translating biomolecular recognition into nanmechanics. *Science*, 288:316–318, 2000.

[Fritz08] J. Fritz. Cantilever biosensors. *The Analyst*, 133(7):855–863, 2008.

[Gfeller05] K. Y. Gfeller, N. Nugaeva, and M. Hegner. Rapid Biosensor for Detection of Antibiotic-Selective Growth of Escherichia coli. *Applied and Environmental Microbiology*, 71:2626–2631, 2005.

[Gimzewski94] J. K. Gimzewski, C. Gerber, E. Meyer, and R. R. Schlittler. Observation of a chemical reaction using a micromechanical sensor. *Chemical Physics Letters*, 217:589–594, 1994.

[Godin04] M. Godin, P. J. Williams, V. Tabard-Cossa, O. Laroche, L. Y. Beaulieu, R. B. Lennox, and P. Grütter. Surface stress, kinetics, and structure of alkanethiol self-assembled monolayers. *Langmuir*, 20(17):7090–7096, 2004.

[Godin10a] M. Godin, F. F. Delgado, S. Son, W. H. Grover, A. K. Bryan, A. Tzur, P. Jorgensen, K. Payer, A. D. Grossman, M. W. Kirschner, and S. R. Manalis. Using buoyant mass to measure the growth of single cells. *Nature Methods*, 7(5):5–10, 2010.

[Godin10b] M. Godin, V. Tabard-Cossa, Y. Miyahara, T. Monga, P. J. Williams, L. Y. Beaulieu, R. Bruce Lennox, and P. Grutter. Cantilever-based sensing: the origin of surface stress and optimization strategies. *Nanotechnology*, 21(7):75501, 2010.

[Hagan02] M. F. Hagan, A. Majumdar, and A. K. Chakraborty. Nanomechanical Forces Generated by Surface Grafted DNA. *The Journal of Physical Chemistry B*, 106(39):10163–10173, 2002.

[Haiss01] W. Haiss. Surface stress of clean and adsorbate-covered solids. *Reports on Progress in Physics*, 64(5):591–648, 2001.

[Hansen01] K. M. Hansen, H. F. Ji, G. Wu, R. Datar, R. Cote, A. Majumdar, and T. Thundat. Cantilever-based optical deflection assay for discrimination of DNA single-nucleotide mismatches. *Analytical Chemistry*, 73(7):1567–1571, 2001.

[Hegner98] M. Hegner and P. Wagner. *Procedures in Scanning Probe Microscopes*, chapter 2.2.4 Ultr, pages 169–175. John Wiley & Sons Ltd, 1998.

[Helm05] M. Helm, J. J. Servant, F. Saurenbach, and R. Berger. Read-out of micromechanical cantilever sensors by phase shifting interferometry. *Applied Physics Letters*, 87(6):064101, 2005.

[Herne97] T. M. Herne and M. J. Tarlov. Characterization of DNA Probes Immobilized on Gold Surfaces. *Journal of the American Chemical Society*, 119(38):8916–8920, 1997.

[Hollander70] J. M. Hollander and W. L. Jolly. X-ray photoelectron spectroscopy. *Accounts of Chemical Research*, 3(6):193–200, 1970.

[Holmgren73] J. Holmgren, I. Lonnroth, and L. Svennerholm. Tissue Receptor for Cholera Exotoxin: Postulated Structure from Studies with GM1 Ganglioside and Related Glycolipids. *Infection and Immunity*, 8(2):208–214, 1973.

[Hopwood07] D. Hopwood, S. Levy, R. P. Wenzel, N. Georgopapadakou, R. H. Baltz, S. Bhavnani, and E. Cox. News Feature: A call to arms. *Nature Reviews Drug Discovery*, 6(1):8–12, 2007.

[Huber06] F. Huber, M. Hegner, C. Gerber, H.-J. Güntherodt, and H. P. Lang. Label free analysis of transcription factors using microcantilever arrays. *Biosensors and Bioelectronics*, 21:1599–1605, 2006.

[Hutter93] J. L. Hutter and J. Bechhoefer. Calibration of atomic-force microscope tips. *Review of Scientific Instruments*, 64(7):1868–1873, 1993.

[Ilic04] B. Ilic, H. G. Craighead, S. Krylov, W. Senaratne, C. Ober, and P. Neuzil. Attogram detection using nanoelectromechanical oscillators. *Journal of Applied Physics*, 95(7):3694, 2004.

[Israelachvili92] J. Israelachvili. *Intermolecular & Surface Forces*. Academic Press, London, 2nd edition, 1992. ISBN 0-12-375181-0.

[Janshoff00] A. Janshoff, H.-J. Galla, and C. Steinem. Piezoelectric Mass-Sensing Devices as Biosensors - An Alternative to Optical Biosensors? *Angewandte Chemie*, 39:4004–4032, 2000.

[Jenkins02] A. T. A. Jenkins, R. J. Bushby, S. D. Evans, W. Knoll, A. Offenhausser, and S. D. Ogier. Lipid Vesicle Fusion on μCP Patterned Self-Assembled Monolayers: Effect of Pattern Geometry on Bilayer Formation. *Langmuir*, 18:3176–3180, 2002.

[Jiang03] K. Jiang, A. Eitan, L. S. Schadler, P. M. Ajayan, R. W. Siegel, N. Grobert, M. Mayne, M. Reyes-Reyes, H. Terrones, and M. Terrones. Selective Attachment of Gold Nanoparticles to Nitrogen-Doped Carbon Nanotubes. *Nano Letters*, 3(3):275–277, 2003.

[Johnson08] C. J. Johnson, N. Zhukovsky, A. E. G. Cass, and J. M. Nagy. Proteomics, nanotechnology and molecular diagnostics. *Proteomics*, 8(4):715–30, 2008.

[Kahne05] D. Kahne, C. Leimkuhler, W. Lu, and C. Walsh. Glycopeptide and lipoglycopeptide antibiotics. *Chemical Reviews*, 105(2):425–448, 2005.

[Keller10] S. Keller, D. Haefliger, and A. Boisen. Fabrication of thin SU-8 cantilevers: initial bending, release and time stability. *Journal of Micromechanics and Microengineering*, 20(4):045024, 2010.

[Kelling09] S. Kelling, F. Paoloni, J. Huang, V. P. Ostanin, and S. R. Elliott. Simultaneous readout of multiple microcantilever arrays with phase-shifting interferometric microscopy. *The Review of Scientific Instruments*, 80(9):093101, 2009.

[Kim08] S. J. Kim, L. Cegelski, D. Stueber, M. Singh, E. Dietrich, K. S. E. Tanaka, T. R. P. Jr, A. R. Far, and J. Schaefer. Oritavancin Exhibits Dual Mode of Action to Inhibit Cell-Wall Biosynthesis in Staphylococcus aureus. *Journal of Molecular Biology*, 377(1):281–293, 2008.

[Kim09] S. Kim, T. Rahman, L. R. Senesac, B. H. Davison, and T. Thundat. Piezoresistive cantilever array sensor for consolidated bioprocess monitoring. *Scanning*, 31(5):204–10, 2009.

[Klug83] A. Klug. From Macromolecules to Biological Assemblies (Nobel Lecture). *Angewandte Chemie International Edition*, 22(8):565–582, 1983.

[Knowles08] T. P. J. Knowles, W. Shu, F. Huber, H. P. Lang, C. Gerber, C. M. Dobson, and M. E. Welland. Label-free detection of amyloid growth with microcantilever sensors. *Nanotechnology*, 19(384007):384007, 2008.

[Kumarasamy10] K. K. Kumarasamy, M. A. Toleman, T. R. Walsh, J. Bagaria, F. Butt, R. Balakrishnan, U. Chaudhary, M. Doumith, C. G. Giske, and S. Irfan. Emergence of a new antibiotic resistance mechanism in India, Pakistan, and the UK: a molecular, biological, and epidemiological study. *The Lancet Infectious Diseases*, 10(9):597–602, 2010.

[Laibinis91] P. E. Laibinis, M. A. Fox, J. P. Folkers, and G. M. Whitesides. Comparisons of self-assembled monolayers on silver and gold: mixed monolayers derived from HS(CH2)21X and HS(CH2)10Y (X, Y = CH3, CH2OH) have similar properties. *Langmuir*, 7:3167–3173, 1991.

[Lam01] C. N. C. Lam, R. H. Y. Ko, L. M. Y. Yu, A. Ng, D. Li, M. L. Hair, and A. W. Neumann. Dynamic Cycling Contact Angle Measurements: Study of Advancing and Receding Contact Angles. *Journal of Colloid and Interface Science*, 243(1):208–218, 2001.

[Lang98] H. P. Lang, R. Berger, C. Andreoli, J. Brugger, M. Despont, P. Vettiger, C. Gerber, J. K. Gimzewski, J. P. Ramseyer, E. Meyer, and H.-J. Guntherodt. Sequential position readout from arrays of micromechanical cantilever sensors. *Applied Physics Letters*, 72:383–385, 1998.

[Lang02] H. P. Lang, M. Hegner, E. Meyer, and C. Gerber. Nanomechanics from atomic resolution to molecular recognition based on atomicforce microscopy technology. *Nanotechnology*, 13:R29–R36, 2002.

[Lang05] H. P. Lang, M. Hegner, and C. Gerber. Cantilever array sensors. *Materials Today*, 8(4):30–36, 2005.

[Lang07] H. P. Lang, J. P. Ramseyer, W. Grange, T. Braun, D. Schmid, P. Hunziker, C. Jung, M. Hegner, and C. Gerber. An Artificial Nose Based on Microcantilever Array Sensors. *Journal of Physics: Conference Series*, 61(1):663–667, 2007.

[Lang09] H. Lang, A. Filippi, A. Tonin, F. Huber, N. Backmann, J. Zhang, and C. Gerber. Towards a modular, versatile and portable sensor system for measurements in gaseous environments based on microcantilevers. *Procedia Chemistry*, 1(1):208–211, 2009.

[Langmuir18] I. Langmuir. The adsorption of gases on plane surfaces of glas, mica and platinum. *Journal of the American Chemical Society*, 40(9):1361–1403, 1918.

[Lavrik04] N. V. Lavrik, M. J. Sepaniak, and P. G. Datskos. Cantilever transducers as a platform for chemical and biological sensors. *Review of Scientific Instruments*, 75:2229–2253, 2004.

[Lee Ligon04] B. Lee Ligon. Penicillin: its discovery and early development. *Seminars in Pediatric Infectious Diseases*, 15(1):52–57, 2004.

[Lehn95] J.-M. Lehn. *Supramolecular Chemistry*. VCH Verlagsgesellschaft, Weinheim, 1995. ISBN 3-527-29311-6.

[Li10] F. Li, L. Tang, W. Zhou, and Q. Guo. Resolving the Au-adatom-alkanethiolate bonding site on Au(111) with domain boundary imaging using high-resolution scanning tunneling microscopy. *Journal of the American Chemical Society*, 132(37):13059–63, 2010.

[Lingler97] S. Lingler, I. Rubinstein, W. Knoll, and A. Offenhäusser. Fusion of Small Unilamellar Lipid Vesicles to Alkanethiol and Thiolipid Self-Assembled Monolayers on Gold. *Langmuir*, 13(26):7085–7091, 1997.

[Liu04] K. Liu and H.-F. Ji. Detection of Pb2+ using a hydrogel swelling microcantilever sensor. *Analytical Sciences*, 20(1):9–11, 2004.

[Loll97] P. J. Loll, A. E. Bevivino, B. D. Korty, and P. H. Axelsen. Simultaneous Recognition of a Carboxylate-Containing Ligand and an Intramolecular Surrogate Ligand in the Crystal Structure of an Asymmetric Vancomycin Dimer. *Journal of the American Chemical Society*, 119(7):1516–1522, 1997.

[Loll98] P. J. Loll, R. Miller, C. M. Weeks, and P. H. Axelsen. A ligand-mediated dimerization mode for vancomycin. *Chemistry & Biology*, 5(5):293–298, 1998.

[Loll00] P. J. Loll and P. H. Axelsen. The structural biology of molecular recognition by vancomycin. *Annual Review of Biophysics and Biomolecular Structures*, 29:265–289, 2000.

[Love05] J. C. Love, L. A. Estroff, J. K. Kriebel, R. G. Nuzzo, and G. M. Whitesides. Self-Assembled Monolayers of Thiolates on Metals as a Form of Nanotechnology. *Chemical Reviews*, 105:1103–1170, 2005.

[Mackay94] J. P. Mackay, U. Gerhard, D. A. Beauregard, R. A. Maplestone, and D. H. Williams. Dissection of the Contributions toward Dimerization of Glycopeptide Antibiotics. *Journal of the American Chemical Society*, 116(11):4573–4580, 1994.

[Madigan01] M. T. Madigan, J. M. Martinko, and J. Parker. *Brock Mikrobiologie*. Spektrum Akademischer Verlag, Heidelberg, 2001. ISBN 3-8274-0566-1.

[Maksymovych10] P. Maksymovych, O. Voznyy, D. B. Dougherty, D. C. Sorescu, and J. T. Yates Jr. Gold adatom as a key structural component in self-assembled monolayers of organosulfur molecules on Au(111). *Progress in Surface Science*, 85(5-8):206–240, 2010.

[Malabarba97] A. Malabarba, T. I. Nicas, and R. C. Thompson. Structural modifications of glycopeptide antibiotics. *Medicinal Research Reviews*, 17(1):69–137, 1997.

[Maraldo07] D. Maraldo, F. U. Garcia, and R. Mutharasan. Method for quantification of a prostate cancer biomarker in urine without sample preparation. *Analytical Chemistry*, 79(20):7683–90, 2007.

[McKendry02] R. McKendry, J. Zhang, Y. Arntz, T. Strunz, M. Hegner, H. P. Lang, M. K. Baller, U. Certa, E. Meyer, H.-J. Güntherodt, and C. Gerber. Multiple label-free biodetection and quantitative DNA-binding assays on a nanomechanical cantilever array. *PNAS*, 99:9783–9788, 2002.

[Merritt94] E. A. Merritt, S. Sarfaty, F. van Den Akker, C. L'Hoir, J. A. Martial, and W. G. Hol. Crystal structure of cholera toxin B-pentamer bound to receptor GM1 pentasaccharide. *Protein Science*, 3(2):166–75, 1994.

[Merritt98] E. A. Merritt, P. Kuhn, S. Sarfaty, J. L. Erbe, R. K. Holmes, and W. G. Hol. The 1.25 A resolution refinement of the cholera toxin B-pentamer: evidence of peptide backbone strain at the receptor-binding site. *Journal of Molecular Biology*, 282(5):1043–59, 1998.

[Mertens04] J. Mertens, E. Finot, M.-H. Nadal, V. Eyraud, O. Heintz, and E. Bourillot. Detection of gas trace of hydrofluoric acid using microcantilever. *Sensors and Actuators B*, 99(1):58–65, 2004.

[Mertens08] J. Mertens, C. Rogero, M. Calleja, D. Ramos, J. A. Martín-Gago, C. Briones, and J. Tamayo. Label-free detection of DNA hybridization based on hydration-induced tension in nucleic acid films. *Nature Nanotechnology*, 3(5):301–7, 2008.

[Meyer88] G. Meyer and N. M. Amer. Novel optical approach to atomic force microscopy. *Applied Physics Letters*, 53(12):1045, 1988.

[Mukhopadhyay05] R. Mukhopadhyay, M. Lorentzen, J. Kjems, and F. Besenbacher. Nanomechanical sensing of DNA sequences using piezoresistive cantilevers. *Langmuir*, 21:8400–8408, 2005.

[Ndieyira08] J. W. Ndieyira, M. Watari, A. D. Barrera, D. Zhou, M. Vögtli, M. Batchelor, M. A. Cooper, T. Strunz, M. A. Horton, C. Abell, T. Rayment, G. Aeppli, and R. A. McKendry. Nanomechanical detection of antibiotic-mucopeptide binding in a model for superbug drug resistance. *Nature Nanotechnology*, 3:691–696, 2008.

[Nieba96] L. Nieba, A. Krebber, and A. Plückthun. Competition BIAcore for measuring true affinities: large differences from values determined from binding kinetics. *Analytical Biochemistry*, 234(2):155–65, 1996.

[Nieto71] M. Nieto and H. R. Perkins. Modifications of the acyl-D-alanyl-D-alanine terminus affecting complex-formation with vancomycin. *Biochemical Journal*, 123:789–803, 1971.

[Nitanai09] Y. Nitanai, T. Kikuchi, K. Kakoi, S. Hanamaki, I. Fujisawa, and K. Aoki. Crystal Structures of the Complexes between Vancomycin and Cell-Wall Precursor Analogs. *Journal of Molecular Biology*, 385(5):1422–1432, 2009.

[Nordström07] M. Nordström, D. A. Zauner, M. Calleja, J. Hübner, and A. Boisen. Integrated optical readout for miniaturization of cantilever-based sensor system. *Applied Physics Letters*, 91(10):103512, 2007.

[Nordström08] M. Nordström, S. Keller, M. Lillemose, A. Johansson, S. Dohn, D. Haefliger, G. Blagoi, M. Havsteen-Jakobsen, and A. Boisen. SU-8 Cantilevers for Biochemical Sensing; Fabrication, Characterisation and Development of Novel Read-out Methods. *Sensors*, 8:1595–1612, 2008.

[Nuzzo83] R. G. Nuzzo and D. L. Allara. Adsorption of bifunctional organic disulfides on gold surfaces. *Journal of the American Chemical Society*, 105:4481–4483, 1983.

[Nuzzo87] R. G. Nuzzo, B. R. Zegarski, and L. H. Dubois. Fundamental studies of the chemisorption of organosulfur compounds on gold(111). Implications for molecular self-assembly on gold surfaces. *Journal of the American Chemical Society*, 109:733–740, 1987.

[Oliver09] N. S. Oliver, C. Toumazou, A. E. G. Cass, and D. G. Johnston. Glucose sensors: a review of current and emerging technology. *Diabetic Medicine*, 26(3):197–210, 2009.

[Opar07] A. Opar. Bad bugs need more drugs. *Nature Reviews Drug Discovery*, 6(12):943–944, 2007.

[Pei04] J. Pei, F. Tian, and T. Thundat. Glucose biosensor based on the microcantilever. *Analytical chemistry*, 76(2):292–7, 2004.

[Pera07] I. Pera and J. Fritz. Sensing lipid bilayer formation and expansion with a microfabricated cantilever array. *Langmuir*, 23(3):1543–7, 2007.

[Perkins69] H. R. Perkins. Specificity of combination between mucopeptide precursors and vancomycin or ristocetin. *Biochem. J*, 111:195–205, 1969.

[Pinnaduwage04] L. A. Pinnaduwage. Detection of trinitrotoluene via deflagration on a microcantilever. *Journal of Applied Physics*, 95(10):5871, 2004.

[Poirier97] G. Poirier. Characterization of Organosulfur Molecular Monolayers on Au(111) using Scanning Tunneling Microscopy. *Chemical Reviews*, 97:1117–1128, 1997.

[Porter07] T. L. Porter, T. L. Vail, M. P. Eastman, R. Stewart, J. Reed, R. Venedam, and W. Delinger. A solid-state sensor platform for the detection of hydrogen cyanide gas. *Sensors and Actuators B: Chemical*, 123(1):313–317, 2007.

[Raiteri01] R. Raiteri, M. Grattarola, H. J. Butt, and P. Skládal. Micromechanical cantilever-based biosensors. *Sensors and Actuators B*, 79(2-3):115–126, 2001.

[Raiteri02] R. Raiteri, M. Grattarola, and R. Berger. Micromechanics senses biomolecules. *Materials Today*, 5(1):22–29, 2002.

[Rao99] J. Rao, L. Yan, B. Xu, and G. M. Whitesides. Using Surface Plasmon Resonance to Study the Binding of Vancomycin and Its Dimer to Self-Assembled Monolayers Presenting d Ala-d-Ala. *Journal of the American Chemical Society*, 121(11):2629–2630, 1999.

[Richter06] R. P. Richter, R. Bérat, and A. R. Brisson. Formation of solid-supported lipid bilayers: an integrated view. *Langmuir*, 22(8):3497–505, 2006.

[Rothemund06] P. W. K. Rothemund. Folding DNA to create nanoscale shapes and patterns. *Nature*, 440(7082):297–302, 2006.

[Rotschafer82] J. C. Rotschafer, K. Crossley, D. E. Zaske, K. Mead, R. J. Sawchuk, and L. D. Solem. Pharmacokinetics of vancomycin: observations in 28 patients and dosage recommendations. *Antimicrobial Agents and Chemotherapy*, 22(3):391–394, 1982.

[Rowe08] A. C. H. Rowe, A. Donoso-Barrera, C. Renner, and S. Arscott. Giant Room-Temperature Piezoresistance in a Metal-Silicon Hybrid Structure. *Physical Review Letters*, 100:145501–145504, 2008.

[Savran03] C. A. Savran, T. P. Burg, J. Fritz, and S. R. Manalis. Microfabricated mechanical biosensor with inherently differential readout. *Applied Physics Letters*, 83(8):1659–1661, 2003.

[Savran04] C. A. Savran, S. M. Knudsen, A. D. Ellington, and S. R. Manalis. Micromechanical detection of proteins using aptamer-based receptor molecules. *Analytical chemistry*, 76(11):3194–8, 2004.

[Schäfer96] M. Schäfer, T. R. Schneider, and G. M. Sheldrick. Crystal structure of vancomycin. *Structure*, 4:1509–1515, 1996.

[Schmid08] D. Schmid, H. Lang, C. Gerber, and P. Hunziker. Diagnosing disease by nanomechanical olfactory sensors - system design and clinical validation. *European Journal of Nanomedicine*, 1(1):44–47, 2008.

[Schreiber00] F. Schreiber. Structure and growth of self-assembling monolayers. *Progress in Surface Science*, 65:151–257, 2000.

[Schwartz01] D. K. Schwartz. Mechanisms and kinetics of self-assembled monolayer formation. *Annual Reviews in Physical Chemistry*, 52:107–137, 2001.

[Schwendel03] D. Schwendel, T. Hayashi, R. Dahint, A. Pertsin, M. Grunze, R. Steitz, and F. Schreiber. Interaction of Water with Self-Assembled Monolayers: Neutron Reflectivity Measurements of the Water Density in the Interface Region. *Langmuir*, 19:2284–2293, 2003.

[Shekhawat06] G. Shekhawat, S.-H. Tark, and V. P. Dravid. MOSFET-Embedded Microcantilevers for Measuring Deflection in Biomolecular Sensors. *Science*, 311:1592–1595, 2006.

[Sheng07] P. P. Sheng and T. H. Etsell. Recovery of gold from computer circuit board scrap using aqua regia. *Waste Management & Research*, 25(4):380–383, 2007.

[Shu07] W. Shu, E. D. Laue, and A. A. Seshia. Investigation of biotin-streptavidin binding interactions using microcantilever sensors. *Biosensors and Bioelectronics*, 22:2003–2009, 2007.

[Shuttleworth50] R. Shuttleworth. The Surface Tension of Solids. *Proceedings of the Physical Society*, 63(5):444–457, 1950.

[Singh06] S. B. Singh and J. F. Barrett. Empirical antibacterial drug discovery–Foundation in natural products. *Biochemical Pharmacology*, 71(7):1006–1015, 2006.

[Smith80] T. Smith. The hydrophilic nature of a clean gold surface. *Journal of Colloid and Interface Science*, 75(1):51–55, 1980.

[Spencelayh06] M. J. Spencelayh, Y. Cheng, R. J. Bushby, T. D. H. Bugg, J.-J. Li, P. J. F. Henderson, J. O'Reilly, and S. D. Evans. Antibiotic action and peptidoglycan formation on

tethered lipid bilayer membranes. *Angewandte Chemie International Edition*, 45(13):2111–6, 2006.

[Srinivasan08] V. Srinivasan, G. Cicero, and J. C. Grossman. Adsorption-Induced Surface Stresses in Alkanethiolate-Au Self-Assembled Monolayers. *Physical Review Letters*, 101(18):185504, 2008.

[Stachowiak06] J. C. Stachowiak, M. Yue, K. Castelino, A. Chakraborty, and A. Majumdar. Chemomechanics of surface stresses induced by DNA hybridization. *Langmuir*, 22(1):263–268, 2006.

[Stauffer94] D. Stauffer and A. Aharony. *Introduction to percolation theory*. CRC press, 1994.

[Stoney09] G. G. Stoney. The Tension of Metallic Films Deposited by Electrolysis. *Proceedings of the Royal Society of London*, 82(553):172–175, 1909.

[Strong88] L. Strong and G. M. Whitesides. Structures of self-assembled monolayer films of organosulfur compounds adsorbed on gold single crystals: electron diffraction studies. *Langmuir*, 4:546–558, 1988.

[Su02] J. Su and M. Mrksich. Using mass spectrometry to characterize self-assembled monolayers presenting peptides, proteins, and carbohydrates. *Angewandte Chemie International Edition*, 41(24):4715–8, 2002.

[Sushko09] M. L. Sushko. Nanomechanics of organic/inorganic interfaces: a theoretical insight. *Faraday Discussions*, 143:63, 2009.

[Tark09] S.-H. Tark, A. Srivastava, S. Chou, G. Shekhawat, and V. P. Dravid. Nanomechanoelectronic signal transduction scheme with metal-oxide-semiconductor field-effect transistor-embedded microcantilevers. *Applied Physics Letters*, 94(10):104101, 2009.

[Taubes08] G. Taubes. The Bacteria Fight Back. *Science*, 321:356–361, 2008.

[Terrettaz93] S. Terrettaz, T. Stora, C. Duschl, and H. Vogel. Protein Binding to Supported Lipid Membranes : Investigation of the Cholera Toxin-Ganglioside Interaction by Simultaneous Impedance Spectroscopy and Surface Plasmon Resonance. *Langmuir*, 9:1361–1369, 1993.

[Thundat94] T. Thundat, R. J. Warmack, G. Y. Chen, and D. P. Allison. Thermal and ambient-induced deflections of scanning force microscope cantilevers. *Applied Physics Letters*, 64(21):2894, 1994.

[Tompkins05] H. G. Tompkins and E. A. Irene. *Handbook of Ellipsometry*. William Andrew Publishing, Norwich, 2005. ISBN 0-8155-1499-9.

[Tortonese93] M. Tortonese, R. C. Barrett, and C. F. Quate. Atomic resolution with an atomic force microscope using piezoresistive detection. *Applied Physics Letters*, 62:834–836, 1993.

[Ulman96] A. Ulman. Formation and structure of self-assembled monolayers. *Chemical Reviews*, 96:1533–1554, 1996.

[Uttley88] A. H. Uttley, C. H. Collins, J. Naidoo, and R. C. George. Vancomycin-resistant enterococci. *Lancet*, 1(8575-6):57–58, 1988.

[vanHeijenoort01] J. van Heijenoort. Recent advances in the formation of the bacterial peptidoglycan monomer unit. *Natural Product Reports*, 18(5):503–519, 2001.

[Velanki06] S. Velanki and H.-F. Ji. Detection of feline coronavirus using microcantilever sensors. *Measurement Science and Technology*, 17(11):2964–2968, 2006.

[Velanki07] S. Velanki, S. Kelly, T. Thundat, D. a. Blake, and H.-F. Ji. Detection of Cd(II) using antibody-modified microcantilever sensors. *Ultramicroscopy*, 107(12):1123–8, 2007.

[Voiculescu05] I. Voiculescu, M. Zaghloul, R. McGill, E. Houser, and G. Fedder. Electrostatically actuated resonant microcantilever beam in CMOS technology for the detection of chemical weapons. *IEEE Sensors Journal*, 5(4):641–647, 2005.

[Walsh96] C. T. Walsh, S. L. Fisher, I. S. Park, M. Prahalad, and Z. Wu. Bacterial resistance to vancomycin: five genes and one missing hydrogen bond tell the story. *Chemistry & Biology*, 3(1):21–28, 1996.

[Waltho89] J. P. Waltho and D. H. Williams. Aspects of Molecular Recognition: Solvent Exclusion and Dimerization of the Antibiotic Ristocetin When Bound to a Model Bacterial Cell-Wall Precursor. *Journal of the American Chemical Society*, 111:2475–2480, 1989.

[Wanunu04] M. Wanunu, A. Vaskevich, and I. Rubinstein. Widely-Applicable Gold Substrate for the Study of Ultrathin Overlayers. *Journal of the American Chemical Society*, 126:5569–5576, 2004.

[Watari07a] M. Watari. *In-plane Mechanochemistry at Model Biological Interfaces*. Ph.D. thesis, University College London, 2007.

[Watari07b] M. Watari, J. Galbraith, H.-P. Lang, M. Sousa, M. Hegner, C. Gerber, M. A. Horton, and R. A. McKendry. Investigating the molecular mechanisms of in-plane mechanochemistry on cantilever arrays. *Journal of the Americal Chemical Society*, 129(3):601–609, 2007.

[Watari10] M. Watari, J. W. Ndieyira, and R. A. McKendry. Chemically programmed nanomechanical motion of multiple cantilever arrays. *Langmuir*, 26(7):4623–6, 2010.

[Wee05] K. W. Wee, G. Y. Kang, J. Park, J. Y. Kang, D. S. Yoon, J. H. Park, and T. S. Kim. Novel electrical detection of label-free disease marker proteins using piezoresistive self-sensing micro-cantilevers. *Biosensors and Bioelectronics*, 20:1932–1938, 2005.

[Wehrmeister07] J. Wehrmeister, A. Fuss, F. Saurenbach, R. Berger, and M. Helm. Readout of micromechanical cantilever sensor arrays by Fabry-Perot interferometry. *Review of Scientific Instruments*, 78:104105–104109, 2007.

[Whitesides90] G. M. Whitesides and P. E. Laibinis. Wet chemical approaches to the characterization of organic surfaces: self-assembled monolayers, wetting, and the physical-organic chemistry of the solid-liquid interface. *Langmuir*, 6:87–96, 1990.

[Whitesides91] G. Whitesides, J. Mathias, and C. Seto. Molecular self-assembly and nanochemistry: a chemical strategy for the synthesis of nanostructures. *Science*, 254(5036):1312–1319, 1991.

[Whitesides02] G. M. Whitesides and B. Grzybowski. Self-assembly at all scales. *Science*, 295(5564):2418–21, 2002.

[Williams83] D. H. Williams, M. P. Williamson, D. W. Butcher, and S. J. Hammond. Detailed binding sites of the antibiotics vancomycin and ristocetin A: determination of intermolecular distances in antibiotic/substrate complexes by use of the time-dependent NOE. *Journal of the American Chemical Society*, 105(5):1332–1339, 1983.

[Williams84] D. H. Williams. Structural studies on some antibiotics of the vancomycin group, and on the antibiotic-receptor complexes, by proton NMR. *Accounts of Chemical Research*, 17(10):364–369, 1984.

[Williams96] D. H. Williams. The glycopeptide story - how to kill the deadly 'superbugs'. *Natural Product Reports*, 13:469–477, 1996.

[Williams99] D. H. Williams and B. Bardsley. The Vancomycin Group of Antibiotics and the Fight against Resistant Bacteria. *Angewandte Chemie International Edition*, 38:1172–1193, 1999.

[Wu01a] G. Wu, R. H. Datar, K. M. Hansen, T. Thundat, R. J. Cote, and A. Majumdar. Bioassay of prostate-specific antigen (PSA) using microcantilevers. *Nature Biotechnology*, 19:856–860, 2001.

[Wu01b] G. Wu, H. Ji, K. Hansen, T. Thundat, R. Datar, R. Cote, M. F. Hagan, A. K. Chakraborty, and A. Majumdar. Origin of nanomechanical cantilever motion generated from biomolecular interactions. *PNAS*, 98(4):1560–4, 2001.

[Xu10] S. Xu and R. Mutharasan. Rapid and sensitive detection of Giardia lamblia using a piezoelectric cantilever biosensor in finished and source waters. *Environmental Science & Technology*, 44(5):1736–41, 2010.

[Yan06] X. Yan, X. Shi, K. Hill, and H.-F. Ji. Microcantilevers modified by horseradish peroxidase intercalated nano-assembly for hydrogen peroxide detection. *Analytical Sciences*, 22(2):205–8, 2006.

[Yang03] G. Yang and G.-y. Liu. New Insights for Self-Assembled Monolayers of Organothiols on Au(111) Revealed by Scanning Tunneling Microscopy. *Journal of Physical Chemistry B*, 107:8746–8759, 2003.

[Yaralioglu98] G. G. Yaralioglu, A. Atalar, S. R. Manalis, and C. F. Quate. Analysis and design of an interdigital cantilever as a displacement sensor. *Journal of Applied Physics*, 83(12):7405, 1998.

[Yoshikawa09] G. Yoshikawa, H.-P. Lang, T. Akiyama, L. Aeschimann, U. Staufer, P. Vettiger, M. Aono, T. Sakurai, and C. Gerber. Sub-ppm detection of vapors using piezoresistive microcantilever array sensors. *Nanotechnology*, 20(1):015501, 2009.

[Zaritsky79] A. Zaritsky, C. Woldringh, and D. Mirelman. Constant peptidoglycan density in the sacculus of Escherichia coli B/r .... *FEBS Lett*, 1979.

[Zhang95] R. G. Zhang, D. L. Scott, M. L. Westbrook, S. Nance, B. D. Spangler, G. G. Shipley, and E. M. Westbrook. The three-dimensional crystal structure of cholera toxin. *Journal of Molecular Biology*, 251(4):563–73, 1995.

[Zhang06] J. Zhang, H. P. Lang, F. Huber, A. Bietsch, W. Grange, U. Certa, R. McKendry, H.-J. Güntherodt, M. Hegner, and C. Gerber. Rapid and label-free nanomechanical detection of biomarker transcripts in human RNA. *Nature Nanotechnology*, 1(3):214–220, 2006.